An anti-solvent/solvent mixture approach for pharmaceutical cocrystals and salt at pilot-scale

ODIASE, ISAAC,UHUNOMAH

How to cite:

ODIASE, ISAAC,UHUNOMAH (2014) *An anti-solvent/solvent mixture approach for pharmaceutical cocrystals and salt at pilot-scale*, Durham theses, Durham University. Available at Durham E-Theses Online: http://etheses.dur.ac.uk/10566/

An anti-solvent/solvent mixture approach for pharmaceutical cocrystals and salt at pilot-scale

Isaac Uhunomah Odiase

A thesis submitted for the degree of Doctor of Philosophy at the University of Durham

Department of Chemistry

October 2013

Abstract

Cocrystals have generated a lot of interest due their ability to influence: physiochemical properties, optical properties etc. These properties are important in the pharmaceutical and food industry.

In this thesis, the scale up of cocrystal synthesis is studied using a novel slurry cocrystallisation approach involving an anti-solvent and solvent mixture. The anti-solvent composition is typically > 97 %, with the solvent comprising the rest. This counter-intuitive approach resulted in > 95 % caffeine-oxalic acid cocrystal yield in less than 2 hrs. The mixed anti-solvent/solvent approach was applied successfully to four other cocrystal systems and a salt.

The level of caffeine-oxalic acid cocrystal yield observed varied with the solvent used in the mixture. Using statistical analysis, it was shown that the hydrogen bonding Hansen solubility parameter (δ_H) of the solvent and oxalic acid solubility were the two most important factors for increasing cocrystal yield. The parameter $\frac{\mathrm{Ra}}{\mathrm{Oxalic\ acid}}$, however, showed even better correlation (94.2 %) with caffeine-oxalic acid cocrystal yield than both δ_H (78 %) and oxalic acid solubility (88 %). Ra is the Hansen solubility distance between the solvent and the coformer (oxalic acid) and includes all three Hansen solubility parameters (δ_D, δ_P, δ_H).

Four new cocrystals (**A**-**D**) of 2-aminopyrimdine-glutaric acid were crystallised from three different solvents and their crystal structures reported. Two of them (**A** and **B**) are 1:1 polymorphs. The glutaric acid molecule in **A** has a linear conformation but it is twisted in **B**. Variable temperature PXRD analysis indicates that **A** and **B** are monotropic polymorphs, with **A** transforming to **B** at ≈73°C, prior to the melting of **B**. **D** is a cocrystal-salt hybrid. **D** was crystallised from the same solvent as cocrystal **B** supporting the idea of a cocrystal-salt continuum when both the neutral and ionic forms are present in appreciable concentrations in solution.

Acknowledgements

I want to thank my supervisor Dr. Sharon Cooper for her advice, encouragement and support throughout the PhD research. I also want to show my appreciation for support from the following colleagues: Dr. Cen Chen, Dr. Catherine Nicholson, Natasha Hargreaves, Dr. Reduwan Billah, Merhwin Chowdhury, Helen Ramsey, Janet French, Nyasha Ntola and Helen Riggs.

My appreciation goes to Dr. Paul Hodgkinson, Dr. David Apperley and Frasier Markwell for their advice and suggestions in solid-state nuclear magnetic resonance analysis; and to Dr. Dmitry Yufit for the X-ray crystallography analysis.

My gratitude goes to the following colleagues at the Centre for Process Innovation (CPI): Dr. Ruksanna Ahmad, Dr. Jerry Cooper, Dr. Scot Sanders, Dr. Emma Stokes, Dr. Malcolm Lock, Ivan Lowdon, Dr. Peter Setchell, Denis Wray, Daniel Wallis and Alison Kent; for their support and advice during the industrial aspect of the research.

I want to acknowledge the Technical Strategy Board (TSB), CPI and Durham University for funding the Knowledge Transfer Partnership (KTP).

My heartfelt appreciations go to my family and friends for their support. To my wife Catherine and my sons Daniel and Raphael for their love, patience and for allowing me to spend late hours away from home during this period.

Finally my appreciation goes to God for sustaining me throughout my PhD.

Statement of Copyright

List of abbreviations

API	Active Pharmaceutical Ingredient
ATR-FTIR	Attenuated Total Reflection Fourier Transform Infrared
CNT	Classical Nucleation Theory
CV	Coefficient of Variance
CP	Cross Polarisation
CPI	Centre for Process Innovation
DAD	Diode Array Detector
DSC	Differential Scanning Calorimetry
KTP	Knowledge Transfer Partnership
LOQ	Limit of Quantification
LOD	Limit of Detection
MAS	Magic Angle Spinning
OBR	Oscillatory Baffle Reactor
o.d	Outer diameter for solid state nuclear magnetic simple rotor
PFA	Polyfluoroalkoxy
PPU	Particulate Processing Unit
PSD	Particle Size Distribution
PTFE	Polytetrafluoroethylene
PXRD	Powder X-ray Diffraction
rpm	Revolution per minute
S.E	Standard Error
SSNMR	Solid State Nuclear Magnetic Resonance
STR	Stirred Tank Reactor
SVC	Single Vertical Column
TSB	Technical Strategy Board

List of symbols

$\Delta\mu$	Change in chemical potential
γ	Interfacial energy
ΔG_{het}^{*}	Gibbs energy for heterogeneous nucleation
ΔG_{homo}^{*}	Gibbs energy for homogeneous nucleation
$\mathcal{F}(\theta)$	Wetting function for heterogeneous nucleation
J	Nucleation rate
Ω	Pre-exponential factor for nucleation rate
Re_o	Oscillatory Reynolds number
Re_n	Net flow Reynolds number
x_O	Stroke amplitude of the pump in meters (m)
ρ	Density of the fluid in kg m^{-3}
μ	Viscosity of the fluid in kg m^{-1} s^{-1}
D	Diameter of the tubular reactor in meters (m)
f	Oscillating frequency of the pump in hertz (Hz)
^{13}C	Carbon-13 isotope
s	Standard deviation
$\bar{x}$	Mean
r	Correlation coefficient
R^2	Coefficient of determination
δ_T	Hildebrand solubility parameter
δ_P	Hasen solubility parameter for dipole-dipole force density
δ_H	Hansen solubility parameter for hydrogen bonding force density
δ_D	Hansen solubility parameter for non-polar atomic forces density
Ra	Hansen solubility parameter distance
Da	Damkohler number
τ_{mix}	Time for complete phase mixing
$\tau_{precipitation}$	Time delay for precipitation to occur

List of Figures

Chapter 1

Chapter 2

Chapter 3

Chapter 4

Chapter 5

Chapter 6

List of Tables

Chapter 1

Chapter 2

Chapter 3

Chapter 4

Chapter 6

Table of Contents

Chapter 1 Introduction

1.1 Background

This project is a Knowledge Transfer Partnership (KTP) between the Centre for Process Innovation (CPI) and Durham University funded by the UK Technical Strategy Board (TSB). The aim is to scale up the manufacture of pharmaceutical cocrystal in an oscillatory baffle reactor (OBR) to allow for continuous manufacture of pharmaceutical cocrystals. Hydrogen-bonded cocrystals are the focus of this project because of their higher prevalence in the literature compared to other types of cocrystal bonds.

Cocrystals are a class of multi-component crystals that have two or more different molecules residing in a single crystal lattice. This class of crystals have applications in agrochemicals, as optical crystals, as dyes and in the pharmaceutical industry[1,2].

In the pharmaceutical industry, the delivery of an API (active pharmaceutical ingredient) in drug form which is safe, cost effective and efficient is largely governed by the physiochemical properties of the API in the solid state[3]. Improvement of physiochemical properties of the API solid forms are done through: control of polymorphism, salt screens, hydrates/solvates formation and cocrystal formation. The importance of the solid state form is readily apparent when one considers that more than half of the drugs in the pharmaceutical market are produced in solid form[4,5].

This literature review focuses on the cocrystal class of multi-component crystals. It covers the definition, emergence, engineering, solubility, stability and analysis of cocrystals, with particular emphasis on the relevance of cocrystals to the pharmaceutical industry**.**

1.1.1 What are Cocrystals?

Cocrystal multi-component crystals consist of two or more molecules held together by non-covalent bonds (e.g. hydrogen bonding, halogen bonding, π-stacking etc) in stoichiometric ratio. The components could be neutral or ionic molecules, which are solids at ambient temperature and pressure[6].

The criteria that cocrystal components should be solids at ambient temperature and pressure[2,6] distinguishes cocrystal from other multi-component crystals such as solvates and hydrates. Fig. 1.1 is a pictorial illustration of the different types of crystals.

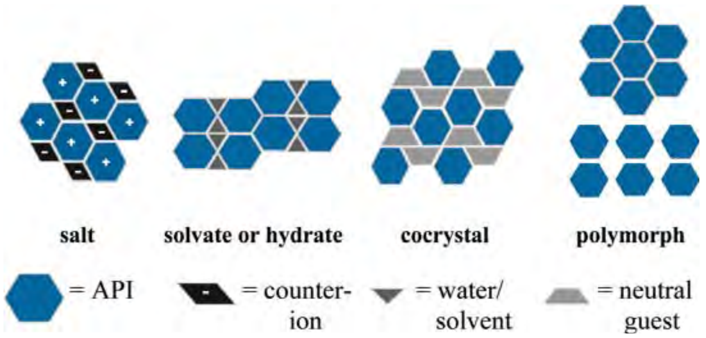

Fig. 1.1 Pictorial description of different crystal type[4]. Polymorphism can exist in salt, cocrystal, salts and hydrates.

Solvates and hydrates often form without being designed and so their exclusion from the definition of a cocrystal helps preserve the design approach inherent in cocrystal engineering[2]. The design approach in cocrystal engineering is useful in patent applications for cocrystal compounds.

The requirement that all components exist as solid at room temperature is still debated[7]; the counter argument allows for components to be liquid at room temperature[8,9], instead focusing on the neutrality of the resulting multi-component crystal and can be valid when viewing cocrystals and salts as two ends of a continuum. In comparison, the definition of a salt does not require components to be solid at room temperature or pressure. However, the exclusion of solvates and hydrates from the definition of a cocrystal does not have an adverse effect, whereas their inclusion in the same class with cocrystal could blur the design approach in cocrystal engineering.

1.1.2 Pharmaceutical Cocrystals

Pharmaceutical cocrystals consist of an API and a coformer, with the API having a desirable pharmaceutical activity. Coformers are crystalline solids usually selected from the generally recognized as safe-(GRAS) or EAFUS (Everything Added to Food in the US) list of the America Food and Drug Agency (FDA). A coformer often forms hydrogen bonds with the API to modify its physiochemical properties.

Pharmaceutical cocrystals are not dissimilar from pharmaceutical salts; they are both classified as multi-component crystals and both exhibit polymorphism. Salts are well established in the pharmaceutical industry, and are used for improving physicochemical properties of ionisable API’s. Salts are formed between the basic and acidic functionality in the reacting components; a complete proton transfer from the acid to the base occurs resulting in an ionic bond. In cocrystals, molecular recognition between the components results in the formation of non-covalent bonds without the transfer of a proton [8,10].

In recent years[11-13] the pharmaceutical industry's interest in cocrystals has increased. This is due to the potential of designing drug delivery at the molecular level[14]. Cocrystals open up the opportunity for extending intellectual property life over existing drug molecules. Other benefits of cocrystal technology are:

1 The potential of forming solid forms of drug molecules that do not have the ionisable functionality (acid or base) required for salt formation[8,13], because cocrystals can be formed via halogen bonding, π-stacking etc.

2 The list of possible coformer molecules for cocrystal screening are much larger than for salt screening[10,13,15].

3. The physiochemical properties of the existing API i.e. solubility[16], dissolution rate, stability[17], mechanical property[18], compacting property[19], moisture-uptake[17] etc. can be improved with cocrystal technology e.g. the API Itraconazole, showed improved solubility and dissolution when cocrystallised with carboxylic acids[20].

5. The potential to design drug-drug cocrystals (by substituting the coformer with another API) to produce novel therapeutic agents. Reported examples of this approach are: anti-HIV drugs Lamivudine and Zidovudine[11], Theophylline, an asthma drug, and Sulfamethazine, an anti-bacteria drug[14]. This approach allows simultaneous drug delivery, helping to prevent the occurrence of drug resistant strains[21] and reducing the number of tablets taken by patients.

6. Cocrystals are potentially more stable that solvates or hydrates as solid drug forms in storage, thereby they have the potential for a long shelf life. This is so because coformers are solids at ambient, they are less mobile than solvents or water so there is a reduced tendency for evaporation, resulting in a phase changes[2].

The condition in premature babies leading to cessation of breathing and referred to as "Apnea of pre-maturity" is treated with a mixture of caffeine-citrate. This mixture is believed to be a cocrystal of caffeine and citric acid[15] and is evidence that cocrystal already plays a role in the pharmaceutical industry.

However, despite the interest in pharmaceutical cocrystals, there are still hurdles to be scaled for this technology to become widely accepted. Some of these challenges are:

- The development of a scaleable process to enable large scale manufacture of cocrystals[22]. In particular, many of the methods adopted for laboratory scale synthesis of cocrystals, that is grinding, melting etc., are not easily scaleable[23]. Solution cocrystallisation represents the best option for large scale manufacture of cocrystals because solution crystallisation processes are established in the pharmaceutical industry. Solution cocrystallisation does have its challenges, though. It requires a proper understanding of the phase diagram and interaction of all components in solution, which is not easy to determine[13] and it is also affected by changes in solvent.
- Cocrystal screening is done by a trial and error approach[13], as the level of understanding of cocrystal formation does not allow for easy prediction of its occurrence. The large number of possible coformers, solvents, stoichiometric ratios etc., also adds to the challenge.
- The classification of pharmaceutical cocrystals by the food and drug agency (FDA)[24] could impact on the perceived attractiveness of cocrystals as potential target drug molecules. The draft classification guideline currently does not view cocrystals as novel molecules hence making intellectual property protection on new cocrystals difficult[25].

1.2 Crystallisation

Cocrystallisation involves the crystallisation of two or more different molecules in a single crystal lattice. Crystallisation can be broken into two stages: nucleation and crystal growth. Nucleation involves the transport of molecules from the gas or liquid phase to the solid phase to form a nucleus that is stable. This is favoured when the concentration of the nucleating species exceeds its solubility limit, which is the maximum concentration permissible in the solvent (liquid or gas) phase at the given pressure and temperature for the system. Crystal growth covers the growth post nucleation. A review of crystal nucleation and growth is necessary for studying cocrystallisation.

1.2.1 Crystallisation Theory

Matter exists in three main phases: gas, liquid or solid, with an imaginary boundary separating the different phases (Fig. 1.2). The boundary is specific for different matter and varies with the pressure and temperature of the system. Energy change is required for transition from one phase to another.

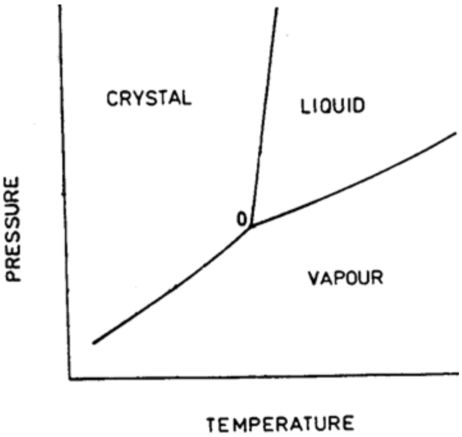

Fig. 1.2 Phase diagram of a single component system in P-T co-ordinates[26].

A phase transition occurs spontaneously if there is sufficient available energy (at constant pressure, this is the Gibbs energy) to drive it. A favourable transition results in the utilisation of this driving force (G), until equilibrium is attained ($\Delta G = 0$), at which point no net transition is observed. For a system at constant temperature and pressure, the Gibbs free energy change (ΔG), can be expressed in terms of enthalpy (ΔH) and entropy (ΔS) contributions (Eqn. 1.1):

$$\Delta G = \Delta H - T\Delta S \qquad \text{Eqn. 1.1}$$

When the Gibbs energy is negative the given transition is favoured and occurs spontaneously until equilibrium is attained. For a multiphase system, the Gibbs free energy is the sum of the driving energy for each phase, described by the chemical potential (μ) given in Eqn. 1.2.

$$\mu_i = \frac{\partial G}{\partial n_i} \qquad \text{Eqn. 1.2}$$

If the chemical potential difference ($\Delta\mu$) of the component in the different phases = 0, equilibrium is achieved. No net transition between phases is observed because of the absence of a driving force for a phase transition. When a chemical potential differences ($\Delta\mu$) exist between phases, a net phase transition can occur. The chemical potential difference ($\Delta\mu$) depends on the concentration of the nucleating species in the different phases involved.

For liquid/solid phases (Fig. 1.3 and 1.4), the solubility of a solute (C_{Solution}) varies with temperature and pressure. At constant temperature and pressure, a limit of solubility is attained when no more solute dissolves in the solvent, this is called the saturation point and can be represented as $C_{\text{equilibrium}}$. Fig. 1.4 shows a hypothetical solubility curve and the different regions of saturation.

When the chemical potential (μ) in the liquid phase is higher than in the solid phase, a phase transition from solute to crystal is favoured.

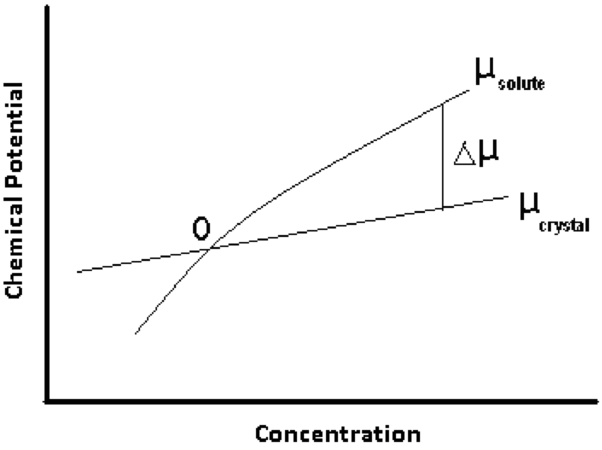

Fig. 1.3 Illustration of change in chemical potential with concentration at constant temperature[26].

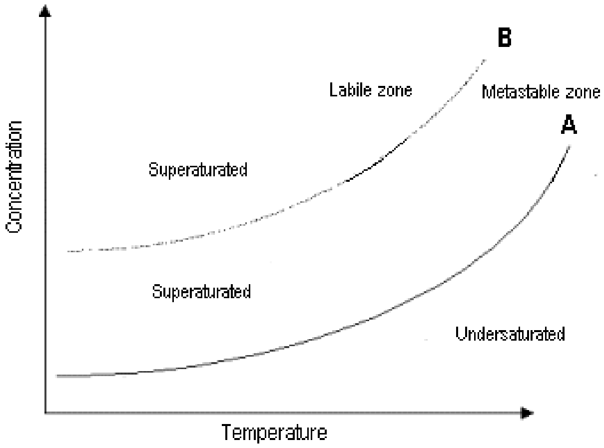

Fig. 1.4 Illustration of crystallisation using solubility curve.

Below curve A in Fig. 1.4, the solution is said to be undersaturated because the solute solubility limit has not been attained ($\Delta\mu < 0$) and no driving force exists for crystallisation.

$$C_{\text{Solution}} < C_{\text{equilibrium}}$$

Curve A represents the equilibrium saturation concentration, along this line the solubility limit of the solute is reached but no solid (crystal) is present, here

$$\Delta\mu = 0 \text{ and } C_{\text{Solution}} = C_{\text{equilibrium}}$$

Above A, the concentration limit of the solute is exceeded, $C_{\mathrm{Solution}} > C_{\mathrm{equilibrium}}$, the system is supersaturated (Δμ > 0) and a driving force for crystallisation exists.

The level of supersaturation (Δμ) for an ideal solution is given by[27]:

$$\Delta\mu = RT \ln \frac{C_{\mathrm{solution}}}{C_{\mathrm{equilibrium}}} \quad \text{Eqn. 1.3}$$

For non-ideal solutions, the concentrations in Equation 1.3 need to be replaced by activities, but often ideal behaviour is assumed. The supersaturated region is divided into two zones; the metastable zone and the labile zone. The metastable zone is the region between curve A and B in Fig. 1.4. In this region, Δμ is positive but has a low value. Here nucleation can occur but the number of new nuclei formed is very low and crystal growth occurs in preference to further nucleation (the energy requirements for crystal growth is lower than that for nucleation). This region favours the growth of single crystals for PXRD single crystal analysis.

The labile region above curve B represents the high end of the supersaturation region. In this region, nucleation can be faster than crystal growth. An understanding of the metastable zone width can provide useful information for controlling nucleation density and crystal size distribution during crystallisation.

1.2.2 Nucleation

The classical nucleation theory (CNT) explains in the simplest terms the nucleation process in crystals; it assumes a spherical droplet shape for the new nuclei. Nucleation can either be homogeneous or heterogeneous depending on whether nucleation is from the bulk liquid/solution or onto a surface present in the system.

1.2.3 Homogeneous nucleation

Homogeneous nucleation occurs from within the bulk of a uniform system that is supersaturated. The Gibbs energy change (ΔG) for formation of a spherical nucleus is given by[27]:

$$\Delta G = -\frac{4\pi r^3}{3\nu_c}(\Delta\mu) + 4\pi r^2 \gamma \qquad \text{Eqn. 1.4}$$

where ν_c is the molecular volume of the cluster and Δμ is the chemical potential difference between the crystal and solute phases.

The first term ($-\frac{4\pi r^3}{3\nu_c}(\Delta\mu)$) in Eqn. 1.4 is the energy released during nucleation. The second term ($4\pi r^2 \gamma$) is the work required to create the interface between the solute and crystal. The contribution of these competing energy terms for homogeneous nucleation is illustrated in Fig. 1.5. In Eqn. 1.3, r, the radius of the cluster, increases by a power of 3 in the first term but by a power of 2 in the second term. Initially as the cluster grows, the work requirement dominates over the energy released but as the cluster continues to grow by the addition of new solute onto its surface, a radius maximum r^* is attained. After this point, the probability for further growth occurring is higher than that for dissolution. The radius r^* is referred to as the critical nucleus radius.

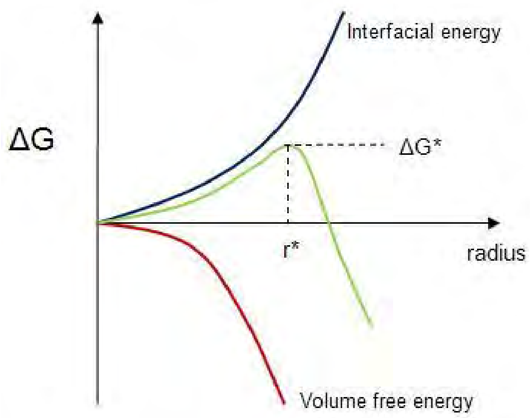

Fig. 1.5 Illustration on Gibbs energy change during homogeneous nucleation.

Below r^* any nuclei formed will tend to re-dissolve, while above r^* clusters tend to grow.

Differentiating Eqn. 1.4 with respect to r gives:

$$\frac{\mathrm{d}\Delta \mathrm{G}}{\mathrm{dr}} = -\frac{4\pi \mathrm{r}^2}{\nu_c}\Delta\mu + 8\pi \mathrm{r}\gamma \qquad \text{Eqn. 1.5}$$

Equating Eqn. 1.5 to zero gives the maximum for r, i.e. the critical cluster radius, r^* :

$$\mathrm{r}^* = \frac{2\gamma\nu_c}{\Delta\mu} \qquad \text{Eqn. 1.6}$$

Substituting Eqn. 1.6 into Eqn. 1.4 gives the energy barrier for nucleation in a supersaturated system.

$$\Delta \mathrm{G}^* = \frac{16\pi\gamma^3\nu_c^2}{3\Delta\mu^2} \qquad \text{Eqn. 1.7}$$

Substituting for $\Delta\mu$ in Eqn 1.7 with r^* in Eqn 1.6 gives the nucleation energy barrier in terms of the interfacial tension:

$$\Delta \mathrm{G}^* = \frac{4\pi\gamma \mathrm{r}^{*2}}{3} \qquad \text{Eqn. 1.8}$$

where $4\pi r^{*2}$ is the total surface area of the critical nucleus. This is a universal equation and shows that the nucleation barrier, assuming a spherical nucleus shape, is a third of the total surface energy of the critical nucleus.

1.2.4 Heterogeneous nucleation

Heterogeneous nucleation is more common[28] than homogeneous nucleation because its energy requirement is lower. It requires the presence of a foreign body or surface. This body or surface adsorbs the solute (wetting), resulting in a contact angle θ between the solute and surface (Fig. 1.6).

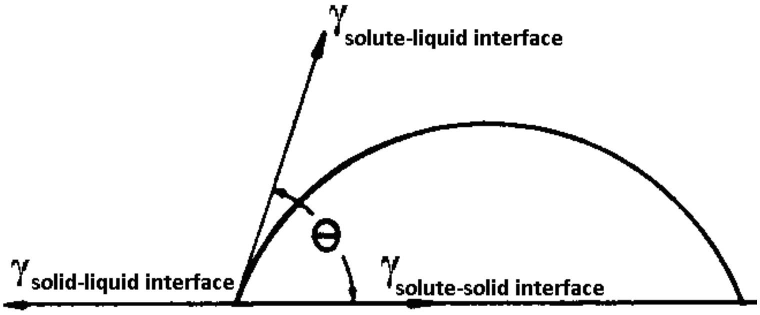

Fig. 1.6 Contact angle and interfacial tension in heterogeneous nucleation[27].

This wetting reduces the critical nucleus size and the interfacial energy requirement for nucleation[29], thereby lowering the energy barrier (ΔG^*_{het}) for nucleation. The Gibbs energy change for heterogeneous nucleation is given by Eqn. 1.9.

$$\Delta G^*_{\text{het}} = \Delta G^*_{\text{homo}} \mathcal{F}(\theta) \qquad \text{Eqn. 1.9}$$

where ΔG^*_{homo} is the Gibbs energy for homogeneous nucleation and $F(\theta)$ is the wetting function, representing the energetic influence of the foreign body or surface in reducing the work requirement for nucleation. The wetting function depends on the contact angle, θ, and is given by Eqn. 1.10.

$$\mathcal{F}(\theta) = \frac{2-3\cos\theta+\cos^3\theta}{4} \qquad \text{Eqn. 1.10}$$

$F(\theta)$ is the ratio of the volume of the heterogeneous critical nucleus to the volume of the corresponding homogeneous critical nucleus. This indicates that the reduction in the nucleation energy barrier for heterogeneous nucleation arises from the smaller critical nucleus size. Combining Eqns. 1.7, 1.9 and 1.10, the Gibbs free energy (ΔG^*_{het}) for the heterogeneous nucleation is given by Eqn. 1.11.

$$\Delta G^* = \frac{16\pi\gamma^3 v_c^2}{3\Delta\mu^2} \times \frac{2-3\cos\theta+\cos^3\theta}{4} \qquad \text{Eqn. 1.11}$$

1.2.5 Nucleation rate

The nucleation rate (I) is a measure of how fast new nuclei are formed and is the product of the attachment rate (W) onto the critical nuclei and the concentration of critical nuclei at equilibrium (Eqn. 1.12).

$$J = W[n]e^{\left(\frac{-\Delta G^*}{KT}\right)} \qquad \text{Eqn. 1.12}$$

Substituting for ΔG^* from Eqn. 1.7 gives Eqn. 1.13

$$J = W[n]e^{\left(\frac{-16\pi\gamma^3 v_c^2}{3\Delta\mu^2 KT}\right)} \qquad \text{Eqn. 1.13}$$

Or Eqn. 1.14

$$J = \Omega e^{\left(\frac{-16\pi\gamma^3 v_c^2}{3\Delta\mu^2 KT}\right)} \qquad \text{Eqn. 1.14}$$

Where Ω is known as the pre-exponential factor and is independent of supersaturation and temperature.

From Eqns. 1.13 or 1.14, at low supersaturation $\Delta\mu$ (i.e. in the metastable region), the rate of nucleation $J \approx 0$ and the formation of critical nuclei is difficult, but at high supersaturation the nucleation rate increases rapidly (i.e. the system is in the labile region), this variation of nucleation rate (J) with the level of supersaturation ($\Delta\mu$) is illustrated in Fig. 1.7 below.

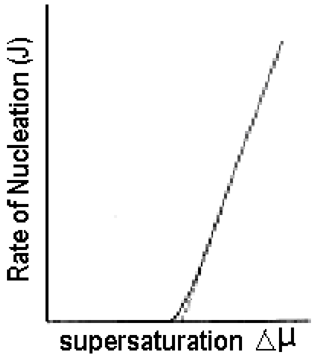

Fig. 1.7 Plot of supersaturation ($\Delta\mu$) against nucleation rate (J), showing a initial lag in rate of nucleation at low levels of supersaturation.

1.2.6 Crystal growth

Crystal growth depends upon the probability of solutes attaching or detaching from the surface of a growing crystal surface exposed to the supersaturated mother phase. Using a simple cubic Kossel crystal model (Fig. 1.8), the various probabilities for crystal growth can be explained.

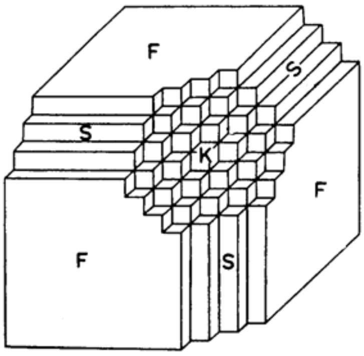

Fig. 1.8 Surface for crystal growth[27], showing the different type of crystal surfaces available for crystal growth to occur.

Fig. 1.8 shows the three different surfaces common in growing crystals; flat (F), step (S) and kink (K) surfaces. Step (S) and kink (K) surfaces are atomically rough surfaces; while a flat (F) is an atomically smooth surface. The surface present in the growing crystals influences the shape of the final crystal[26].

When adatoms attach and detach from the surface of a crystal, the surface energy of the crystal changes. The change depends on the number of neighbouring bonds the adatom has with the crystal. Assuming the shape of the adatom is a cube, when an adatom attaches to a kink site (K), it has three of its six surfaces bonded to the crystal and three surfaces exposed to the mother phase, so detaching this solute will not result in any net change in the surface energy of the crystal. Consequently, growth on kink sites is always favourable for a supersaturated system.

For an adatom attaching itself to a step site (S), it has two surface bonded to the crystal and four sides exposed to the mother phase; detachment from a step site to the mother phase occurs quicker than at a kink site, making the step site less favourable than the kink site for crystal growth. For a Flat (F) surface, the solute has only one surface bond with the crystal, making this site the least favourable for crystal growth compared with Step or Kink sites.

The crystal growth rate (R) on rough crystal surfaces such as step (S), kink (K) and a flat (F) face above its roughening transition temperature, is expressed in Eqn. 1.15[27].

$$\mathrm{R} = \lambda \Delta \mu \qquad \text{Eqn. 1.15}$$

where λ is the kinetic coefficient. From Eqn. 1.15 the crystal growth rate depends linearly on the supersaturation (Δμ). The kinetic coefficient (λ) is proportionally related to the roughness of the crystal face.

As adatoms attach unto the kink and step sites, a smooth flat surface ultimately will be created. Crystal growth rate on a flat (F) face without defects and below the crystal roughening transition temperature, does not have a linear relation with supersaturation (Δμ) because any new nuclei adsorbed unto the flat (F), will have only one neighbouring bond with surface, so will tend to dissolve back into the mother phase because this is not a thermodynamically favourable site for spontaneous crystal growth. Crystal growth then depends on the rate of formation of a 2-D disc-shaped critical nucleus, similar to heterogeneous nucleation. This 2D nucleation process leads to the development of a thermodynamically favourable surface for spontaneous growth. A relatively high level of critical supersaturation is required for 2-D nucleation on a flat crystal surface.

The observation of crystal growth on flat surfaces at supersaturations significantly below the critical supersaturation required 2-D nucleation led to the discovery of another mechanism for crystal growth on a flat crystal surfaces known as the “spiral growth” mechanism (Fig. 1.9).

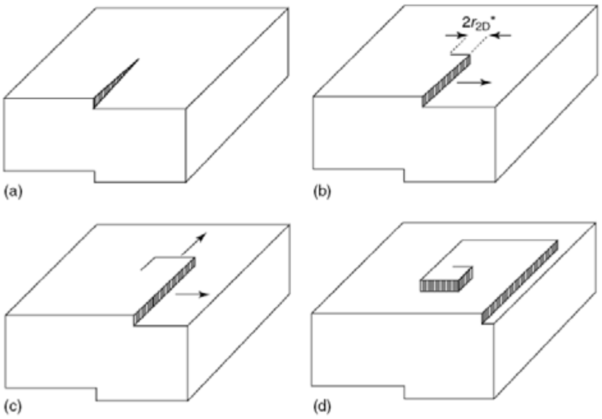

Fig. 1.9 Illustration of spiral growth process[27].

Flat faces are not completely atomically smooth. The presence of screw dislocations on flat crystal surfaces provides a step for spontaneous crystal growth, alleviating the need for 2-D nucleation and so this critical supersaturation is not required. During spiral growth, the dislocation grows parallel to itself creating a second step normal to the first (Fig. 1.9), so continuous growth is possible without 2-D nucleation. Flat faces grow by this screw disclocation mechanism at low supersaturations, but at higher supersaturations, the 2D nucleation mechanism can dominate, since 2D nucleation can occur anywhere on the crystal surface whereas the screw dislocation mechanism is limited to existing screw dislocation sites.

1.3 Cocrystal engineering and design

Crystal engineering is a field of solid-state chemistry that uses the knowledge of non-covalent intermolecular bonds to design and produce supramolecules with target structure and predetermined properties[30]. Cocrystals can be viewed as a product of crystal engineering, which aims to bring two or more different molecules via non-covalent interaction e.g. hydrogen bonds, within the same crystal lattice without breaking any covalent bond[1].

In designing cocrystals, an important factor for consideration is which of the two possible intermolecular bondings is favoured, heteromeric (cocrystal) or homomeric (single molecule)? Functional groups that show a high tendency for forming heteromeric interaction include carboxylic acid, pyridine and amide functionalities[2] and so these are good supramolecular synthons for cocrystal formation. These functional groups have a pKa difference (ΔpKa) that favours heteromeric hydrogen-bonding interactions.

The pKa is the negative logarithm of Ka (Eqn. 1.16); Ka refers to the degree of dissociation that is observed in a Bronsted-Lowry acid (Eqn. 1.17). The stronger the acid, the higher the tendency is to donate a proton, so the higher the value of the dissociation constant (Ka). This leads to a more stable conjugate base ($\mathrm{A^-}$) and a lower pKa value.

$$\mathrm{pKa} = -\log_{10}(\mathrm{Ka}) \qquad \text{Eqn. 1.16}$$

$$\mathrm{Ka} = \frac{[\mathrm{H^+}][\mathrm{A^-}]}{[\mathrm{HA}]} \qquad \text{Eqn. 1.17}$$

The pKa difference (ΔpKa = pKa(base)-pKa(acid))[26] between the supramolecular synthons has been used as a tool for predicting if a cocrystal or a salt will be formed. As a general rule, a pKa difference of less than 3.75 tends to favour a heteromeric hydrogen bonding interaction[17,31,32]. This 3.75 value was determined from an infrared study of the intermediate state of 20 different substituted benzoic acid and pyridine solid-state complexes[32]. A change in the number of OH stretching peaks of the benzoic acid, from two broad peaks to a single broad peak in the 1900 to 2600 $\mathrm{cm^{-1}}$ region, was used as an indication of the transition point from un-ionised (neutral) to ionised (salt) bonding. However, exceptions to this rule were observed where neutral species existed above the 3.75 value and ionised species were observed below this pKa.

The above exceptions suggest a ΔpKa region exists where either a salt or cocrystal could be formed[33,34]. This salt-cocrystal continuum has been suggested to exist between ΔpKa 0-3[34]. In this ΔpKa region, the ratio of ionised and un-ionised species at equilibrium in solution is relatively close to 1. This can be seen as follows. For an acid AH+ and base B, then

$\mathrm{AH^+} \rightarrow \mathrm{A} + \mathrm{H^+}$ is represented by $\mathrm{K_{a\_A}} = \frac{[\mathrm{A}][\mathrm{H^+}]}{[\mathrm{AH^+}]}$ Eqn. 1.18

$\mathrm{B} + \mathrm{B^-} + \mathrm{H^+}$ is represented by $\mathrm{K_{a\_B}} = \frac{[\mathrm{B^-}][\mathrm{H^+}]}{[\mathrm{B}]}$ Eqn. 1.19

ΔpKa = pKa (base)-pKa (acid) = $-\log_{10}(\mathrm{K_{a\_B}}/\mathrm{K_{a\_A}})$ Eqn. 1.20

The equilibrium between the charged and neutral species of A and B in solution is given by:

$$\mathrm{A} + \mathrm{B} \rightarrow \mathrm{AH^+} + \mathrm{B^-}$$

For which the equilibrium constant $\mathrm{K_{eq}}$ is:

$$\mathrm{K_{eq}} = \frac{[\mathrm{AH^+}][\mathrm{B^-}]}{[\mathrm{A}][\mathrm{B}]} = \frac{\mathrm{K_{a\_B}}}{\mathrm{K_{a\_A}}} = 10^{\Delta\mathrm{pKa}} \qquad \text{Eqn. 1.21}$$

Hence, for ΔpKa = 0.5, $\mathrm{K_{eq}}$ is given by:

$$\mathrm{K_{eq}} = \frac{[\mathrm{AH^+}][\mathrm{B^-}]}{[\mathrm{A}][\mathrm{B}]} = \frac{\mathrm{K_{a\_B}}}{\mathrm{K_{a\_A}}} = 10^{0.5} = 3.16$$

And although there are more ionic species in solution than neutral ones, solid cocrystal formation is still possible. When ΔpKa = 4, however:

$$\mathrm{K_{eq}} = \frac{[\mathrm{AH^+}][\mathrm{B^-}]}{[\mathrm{A}][\mathrm{B}]} = \frac{\mathrm{K_{a\_B}}}{\mathrm{K_{a\_A}}} = 10^{4} = 10{,}000$$

and overwhelmingly the species in solution at equilibrium will be ionic, ensuring solid salt formation instead of cocrystal formation when the solution is supersaturated.

Thus, when ΔpKa 0-3 other factors like solvent and lattice environment can influence the likelihood of proton transfer. In contrast, outside this ΔpKa region, the ratio of ionised and neutral species is either extremely high or extremely low, so that only one species, neutral or ionic dominates in solution, with ΔpKa becoming the sole determining factor for proton transfer or not.

Consequently, the design of a pharmaceutical cocrystallisation screen requires choosing appropriate API/coformer (retro-synthetic synthons[30]) systems for the screen and trial processes with the various cocrystallisation techniques available.

1.3.1 Intermolecular interactions in cocrystals

The common intermolecular bonds present in cocrystals are: hydrogen bonding, halogen bonding, van der Waals interactions and pi stacking, but the focus of this project is on hydrogen-bonded cocrystals.

The hydrogen bond is the most reliable non-covalent directional bond capable of effecting a molecular recognition interaction[30,35]. This directional bonding is sufficiently strong between ≈ 120 to 4 kJ mol^{-1} [36], to direct molecular assemblies in supramolecules[35]. Although halogen bonds are able to affect molecular recognition[37], hydrogen bonding is by far the most frequently occurring non-covalent bonding in molecular assembly processes[1,38]. Hydrogen bonding can be categorised into three groups based on bond length, bond energy and bond angles.

Table 1.1 Three categories of hydrogen bonding (A⋯⋯H⋯⋯B) classification[36].

	Strong	Moderate	Weak
Bond length (Å)	2.2-2.5	2.5-3.2	3.2-4.0
Bond angle (^{o})	175-180	130-180	90-150
Bond energy(kJ mol^{-1})	60-120	16-60	<12

There are rules that help determine the selectivity inherent in hydrogen bonding of organic molecules during molecular recognition processes in crystal engineering. These rules are useful guides for hierarchical selectivity of hydrogen bond formation by determining which are energetically favourable when more than one hydrogen bond donor or acceptor functionality of different strengths exists[1,39]. The rules are as follows:

- The best hydrogen bond donor and the best hydrogen bond acceptor will preferentially form hydrogen bonds with one another.
- All available acidic hydrogens in a molecule will be used in hydrogen bonding in its crystal structure.
- Six member intra-molecular hydrogen bond rings will form in preference to intermolecular hydrogen bonds.

- The best hydrogen bond acceptor and donor available after intramolecular hydrogen bonding will form intermolecular bonds.

1.3.2 Graph Sets

In the study of crystal structures, graph sets are used to describe the bonding motif types present in complex hydrogen bonding networks. It is a useful chemical language. Description is made by identifying subsets of hydrogen bonding networks of similar types, referred to as motifs. All hydrogen bonding networks are described by four simple patterns: Chains (C), Rings (R), Finite/discreet (D) and intramolecular/self (S)[40].

A typical graph set descriptor is written in the form, $\mathrm{G}_{\mathrm{d}}^{\mathrm{a}}(\mathrm{n})$, where G denotes the type of pattern (C, R, D or S) present in the motif, the superscript number (a) is used to denote the number of hydrogen bond acceptors in the motif, the subscript number (d) is used to denote the number of hydrogen bond donor in the motif and n represents the total number of atoms involved in the motif.

The motif in Fig. 1.10, which will be referred to as motif M1 will be used as an example to demonstrate the graph set approach. M1 hydrogen bonding forms a ring so the pattern abbreviation R is used. The number of hydrogen bond donors (d) and acceptors (a) are both the same at 2 and the total number of atoms (n) in M1 is 8. So the graph set description for M1 is R_2^2 (8).

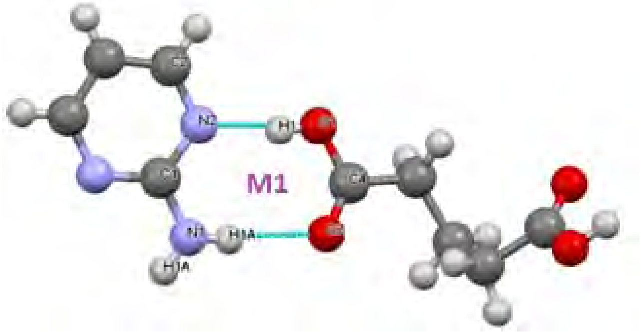

Fig. 1.10 Example of a graph set description of hydrogen bonding motif M1. M1 has a graph set of R_2^2 (8).

1.3.3 Cocrystal solubility and stability

Cocrystal solubility at equilibrium can be represented by Eqn. 1.22[41], when its components do not ionise in solution but dissociate into neutral components.

$$A_aB_{b\ \ solid} \rightleftharpoons aA_{solution} + bB_{solution} \qquad \text{Eqn. 1.22}$$

The equilibrium constant ($\mathrm{K_{eq}}$) for the cocrystal solubility represented in Eqn. 1.22 is given by[41]:

$$\mathrm{K_{eq}} = \frac{\mathrm{X_A^a X_B^b}}{\mathrm{X_{ab}}} \qquad \text{Eqn. 1.23}$$

where X is the activity of the cocrystal and its components. Assuming the activity of the solid is constant and set to 1, then the solubility product (K_{sp}) is given by the concentration (or more correctly activities) of the cocrystal components[41].

$$K_{sp} = [A]^a[B]^b \qquad \text{Eqn. 1.24}$$

The stability of a cocrystal relative to its components depends on the activity of its components in the solution. When a solution is saturated with the cocrystal components, but supersaturated with respect to the cocrystal, then the cocrystal becomes the most stable solid phase. The solubility of the cocrystal will depend upon the relative amounts of its components as follows[42]. For a 2:1 cocrystal D_2L, where D is the drug and L is the ligand, the equilibrium reaction for cocrystal dissociation in solution is given as

$$\mathrm{D_2L_{(solid)}} \overset{\mathrm{K}}{\rightleftharpoons} \mathrm{2D_{(solution)}} + \mathrm{L_{(solution)}} \qquad \text{Eqn. 1.25}$$

where *K* is the equilibrium constant for the reaction:

$$\mathrm{K} = \frac{\mathrm{a_D^2 a_L}}{\mathrm{a_{D_2L}}} \qquad \text{Eqn. 1.26}$$

$\mathrm{a_D}$and $\mathrm{a_L}$ are the activities of D and L in solution, and $\mathrm{a_{D_2L}}$ is the activity of the solid. Assuming the activity of the solid D_2L is 1, the above relation yields the solubility product ($\mathrm{K_{sp}}$) for the cocrystal:

$$\mathrm{K_{sp}} = \mathrm{a_D^2 a_L} \qquad \text{Eqn. 1.27}$$

Assuming ideal conditions, activities can be replaced with concentrations
to give:

$$\mathrm{K_{sp}} = \mathrm{[D]^2[L]} \qquad \text{Eqn. 1.28}$$

Rearranging then gives:

$$\mathrm{[D]} = \sqrt{\frac{\mathrm{K_{sp}}}{\mathrm{[L]}}} \qquad \text{Eqn. 1.29}$$

showing that the solubility of the drug component D will decrease if there is excess ligand, L, This relationship is important in our studies where we use an anti-solvent/solvent approach, with the anti-solvent as the majority phase, as it shows that if one solid component is added in large excess, the solubility of the other cocrystal coformer may decrease and in this case ultimately less cocrystal product will arise. For this reason, stoichiometric quantities of the cocrystal components were used

1.4 Methods for making cocrystals

This section focuses on the various techniques for making and screening for cocrystals on a laboratory scale. The methods can be subdivided into four main types:

1. Solution-mediated cocrystallisation.
2. Melt cocrystallisation.
3. Mechano-chemical cocrystallisation.
4. Sublimation cocrystallisation.

1.4.1 Solution cocrystallisation

This method involves crystallising the cocrystal from solution above the saturation concentration of the cocrystal. Supersaturation can be induced by sonication, cooling, using anti-solvent etc. Slurries or suspensions of the API and coformer can also be used, as well as solutions of the cocrystal components.

The use of solution cocrystallisation is hindered by the challenges of the non-congruent solubility of most APIs and coformers, as well as the competition of the solvent to form solvates with either the API or coformer[9]. It is sometimes problematic to produce cocrystals from solution cocrystallisation even though the cocrystals have previously been obtained via mechano-chemical cocrystallisation[43]. This is due to the difference in cocrystallisation environment between solution and mechano-chemical (section 1.4.3).

1.4.2 Melt cocrystallisation

Melt cocrystallisation involves heating the reagents to above their melting point and bringing the melts in contact with one another This is a particularly useful method for a fast screen of cocrystals[16], but has limited applications. It cannot be used for: thermally unstable reagent, volatile reagents, and reagents and cocrystals that undergo polymorphic or other transitions at elevated temperature[44].

1.4.3 Mechano-chemical cocrystallisation

Cocrystallisation processes initiated by mechanical grinding, often with a mortar and pestle, to form cocrystal products are classified as mechano-chemical cocrystallisation. This approach is viewed as a green process because little or no solvent is used and minimal energy input is required.

Grinding cocrystallisation has a higher rate of cocrystal formation success when compared against solution and melt cocrystallisation[9,15] i.e. cocrystals that may not be formed via solution or melt cocrystallisation can be formed via grinding. When a few drops of solvent are added during grinding, it is referred to as liquid-assisted grinding (LAG) cocrystallisation. The addition of the solvent is believed to catalyse the cocrystallisation process by improving molecular mobility.

In grinding cocrystallisation, cocrystals are formed by either or both the API and coformer transforming to a more energetic intermediate phase prior to cocrystallisation. The intermediate state could be: gaseous, melt or amorphous[9]. This increases the molecular mobility making cocrystallisation possible. More than one intermediate phase may be present at the same time and the intermediate state (gas, liquid or amorphous) depends on the physical properties of the components.

Mechanical grinding of a reagent can result in localised heat generation due to friction during grinding process leading to the breaking up of intermolecular forces present in the crystalline phase. If one of the cocrystal components has a low vapour pressure or is a volatile solid, localised heating can volatilise the solid leading to an intermediate gas phase prior to cocrystallisation.

1.4.4 Sublimation cocrystallisation

In sublimation cocrystallisation, one of the cocrystal components is sublimed, by the application of heat, to the gaseous phase[45]. Gas can diffuse rapidly through solids leading to cocrystallisation[39]. The rate of cocrystallisation is affected by the surface area available to the gas for diffusion and the ease of gas molecules penetrating the solid phase[9].

1.5 Cocrystal analysis

Analysis is crucial for process optimisation as decision making during process optimisation has to be based on facts or data; and the data acquired are only as good as the analytical process used in generating them. During this work, a substantial amount of effort was put into developing a robust quantitative analytical method for determining cocrystal yield.

Analytical emphasis in cocrystal engineering is mainly focused on qualitative analytical techniques; reports on quantitative analysis of cocrystal are rare. Qualitative analysis focuses on structural elucidation and identification of new cocrystal forms carried out with analytical techniques such as: powder x-ray diffraction (PXRD), solid state nuclear magnetic resonance (SSNMR), Fourier transform infra-red spectroscopy (FTIR), Raman spectroscopy, Differential scanning calorimetry (DSC) etc. Intermolecular bonding in cocrystals are weaker compared to covalent bonding, so solid state analysis requirement is important for ensuring that the cocrystal doesn't revert back to its components during analysis. A brief survey of major analytical techniques and their application in cocrystal analysis is presented below.

1.5.1 Differential scanning calorimetry (DSC)

DSC is a thermal analytical technique that measures changes in a substance's heat capacity at constant pressure (enthalpy) against temperature to give a thermogram. During 1st order phase transitions, the sample undergoing the transition absorbs/releases heat. The enthalpy of the transition is measured by monitoring the difference in the energy requirement to keep the temperature of both the sample undergoing the phase transition and a reference, the same. 1st order phase transition enthalpies measured using DSC includes: melting and crystallisation, with the transition shown by a peak in the DSC scan. In addition, second order phase transitions, such as glass transitions can be seen on the DSC scan as a change in the gradient of heat intake verses temperature, as this corresponds to a change in the heat capacity of the sample.

DSC is used in screening for cocrystal formation using melts of components and for qualitative analysis of cocrystals[13,23] by monitoring melting point differences between the cocrystal sample and its component. DSC analysis can be carried out on solids, so cocrystal bonding samples are stable during analysis.

1.5.2 Powder x-ray diffraction (PXRD) analysis

PXRD is a non-destructive analytical technique and is used extensively for confirming cocrystal formation on the laboratory scale[4,46]

The inter-planar spacing of a crystal is a unique feature and depends on the repeating crystal unit cell. When an API and coformer forms a cocrystal, the molecular interaction in the cocrystal unit cell is different from that found in the API or coformer, resulting in a different inter-planar spacing. This change is observed by the appearance or disappearance of peaks in the PXRD trace. Further reviews of this technique are presented in chapter 2 and 3.

1.5.3 Fourier transform infra-red (FTIR)

FTIR is also a non-destructive analytical technique. It is based on the unique vibrational frequencies of a compound and is used in qualitative analysis. FTIR analysis can handle solid samples and so is ideal for cocrystal analysis. FTIR analysis can distinguish between vibrations for ionised and un-ionised O—H······N [4,47] hydrogen-bonded functional groups. This distinction is observed as changes in the FTIR spectra going from components to the cocrystal molecule. Changes could be a shift in wavelength of absorption, disappearance or appearance of peaks in the FTIR spectrum.

1.5.4 Solid state nuclear magnetic resonance (SSNMR)

SSNMR is another non-destructive analytical technique and makes use of solid powder samples in the analysis. The SSNMR principle is based on the interaction (Zeeman interaction) between the spinning nuclei in the sample and an applied external magnetic field, resulting in the splitting of energy orbitals in the powder sample. A comprehensive review of SSNMR is presented in chapter 3.

1.6 Hansen solubility parameter

The Hansen solubility parameter is derived from the Hildebrand solubility parameter (δ_T). The Hildebrand solubility parameter is a measure of the total cohesive energy density of a compound, it is the sum of the total of all forces of cohesion in a molecule e.g. ionic bonding, hydrogen bonding, van dar Waal forces, covalent bond etc. It is also the energy required to vapourise a substance divided by its molar volume. It is used in predicting solubility between substances based on the "like dissolve like" principle; substances with similar Hildebrand solubility parameters have high affinity for each other and a high probability of forming a solution with each other[30,31].

$$\delta_T = \left(\frac{E}{V}\right)^{\frac{1}{2}} \qquad \text{Eqn. 1.30}$$

where E = energy of vaporisation and V = molar volume, its unit is $\mathrm{Pa}^{\frac{1}{2}}$.

The Hildebrand solubility parameter prediction of solubility is limited, because it assumes no form of association exists between molecules. This assumption is largely true for non-polar systems but not for polar systems. The Hildebrand solubility parameter is split into three components, the Hansen solubility parameters, which incorporates cohesive energy densities and account for molecule association. These components are: dispersive (δ_D) referring to the non-polar atomic forces density, polarisability (δ_P) referring to permanent dipole-dipole intermolecular force density and hydrogen bonding (δ_H) referring to intermolecular hydrogen bonding force density[31,32]. These components have been used for predicting cocrystal formation[33].

$$\delta_T^2 = \delta_D^2 + \delta_P^2 + \delta_H^2 \qquad \text{Eqn. 1.31}$$

The Hansen parameter is used in explaining cocrystallisation trends in Chapter 4.

1.7 Oscillatory baffle reactors

In a chemical reactor, uniform composition, energy transfer and removal are important for controlling side reactions and the formation of impurities, which can result in poor yields and difficult downstream processing. For crystallisation to occur, supersaturation is required and mixing plays an important role in determining the local solute concentration and hence supersaturation, rate of nucleation and crystal growth rate. Achieving efficient mixing and heat removal is difficult because during scale-up the increase in reactor volume rises faster than the surface area. The reduced surface area to volume ratio impacts on surface area availability for heat control. The increase in volume results in difficulty in replicating mixing.

Oscillatory Baffle reactors (OBR) are tubular reactors with equidistant spaced baffle plates with orifices at the centre of each plate. Mixing is achieved by means of eddies generated from the interaction of the fluid reversed flow through the orifice (Fig. 1.11). An oscillatory motion is imposed on the fluid medium by either pulsating with a pump or moving the baffles. An OBR offers a linear scale up approach from laboratory to plant scale.

The OBR is also capable of achieving “plug flow”, a state of ideal mixing when the composition of the reactor is only dependent on the residence time in the tube, thus improving mixing and heat transfer compared to the conventional batch reactor.

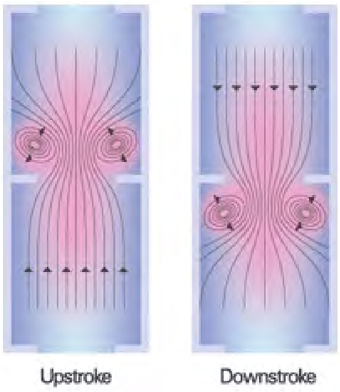

Fig. 1.11 Illustration showing eddies generation during forward and backward stroke of oscillatory mixing, respectively[48].

Efficient mass transfer reduces the occurrence of variations in the metastable zone width during crystallisation, which is difficult to achieve in normal crystallisers[49].

Mixing in OBR's is measured using a dimensionless quantity called the Reynolds number. The oscillatory Reynolds number ($\mathrm{Re_o}$) measures the mixing intensity in the tubular reactor. Reynolds numbers < 2000 correspond to laminar flow while >2000 correspond to turbulent flow. The Reynolds number is given by Eqn. 1.32.

$$\mathrm{Re_o} = \frac{2\pi f x_O \rho D}{\mu} \qquad \text{Eqn. 1.32}$$

where μ is the viscosity (kg m^{-1} s^{-1}) of the fluid, ρ is the density (kg m^{-3}) of the fluid, f is the oscillating frequency of the pump in Hz, D is the diameter of the tubular reactor (m) and x_O is the stroke of the pump (m). For a continuous process, the net flow Reynolds number ($\mathrm{Re_n}$) measures mixing intensity and is given by Eqn. 1.33.

$$\mathrm{Re_n} = \frac{\rho D u}{\mu} \qquad \text{Eqn. 1.33}$$

where u is the net flow velocity (ms^{-1}) of the reaction, the rate at which the reaction phase moves through the reactor, D is the diameter of the tubular reactor (m), ρ is the density (kg m^{-3}) of the fluid and μ is the viscosity (kg m^{-1} s^{-1}) of the fluid.

The oscillatory and net flow Reynolds number are parameters used for scaling up the reaction from laboratory to plant scale in oscillatory baffle reactors.

1.7 Project background and goal

The Centre for Process Innovation (CPI) has a pilot scale OBR called the Particulate Processing Unit (PPU). The PPU unit is an advanced manufacturing continuous baffle reactor system and CPI is exploring this technology for cocrystal scale up. Previous attempts at scaling up cocrystallisations have involved the use of solution or seeding cocrystallisation and the use of a twin screw extrusion (TSE) at elevated temperature[52]. The focus of the research discussed in this thesis is two-fold. Firstly to determine whether cocrystallisation is commercially feasible using oscillatory baffle reactors and secondly to investigate cocrystallisation in hydrogen-bonded crystals. A single vertical column (SVC) incorporating baffles and the larger PPU unit were used for the first purpose, whilst the system comprising 2-aminopyrmidine and glutaric acid was used for the second, leading to the discovery of new cocrystals and polymorphism in this system.

References

(1) Braga, D.; Grepioni, F. *Making crystals by design : methods, techniques and applications*; Wiley-VCH: Weinheim, **2007**

(2) Almarsson, O.; Zaworotko, M. J. *Chemical Communications* **2004**, 1889.

(3) Blagden, N.; Berry, D. J.; Parkin, A.; Javed, H.; Ibrahim, A.; Gavan, P. T.; De Matos, L. L.; Seaton, C. C. *New Journal of Chemistry* **2008**, *32*, 1659.

(4) Schultheiss, N.; Newman, A. *Cryst. Growth Des.* **2009**, *9*, 2950.

(5) Hoff, C.; Lee, S. In *Handbook of Pharmaceutical salts: Properties, Selection and Use*; Stahl, P. H., Wermuth, C. G., Eds.; Wiley-VCH: **2002**,Large scale aspect of salt formation: Processing of intermediate and Final Product,p 191.

(6) Vogt, F. G.; Clawson, J. S.; Strohmeier, M.; Edwards, J. A.; Pham, T. N.; Watson, S. A. *Cryst. Growth Des.* **2009**, *9*, 921.

(7) Desiraju, G. R. *Crystengcomm* **2003**, *5*, 466.

(8) Haynes, A. D.; Jones, W.; Motherwell, W. D. S. *Crystengcomm* **2006**, *8*, 883.

(9) Friscic, T.; Jones, W. *Cryst. Growth Des.* **2009**, *9*, 1621.

(10) AG, S. Co-Crystals-An Attractive Alternative for Solid Forms. *Pharmaceutical international*. Published Online: **2007**. http://www.pharmaceutical-int.com/article/co-crystals-an-attractive-alternative-for-solid-forms.html (accessed 01/03/2011).

(11) Bhatt, P. M.; Azim, Y.; Thakur, T. S.; Desiraju, G. R. *Cryst. Growth Des.* **2009**, *9*, 951.

(12) Friscic, T.; Jones, W. *Journal of Pharmacy and Pharmacology* **2010**, *62*, 1547.

(13) Leung, D. H.; Lohani, S.; Ball, R. G.; Canfield, N.; Wang, Y.; Rhodes, T.; Bak, A. *Cryst. Growth Des.* **2012**, *12*, 1254.

(14) Lu, J.; Rohani, S. *Journal of Pharmaceutical Sciences* **2010**, *99*, 4042.

(15) Friscic, T.; Jones, W. *Journal of Pharmacy and Pharmacology* **2010**, *62*, 1547.

(16) Berry, D. J.; Seaton, C. C.; Clegg, W.; Harrington, R. W.; Coles, S. J.; Horton, P. N.; Hursthouse, M. B.; Storey, R.; Jones, W.; Friscic, T.; Blagden, N. *Cryst. Growth Des.* **2008**, *8*, 1697.

(17) Trask, A. V.; Motherwell, W. D. S.; Jones, W. *Cryst. Growth Des.* **2005**, *5*, 1013.

(18) Jayasankar, A.; Somwangthanaroj, A.; Shao, Z. J.; Rodriguez-Hornedo, N. *Pharmaceutical Research* **2006**, *23*, 2381.

(19) K. Seefeldt, J. M., F. Alvarez-nunez, N. Rodriguez-Hornedo *Journal of Pharmaceutical Sciences* **2007**, *96*, 1147.

(20) Shevchenko, A.; Bimbo, L. M.; Miroshnyk, I.; Haarala, J.; Je;omkova, K.; Syrjannen, K.; van Veen, B.; Kiesvaara, J.; Santos, H. A.; Yliruusi, J. *International Journal of Pharmaceutics* **2012**, *436*, 403.

(21) Pawel Grobelny. *CrystEngComm* **2011**.

(22) Vogt, F. G.; Clawson, J. S.; Strohmeier, M.; Edwards, A. J.; Pham, T. N.; Watson, S. A. *Cryst. Growth Des.* **2009**, *9*, 921.

(23) In *RSC Drug Discovery Series*; RSC Publishing: **2012**.

(24) *Guidance for Industry Regulatory Classification of Pharmaceutical Cocrystal*, **2011.**

(25) Aitipamula, S.; et.al *Cryst. Growth Des.* **2012**, *12*, 21.

(26) Markov, I. V. *Crystal growth for beginners : fundamentals of nucleation, crystal growth and epitaxy*; 2nd ed.; World Scientific: Singapore ; River Edge, N.J., **2003**

(27) Cooper, S. J. Contemporary Chemistry - Crystallisation Kinetics lecture notes, **2001**.

(28) de Castro, M. D. L.; Priego-Capote, F. *Ultrason Sonochem* **2007**, *14*, 717.

(29) Di Profio, G.; Curcio, E.; Ferraro, S.; Stabile, C.; Drioli, E. *Cryst. Growth Des.* **2009**, *9*, 2179.

(30) Desiraju, G. R. *Angew Chem Int Edit* **1995**, *34*, 2311.

(31) Shattock, T. R.; Arora, K. K.; Vishweshwar, P.; Zaworotko, M. J. *Cryst. Growth Des.* **2008**, *8*, 4533.

(32) Johnson, S. L.; Rumon, K. A. *Journal of Physical Chemistry A,* **1965**, *69*, 74.

(33) Thakuriaa, R.; Deloria, A.; Jones, W.; Lipertb, M. P.; Roy, L.; Rodríguez-Hornedo, N. *International Journal of Pharmaceutics,* **2013**.

(34) Childs, S. L.; Stahly, G. P.; Park, A. *Molecular Pharmaceutics* **2007**, *4*, 323.

(35) Desiraju, G. R.; Steiner, T. *The weak hydrogen bond in structural chemistry and biology*; Oxford University Press: Oxford, **1999**

(36) Steed, W. J.; Atwood, J. L. *Supramolecular chemistry*; John Wiley & Sons, **2002**, p.23.

(37) Cincic, D.; Friscic, T.; Jones, W. *Journal of the American Chemical Society,* **2008**, *130*, 7524.

(38) Metrangolo, P.; Neukirch, H.; Pilati, T.; Resnati, G. *Accounts Chem Res.* **2005**, *38*, 386.

(39) Etter, M. C. *J Phys Chem-Us,* **1991**, *95*, 4601.

(40) Bernstein, J.; Davis, R. E.; Shimoni, L.; Chang, N. L. *Angewandte Chemie-International Edition* **1995**, *34*, 1555.

(41) Nehm, S. J.; Rodrıguez-Spong, B.; Rodrıguez-Hornedo, N. *Cryst. Growth Des.* **2006**, *6*, 592.

(42) Jayasankar, A.; Reddy, L. S.; Bethune, S.; Rodrıguez-Hornedo, N. *Cryst. Growth Des.* **2009**, *9*, 889.

(43) Trask, A. V.; van de Streek, J.; Motherwell, W. D. S.; Jones, W. *Cryst. Growth Des.* **2005**, *5*, 2233.

(44) Enxian Lu, *CrystEngComm* **2008**, *10*, 665.

(45) Rastogi, R. P.; Bassi, P. S.; Chadha, S. L. *J Phys Chem-U,* **1963**, *67*, 2569.

(46) Lee, T.; Wang, P. Y. *Cryst. Growth Des.* **2010**, *10*, 1419.

(47) Aakeroy, C. B.; Salmon, D. J.; and, M. M. S.; Desper, J. *Cryst. Growth Des.* **2006**, *6*, 1033.

(48) NiTech. Oscillatory baffled reactor. Published Online: **2008**. http://en.wikipedia.org/wiki/User:Nitech2008/Oscillatory_baffled_reactor, (accessed 10/07/2013).

(49) Kashchiev, D.; van Rosmalen, G. M. *Cryst Res Techno.* **2003**, *38*, 555.

(52) Medina, C.; Daurio, D.; Nagapudi, K.; Alvarez-Nunez, F. *Journal of Pharmaceutical Sciences,* **2010**, *99*, 1693.

Chapter 2 Experimental techniques

2.1 Oscillatory baffle reactor (OBR)

The oscillatory baffle reactor technology was used in this work for both small and large scale studies. The small scale studies were done in the single vertical column (SVC) and the large scale studies in the particulate processing unit (PPU). Below is a schematic of the anti-solvent/solvent cocrystallisation process.

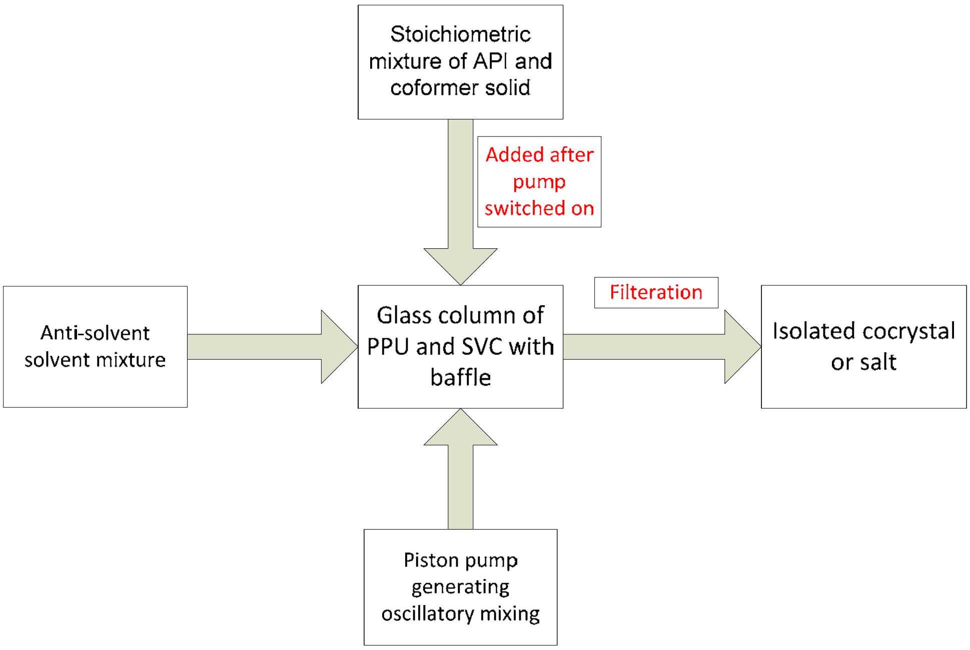

Fig. 2.1 OBR schematic for cocrystallisation.

2.1.1 Single vertical column (SVC) reactor

The single vertical column reactor (SVC) is a batch form of the OBR technology. The SVC consists of a baffle made from stainless steel, with orifices at equidistant intervals from each other. This is inserted into a jacketed glass column (Fig. 2.2). The glass column and baffle are positioned vertically on a piston pump and the liquid medium is pulsed vertically (Fig. 2.3a and 2.3b). Two types of nitrile elastic membrane were inserted between the piston pump and the SVC column (Figs. 2.4a and 2.4b) to enhance safety by preventing exposure of flammable reagent (cyclohexane) to the pump electric system. This also prevented secondary cocrystallisation by the grinding action of the piston bellows on the cocrystal component. Two different column and baffle dimensions were used in this study (Table 2.1).

In the experiments, the liquid phase was added first to the column, then the pulsating pump was set at amplitude of 12.5 mm and a frequency of 1.5 Hz. The API and coformer were added to the column and finally the baffle was inserted. The column jacket was left empty because the reactions were conducted at ambient temperature. Sampling was done by inserting PTFE tubing through the baffle orifice and using a syringe to draw up the reaction mixture (Fig. 2.5). Reaction samples were filtered and dried before analysing.

Table 2.1 SVC column dimensions.

	Orifice diameter	Baffle diameter	Baffle length	Column diameter	Column length
Big column	12 mm	24 mm	500 mm	28 mm	520 mm
Small column	7.5 mm	15 mm	620 mm	16 mm	625 mm

Fig. 2.2 Glass column and stainless baffle used in SVC set up.

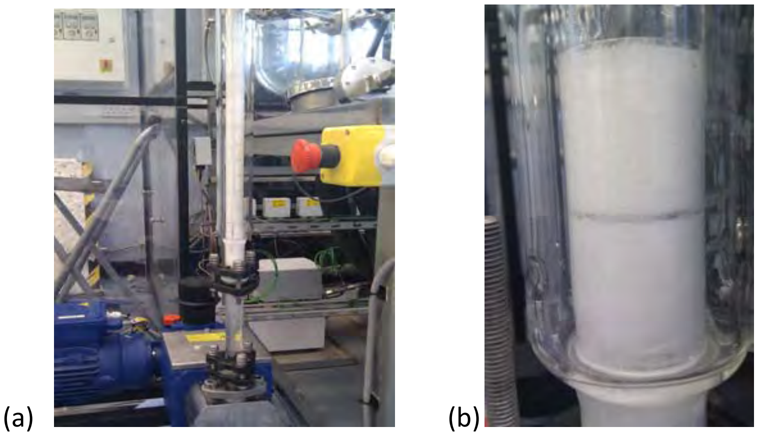

(a) (b)

Fig. 2.3 (a) SVC set up with piston pump. (b) Mixing in SVC column.

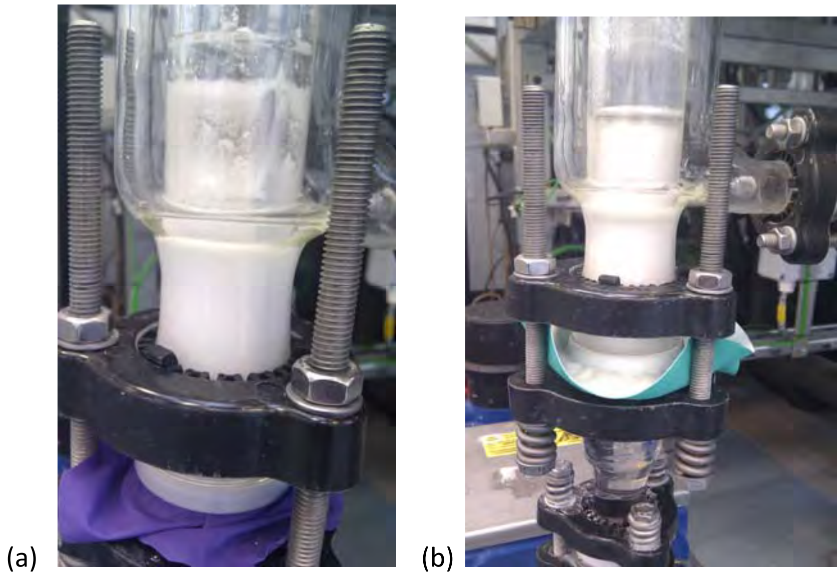

Fig. 2.4 Purple nitrile membrane (a) and Green nitrile membrane (b) used in SVC set up to prevent flammable solvent coming in contact with pump electric system.

Fig. 2.5 PTFE tubing and plastic syringe used for sampling SVC reactions.

2.1.2 Particulate processing unit (PPU)

The PPU is similar to the SVC; it is a series of horizontally linked glass columns with stainless steel baffles inserted in each column (Fig. 2.6). The dimension of each glass column was: length = 1000 mm, diameter = 15 mm and volume = 176.8 ml. The reactor unit consisted of two 30 litre holding vessel with centrifugal pumps (Fig. 2.7) capable of delivering 15 litres of slurry per minute. The tubing used was ½ inch polyfluoroalkoxy (PFA) tubing, which was transparent, allowing for visual monitoring of slurry circulation through the unit. The slurry in the holding vessels were kept in suspension with overhead stirrers and doused into the PPU glass columns via two separate pneumatic valves (Fig. 2.8a) with a control box (Fig. 2.8b). The pneumatic valves sat at the top of the glass column (Fig. 2.9) and were connected to a pressured air-line; this pressure kept the valve shut. When the air was cut-off, the valves opened to douse the slurry into the glass column.

The control box was used to control the delay between valve openings and the volume being doused into the column.

Mixing in the PPU was monitored with (Fig. 2.10a) and without (Fig. 2.10b) the baffles inserted. The mixing was uniform when the baffles were inserted but not without the baffles. The intensity of the mixing of the slurry in the PPU was controlled by the amplitude and frequency of the pulsing piston pump, which were set at 20 mm and 2 Hz respectively. The slurry residence time was controlled with the pneumatic valve by altering the delay between douses. The final slurry was isolated from the outlet of the unit, filtered and dried before analysing.

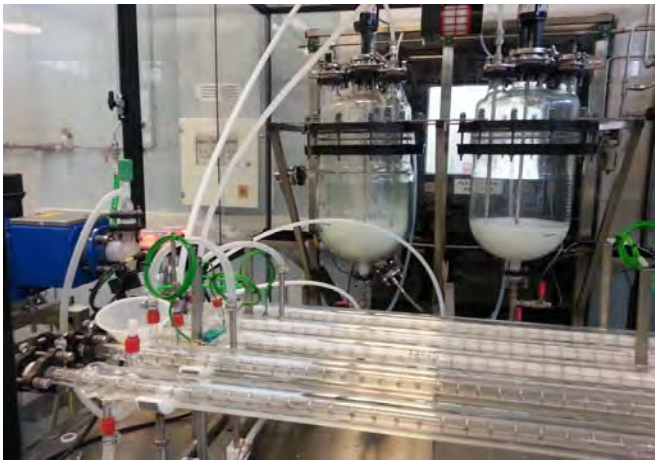

Fig. 2.6 Particulate processing unit reactor (PPU) set up showing the holding vessel with slurry kept in suspension with an overhead stirrer and glass column with slurry mixture.

Fig. 2.7 Centrifugal pump used in circulating the API and coformer slurry mixture in PPU set up.

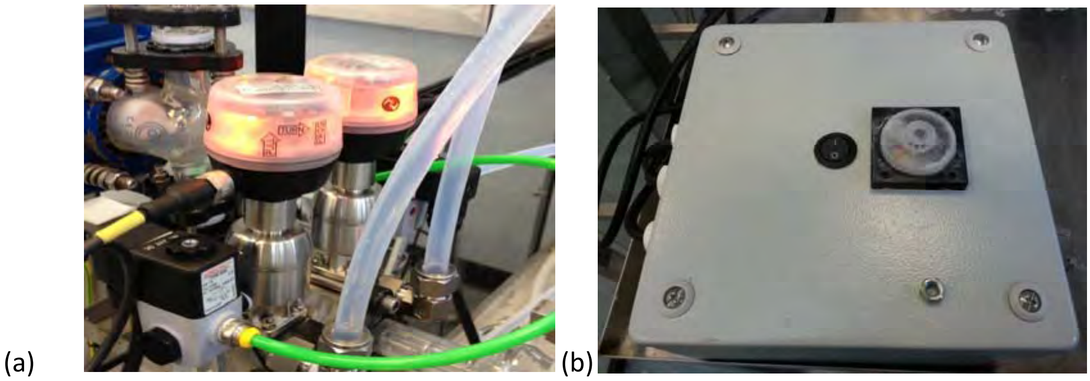

Fig. 2.8 (a) Pneumatic valves for simultaneous slurry dousing from both holding vessels. The two green tubes are the air-lines used for controlling closing and opening of each valve. The red light indicates the valves are shut, which changes to green when the valves are open. (b) Pneumatic valve control box with two dials. The inner dial controls the time delay between valve openings and the outer dial controls how long the valves are opened.

Fig. 2.9 PPU in operation with arrow indicating the position of the pneumatic valve dousing point at the top of the column.

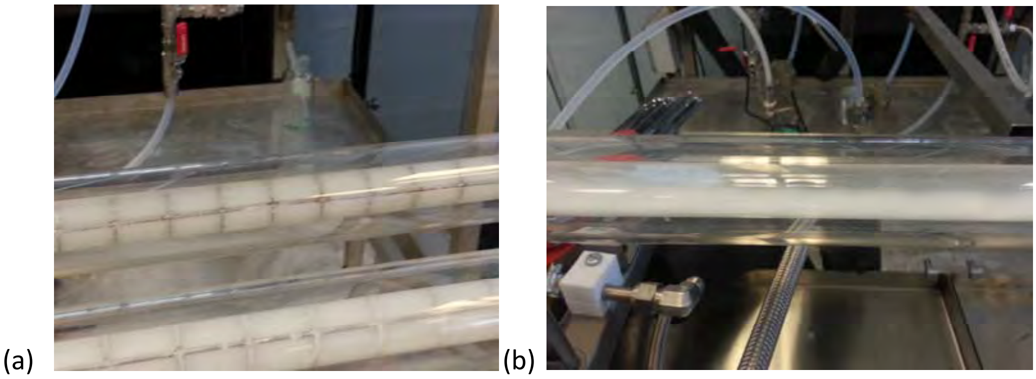

Fig. 2.10 (a) Uniform mixing of slurry in the PPU with baffles. The slurry is uniformly suspended throughout the liquid. (b). Non-uniform mixing of slurry in PPU without baffles. Note the slurry just sits at the bottom of the unit and is not suspended.

2.2 Stirred tank reactor (STR)

A 250 ml flask was fitted with a polytetrafluoroethylene (PTFE) paddle-stirrer and digital overhead stirrer set between 181-195 rpm (Fig. 2.11). The cocrystallisation liquid medium was first weighed into the flask, the stirrer switched on and then a mixture of the API and coformer was added to the flask. Sampling was done by drawing up the reaction slurry with a plastic pipette, which was then filtered and dried before analysing.

Fig. 2.11 Stirred flask reactor with slurry mixture kept in suspension by stirrer.

2.3 X-ray diffraction (XRD) analysis

X-rays are electromagnetic radiation with wavelengths in the order of $10\text{-}10^{-1}$Å; this corresponds to the distance of inter-atomic layers in crystalline solids. XRD uses the characteristic scattering of x-rays by a crystalline solid for identification. The scattering of incident x-rays is based on the internal structure. Crystalline solids consist of imaginary planes of electrons that diffract the incident x-ray at characteristic angles based on Bragg's law into a detector, which records them as peaks on the XRD diffractogram. Bragg's law states the condition for obtaining constructive interference of x-rays after diffraction from a crystalline solid (Eqn. 2.1).

$$n\lambda = 2d\sin\Theta \qquad \text{Eqn. 2.1}$$

where λ is the wavelength of the incident x-ray, d is the lattice plane spacing, n is an integer and Θ is the angle between the incident x-ray and diffracting plane (Fig. 2.12). The XRD analysis carried out used a wide angle x-ray scattering (WAXS) diffractometer and a single crystal x-ray diffractometer (SCXRD).

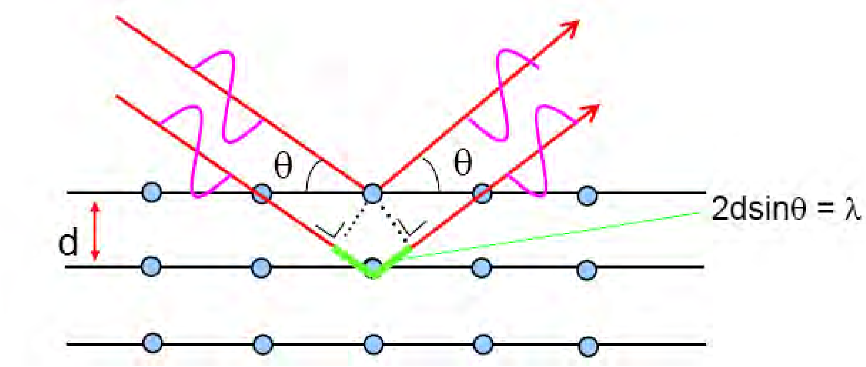

Fig. 2.12 Illustration of Bragg's law[1].

2.3.1 Powder x-ray diffraction (PXRD)

PXRD is used for fingerprint identification of crystalline solids. The Wide Angle X-rays (WAXS) technique does this by probing inter-atomic d-spacing in crystalline solids. For the WAXS analysis, the samples were not ground prior to analysis because this could have initiated cocrystallisation and hence have distorted the results. A Bruker D8 diffractometer (Fig. 2.13) was used. It has a sealed tube X-ray source operating at 40 kV and 40 mA to produce Cu K_α radiation of wavelength 1.54 Å and a Hi-star 2D detector.

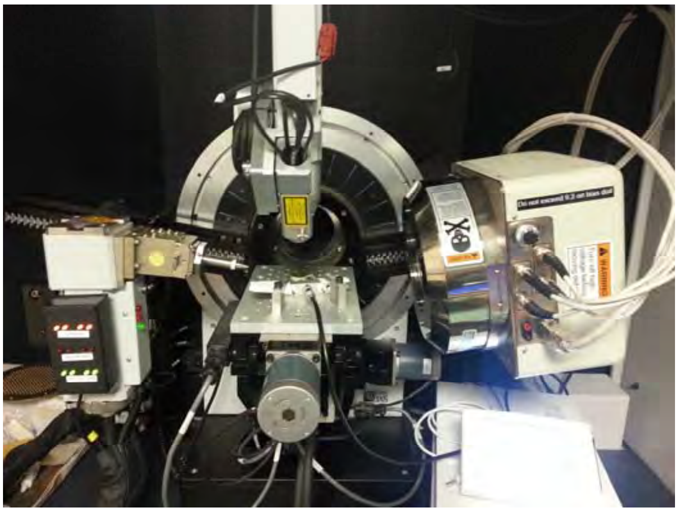

Fig. 2.13 Bruker D8 PXRD equipment.

2.3.2 Single crystal x-ray diffraction (SCXRD)

Single crystal X-ray diffraction (SCXRD) is a technique used to determine the structural information of crystal. The information obtained from SCXRD includes: unit cell dimensions, unit cell symmetries, bond lengths, bond angles and atomic positions.

SCXRD analysis was done through the Durham University Chemistry department crystallography service. Data were collected at 120.0 K except for the 2:3 2-aminopyrimidine-glutaric acid cocrystal-salt hybrid, for which the temperature was 130.0 K. A Bruker SMART CCD 6000 diffractometer with graphite monochromators ($\lambda_{MoK\alpha}$, λ = 0.71073Å), equipped with the Cryostream open-flow nitrogen cryostats, was used. The structures were solved by the direct method and refined by full-matrix least squares on F^2 for all data using OLEX2[2] and SHELXTL[3] software. The crystal data and parameters of the refinement are given in Appendix 6.2.

2.4 Solid state nuclear magnetic resonance (SSNMR) analysis

Solid-state ^{13}C spectra were recorded at 100.56 MHz using a Varian VNMRS spectrometer and a 6 mm (rotor o.d.) magic-angle spinning probe. Spectra were obtained using cross-polarisation with a 30 s recycle delay, 5 ms contact time, at ambient probe temperature (~25 °C) and at a sample spin-rate of 6.8 kHz; with between 40 and 100 repetitions per sample. Spectral referencing was done with respect to an external sample of neat tetramethylsilane (carried out by setting the high-frequency signal from adamantane to 38.5 ppm). A comprehensive review of the SSNMR technique is presented in chapter3.

2.5 Solubility determination by HPLC

The solubilities of the API, coformer and cocrystal in different solvents and solvent mixtures were determined in the laboratory, using high performance liquid chromatography (HPLC) and the gravimetric method. For the solubility determination experiments, an excess of the reagent was stirred for 30 minutes for equilibration, the resulting slurry was filtered to remove the excess solid and the filtrate analysed.

2.5.1 High performance liquid chromatography (HPLC)

The HPLC analysis was carried out on an Agilent 1100 with diode array detector (DAD), Varian Polaris 3µ C_{18} column (150 mm × 4.6mm) and a 0.6 mL min^{-1} flow rate at ambient column temperature. The mobile phases composition consisted of: Phase A = 50mM potassium phosphate (in water) acidified to pH 2.5, and Phase B = methanol.

Results were expressed as the mean of triplicate measurements, with the associated standard error of the mean quoted. The results were corrected for any dilutions performed and were obtained by quantification using 210 nm as the detection wavelength for oxalic acid and 254 nm for caffeine. The analysis assumes the commercial standards used in the solubility test are 100% pure. Results were expressed to 3 decimal places. The limit of quantification (LOQ) and limit of sample detection (LOD) are given in Table 2.2.

Table 2.2 Limits of detection on HPLC for solubility test.

Component	**LOD (mg/g)**	**LOQ (mg/g)**
Caffeine	0.001	0.057
Oxalic Acid	0.001	0.033

2.5.2 Gravimetric method

Two approaches were used: In the first approach, the filtrate from the initial equilibration was transferred into a pre-weighed beaker and allowed to evaporate. The residue was weighed and the solubility reported in milligrams of residue per gram of solvent evaporated.

In the second approach, solvent was added drop wise to a known mass of reagent with stirring. The amount of solvent required to completely dissolve the reagent was recorded and reported as mg per gram of solvent required. Solubility results were reported as the mean of duplicate analyses.

2.6 Fourier Transform Infra-red Spectroscopy (FTIR)

FTIR is based on the principle that functional groups have characteristic molecular vibrations with energies corresponding to the infra-red region of the electromagnetic spectrum. FTIR was done on thermo-scientific Nicolet iS10 IR equipment (Fig. 2.14) with an attenuated total reflection (ATR) accessory fitted with a zinc selenide (ZnSe) crystal. The ATR-FTIR equipment allowed for fast analysis without the need for sample preparation. The scan range was from 600 cm^{-1} to 4000 cm^{-1} collecting 8 to 64 scans per spectrum. Infra-red spectroscopy has been shown to be able to differentiate between ionized and un-ionised O—H······N bonds[4,5].

Fig. 2.14 Thermo-scientific Nicolet iS10 ATR-FTIR equipment.

2.7 Differential Scanning Calorimetry (DSC)

DSC analysis was done on a TA Q20 series instrument (Fig. 2.15) with sample weights ranging between 2-10 mg in aluminium pans. A comprehensive review is presented in chapter 3.

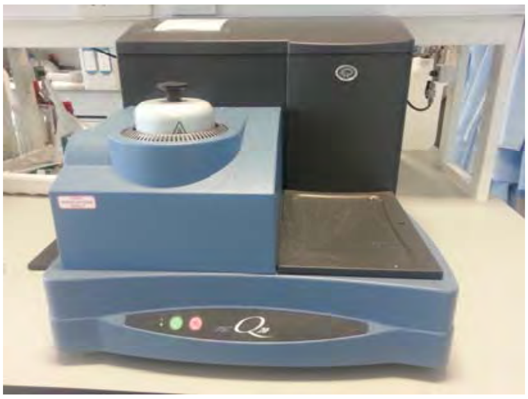

Fig. 2.15 TA Q20 Differential scanning calorimeter (DSC).

2.8 Thermal Gravimetric Analysis (TGA)

TGA analysis was done on a TA Q50 series instrument (Fig. 2.16) with sample weight between 1.4-4.3 mg in a Tzero platinum hermetic lid.

Fig. 2.16 TA Q50 thermal gravimetric analysis.

2.9 Sieve analysis

Particle size determination (PSD) using sieve analysis is very common because it is easy, cheap and can handle large sample amounts. Particle size separation is achieved based on the different mesh sizes of the nested column of sieves used; the largest mesh size of 1 mm at the top and the smallest mesh size of 106 µm at the bottom. The mesh wire and sieves were made from stainless steel (Fig. 2.17).

In this approach, it is assumed that the powder particle shapes are uniform so should pass easily through the mesh. Since particle sizes can vary a lot within a powder. The large sample handling capability is useful for ensuring representative sampling is achieved.

Sieve analysis is not easy to reproduce because the energy input is not constant and this can skew PSD analysis. If sufficient energy is not used, then it may be difficult to break up agglomerates present in the sample and so give a false result suggesting the sample is made up of larger particles than actually is present. However, too much energy is used, it could lead to breakages of fragile particles and give a false result with too low sizes.

For this study, sieving was done manually for 2 minutes and timed with a stop clock. The weight of powder retained in each sieve was weighed and the percentage calculated from total weight of sample using Eqn.2.2.

$$\%\ \text{Retained} = \frac{\text{Wt}_{\text{sieve}}}{\text{Wt}_{\text{total}}} \times 100\% \qquad \text{Eqn. 2.2}$$

Fig. 2.17 Picture of sieve meshes used for PSD determination, with the largest mesh size of 1 mm at the top and the smallest mesh size of 106 µm at the bottom.

References

(1) X-ray diffraction for powder sample, . Published Online: **2013**. http://homepage.ntu.edu.tw/~kcyuan/form/For_Rigaku-Upload_powder.pdf (accessed 10/07/2013).

(2) Dolomanov, O. V.; Bourhis, L. J.; Gildea, R. J.; Howard, J. A. K.; Puschmann, H. *Journal of Applied Crystallography* **2009**, *42*, 339.

(3) Sheldrick, G. M. *Acta Crystallographica* **2008**, *A64*, 112.

(4) Schultheiss, N.; Newman, A. *Cryst. Growth Des.* **2009**, *9*, 2950.

(5) Aakeroy, C. B.; Salmon, D. J.; and M. M. S.; Desper, J. *Cryst. Growth Des.* **2006**, *6*, 1033.

Chapter 3 Development of a quantitative analytical method

3.1 Introduction

This chapter describes the approach used in developing a quantitative analytical protocol for caffeine-oxalic acid cocrystallisation using solid state nuclear magnetic resonance (SSNMR). It includes other analytical techniques considered and the reasons why they were not selected are stated. The precision of the analytical technique for quantitative cocrystal analysis was the determining factor in selecting solid state nuclear magnetic resonance as the analytical technique of choice.

3.1.1 Quantitative analysis

Process optimisation is an integral part of scaling up processes for manufacture; process optimisation aims to establish conditions that will deliver a robust, reproducible process during manufacture. Quantitative analytical data are used for decision making in process optimisation, to monitor the effect of the various process variables, in this case, cocrystallisation process variables.

Different analytical methods were investigated for use in quantifying cocrystal conversion. In short-listing which analytical methods to consider for quantitative cocrystal analysis, the following criteria were adopted:

1. The stability of samples during analysis.
2. The capability of the analytical method to sufficiently differentiate between the starting component and final cocrystal.
3. Existing applications of the analytical technique for quantitative analysis.
4. Reproducibility of the analytical technique.

The caffeine-oxalic acid cocrystal was used as the model system for developing the quantitative method. The analytical methods considered were: high pressure liquid chromatography (HPLC), differential scanning calorimetry (DSC), powder x-ray diffractometry (PXRD) and solid state nuclear magnetic resonance (SSNMR). Due to the fact that samples have to be analysed in solid form, inhomogeneity of a sample is an inherent source of error in whatever analytical method is used; but the focus of this investigation was on the precision and not the accuracy of the analytical technique. By precision, it is meant that the quantitative analytical technique gives reproducible results even though the results may be inaccurate (i.e. not reflective of the true value) because of inherent systematic sources of error like sample inhomogeneity.

3.1.2 Preparation of caffeine-oxalic acid 2:1 cocrystal standard

A sample of caffeine-oxalic acid cocrystal (Fig. 3.1) was prepared as a standard for single crystal x-ray diffraction (SXRD) analysis. Commercial grade (Sigma Aldrich) caffeine and oxalic 2:1 mass ratio were ground for 30 minutes and the solid mix dissolved in 50:50 wt% mixture of anhydrous methanol and anhydrous chloroform. The solution was allowed to evaporate slowly by sealing the vials with parafilm and puncturing small holes into the parafilm to control evaporation rate. The resulting crystals were filtered and allowed to dry.

The caffeine-oxalic acid cocrystal standard was characterised by: SXRD, DSC, ATR-FTIR and SSNMR analyses to confirm first of all that the new 2:1 caffeine-oxalic acid cocrystal phase had been prepared and that each of these techniques could be used to distinguish the cocrystal from its crystalline components.

The generated simulated powder pattern for the cocrystal standard matched the pattern in the Cambridge structure database[1,2] (compare Figs. 3.2 and 3.3) and journal publications[3]. The 2:1 caffeine-oxalic acid cocrystal is most-readily distinguishable from its components by: the disappearance of the caffeine peak at $2\theta = 12^\circ$, the appearance of three new peaks at $2\theta = 8^\circ$, 10° and 12° (Fig. 3.4).

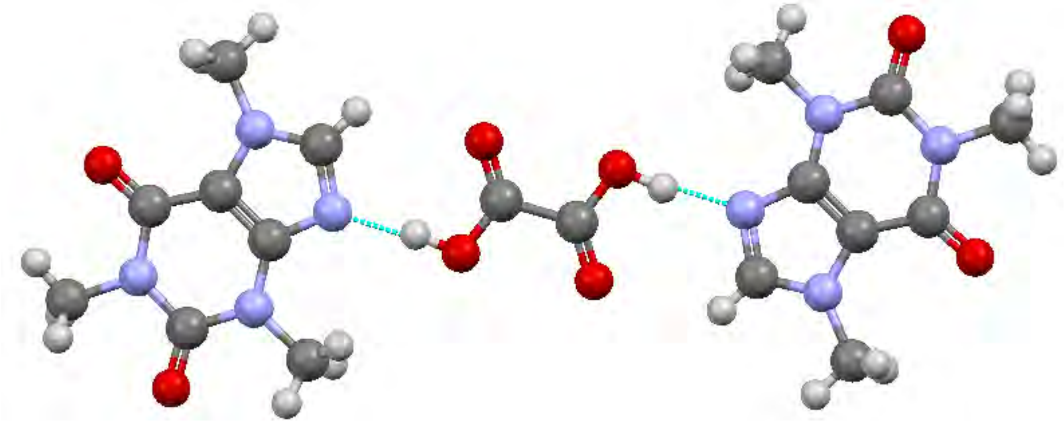

Fig. 3.1 Caffeine-oxalic acid cocrystal single crystal standard.

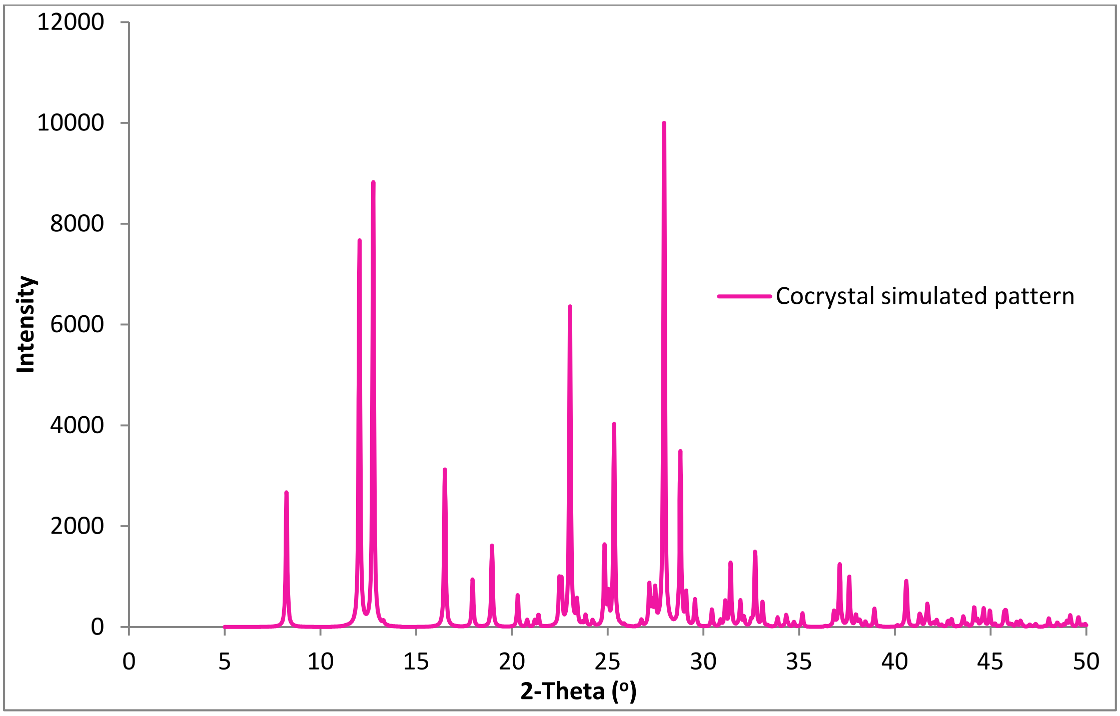

Fig. 3.2 Simulated powder XRD pattern from a single crystal of 2:1 caffeine-oxalic acid grown in the laboratory.

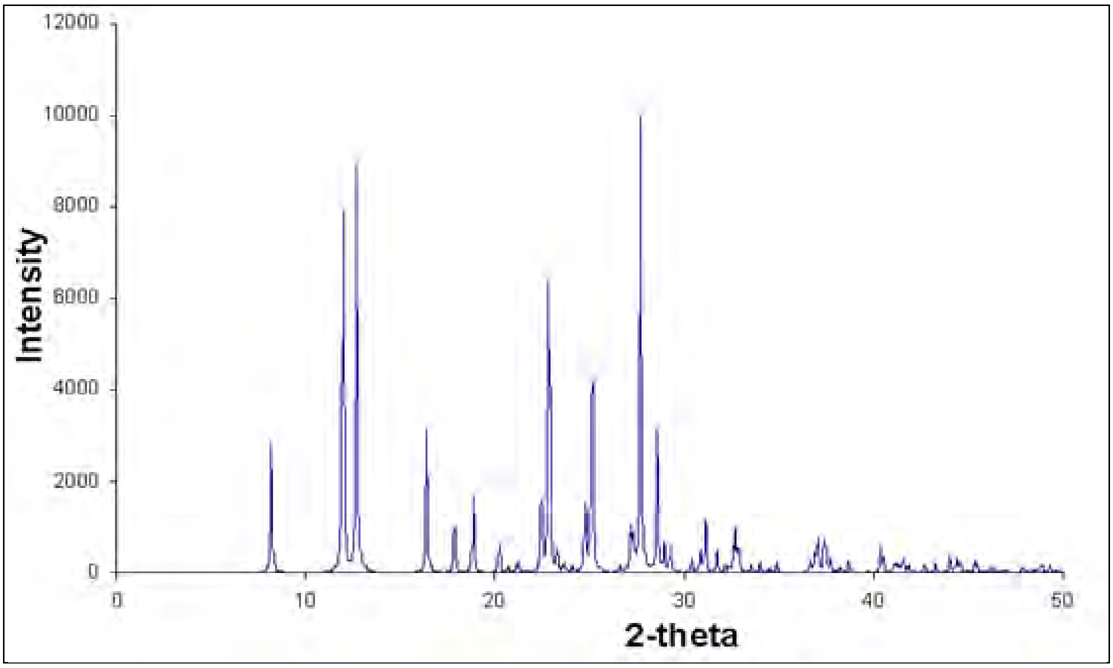

Fig. 3.3 Predicted pattern of the 2:1 caffeine-oxalic acid cocrystal in Cambridge Structural Database (CSD)[1].

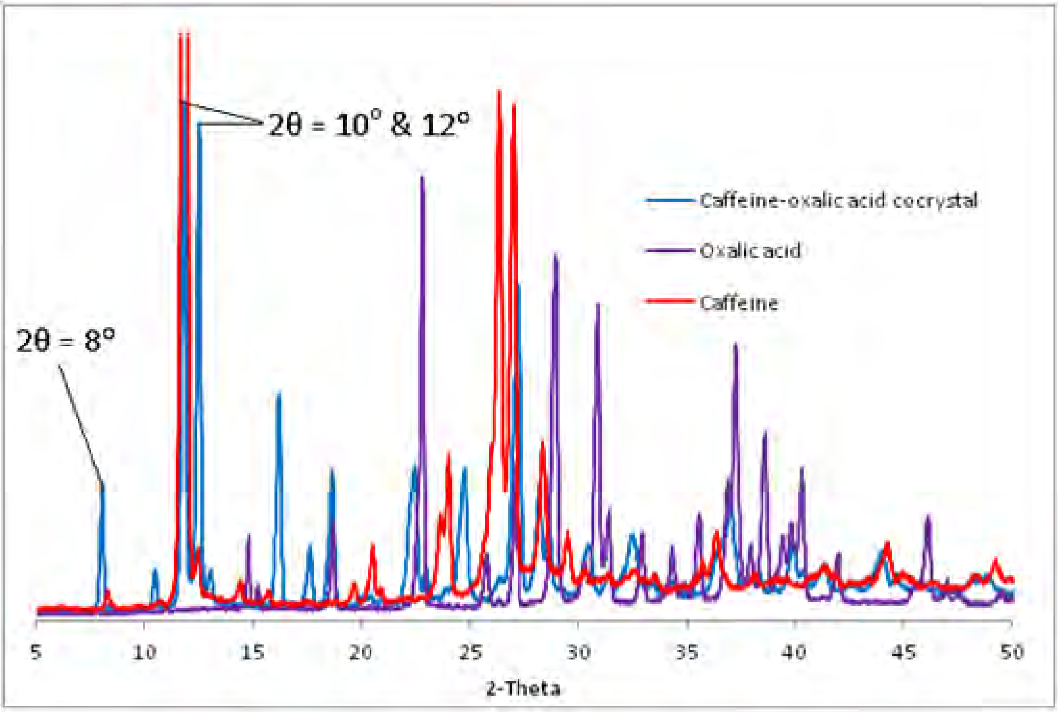

Fig. 3.4 PXRD spectra for commercial sample of caffeine.

The solid state nuclear magnetic resonance analysis of a mixture of caffeine oxalic acid cocrystal, caffeine and oxalic acid shows distinctive chemical shift differences between the cocrystal and its components (Fig. 3.5), which will be discussed later on in this chapter.

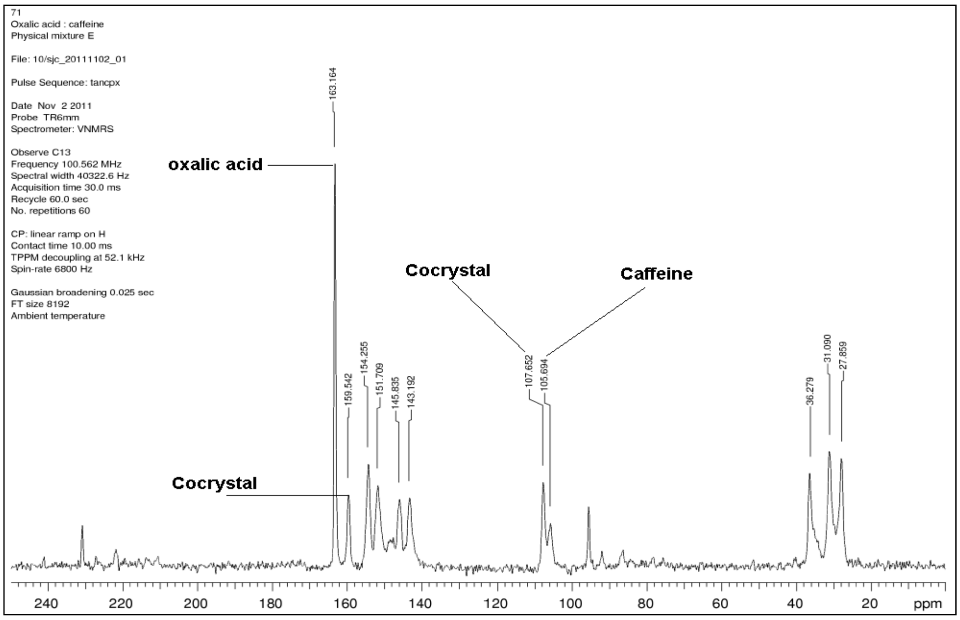

Fig. 3.5 ^{13}C CP/MAS spectra of reaction mixture showing cocrystal, caffeine and oxalic acid peaks.

The ATR-FTIR spectrum for caffeine-oxalic acid cocrystal (Fig.3.6) shows considerable differences with the oxalic acid and caffeine ATR-FTIR spectra (Fig.3.7). The presence of broad peaks at around 2200 to 2800 cm^{-1} in the caffeine-oxalic acid cocrystal ATR-FTIR spectrum is characteristic of O-H stretching of un-ionised, strongly H-bonded carboxylic acid[4]; the presence of two broad bands at 1900 cm^{-1} and 2350 cm^{-1} (Fig.3.7), which are absent in oxalic acid, are also evidences of un-ionised O-H hydrogen bonding stretching of the carboxylic acid[5,6] in the single crystal caffeine-oxalic acid cocrystal.

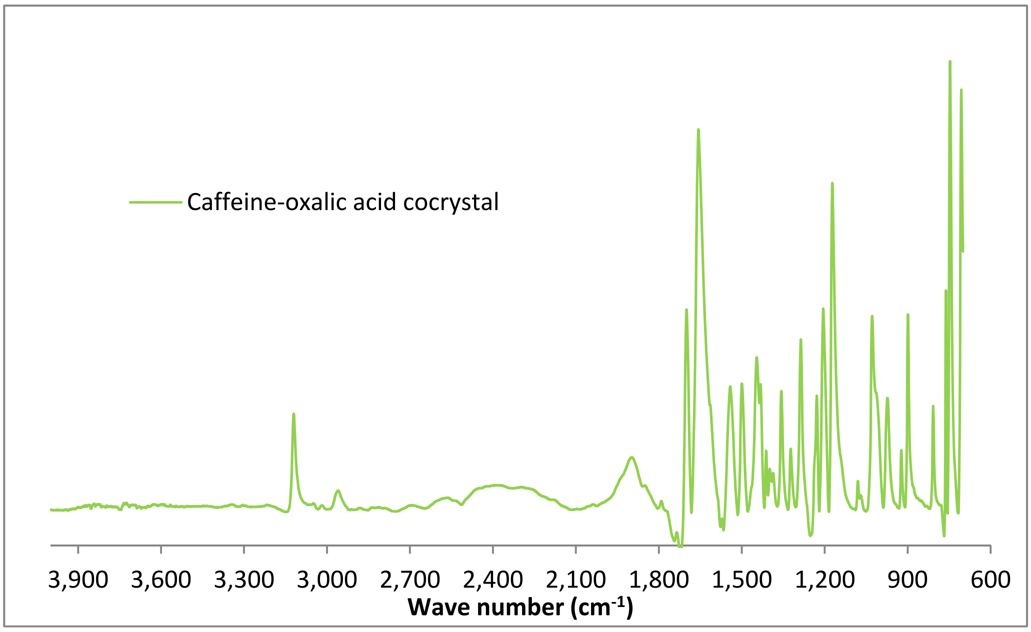

Fig. 3.6 FTIR spectra of caffeine-oxalic acid cocrystal.

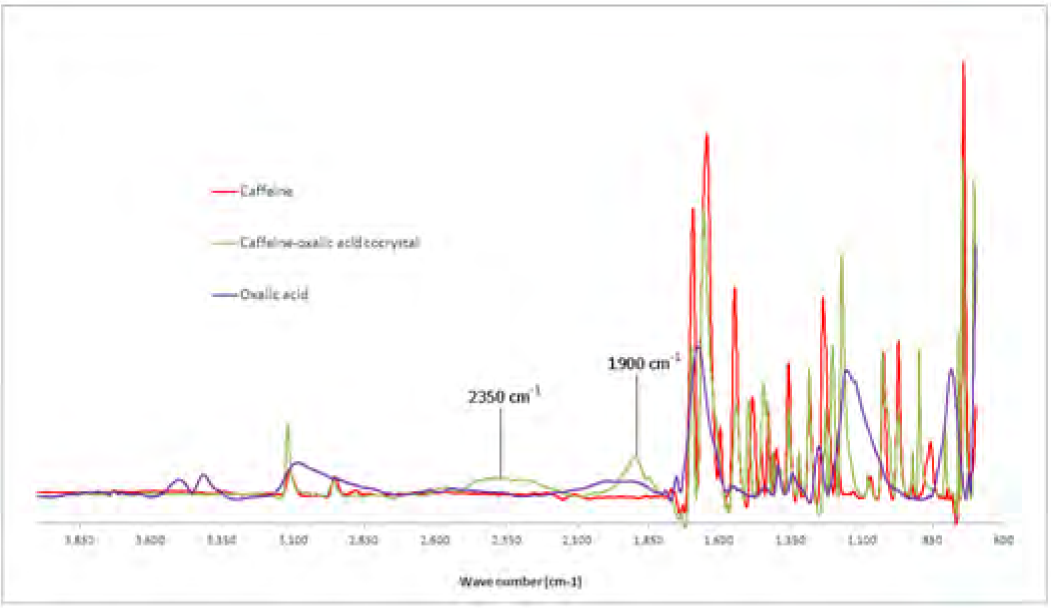

Fig. 3.7 Comparing ATR-FTIR spectra of caffeine-oxalic acid cocrystal and its components.

DSC analysis of the caffeine-oxalic acid cocrystal, caffeine and oxalic acid showed different melting points; the cocrystal displayed an onset melting point of about

206.5 ^{o}C (Fig. 3.8), which is 29.1^{o}C lower than the onset melting point of caffeine 235.6 ^{o}C (Fig. 3.9) and 20.6 ^{o}C higher than the 186.9 ^{o}C melting point of oxalic acid (Fig. 3.10). Consequently, these initial studies have confirmed that the cocrystal has been produced and can be detected using PXRD, ATR-FTIR, SSNMR and DSC techniques. The PXRD, SSNMR and DSC techniques will now be further assessed as to their ability to provide quantitative analysis of the cocrystal yield. The ATR-FTIR technique was not considered further, however, due to the fact that it was not easy to identify distinctive, non-overlapping peaks to distinguish between caffeine-oxalic acid cocrystal, caffeine and oxalic acid (Fig. 3.7). A multivariate approach using more than one peak may overcome this challenge but there was not sufficient time to explore this option. In addition, one further technique, high pressure liquid chromatography, was also investigated to determine its capability in providing quantitative analysis of the cocrystal amount.

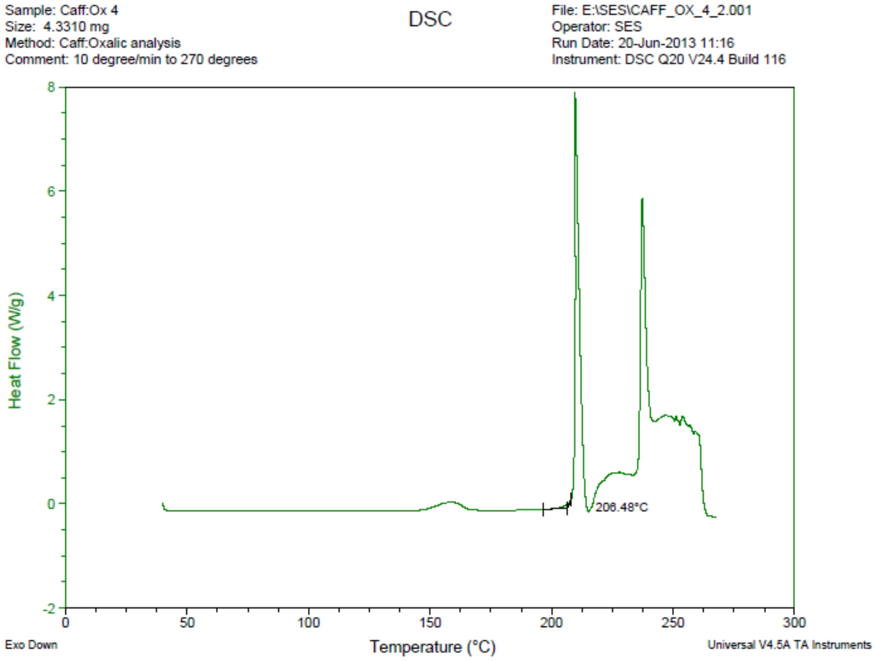

Fig. 3.8 DSC thermogram of caffeine-oxalic acid cocrystal made in laboratory.

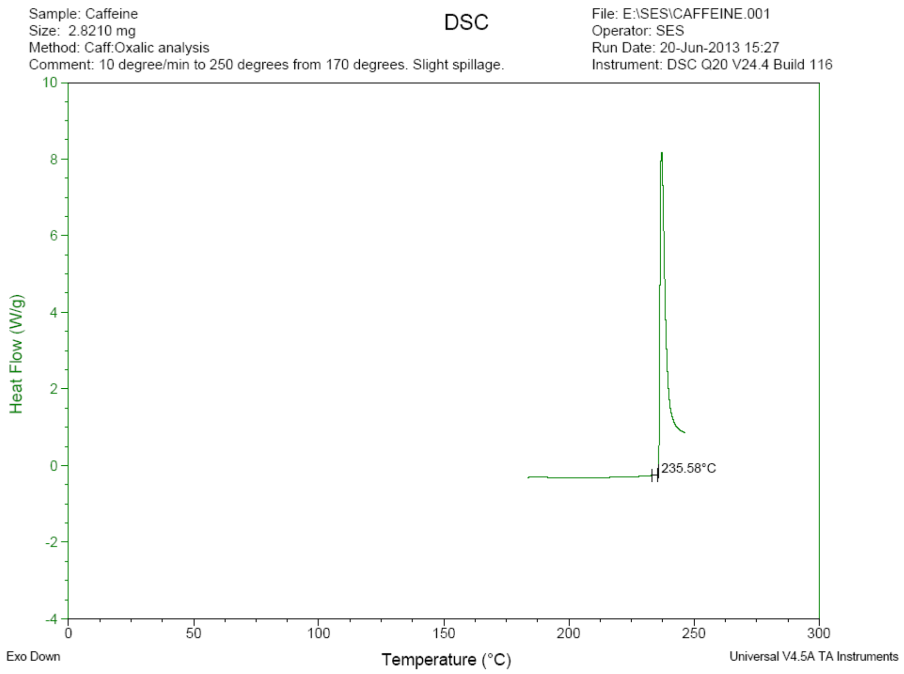

Fig. 3.9 DSC thermogram of commercial sample of caffeine.

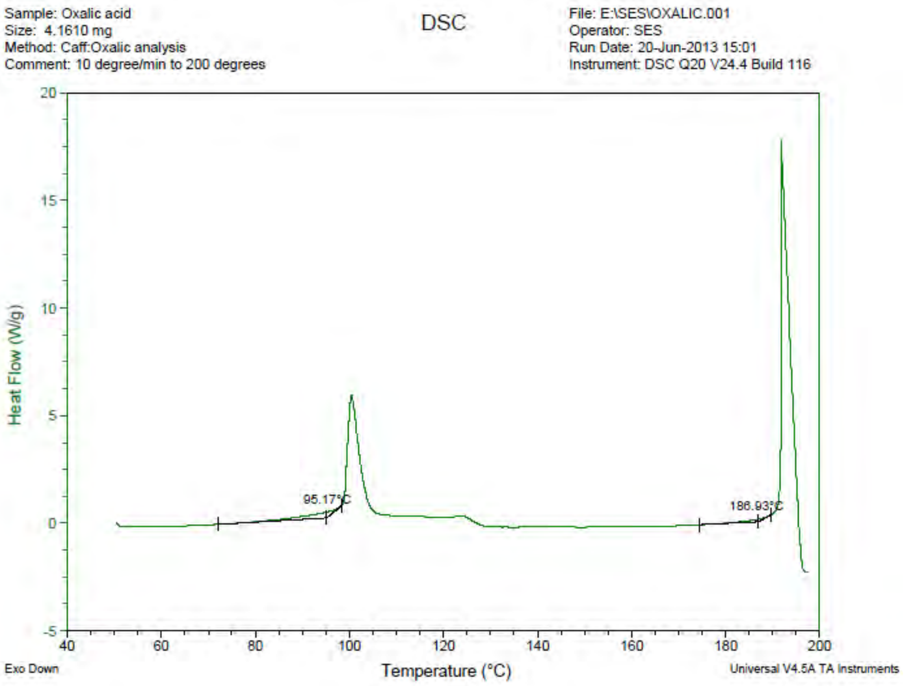

Fig. 3.10 DSC thermogram of commercial sample of oxalic acid.

3.2 High pressure liquid chromatography (HPLC)

The chromatographic method investigated was high pressure liquid chromatography (HPLC). This technique may not satisfy the first selection criteria of maintaining sample stability during analysis because of the possibility of the caffeine-oxalic acid cocrystal dissociating to give caffeine and oxalic acid in solution due to the weakness of the intermolecular hydrogen bonds. However this technique was investigated because Leung et al[7] reported cocrystal quantification using a combination of HPLC and NMR analytical technique.

Caffeine oxalic acid cocrystal (Fig. 3.11), caffeine (Fig. 3.12) and oxalic acid (Fig. 3.13) were dissolved in a suitable solvent and analysed by HPLC. The HPLC chromatogram of caffeine-oxalic acid cocrystal standard (Fig. 3.11) shows three peaks; two main peaks at retention 2.97 minutes and 14.48 minutes corresponding to oxalic acid (Fig. 3.13) and caffeine (Fig. 3.12), respectively, and a third small peak with a retention time of 18.56 minutes. This third peak is most likely an impurity as it is also present in the oxalic acid analysis (Fig. 3.13). Cocrystallisation of caffeine with oxalic acid will change the physicochemical properties and the caffeine-oxalic acid cocrystal would be expected to have intermediate polarity between oxalic acid and caffeine. However, the absence of any additional peaks confirms the fact that the intermolecular hydrogen bonding in caffeine-oxalic acid cocrystal is not stable in solution and so HPLC analysis is not easily applicable for direct cocrystal quantitative analysis. HPLC may be of use for indirect cocrystal quantification by assuming that complete cocrystallisation has been achieved and the concentration of the caffeine and oxalic acid can then be used to determine cocrystal yield. Clearly, though, this approach is prone to a large error if the sample analysed is not 100% pure.

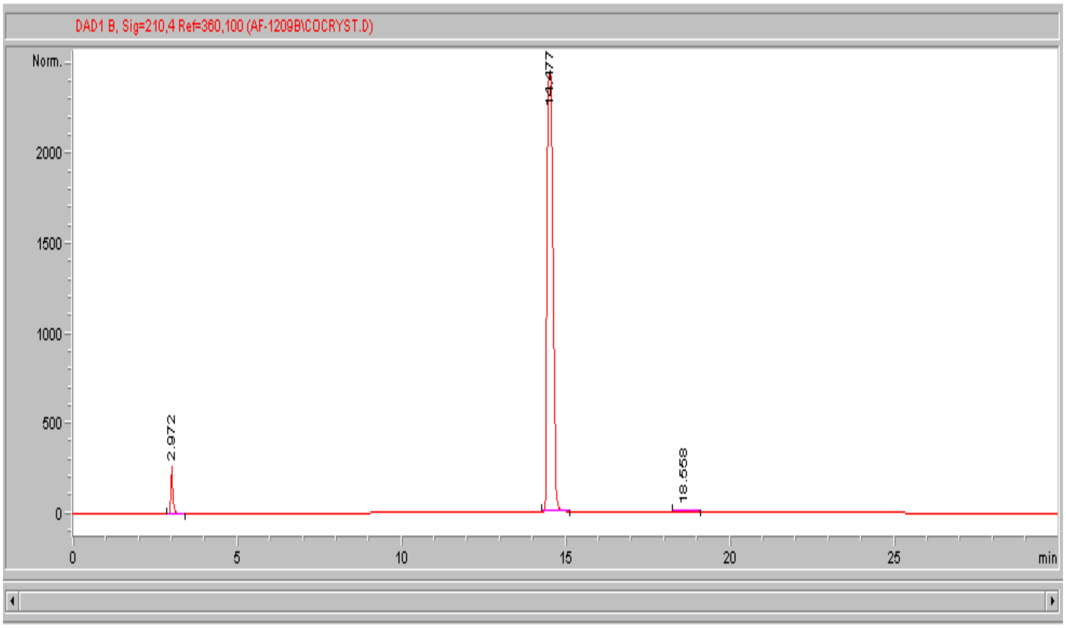

Fig. 3.11 HPLC analysis of caffeine-oxalic acid cocrystal standard showing cocrystal breakdown to oxalic acid, caffeine and an unknown peak.

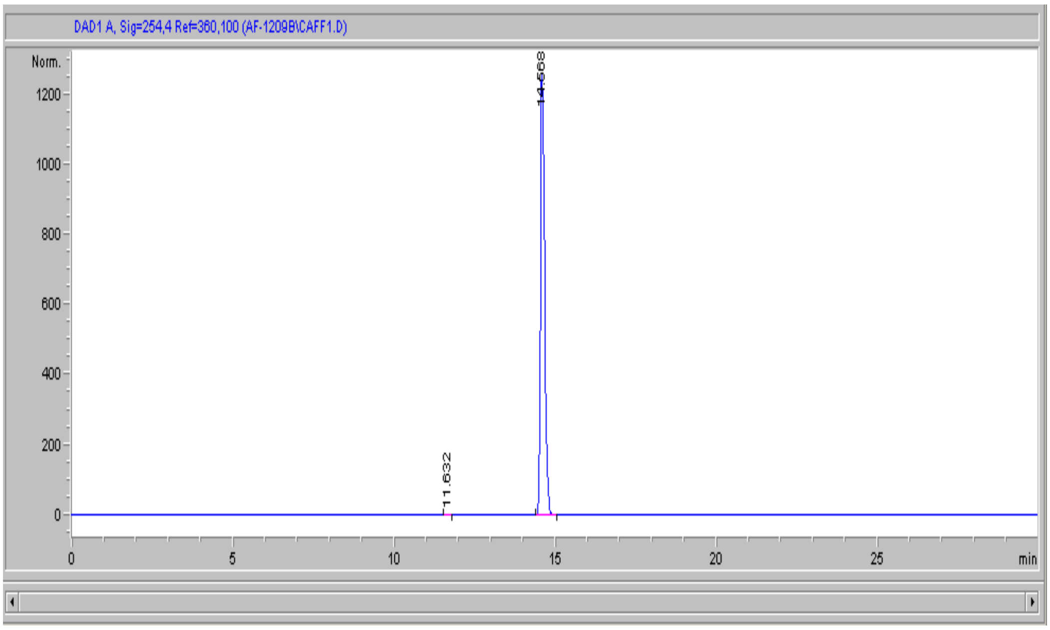

Fig. 3.12 HPLC analysis of commercial grade caffeine.

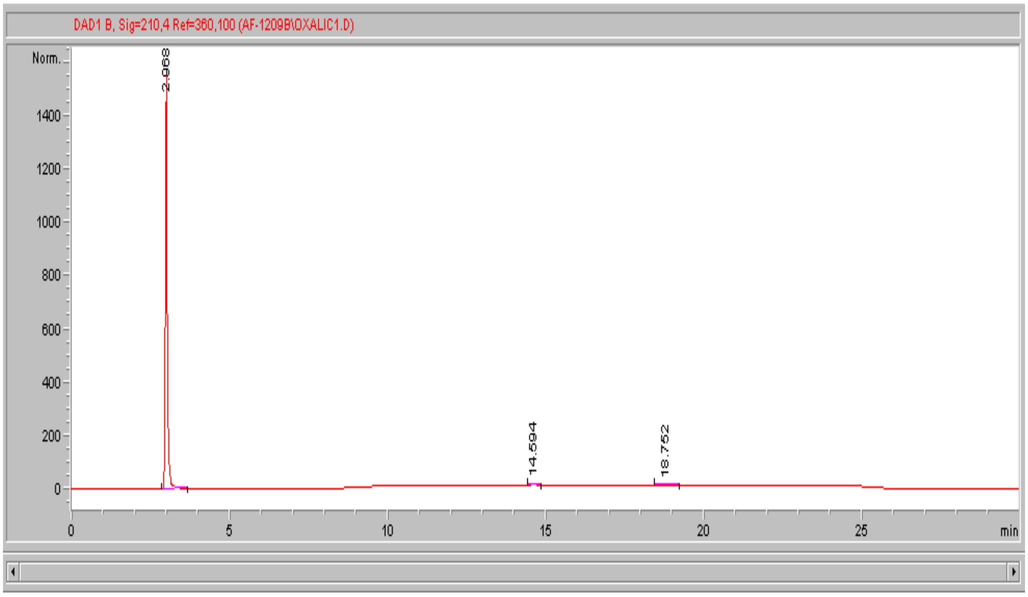

Fig. 3.13 HPLC analysis of commercial grade oxalic acid.

3.3 Differential scanning calorimetry (DSC)

Cocrystallisation alters the physicochemical properties of the API and so cocrystal molecules display a different melting point from the melting points of the cocrystal components; in a review of 50 molecules, 48 (96%) had different melting point to their cocrystal components[6]. This difference in melting point results in a unique enthalpy of fusion, which is why it has been considered for qualitative thermal analysis. The DSC technique satisfies the criteria set out at the beginning of the chapter. However, a shortcoming of the DSC application in quantitative analysis is that it depends on efficient heat transfer from the machine to the sample and heat transfer within solids samples; if both heat transfers are not uniform, it gives rise to a thermal gradient across the sample and an uneven rate of phase transition across the sample.

If the DSC heating program is too fast, the sample and the reference do not have sufficient time to attain equilibrium, resulting in thermal lag and a false thermogram[8,9]. Repeated DSC analysis with different weights of caffeine-oxalic acid cocrystal standard and a heating programme going from 20-300 °C at the rate of 10°C/min were carried out to determine the precision of the DSC technique for quantitative cocrystal analysis. The enthalpy of fusion for the caffeine-oxalic acid cocrystal was determined from the endotherm peak of the melt transition by integrating the peak and getting the heat requirement for the melt transition, i.e. the enthalpy of fusion, measured Joules per gram (J g^{-1}). Eqn. 3.1 shows the relationship between the heat capacity at constant pressure (C_p) and the enthalpy (H).

$$C_p = \left[\frac{\partial H}{\partial T}\right]_p \qquad \text{Eqn 3.1}$$

The results for the repeated DSC analysis of caffeine-oxalic acid cocrystal are tabulated in Table 3.1. A single endotherm peak of melting at ≈214 °C was observed in each caffeine-oxalic acid cocrystal thermogram, confirming the purity of the caffeine-oxalic acid cocrystal standard. The specific heat capacity and enthalpy of fusion in J g^{-1} are intensive properties and so are independent of the amount of sample used in the test. Consequently, the invariance of the enthalpy of fusion provides a test for the precision of the DSC measurements. Table 3.1 shows large variation in the enthalpy of fusion obtained for the caffeine-oxalic acid cocrystal standard, suggesting a lack of measured precision in this quantity.

The reproducibility of the caffeine-oxalic acid cocrystal enthalpy of fusion was measured using the sample standard deviation (s) and the coefficient of variance (CV). The standard deviation (s) measures the variation of the data points around the mean; it is given by the square root of the variance and has the same units as the data. A high standard deviation (s) value suggests a large spread of data points and poor reproducibility of the measurements; a small standard deviation (s) value implies a small spread of data points from the mean suggesting high precision of the measurement method. The standard deviation (s) is given by Eqn.3.2:

$$s = \sqrt{\frac{\sum(\mathcal{X}_i - \bar{\mathcal{X}})^2}{n-1}} \qquad \text{Eqn. 3.2}$$

The mean ($\bar{\mathcal{X}}$) of the caffeine-oxalic acid cocrystal enthalpy of fusion for the DSC analysis was determined (Eqn. 3.3) and used to calculate the standard deviation (Table 3.2)

$$\bar{\mathcal{X}} = \frac{\sum \mathcal{X}}{n} \qquad \text{Eqn. 3.3}$$

$$\bar{\mathcal{X}} = \frac{663.7+955+790.6+955.3+614+346.6}{6} = 720.9$$

$$s = \sqrt{\frac{269404.2}{5}} = 232.12$$

Table 3.1 Specific enthalpy of fusion for caffeine-oxalic acid cocrystal DSC analysis.

Sample description	Sample weight (mg)	Peak temperature (^oC)	J/g
Caffeine-oxalic acid cocrystal	2.894	214.16	663.7
	2.374	213.3	955
	2.158	214.14	790.6
	1.516	213.14	955.3
	2.072	214.23	614
	2.712	213.63	346.6

The coefficient of variance (CV) is used for determining accuracy in a set of data by quantifying the impact of the measurement variability on the measured data as a percentage and is not in the same units as the data; it is the percentage of the data standard deviation (s) and average ($\bar{x}$) and is calculated using Eqn. 3.4. A CV value ≤ 5% indicates that the data is reproducible but an CV value ≥ 10% indicates the data is not very reproducible[10].

$$\mathrm{CV} = \frac{\mathrm{s}}{\bar{\mathrm{x}}} \times 100 \qquad \text{Eqn. 3.4}$$

The CV for the DSC analysis is:

$$\mathrm{CV} = \frac{232.12}{720.9} \times 100$$

CV = 32.2%

Table 3.2 Standard deviation calculation for DSC analysis.

J/g($\mathcal{X}$)	$(\mathcal{X}_i - \bar{\mathcal{X}})$	$(\mathcal{X}_i - \bar{\mathcal{X}})^2$
663.7	-57.2	3268.4
955	234.1	54816.9
790.6	69.7	4862.3
955.3	234.4	54957.4
614	-106.9	11421.2
346.6	-374.3	140078.0
$\sum$		269404.2

The standard deviation of 232.12 and coefficient of variance (CV) of 32.2% are both very high indicating that the fusion enthalpy of caffeine-oxalic acid cocrystal determined using DSC has a large variation and the measurement is not reproducible. This high variation suggests that thermal lag may be occurring during the DSC analysis and that the heating rate of 10^{o}C/min is too fast to attain reproducible DSC analysis.

One way to mitigate against this poor DSC precision would be to reduce the heating rate, which helps improve the sensitivity of the analysis; the slower heating rate allows sufficient time for the sample and reference to equilibrate during analysis, but this extension of the melt transition period may initiate further cocrystallisation if any residual caffeine and oxalic acid is present in the sample via melt cocrystallisation. To test this, the thermal stability of the caffeine-oxalic acid cocrystal in the presence of caffeine and oxalic acid was investigated using solid state nuclear magnetic resonance (SSNMR) analysis at elevated temperature. The solid state spectra of a mixture of caffeine, oxalic acid and caffeine oxalic acid cocrystal were determined using SSNMR (Fig. 3.5). A mixture of caffeine-oxalic acid cocrystal, caffeine and oxalic acid was heated to 80 ^{o}C and held for 2 hrs in the SSNMR spectrometer. Spectra were taken at intervals of 16 minutes (Fig. 3.14). A temperature of 80^{o}C degree was selected because it is the highest temperature that could be used on the SSNMR equipment; going to higher temperatures could result in thermal decarboxylation of oxalic acid raising safety issues. The SSNMR spectra (Fig. 3.14) show a gradual increase in the caffeine-oxalic acid cocrystal peak at chemical shift ≈108 ppm with increasing time of analysis. On the spectra, time increases from the bottom row to the top row, with the bottom row representing the spectra obtained at ambient temperature.

This result shows that extending the DSC analytic time has a high probability for initiating further cocrystallisation during analysis when residual cocrystal component is present. Hence this will have a negative impact on the precision of the DSC technique for cocrystal quantitative analysis. At the caffeine-oxalic acid cocrystal melt transition (≈214 °C) the rate of cocrystallisation induction will be higher compared to the level observed in the SSNMR experiment at 80 °C, as expected from the Arrhenius equation (Eqn. 3.5), which relates the rate of reaction to the temperature.

$$k_r = \mathrm{A}e^{\frac{-\mathrm{E}_a}{RT}} \qquad \text{Eqn. 3.5}$$

Due to all these issues, the development of a DSC cocrystal quantification method was not pursued further for the caffeine-oxalic acid cocrystal.

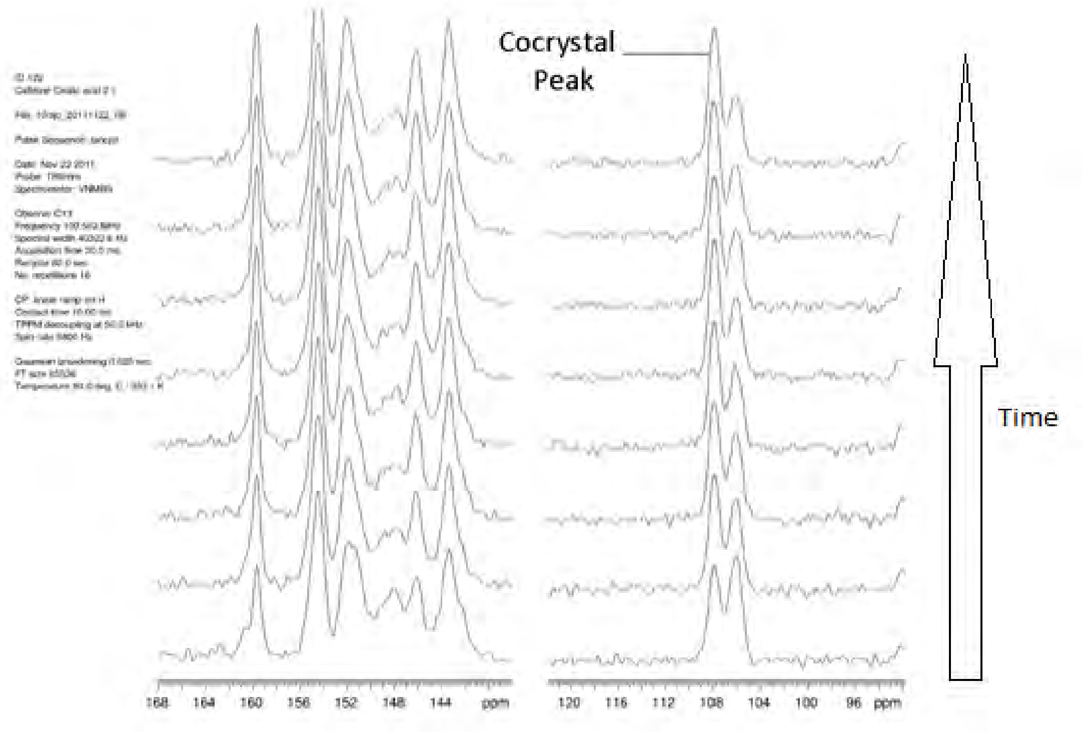

Fig. 3.14 Isothermal SSNMR of 2:1 molar mixture caffeine and oxalic acid at 80°C. SSNMR spectra show a gradual increase in level of caffeine oxalic acid cocrystal with time.

3.4 Powder x-ray diffraction (PXRD)

PXRD is a non-destructive technique that ensures sample stability during analysis. PXRD makes use of solid samples and sample preparation is simple. It is used widely in the pharmaceutical industry and in quantitative analysis[11].

Quantitative analysis using PXRD does have its challenges, though: its precision is affected by preferred orientation[11,12] as a result of sample crystal habit exaggerating peak reflections; and peak broadening also can occur due to very small crystal sizes in the sample. Although preferred orientation can be minimised by grinding the sample to give smaller particle size and more regular shape, grinding can initiate cocrystallisation and hence significantly affect the precision and accuracy of the quantitative result.

3.4.1 Principle of quantitative PXRD

Quantitative PXRD analysis is based on determining the area under a reflection peak of interest in the desired phase; a single peak area, a ratio of more than one peak areas or a ratio of peak and an internal standard peak areas can be used to construct a calibration curve for quantitative analysis. The TOPAS-Academics software was used for determining peak areas in this study. The relationship between the phase amount and reflection intensity determined from the peak area is given by Eqn. 3.6.

$$\mathrm{I}_1 = \frac{\mathrm{K}_1 x_1}{\rho_1\left[x_1\left(\mu_1^* - \mu_\mathrm{M}^*\right) + \mu_\mathrm{M}^*\right]} \qquad \text{Eqn. 3.6}$$

I_1 in Eqn.3.6 is the intensity of the reflection of interest, K_1 is the proportionality constant, ρ_1 is the density of the phase, x_1 is the mass fraction of the phase in the mixture, μ_1^* is the mass absorption coefficient of the phase of interest and μ_M^* is the mass absorption coefficient of the entire sample matrix.

The TOPAS-Academic software uses the Rietveld method for calculating peak intensities. This Rietveld method calculates intensities using a model of the crystalline structure, which is then fitted against the observed PXRD pattern and optimised using the least squares refinement[12,13], the best fit being the model with the lowest least square.

The first goal was to identify suitable peaks in the cocrystal phase to use in testing for precision in the PXRD caffeine-oxalic acid cocrystal quantification. Commercial samples of caffeine (Fig. 3.15), oxalic acid (Fig. 3.16) and laboratory synthesised caffeine oxalic acid cocrystal (Fig. 3.17) were analysed and the resulting spectra were compared (Fig. 3.18) to identify distinguishing peaks that do not overlap between the cocrystal and its components. The caffeine-oxalic acid cocrystal reflection at 2θ≈8.0^{o} and 2θ≈16.11^{o} were selected for this phase because these reflections did not overlap with peaks in caffeine or oxalic acid (Fig. 3.18). Four standard mixtures of caffeine-oxalic acid cocrystal, caffeine and oxalic acid were made up and the PXRD patterns obtained. The samples were analysed using the silicon wafer sample holder on the Bruker D8 equipment. The standard mixtures were in milligram weight as this allowed for analysis of the entire sample, avoiding the need for further sampling which could exaggerate the error due to sample inhomogeneity. The spectra were imported into the TOPAS-Academic V5 software (Fig. 3.19) to determine peak areas.

The software takes into account instrument error by giving the option to specify the instrument type and x-ray source. A comparison is made between the experimental and fitted pattern, which is illustrated by the grey line in the bottom window of Fig. 3.19. The region of 2θ≈8.0^{o} and 2θ≈16.11^{o}, show a good fit.

The peak areas are tabulated in Table 3.3 and 3.4, while the plot of cocrystal amount present in the samples against peak area ratios is presented in Fig. 3.20 and 3.21 (see appendix A for tables of the peak area for the four standards).

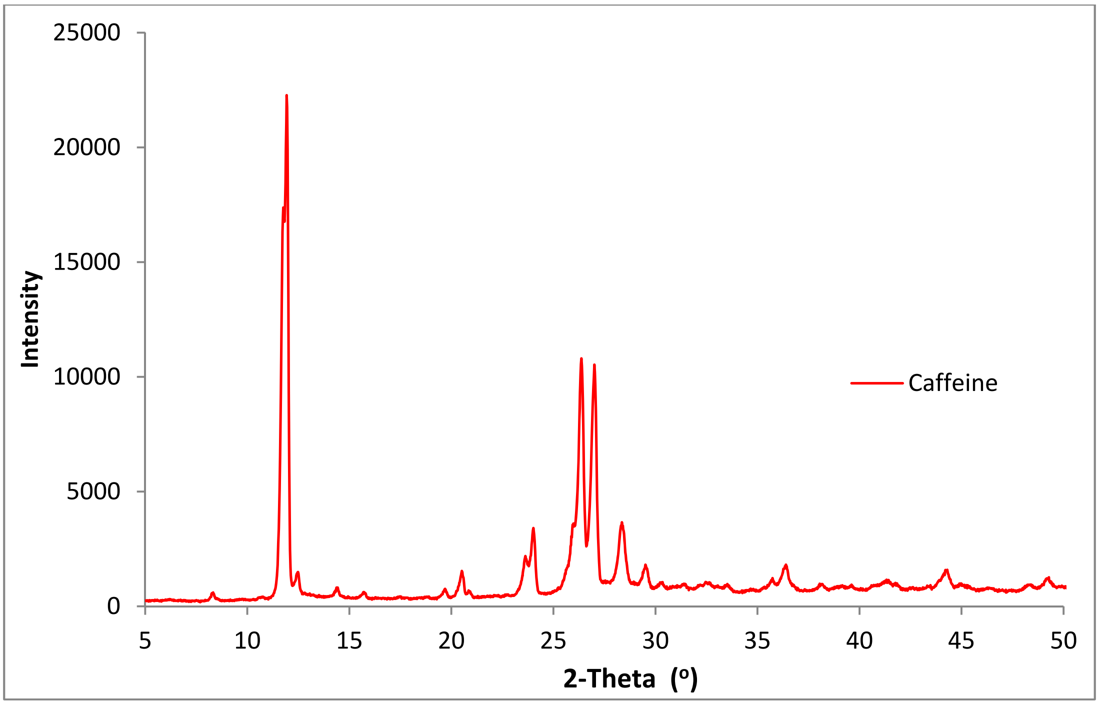

Fig. 3.15 PXRD pattern for commercial sample of caffeine.

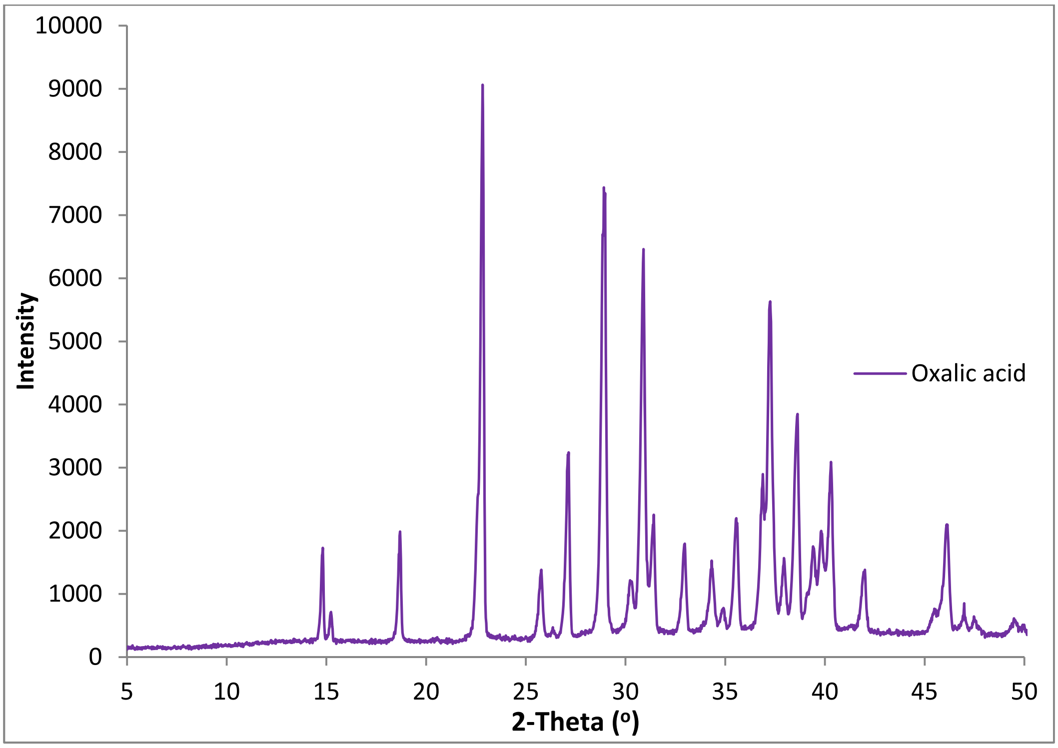

Fig. 3.16 PXRD pattern for commercial sample of oxalic acid.

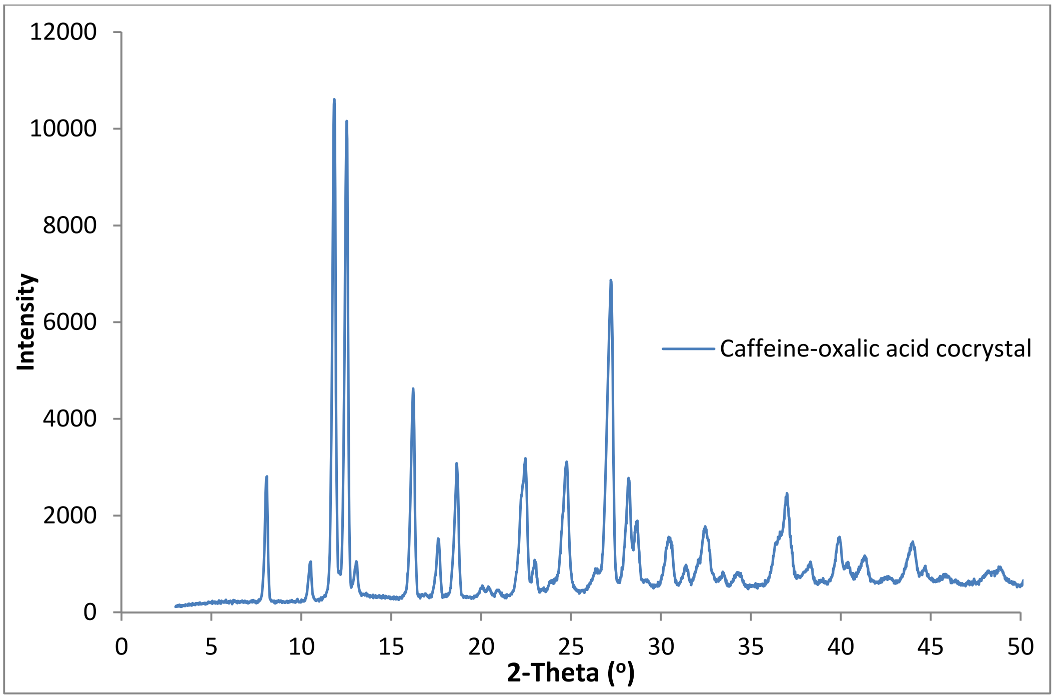

Fig. 3.17 PXRD pattern of laboratory prepared caffeine-oxalic acid cocrystal.

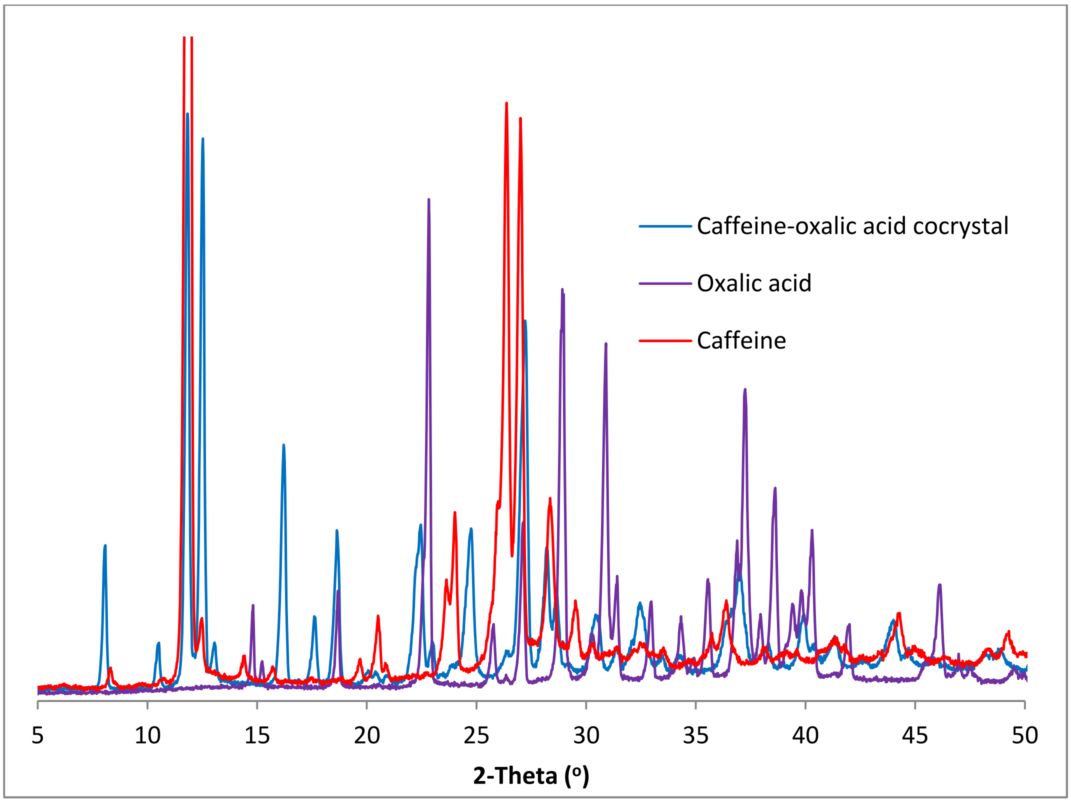

Fig. 3.18 Comparison of PXRD pattern of caffeine, oxalic acid and caffeine-oxalic acid cocrystal.

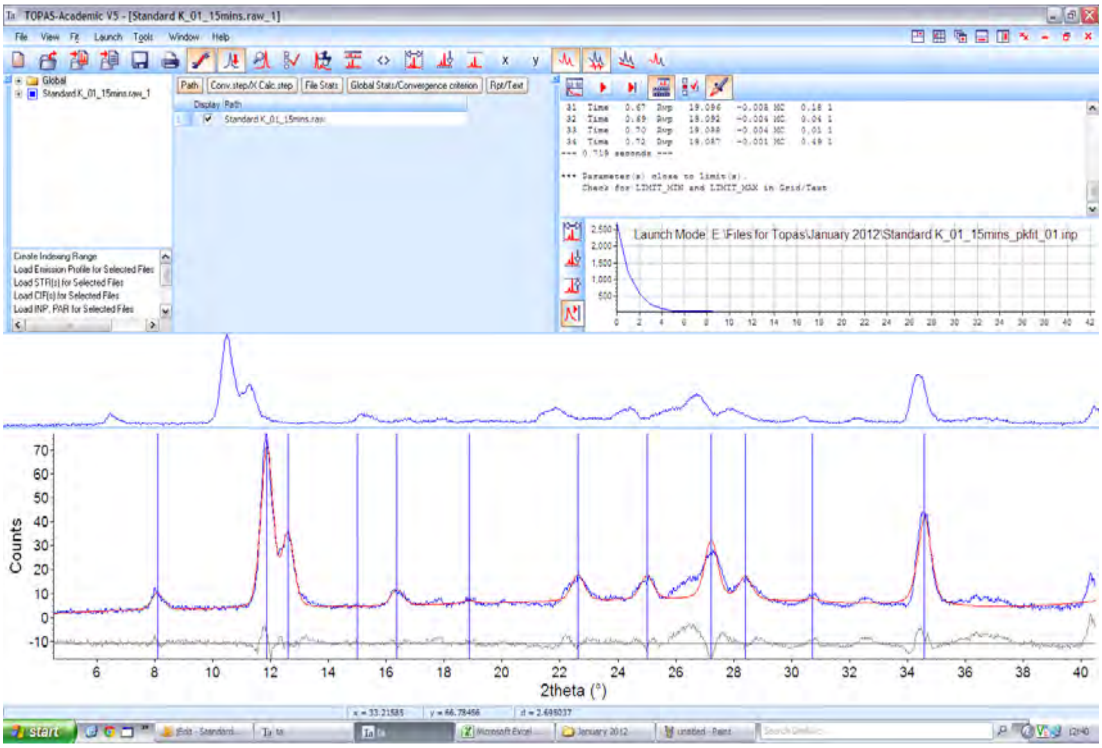

```
31  Time   0.67  Rwp   19.096   -0.008 MC   0.18 1
32  Time   0.69  Rwp   19.092   -0.004 MC   0.04 1
33  Time   0.70  Rwp   19.088   -0.004 MC   0.01 1
34  Time   0.72  Rwp   19.087   -0.001 MC   0.49 1
--- 0.719 seconds ---

*** Parameter(s) close to limit(s).
    Check for LIMIT_MIN and LIMIT_MAX in Grid/Text
```

Fig. 3.19 Picture of TOPAS-Academic V5 display used for peaking fitting and area determination.

Table 3.3. Table of peak area and cocrystal amount for reflection at 2θ≈8.0°

	Cocrystal amount	Refined Peak Area
Standard 1	4.05%	0.00509
Standard 2	49.26%	0.02074
Standard 3	74.20%	0.03274
Standard 4	93.70%	0.02057

Table 3.4 Table of peak area and cocrystal amount for reflection at 2θ≈16.11°

	Cocrystal amount	Refined Peak Area
Standard 1	4.05%	0.02843
Standard 2	49.26%	0.06342
Standard 3	74.20%	0.27988
Standard 4	93.70%	0.18124

A statistical method using correlation analysis was used to interpret the data obtained from the plots. Correlation analysis measures the statistical interdependence/ relationship between two variables: X (the independent variable) and Y (the dependent variable). This measure of interdependency is called the correlation coefficient (r). The correlation coefficient (r) gives an indication of both the strength and direction of the relationship between the variables; it has no unit. The value of the correlation coefficient lies between the ranges $-1 \leq r \geq 1$ with a negative correlation coefficient value indicating that an inverse relationship exists between X and Y i.e. as one variable increases the other reduces, while a positive correlation coefficient value indicates that a linear relationship exists and both variables increase together, as the correlation coefficient value approaches a magnitude of 1, the stronger the interdependency/relationship between the variables. The correlation coefficient is calculated using Eqn. 3.7.

$$r = \frac{\sum_{i=1}^{N}(x_i - \bar{x})(y_i - \bar{y})}{\sqrt{\sum_{i=1}^{N}(x_i - \bar{x})^2 \sum_{i=1}^{N}(y_i - \bar{y})^2}} \qquad \text{Eqn. 3.7}$$

Where $\bar{x}$ and $\bar{y}$ are the mean of the variables. The coefficient of determination (R^2) is a measure of the proportion of the variability in the dependent variable (Y) that is explained by the best possible relationship (regression line) between x and y. It is used to measure the reliability of the statistical predicted relationship. The coefficient of determination (R^2) has no units and lies between $0 \leq R^2 \leq 1$. A value of 1 means the variability in the dependent variable (Y) is perfectly explained by the variation in the independent variable (X) and the regression line is accurate, while a coefficient of determination value of 0 means that the variability in the dependent variable (Y) cannot be explained by the independent variable (X) and the regression line is not significant. The coefficient of determination is calculated using Eqn. 3.8.

$$R^2 = \frac{\sum_{i=1}^{N}(\hat{y}_i - \bar{y})^2}{\sum_{i=1}^{N}(y_i - \bar{y})^2} \qquad \text{Eqn. 3.8}$$

Where $\hat{y}_i$ is the predicted values of Y calculated using the regression line and $\bar{y}$ is the mean value of Y.

The plot of peak areas against cocrystal amount for the 2θ≈8.0^o and 2θ≈16.11^o are shown below (Figs. 3.20 and 3.21). The correlation coefficient between the amount of caffeine-oxalic acid cocrystal in the sample and peak area for both plots are similar at ≈0.78 and the coefficient of determination (R^2) for the plots are 0.6035 and 0.6091, respectively.

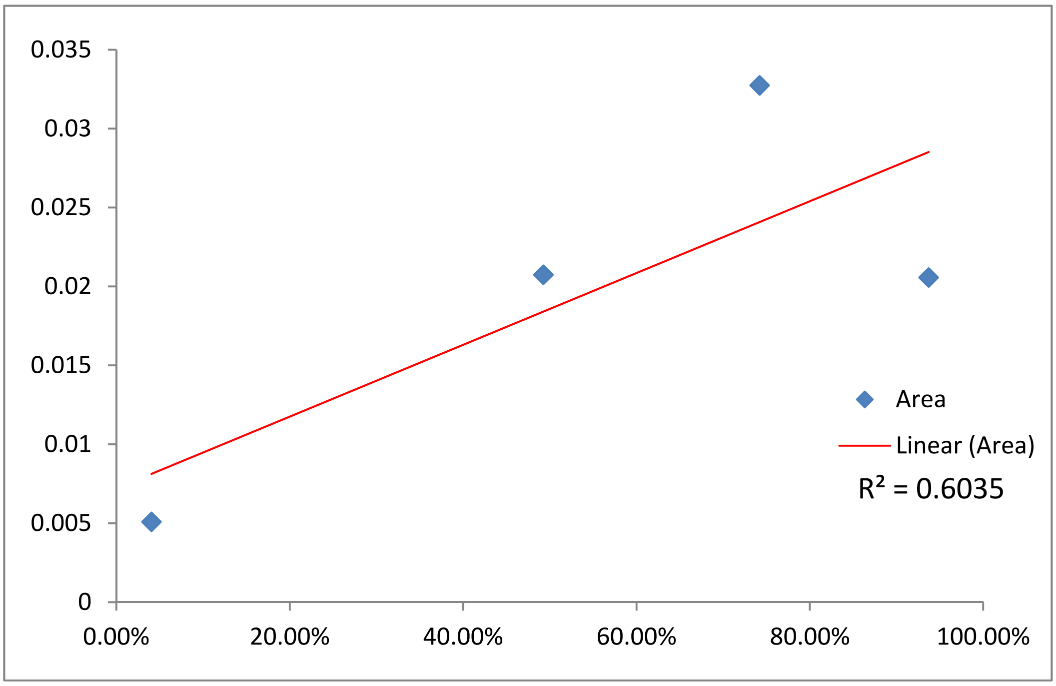

Fig. 3.20 Plot of peak area for 2θ≈8.0^o against caffeine-oxalic acid cocrystal amount.

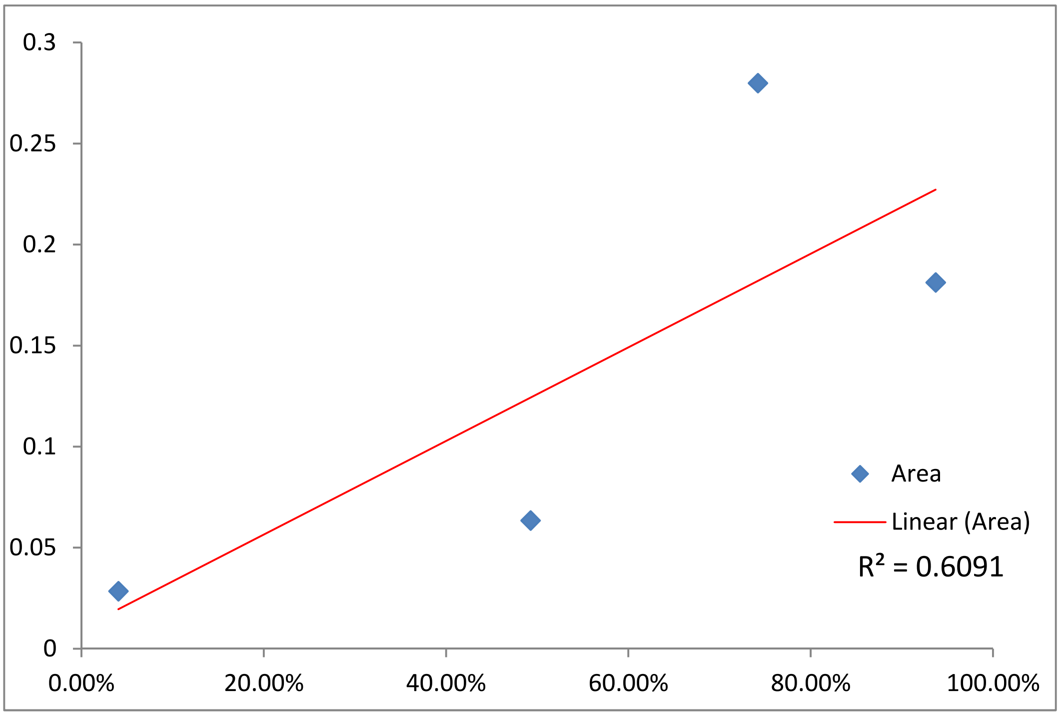

Fig. 3.21 Plot of peak area for 2θ≈16.11° against caffeine-oxalic acid cocrystal amount.

The precision of the PXRD approach for the caffeine-oxalic acid cocrystal system was further tested by carrying out repeated PXRD analysis of the same sample but over different lengths of time, comparing the ratio of the 2θ≈8.0° and 2θ≈16.11° peak areas. The results of the peak area ratios from the repeated PXRD analysis are presented in Table 3.5. The standard deviation for each sample was calculated using Eqn. 3.2 and the coefficient of variance (CV) using Eqn. 3.4; both were used to measure the precision of the PXRD approach using the two identified cocrystal peaks. Although the samples' analytical time varies, because the ratios of the same two peaks in the caffeine-oxalic acid cocrystal phase are used, direct comparison can be applied to the results. There is a lot of variation in the calculated standard deviations. When the coefficients of variances are calculated for each analysis, the CV values range from 6.56% to 51.85 %. In comparison, the CV value for the DSC analysis was 32.2% and lies within the range obtained for the PXRD precision test. Combining all the standard deviations (Table 3.6) and then calculating the coefficient of variances to test for reproducibility across the 6 different analysis, the mean of the standard deviations (s) was obtained as 1.712, see calculation in Table 3.6.

Table 3.5 Peak ratios for repeated PXRD sample analysis.

Sample*	25 mins	20 mins	15 mins	$\bar{\mathcal{X}}$	s	CV
J	3.753	6.802	6.378	5.644	1.652	29.26%
K	11.086	5.200	4.549	6.945	3.601	51.85%
L	2.973	4.138	4.533	3.881	0.811	20.90%
M	3.772	4.474	3.720	3.989	0.421	10.56%
O	39.090	28.942	29.296	32.443	5.759	17.75%
P	5.486	5.162	4.810	5.153	0.338	6.56%

*Samples were omitted because no peak area was obtained from TOPAS.

The mean peak area, standard deviation and the coefficient of variance (CV) were calculated for each analysis using the equations below:

$$s = \sqrt{\frac{\sum(\mathcal{X}_\mathrm{i} - \bar{\mathcal{X}})^2}{n-1}} \qquad \text{Eqn. 3.2}$$

$$\bar{\mathcal{X}} = \frac{\sum \mathcal{X}}{n} \qquad \text{Eqn. 3.3}$$

$$\mathrm{CV} = \frac{\mathrm{s}}{\bar{\mathrm{x}}} \times 100 \qquad \text{Eqn. 3.4}$$

The CV values for the standard deviations were calculated and a value of 103.23% was obtained. This CV value of greater than 100% for the standard deviations of the PXRD analysis shows that the reproducibility is very poor and suggests that the PXRD approach is not suitable for quantitative analysis of caffeine-oxalic acid cocrystal.

Table 3.6 Standard deviation calculation for PXRD coefficient of variance.

$s\,(\mathcal{X}_i)$	$(\mathcal{X}_i - \bar{\mathcal{X}})$	$(\mathcal{X}_i - \bar{\mathcal{X}})^2$	Standard deviation
1.349	-0.363	0.132	1.768
2.940	1.228	1.508	
0.662	-1.050	1.103	
0.344	-1.368	1.871	
4.703	2.991	8.946	
0.276	-1.436	2.062	
$\sum$		15.622	

$$CV = \frac{1.768}{1.712} \times 100 = 103.23\%$$

Visual analysis of the plot of the peak area ratios for each sample (Fig. 3.22) shows that the ratios are not reproducible; this variation may be as a result of preferred orientation, which can impact PXRD analysis negatively. Consequently, PXRD was not considered further for quantitative analysis of the cocrystal yield.

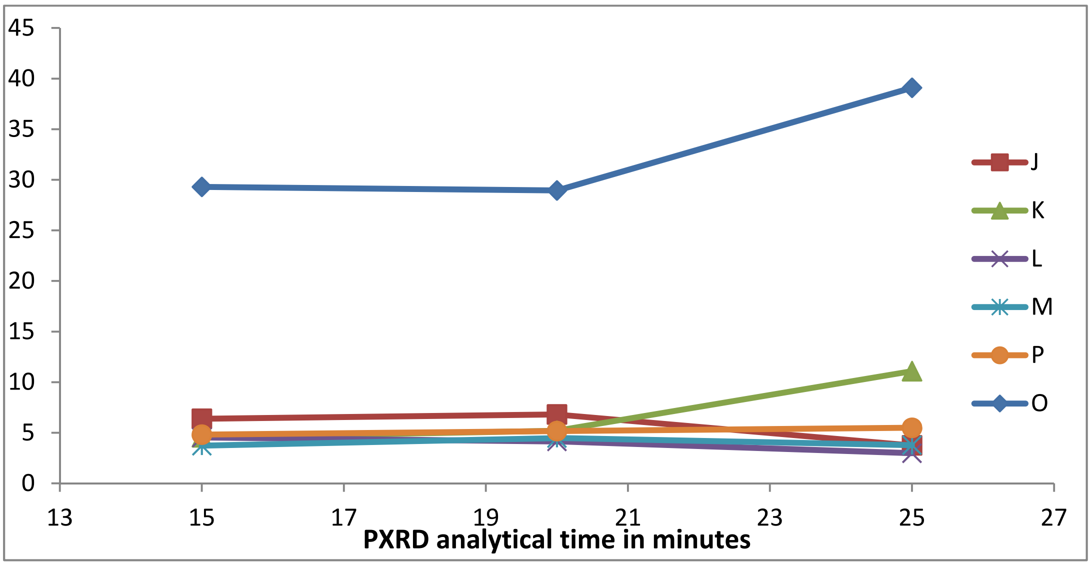

Fig. 3.22 Plot of the six peak area ratio for 2θ≈8.0° and ≈16.11° for three different analysis time of 15 mins, 20 mins and 25 mins.

3.5 Solid state NMR

The solid state NMR (SSNMR) analytical technique does not require elaborate sample preparation, making it suitable for cocrystal analysis. SSNMR has been used to aid structural elucidation of cocrystal molecules especially in cases were single crystal samples are unavailable[14]. Despite its successful application in the field of cocrystal engineering, its use in quantitative determination is not commonly reported. Unlike DSC analysis, SSNMR technique is unlikely to induce cocrystallisation during analysis because it is performed at ambient temperature; DSC requires the caffeine-oxalic acid cocrystal samples to be heated to 214 ^{o}C (the melting point of cocrystal). SSNMR has been used in distinguishing between salts and cocrystals and also in determining structures of cocrystals when the sample is not suitable for single crystal analysis[15]. Gregory et al.[16] reviewed the ^{13}C CP/MAS NMR technique utility for quantitative analysis of pharmaceutical APIs and Dominick et al.[17] estimated the level of cocrystallisation in twin screw extrusion experiments using ^{13}C SSNMR.

The principle behind nuclear magnetic resonance is based on the fact that nuclei with odd mass numbers have a non-zero nuclear spin. When a molecule with non-zero spin nuclei is placed in a strong magnetic field, the angular spin of the nuclei is split into different energy levels. The splitting of the energy levels by the applied magnetic field is called the Zeeman interaction. Nuclei transit from one energy level to the other by absorbing the applied radiofrequency radiation and emitting radiation when returning to their relaxation state when the applied radiofrequency is removed. The utility of SSNMR for analytical purposes has improved due to two developments in nuclear magnetic resonance spectroscopy[18]:

- Magic angle spinning (MAS) and
- Cross polarisation (CP).

In nuclear magnetic resonance analysis, powder samples have poorer peak resolution when compared to solution samples; this is due to peak broadening that can result in peaks overlapping. Peak broadening is due to the anisotropic interaction of nuclei and their surroundings. Spinning the sample at an angle of 54.74^{o} to the applied magnetic field cancels out this aspect and enhances the peak resolution making them narrower; this process is referred to as magic angle spinning (MAS).

The sensitivity of nuclear magnetic resonance (NMR) analysis depends on the relative abundance of the nuclei analysed. Protons (^{1}H) are the most abundant nuclei in organic molecules, so cross polarisation allows for the transfer of sensitivity from abundant nuclei like hydrogen (^{1}H) to less abundant nuclei like carbon (^{13}C).

An advantage of the SSNMR technique over PXRD is that it is insensitive to preferred orientation and particle size, which is a problem with PXRD analysis. This eliminates the need to grind, which is required to minimize preferred orientation in PXRD but is not ideal for cocrystal quantitative analysis, as grinding can initiate cocrystallisation.

3.5.1 Development of a SSNMR method for quantifying cocrystal yield

Samples of caffeine-oxalic acid cocrystal (Fig. 3.23), oxalic acid (Fig. 3.24) and caffeine (Fig. 3.25) were analysed by SSNMR C-13 cross polarisation magical angle spinning (^{13}C CP/MAS) analysis to identify distinctive chemical shift differences between them. The most readily distinguishable chemical shift differences (Fig. 3.5) identified are:

1. 2 ppm shift from 105.8 ppm (caffeine) to 107.7 ppm (caffeine-oxalic acid cocrystal)
2. 4 ppm shift from 163.1 ppm (oxalic acid) to 159.6 ppm (caffeine-oxalic acid cocrystal).

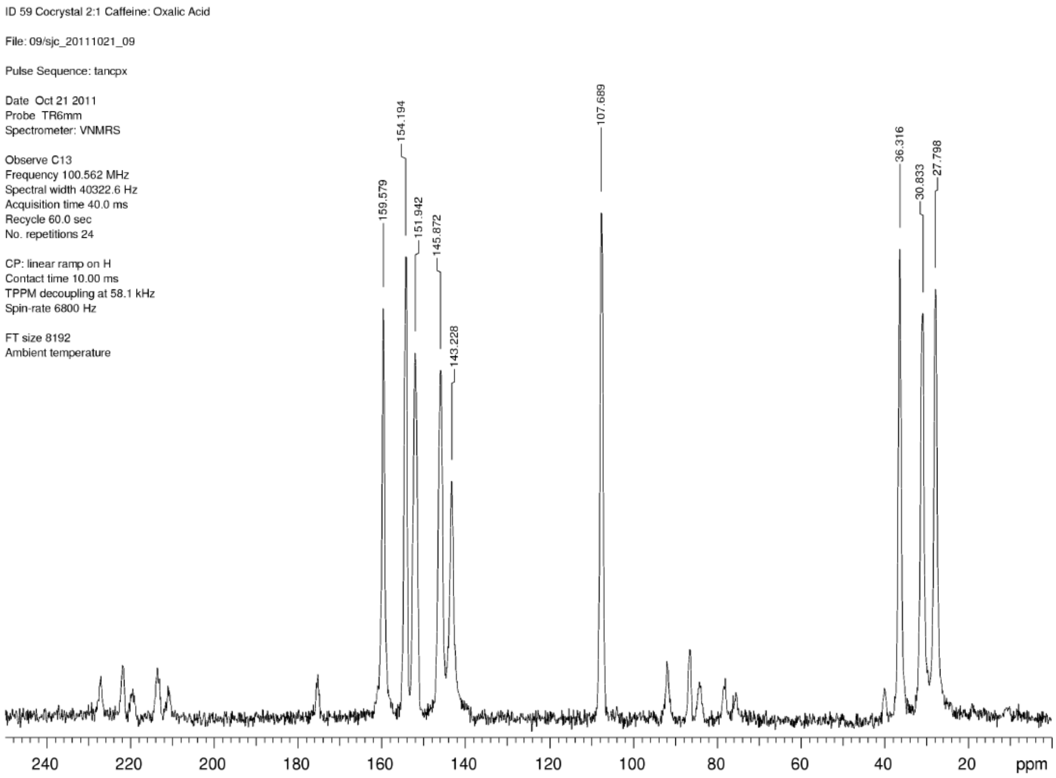

Fig. 3.23 ^{13}C CP/MAS spectra of laboratory synthesised 2:1 caffeine-oxalic acid cocrystal.

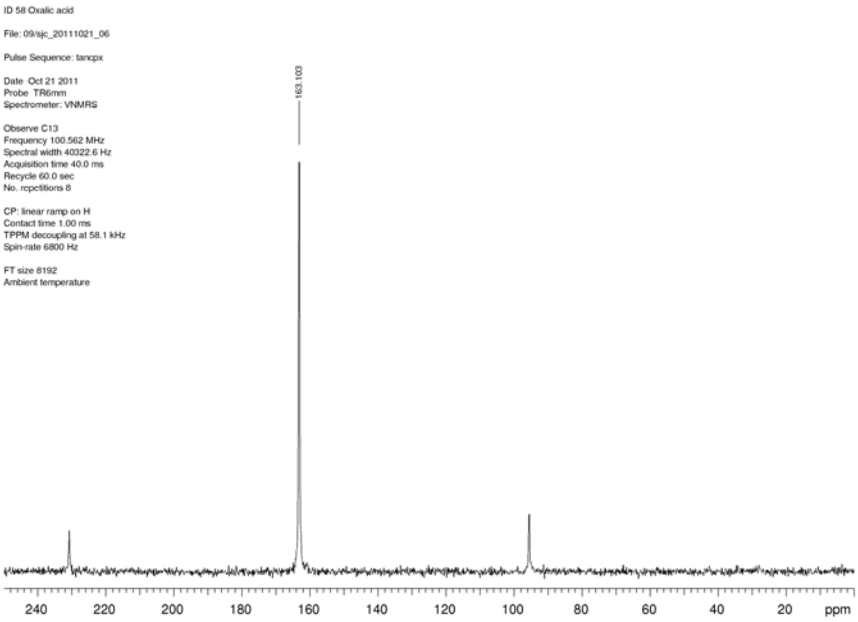

Fig. 3.24 ^{13}C CP/MAS spectra of commercial sample of oxalic acid.

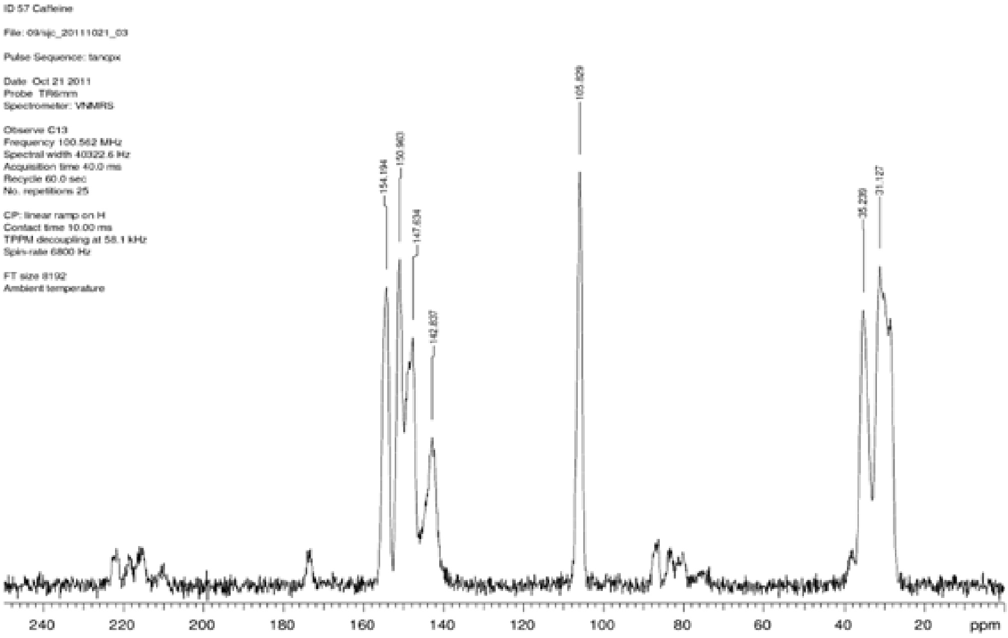

Fig. 3.25 ^{13}C CP/MAS spectra of commercial sample anhydrous caffeine.

3.5.2 Relaxation profile

In SSNMR, the applied radiofrequency is used to excite nuclei to higher energy levels and when the radiofrequency is removed they return back to their relaxed state. The relaxation time (T_1) is the time required for the molecule to return back to its ground (relaxed) state after the radio frequency is switched off. The relaxation time depends on the rigidity in the structure of the molecule; molecules that do not have rigid ring structure or possess flexible aliphatic side chains generally have shorter relaxation times. In ^{13}C cross polarisation (CP), the relaxation time T_1(H) is influenced by the hydrogen environment around the carbon nuclei of interest. The relaxation profile is used to determine the recycle delay time i.e. the delay time between switching off and switching on of the applied radiofrequency, or the time that is allowed to elapse between data acquisition. To attain high signal to noise ratio and improve sensitivity of SSNMR analysis, data acquisition is repeated several times; the improvement in sensitivity is due to the fact that signal increases proportionally to the number of repetitions while the system noise increases more slowly by the square root of the number of repetitions. Hence the longer the recycle delay time, the fewer repetitions possible and the resulting SSNMR spectrum has a poor signal to noise ratio. Sometimes a compromise, i.e. shortening the delay time, is made to allow for improved sensitivity; this compromise may not have any significant impact on the analysis[19].

The ^{13}C CP/MAS relaxation time profile for a particular carbon atom is unique because of the unique hydrogen-carbon environment it experiences. Below (Fig. 3.26) is a relaxation time profile for selected carbon atoms in caffeine (105.8 ppm), oxalic acid (163.1 ppm) and caffeine-oxalic acid cocrystal (107.7 ppm due to the caffeine component and 159.6 ppm due to the oxalic acid component). The oxalic acid relaxation profile (green line) is the fastest profile. This is so because oxalic acid does not have any rigid ring structure unlike caffeine and the caffeine-oxalic acid cocrystal, making it the most flexible of the three molecules. Caffeine (red line) and caffeine-oxalic acid cocrystal (blue line and black line) both show similar patterns because of similar molecular rigidity. Importantly there is a marked difference between the oxalic acid ^{13}C CP/MAS relaxation profile for its carbon at 163.1 ppm and caffeine-oxalic acid cocrystal ^{13}C CP/MAS relaxation profile for its carbon at 159.6 ppm, which corresponds to the oxalic acid carbon in the cocrystal molecule. This difference in relaxation profile implies that both carbons are experiencing different hydrogen environments in their unit cells. In oxalic acid the unit cell consist of oxalic acid molecules but in caffeine-oxalic acid cocrystal the unit cell consist of both oxalic acid and caffeine molecules.

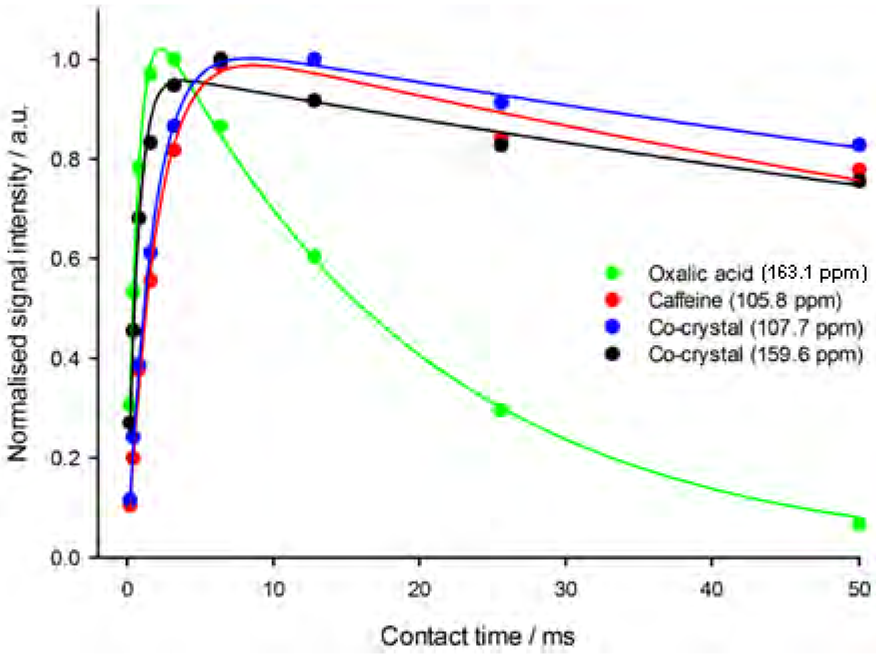

Fig. 3.26 SSNMR relaxation test profile of caffeine-oxalic acid cocrystal, caffeine and oxalic acid, showing different rate of relaxation between cocrystal and components.

The relaxation profiles for both carbon atoms from the caffeine-oxalic acid cocrystal (107.7 ppm and 159.6 ppm) are similar, despite the difference in their chemical shift. This suggests that both are experiencing similar hydrogen environments as a result of both occupying the same unit cell.

In quantitative SSNMR analysis of heterogeneous molecules like cocrystals, there is a tendency for differences between cross polarisation relaxation time for the different components of the cocrystal molecule i.e. oxalic acid and caffeine, which would affect the observed peak intensity of the different components. A difference was observed between the two cocrystal carbon profiles so there is the likelihood that optimum height for both carbons may not be achievable during ^{13}C CP/MAS analysis, this source of error has been eliminated in this study by running both samples and standards under the same condition, so the same level of error is carried through.

3.5.3 Peak deconvolution and integration

The SSNMR spectra of caffeine-oxalic acid cocrystal with residual caffeine and oxalic acid (Figs. 3.27 and 3.29) shows considerable peak overlap between the caffeine peak at 105.8 ppm and the caffeine-oxalic acid cocrystal peak at 107.7 ppm, this peak overlap will require resolution to two component peaks prior to integration and peak area determination for better quantitative analysis. The process for resolving overlapping peaks in SSNMR is called deconvolution. The peak deconvolution process involves specifying the number of peaks expected to be present in the overlap prior to peak fitting. From the ^{13}C CP/MAS spectra of the caffeine-oxalic acid cocrystal (Fig. 3.23) and caffeine (Fig. 3.25), two peaks are expected in the region between 100 to 120 ppm chemical shifts, so this is specified in the peak deconvolution (Figs. 3.28 and 3.30).

Combinations of Gaussian and Lorentzian line shapes are used to fit a calculated model spectrum to the observed ^{13}C CP/MAS spectra because it is more likely that the SSNMR spectra will have a combination of both peak shapes rather than just one shape, so the combination approach gives a higher probability of getting a more accurate peak resolution. The best fit is the calculated spectra with the least square; this least square is represented as the Chi squared value (Figs. 3.28 and 3.30). The lower the chi squared value, the better the peak fitting.

The peaks in the best fit spectrum are integrated using the width at half the peak height as an approximation to the area under each peak.

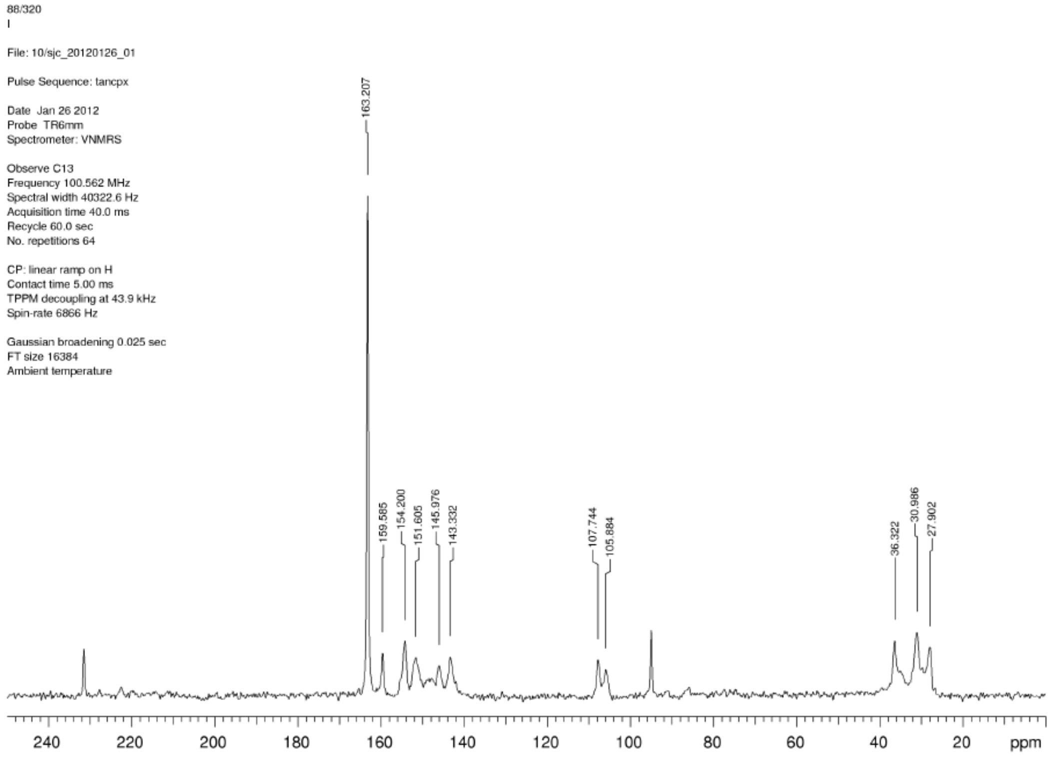

Fig. 3.27 ^{13}C CP/MAS spectra for standard I.

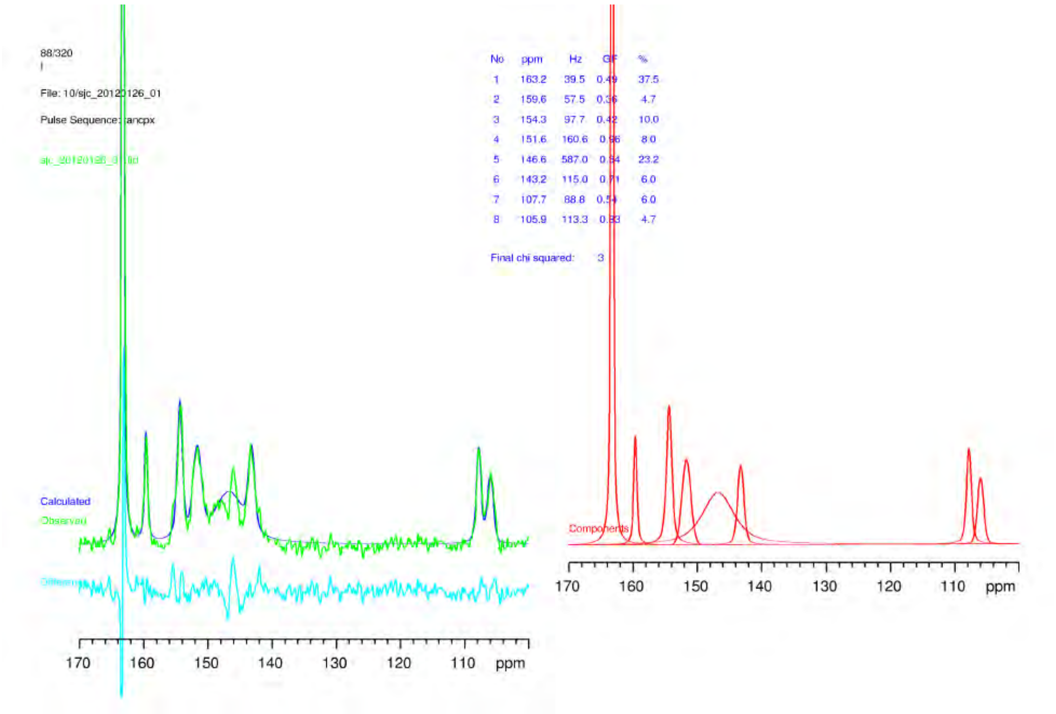
88/320
I

File: 10/sjc_20120126_01

Pulse Sequence: tancpx

sjc_20120126_01.fid

No	ppm	Hz	GF	%
1	163.2	39.5	0.49	37.5
2	159.6	57.5	0.36	4.7
3	154.3	97.7	0.42	10.0
4	151.6	160.6	0.96	8.0
5	146.6	587.0	0.54	23.2
6	143.2	115.0	0.71	6.0
7	107.7	88.8	0.54	6.0
8	105.9	113.3	0.83	4.7

Final chi squared: 3

Fig. 3.28 SSNMR spectra showing the process of peak fitting and deconvolution of overlapping peaks in Standard I.

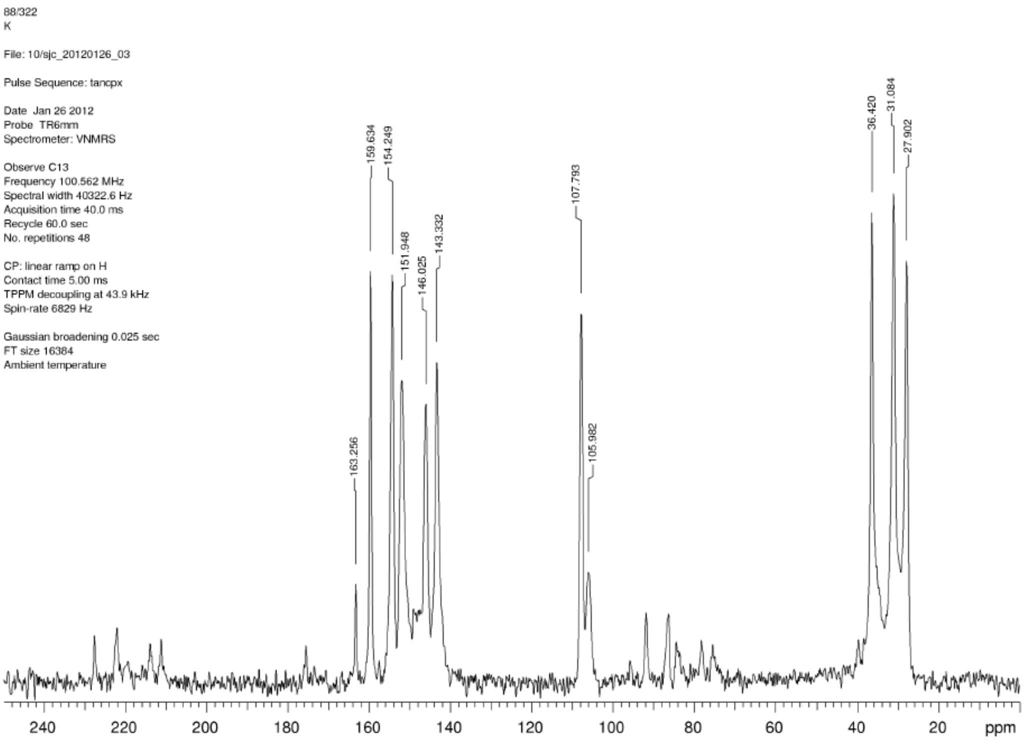
88/322
K

File: 10/sjc_20120126_03

Pulse Sequence: tancpx

Date Jan 26 2012
Probe TR6mm
Spectrometer: VNMRS

Observe C13
Frequency 100.562 MHz
Spectral width 40322.6 Hz
Acquisition time 40.0 ms
Recycle 60.0 sec
No. repetitions 48

CP: linear ramp on H
Contact time 5.00 ms
TPPM decoupling at 43.9 kHz
Spin-rate 6829 Hz

Gaussian broadening 0.025 sec
FT size 16384
Ambient temperature

Fig. 3.29 ^{13}C CP/MAS spectra for standard K.

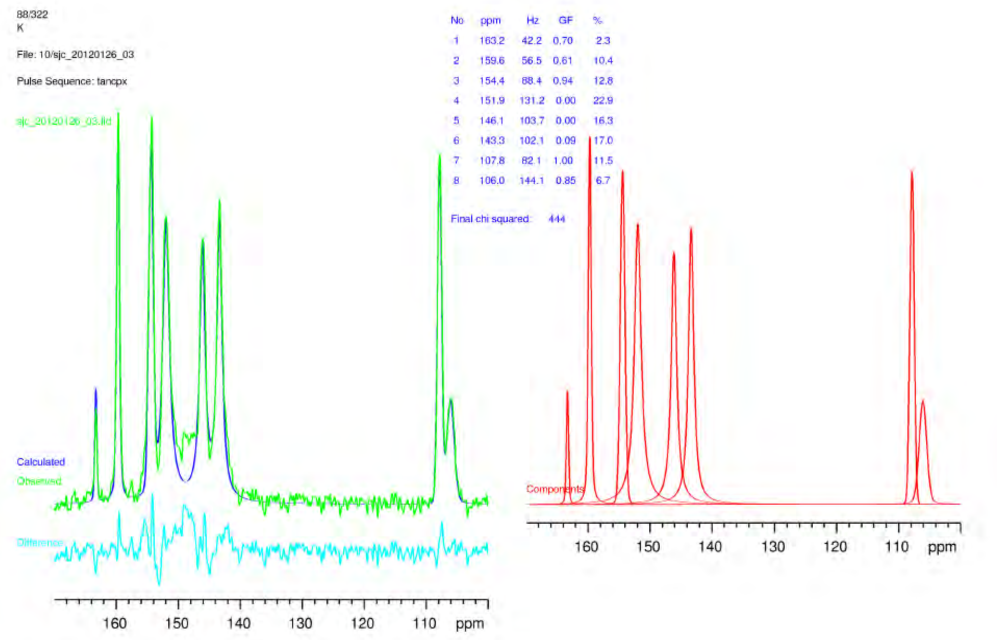
88/322
K

File: 10/sjc_20120126_03

Pulse Sequence: tancpx

No	ppm	Hz	GF	%
1	163.2	42.2	0.70	2.3
2	159.6	56.5	0.61	10.4
3	154.4	88.4	0.94	12.8
4	151.9	131.2	0.00	22.9
5	146.1	103.7	0.00	16.3
6	143.3	102.1	0.09	17.0
7	107.8	82.1	1.00	11.5
8	106.0	144.1	0.85	6.7

Final chi squared: 444

Fig. 3.30 SSNMR spectra showing the process of peak fitting and deconvolution of overlapping peaks in standard K.

3.5.4 SSNMR precision test

The precision of SSNMR for quantitative analysis of the caffeine-oxalic acid cocrystal was tested by running repeated SSNMR analysis of the same sample (Figs. 3.31 and 3.32) and calculating the standard deviation (Table 3.7 and 3.8) and coefficient of variance.

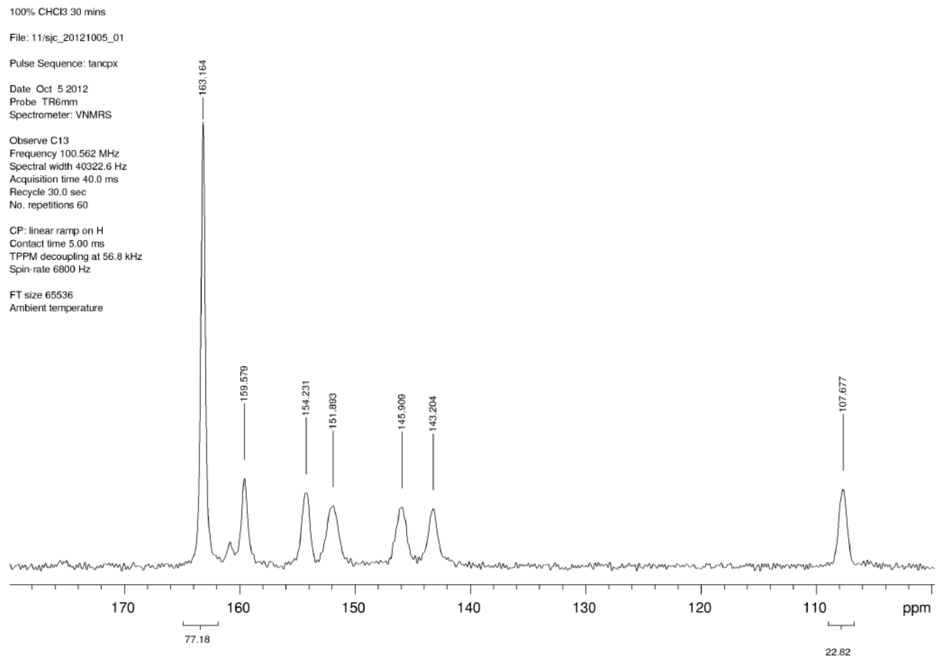
100% CHCl3 30 mins

File: 11/sjc_20121005_01

Pulse Sequence: tancpx

Date Oct 5 2012
Probe TR6mm
Spectrometer: VNMRS

Observe C13
Frequency 100.562 MHz
Spectral width 40322.6 Hz
Acquisition time 40.0 ms
Recycle 30.0 sec
No. repetitions 60

CP: linear ramp on H
Contact time 5.00 ms
TPPM decoupling at 56.8 kHz
Spin-rate 6800 Hz

FT size 65536
Ambient temperature

Fig. 3.31 ^{13}C CP/MAS spectra of the caffeine-oxalic acid cocrystal precision test sample

Table 3.7 SSNMR peak area ratios for oxalic acid peak at 163 ppm and caffeine-oxalic acid cocrystal peak at 108 ppm.

	163 ppm peak by direct integration	108 ppm peak by direct integration	Ratio 163:108 ppm peaks from direct integration	163 ppm peak from deconvolution	108 ppm peak from deconvolution	Ratio 163:108 ppm peaks from deconvolution
Run 1	76.1	23.9	3.18	34.1	10.2	3.34
Run 2	76.2	23.8	3.20	34.2	11.3	3.03
Run 3	76.6	23.4	3.27	34.5	10.7	3.22
Run 4	75.7	24.3	3.12	34.0	11.0	3.09
Run 5	77.2	22.8	3.39	33.7	11.0	3.06
Average	76.4	23.6	3.23	34.1	10.8	3.15
Range	75.7-77.2	22.8-24.3	3.12-3.39	33.7-34.5	10.2-11.3	3.03-3.34

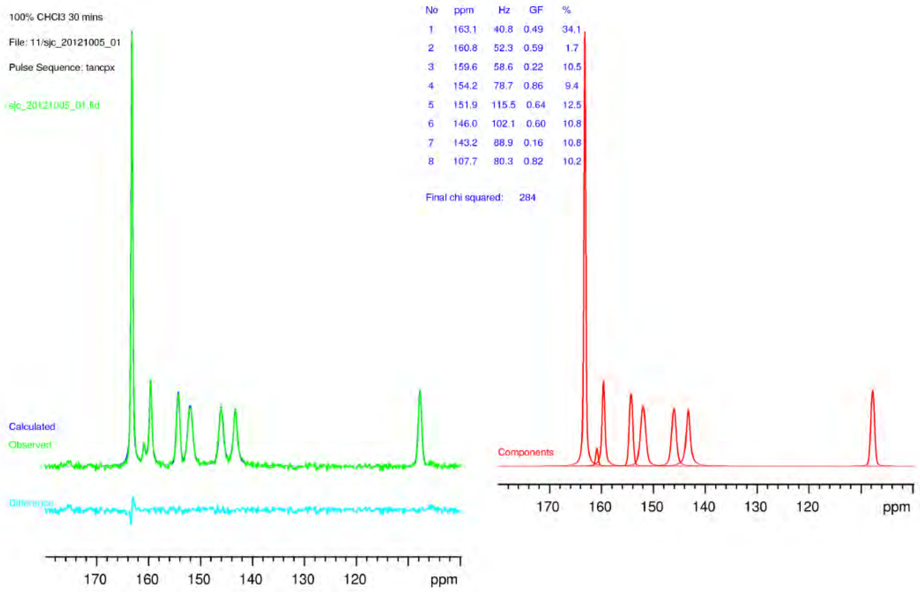

No	ppm	Hz	GF	%
1	163.1	40.8	0.49	34.1
2	160.8	52.3	0.59	1.7
3	159.6	58.6	0.22	10.5
4	154.2	78.7	0.86	9.4
5	151.9	115.5	0.64	12.5
6	146.0	102.1	0.60	10.8
7	143.2	88.9	0.16	10.8
8	107.7	80.3	0.82	10.2

Final chi squared: 284

Fig. 3.32 Deconvolution and peak fitting of the sample of caffeine-oxalic acid cocrystal used for SSNMR precision testing.

$$s = \sqrt{\frac{0.07}{4}} \qquad = 0.13$$

$$\mathrm{CV} = \frac{0.13}{3.15} \times 100 = 4.13\%$$

The standard deviation and the coefficient of variance (CV) for SSNMR technique are 0.13 and 4.13% respectively. The CV for SSNMR precision test is lower and better than the values obtained for DSC or PXRD (Table 3.9), this makes SSNMR analysis the best option of the three considered for quantitative analysis of the caffeine-oxalic acid cocrystal.

Table 3.8 Standard deviation calculation for SSNMR peak area ratios

Ratio 163:108 from deconvolution ($\mathcal{X}$)	$(\mathcal{X}_i - \bar{\mathcal{X}})$	$(\mathcal{X}_i - \bar{\mathcal{X}})^2$
3.34	0.19	0.04
3.03	-0.12	0.01
3.22	0.07	0.00
3.09	-0.06	0.00
3.06	-0.09	0.01
$\sum$		0.07

Table 3.9 Comparison of coefficient of variance of three analytical techniques.

	SSNMR	DSC	PXRD
Coefficient of variance	4.13%	32.2%	6.56 – 51.85%

3.5.5 Development of a SSNMR calibration curve

To develop a quantitative method for analysis, standard mixtures of caffeine, oxalic acid and caffeine-oxalic acid cocrystal were made (Table 3.10) and analysed by SSNMR, the peak areas for the chemical shifts at 105 ppm, 107 ppm, 159 ppm and 163 ppm were integrated and the ratios used for developing a quantitative analytical method[16]. The percentage composition of caffeine-oxalic acid cocrystal in each sample was divided by the percentage composition of oxalic acid and caffeine in Table 3.10 to give $wt\ \%$ (Table 3.11 and 3.12). The corresponding intensity ratios were obtained by dividing the areas under cocrystal peaks at 107 ppm and 159 ppm by the areas under the corresponding oxalic acid peak at 163 ppm (Table 3.11) and caffeine peak at 106 ppm (Table 3.12).

Table 3.10 Standard mixtures of caffeine, oxalic acid and caffeine-oxalic acid cocrystal

Standard	Cocrystal	Caffeine	Oxalic acid
1	12.69%	35.05%	52.27%
2	33.30%	31.95%	34.75%
3	57.41%	37.27%	5.31%
4	67.85%	13.93%	18.22%
5	12.53%	78.34%	9.14%
6	7.38%	15.19%	77.43%
7	14.46%	8.61%	76.93%
8	92.56%	4.44%	3.00%
9	74.78%	16.05%	9.17%
10	88.63%	8.42%	2.95%
11	41.37%	20.49%	38.14%

A scatter plot of the $wt\ \%$ for each standard and the observed intensity ratios (Figs. 3.33 and 3.34) was plotted. Regression analysis was used to determine the best statistical relationship between the variables represented by the best-fit line and the equation of the regression line used as a calibration curve for interpolating levels of caffeine, oxalic acid and caffeine-oxalic acid cocrystal in subsequent SSNMR analysis. Correlation analysis was used to test the interdependency between the intensity ratio and the $wt\,\%$ in the standard mixtures analysed to see if any significant relationship existed.

Table 3.11 Caffeine-oxalic acid cocrystal and oxalic acid intensity ratio in ascending order.

Sample	Intensity ratio	$wt\,\%$
6	0.041	0.10
7	0.074	0.19
1	0.125	0.24
2	0.437	0.96
11	0.439	1.08
5	1.149	1.37
4	1.282	3.72
9	2.857	8.15
3	4.545	10.81
10	10	30.07
8	11.111	30.90

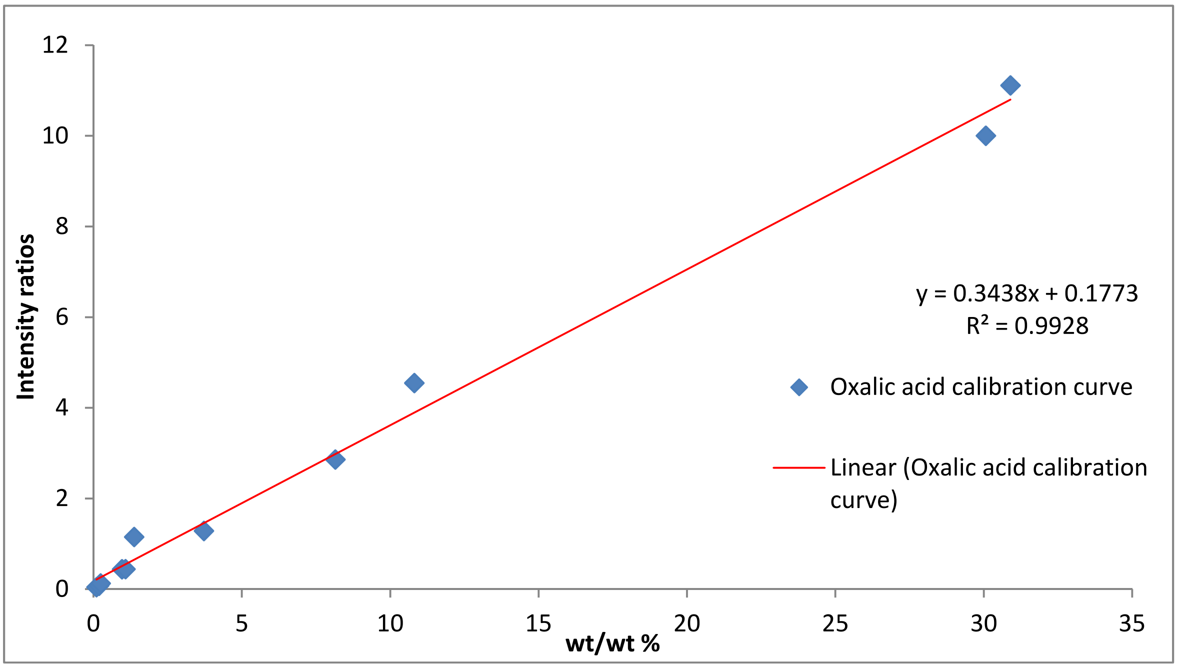

Fig. 3.33 Plot of cocrystal/oxalic acid $wt\,\%$ ratio against observed SSNMR intensity ratio.

Table 3.12 Caffeine-oxalic acid cocrystal and caffeine intensity ratio in ascending order.

Sample	Intensity ratio	$wt\ \%$
5	0.51	0.16
1	1.28	0.36
3	1.72	1.54
6	1.96	0.49
7	2.22	1.68
2	2.48	1.04
11	3.15	2.02
9	4.94	4.66
4	4.96	4.87
10	24.9	10.53
8	32.8	20.83

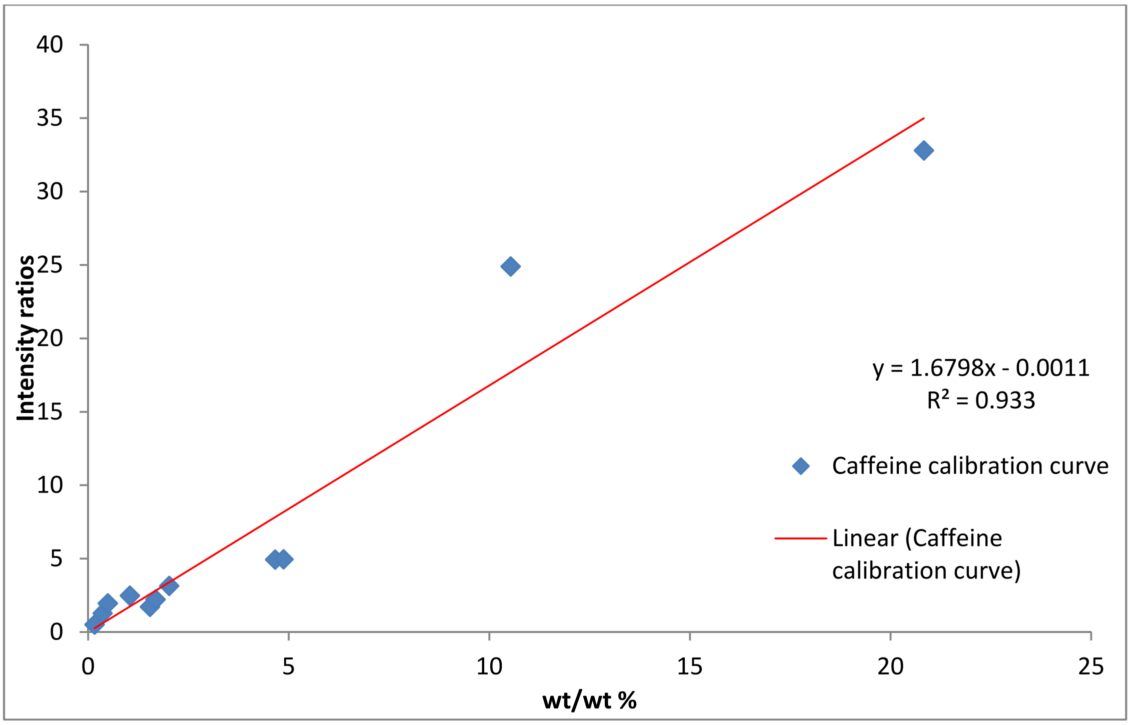

Fig. 3.34 Plot of cocrystal/caffeine $wt\ \%$ ratio against intensity ratio.

3.6 Discussion on calibration curves.

The standard ratios used were chosen to give a broad range of mixtures incorporating a wide range of caffeine-oxalic acid cocrystal (7-92%), caffeine (4-78%) and oxalic acid (3-77%) amounts (Table 3.10); this makes the calibration curves valid for determining caffeine-oxalic acid cocrystal levels of up to 92%. The estimated instrument error is ≈ 5%[20], this is done by calculating the percentage of the instrument noise (baseline) to the peak height of interest. The plot of the intensity ratio against the residual (Figs. 3.35 and 3.36) gives an indication of the presence of other significant sources of error in the regression model (Eqn. 3.9 and 3.11). The residual is the difference between the observed intensity ratios and the predicted value from the regression model. A random spread on the residual scatter plot implies that experimental error is the only significant source of error in the data but a linear spread of the residual scatter plot implies other significant sources of error apart from experimental error are present in the regression model and so the model may not be reliable.

3.6.1 Oxalic acid calibration curve

A summary of the regression analysis for the cocrystal/oxalic acid plot is in Table 3.13.

Table 3.13 Summary of regression analysis for oxalic acid plot.

Regression summary	
Multiple R (r)	0.996
R Square (R^2)	0.993

The correlation coefficient (r) = 0.996; this value is close to 1, indicating a strong interdependency exists between the intensity and wt % ratios for caffeine-oxalic acid cocrystal and oxalic acid. The coefficient of determination (R^2) = 0.993, means that more than 99% of variation in the plot is explained by the regression model suggesting that the model is a very good fit and the calibration curve is reliable. The regression model (best-fit line) is given by the equation:

$$y = 0.344x - 0.177 \qquad \text{Eqn. 3.9}$$

y in this Eqn. 3.9 represents the unknown intensity ratio of caffeine-oxalic acid cocrystal: oxalic acid peak and x the known wt % ratio of caffeine-oxalic acid. During experimental work, the intensity ratio (y) will be the known and the wt % (x) ratio the unknown for laboratory samples, this mean that for quantitative determination Eqn. 3.9 requires transformation to Eqn. 3.10.

$$x = 2.907y + 0.515 \qquad \text{Eqn. 3.10}$$

A scatter plot of the residual and the predicted intensity ratios between oxalic acid and cocrystal using the regression is shown in Fig. 3.35. The absence of a linear pattern in the residual plot suggests that no other significant error is present in the regression line.

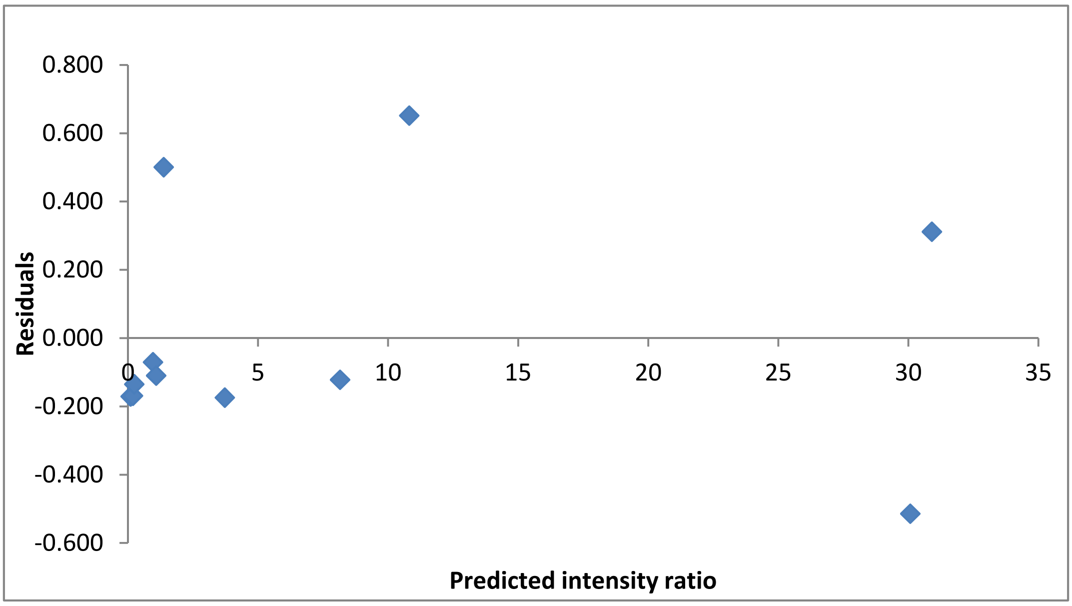

Fig. 3.35 Residual plot for oxalic acid calibration curve showing non-linear pattern.

3.6.2 Caffeine calibration curve

For the caffeine-oxalic acid cocrystal/caffeine peaks, baseline resolution of the cocrystal (107 ppm)/caffeine (106 ppm) peaks required deconvolution unlike in the cocrystal (159 ppm)/oxalic acid (163 ppm) peaks; this additional software manipulation prior to peak area determination adds another source of error in the regression model and could account for the slightly poorer correlation coefficient and coefficient of determination (Table 3.15) observed for the scatter plot of caffeine-oxalic acid cocrystal and caffeine.

The summary result of the regression analysis of the cocrystal/caffeine scatter plot is shown in Table 3.14 below.

Table 3.14. Summary of regression analysis of cocrystal/caffeine plot.

Regression Summary	
Multiple R (r)	0.966
R Square (R^2)	0.933

The correlation coefficient (r)=0.966 is close to 1 and indicates a strong interdependency exist between the intensity and wt % ratios but not as strong as in the case of the oxalic acid calibration curve. The coefficient of determination (R^2)=0.933 means that more than 93% of variation in the plot is explained by the regression model suggesting that the model is a very good fit and the calibration curve reliable. The regression model (best-fit line) is given by the equation:

$$y = 1.68x - 0.001 \qquad \text{Eqn. 3.11}$$

As stated previously for the caffeine-oxalic acid cocrystal/oxalic acid regression model, the regression equation will have to be transformed to determine the $wt\ \%$ ratio from the intensity ratio, thus Eqn. 3.11 becomes:

$$x = 0.595y + 0.001 \qquad \text{Eqn. 3.12}$$

A scatter plot of the residual and the predicted intensity ratios between caffeine and caffeine-oxalic acid cocrystal using the regression model is presented in Fig. 3.36. The absence of a linear pattern in the residual plot suggests that no other significant error is present in the regression line.

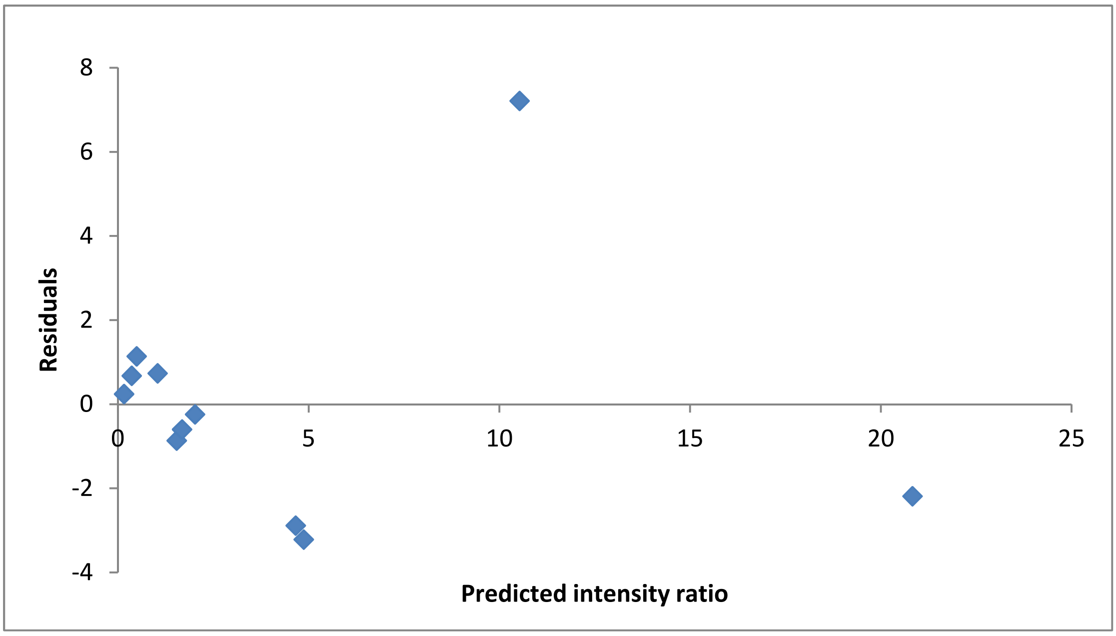

Fig. 3.36 Residual plot for caffeine calibration curve showing non-linear pattern.

The validity of both calibration curves for quantitative determination of caffeine-oxalic acid cocrystal is limited to the range 7 – 93%; above and below this range the regression model may not be valid.

3.6.3 Calculation to determine cocrystal conversion

When the peak areas of the relevant chemical shifts (105 ppm, 107 ppm, 159 ppm and 163 ppm) are determined from the SSNMR analysis, caffeine-oxalic acid cocrystal conversion is determined using the process shown below.

The area % of caffeine-oxalic acid cocrystal peak at 159 ppm is divided by the area % of the oxalic acid peak at 163 ppm (Eqn. 3.13) and this is repeated with the caffeine-oxalic acid cocrystal peak at 107 ppm and caffeine peak at 105 ppm (Eqn.3.14).

$$\frac{\text{Cocrystal}}{\text{Oxalic acid}} = \frac{\text{Peak area for 159 ppm}}{\text{Peak area for 163 ppm}} = y_{\text{oxalic acid}}{:}\,1 \qquad \text{Eqn. 3.13}$$

$$\frac{\text{Cocrystal}}{\text{Caffeine}} = \frac{\text{Peak area for 107 ppm}}{\text{Peak area for 105 ppm}} = \text{y}_{\text{caffeine}}{:}\,1 \qquad \text{Eqn. 3.14}$$

The numerator from Eqn. 3.13 and 3.14 is inserted Eqn. 3.10 and Eqn. 3.12 respectively, to calculate the corresponding $x_{\text{oxalic acid}}$ and x_{caffeine} wt % ratio.

The inverse of the corresponding $\frac{1}{x_{\text{oxalic acid}}}$ and $\frac{1}{x_{\text{caffeine}}}$ are determined to get the mass ratio of oxalic acid and caffeine in the sample with the cocrystal value set at 1. These three values are summed up and used to calculate the percentage (%) of oxalic acid, caffeine and caffeine-oxalic acid cocrystal (Eqn. 3.15 to 3.18).

$$\frac{1}{x_{\text{oxalic acid}}} + \frac{1}{x_{\text{caffeine}}} + 1_{\text{cocrystal}} = \text{Total} \qquad \text{Eqn. 3.15}$$

% composition of caffeine-oxalic acid cocrystal = $\frac{1_{\text{cocrystal}}}{\text{Total}} \times 100$ Eqn. 3.16

% composition of oxalic acid = $\frac{\frac{1}{x_{\text{oxalic acid}}}}{\text{Total}} \times 100$ Eqn.3.17

% composition of caffeine = $\frac{\frac{1}{x_{\text{caffeine}}}}{\text{Total}} \times 100$ Eqn.3.18

The computed value is given in %.

3.7 Conclusion

In this Chapter, four different analytical techniques: HPLC, DSC, PXRD and SSNMR; were considered and three compared for quantitative cocrystal analysis with caffeine-oxalic acid cocrystal as a model system. These techniques were picked based on criteria set at the beginning of the chapter. The ATR-FTIR technique was not investigated for the caffeine-oxalic acid cocrystal system because non-overlapping peaks were not identified; the situation may differ for other cocrystal systems where distinct peaks may arise. A multivariate FTIR analytical technique may be used to resolve the issue of overlapping peaks but this expertise was not accessible during the project.

The precision of each technique was assessed by calculating their coefficients of variances from repeated analyses of samples. SSNMR was selected for developing a quantitative method for caffeine-oxalic acid cocrystal because it gave the best coefficient of variance (CV) compared to the DSC and PXRD. The caffeine-oxalic acid cocrystal dissociated during the HPLC analysis so the coefficient of variance was not determined.

The coefficient of determinant (R^2) and the correlation coefficient (r), for caffeine and oxalic acid were both above 90 % using the SSNMR technique. The SSNMR regression analysis for caffeine-oxalic acid cocrystal system shows a good fit of the regression models. The fit for oxalic acid was higher than caffeine because of the requirement for peak deconvolution for the caffeine regression model.

References

(1) Trask, A. V.; Motherwell, W. D. S.; Jones, W. *Cryst. Growth Des.* **2005**, *5*, 1013.

(2) Macrae, C. F.; Bruno, I. J.; Chisholm, J. A.; Edgington, P. R.; McCabe, P.; Pidcock, E.; Rodriguez-Monge, L.; Taylor, R.; van de Streek, J.; Wood, P. A. *J. Appl. Cryst.* **2008** *41*, 466.

(3) Cesar Medina, D. D., Karthik Nagapudi, Fernando Alvarez-Nunez *Journal of Pharmaceutical Sciences* **2010**, *99*, 1693.

(4) Trask, A. V.; Samuel Motherwell, W. D.; Jones, W. *Cryst. Growth Des.* **2005**, *5*, 1013.

(5) Johnson, S. L.; Rumon, K. A. *Thc Journal of Physical Chemistry* **1965**, *69*, 74.

(6) Schultheiss, N.; Newman, A. *Cryst. Growth Des.* **2009**, *9*, 2950.

(7) Leung, D. H.; Lohani, S.; Ball, R. G.; Canfield, N.; Wang, Y.; Rhodes, T.; Bak, A. *Cryst. Growth Des.* **2012**, *12*, 1254.

(8) Zeng, J.; Fan, L. T.; Schlup, J. R. *Journal of Thermal Analysis* **1998**, *51*, 205.

(9) Whiting, L. F.; Carr, P. W. *Analytical Chemistry* **1978**, *50*, 1977.

(10) Westgard, J. Z-4: Mean, Standard Deviation, And Coefficient Of Variation**,** **1999**. http://www.westgard.com/lesson34.html (accessed 19/06/2013).

(11) Srodon, J.; Drits, V. A.; McCarty, D. K.; Hsieh, J. C.; Eberl, D. D. *Clays and Clay Minerals* **2001**, *49*, 514.

(12) Stephenson, G. A.; Forbes, R. A.; Reutzel-Edens, S. M. *Advanced Drug Delivery Reviews* **2001**, *48*, 67.

(13) Walenta, G.; Füllmann, T. *JCPDS - International Centre for Diffraction Data 2004, Advances in X-ray Analysis.* **2004**, *47*, 287.

(14) Vogt, F. G.; Clawson, J. S.; Strohmeier, M.; Edwards, J. A.; Pham, T. N.; Watson, S. A. *Cryst. Growth Des.* **2009**, *9*, 921.

(15) Friscic, T.; Jones, W. *Cryst. Growth Des.* **2009**, *9*, 1621.

(16) Gregory A. Stephenson; Robert A. Forbes; Reutzel-Edens, S. M. *Advanced Drug Delivery Reviews* **2001**, *48*, 67.

(17) Dominick D., C. M., Robert S., Karthik N. and Fernando A. *Pharmaceutics* **2011**, *3*, 582.

(18) Kenneth J.D. Mackenzie, M. E. S. *Multinuclear Solid-State Nuclear Magnetic Resonance of Inorganic Materials* Pergamon, **2002**

(19) Virtanen, T.; Maunu, L. S. *International Journal of Pharmaceutics* **2010**, *394*, 18.

(20) Discussions with Apperley, D. C., *Senior Experimental officer SSNMR (Durham)*.**2012.**

Chapter 4 Process optimisation

4.1 Introduction

The approach adopted in scaling up the cocrystallisation is outlined in this chapter. Quantitative analytical data from solid state nuclear magnetic resonance (SSNMR), using the method developed in chapter 3, were used in monitoring cocrystal yields and for the decision-making during process optimisation. The cocrystallisation approach uses slurry cocrystallisation but unlike other slurry approaches,[1-4] which make use of a high solid loading in a solvent, a low solid loading in an anti-solvent/solvent mixture was used. This approach offers the following advantages:

- Better cocrystal recovery due to the low solubility of cocrystal in anti-solvent/solvent mixture compared to solvent cocrystallisation with higher cocrystal solubility in solvent[5,6].
- The low solubility of the cocrystal components in the anti-solvent/solvent mixture means cocrystallisation is less sensitive to non-congruent solubility of components, which can result in no cocrystallisation due to the preferential precipitation of the less soluble component[7].
- API or coformer can show tendencies to form solvates, which could precipitate along with the cocrystal acting as an impurity. This problem is minimised due to the low level of solvent in the system[8,9].

At the end of the cocrystallisation process, the product is isolated by filtration. This cocrystallisation process does not require any heating, cooling or seeding to initiate the nucleation of the cocrystal. The liquid phase is a homogeneous mixture of an anti-solvent and a solvent. A "solvent" for the purpose of this investigation is regarded as an organic solvent (including water) in which both the API and coformer have a solubility of greater than 1 mg/g and an "anti-solvent" is an organic solvent in which both API and coformer have a solubility of less than 1 mg/g.

In slurry cocrystallisation, as with other crystallisations, supersaturation acts as the driver for nucleation to occur. An inverse relationship exists between the free energy of nucleation energy, ΔG^{*}, and the chemical potential difference, $\Delta\mu$, (Eqn. 4.1) of the solute species. The degree of cocrystal supersaturation, $\Delta\mu_{cocrystal}$, is given by the chemical potential difference between the solute and crystal phase (Eqn. 4.2), so the chemical potential can be substituted by the degree of supersaturation of the system. According to classical nucleation covered in chapter 1, the nucleation barrier for homogeneous nucleation is given by:

$$\Delta G^* = \frac{16\pi\gamma^3 \nu_c^2}{3\Delta\mu^2} \qquad \text{Eqn. 4.1}$$

with

$$\Delta\mu_{cocrystal} = R\mathrm{T}ln\frac{C_{supersaturation}}{C_{equilibrium}} \qquad \text{Eqn. 4.2}$$

From Eqn. 4.1 and 4.2, the higher the degree of cocrystal supersaturation ($\Delta\mu_{cocrystal}$), the lower the nucleation energy (ΔG^*) requirement. If an anti-solvent is added to a saturated, or near saturated solution of the cocrystal in a good solvent, then high levels of cocrystal supersaturation can be achieved because of the low solubility of the cocrystal components in the resulting anti-solvent/solvent mixture. Whilst this increases the nucleation rate, the quality of the crystals produced can be poor. In our system, the solid API and coformers are added to an already formed anti-solvent/solvent mixture, in which the anti-solvent is the main component. Consequently, a relatively low saturation concentration of the API and coformer arises in this anti-solvent/solvent mixture, and a relatively low cocrystal supersaturation arises, which may lower the nucleation rate but improve cocrystals quality. Cocrystallisation is an equilibrium process between the cocrystal and its component; the high degree of insolubility of the cocrystal in the anti-solvent/solvent mixture prevents dissolution of the cocrystal product,[3,10] thus helping to drive the equilibrium towards cocrystal formation.

4.2 Model system: Caffeine-oxalic acid cocrystallisation

The choice of the model cocrystal system, caffeine-oxalic acid, was based on previous experimental work carried out at the Centre for Process Innovation (CPI), the industrial partner for the research project. CPI successfully cocrystallised caffeine-oxalic acid (Fig. 4.1) using an oscillatory reactor system, starting with 20.17g (0.1 mole) of caffeine and 9.24g (0.1 mole) of oxalic acid in the solid phase. Powder x-ray diffraction analysis was used to confirm formation of the cocrystal by comparing with powder pattern for a commercial sample of caffeine, oxalic acid and simulated powder pattern from single analysis of caffeine-oxalic acid cocrystal (Figs. 4.2, 4.3 and 4.4).

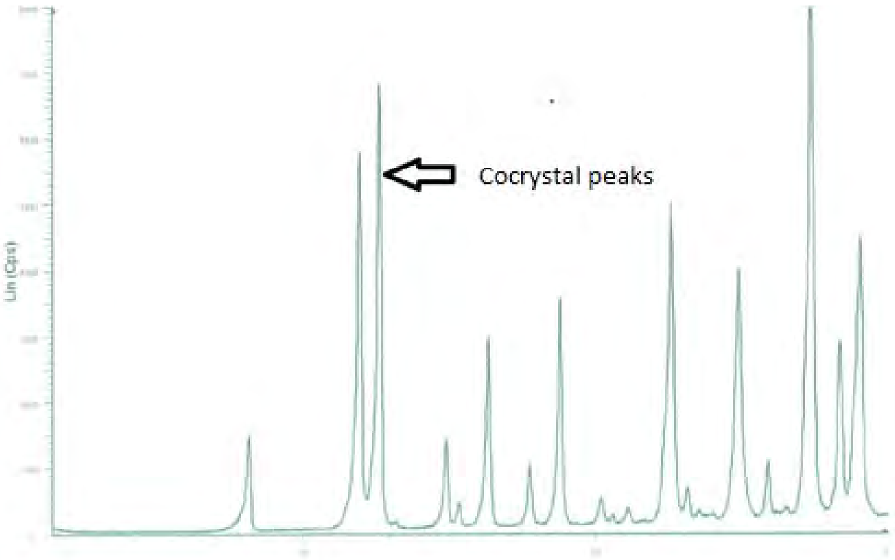

Fig. 4.1. PXRD analysis of caffeine-oxalic acid cocrystal made by CPI smart chemistry team.

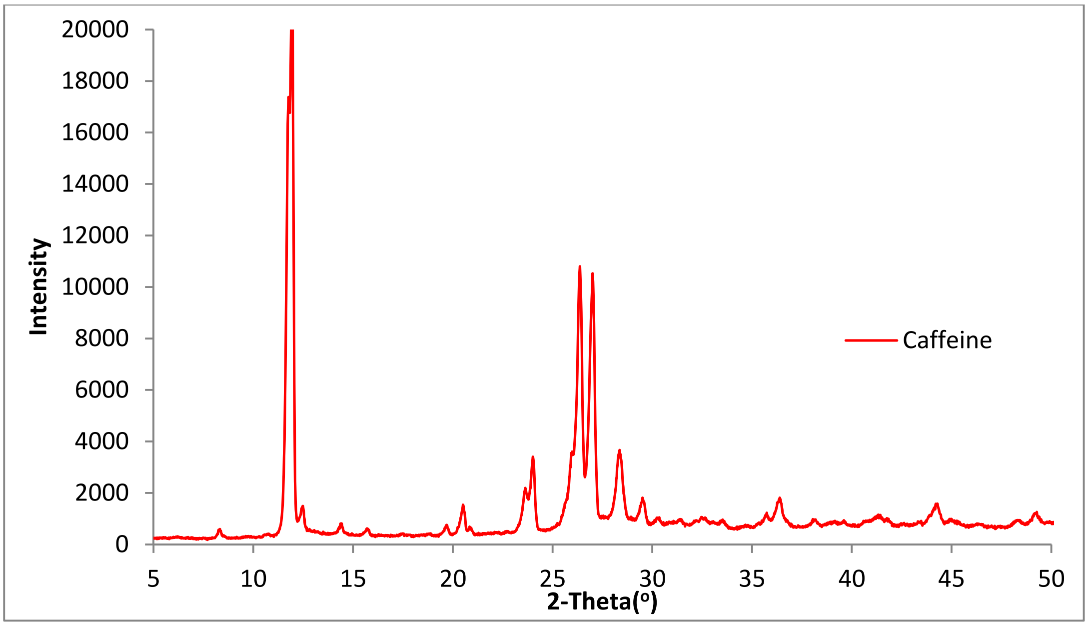

Fig. 4.2 PXRD pattern for commercial sample of caffeine.

The carboxylic acid /N-heterocyclic hydrogen bonding motif present in the caffeine and oxalic acid cocrystal (Fig. 4.5) have high selectivity for hetero-synthon bonding, which accounts for a large proportion of cocrystal supramolecules[11-13] in the Cambridge Structural Database (CSD)[14]. Caffeine and oxalic acid both exhibit polymorphism;[15-17] this implies that their crystal structure is flexible and has an increased probability of accommodating guest molecules within their lattice, thereby facilitating cocrystal formation[12,18]. The caffeine-dicarboxylic cocrystal system is well documented in journal publications[19,20] and the PXRD pattern is available for monitoring cocrystal formation.

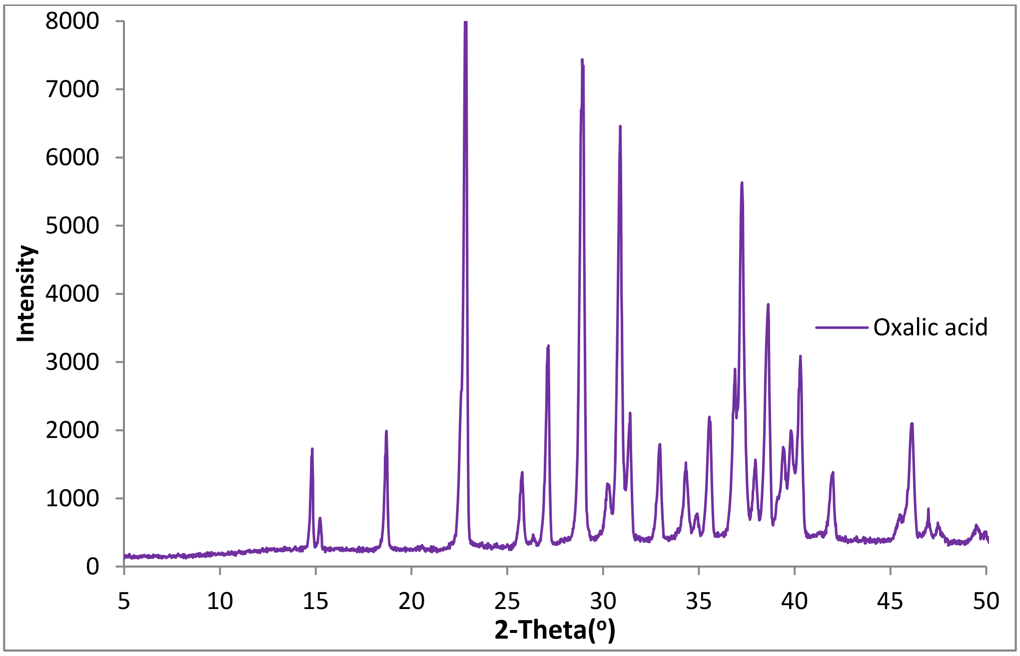

Fig. 4.3 PXRD pattern for commercial sample of oxalic acid.

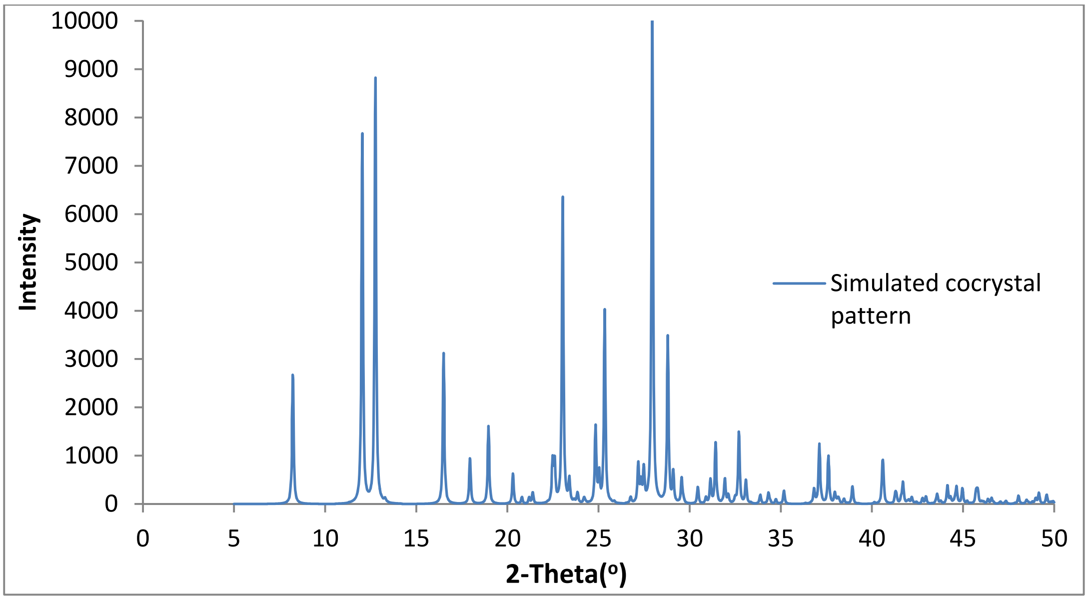

Fig. 4.4 Simulated PXRD pattern from a single crystal of 2:1 caffeine-oxalic acid prepared in the laboratory.

Caffeine is an API that works by stimulating the central nervous system. It is taken in beverages and helps improve attention and maintain alertness; it is one of the most widely taken psychoactive drugs in the world[21]. Caffeine and its metabolites are suspected to have anticancer properties and consumption of caffeine reduces mortality rate in cancer patients[22].

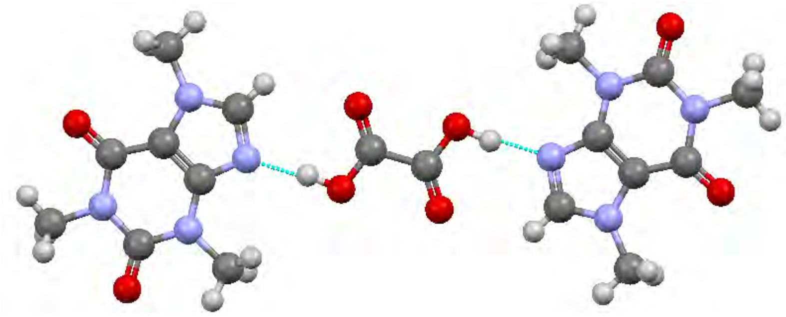

Fig. 4.5 Caffeine-oxalic acid cocrystal crystal synthons.

4.3 Caffeine-oxalic acid cocrystallisation in cyclohexane

Prior to my PhD commencement, CPI cocrystallised caffeine-oxalic acid on an advanced batch baffle reactor system called the single vertical column (SVC) (Fig. 4.6a), in an anti-solvent liquid system of anhydrous cyclohexane. Mixing within the SVC is by the formation of eddies via oscillatory motions in the liquid phase generated with a diaphragm pump (see section 1.6 and 2.1.1). A sample from the reaction was analysed by powder x-ray diffractomety (PXRD) and confirmed to contain the caffeine-oxalic acid cocrystal (Fig. 4.2) with no sign of residual caffeine or oxalic acid.

The initial task was to repeat the CPI cocrystallisation experiment, except that the pump system was changed from a diaphragm to a piston pump; this change was to improve the oscillatory mixing within the SVC and minimise the probability of initiating cocrystallisation by grinding of the cocrystal components. The probability of grinding is higher with the diaphragm pump system. The original hypothesis for this approach was that solid attrition between caffeine and oxalic acid particles facilitated cocrystallisation by mimicking the grinding process in mechano-chemical cocrystallisation process[23]. Solid settling during experimentation on the SVC was minimised by inserting a solvent-compatible elastic membrance between the column and the piston pump (Fig. 4.6b). Samples were analysed by PXRD to confirm cocrystallisation. The replacement of a peak from caffeine by two peaks[20,24] at about $2\theta \approx 10^{o}$ was used initially as an indicator that cocrystallisation had occurred. Later on, the quantitative SSNMR method in chapter 3 showed that at a low level of cocrystallisation, a single peak at $2\theta \approx 10^{o}$ is still observed because the caffeine peak overlays the two peaks for the cocrystal. Consequently, the absence of these peaks does not necessarily mean that no cocrystallisation has occurred, but, at best, the cocrystallisation was minimal. PXRD analysis on the attempted cocrystallisation using 100% cyclohexane in the SVC with the piston pump did not have two cocrystal peaks, so no cocrystallisation was concluded (Fig. 4.7).

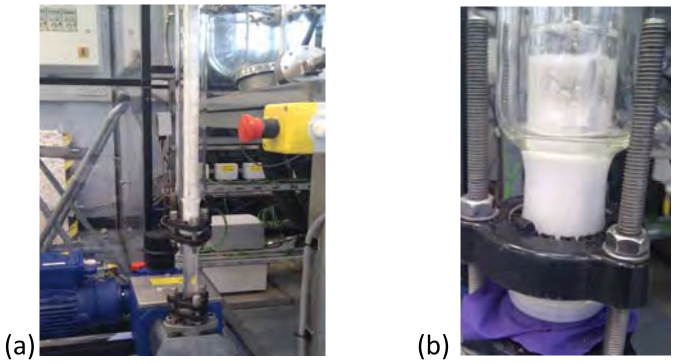

Fig.4.6 (a) Single vertical column (SVC) (b) membrane separation of piston and glass column.

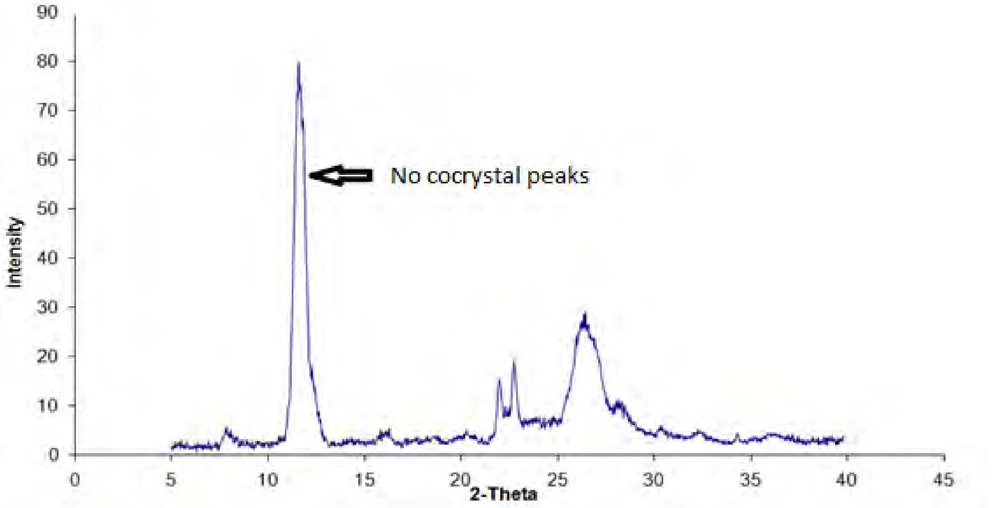

Fig. 4.7 PXRD analysis of cocrystallisation sample in 100% cyclohexane after 5hrs. PXRD does not show two cocrystal peaks so no cocrystallisation of caffeine and oxalic acid.

4.3.1 Caffeine-oxalic acid mixed solvent/anti-solvent cocrystallisation

The negative SVC cocrystallisation result in cyclohexane suggested a different approach was required to achieve high levels of cocrystallisation. In particular, it was considered that the use of 100% of an antisolvent was causing the problem and that cocrystallisation was not able to occur by the solid-state mechanism of grinding via particle attrition as previously thought. Consequently, some solvent needed to be added to the antisolvent, so that a solute-mediated cocrystallisation could occur. Caffeine-oxalic acid cocrystal has been cocrystallised by slow evaporation from a methanol/chloroform solvent system[20]. Single crystals of caffeine-oxalic acid cocrystal were also made from slow evaporation of a solution of 2 :1 caffeine:oxalic acid in a 50:50 wt mixture of methanol/chloroform (section 3.2). The next approach investigated was to mix methanol with cyclohexane. Methanol was picked over chloroform because it is easier to handle[6] and chloroform is a carcinogen. The optimum solubility of methanol in cyclohexane was determined to be $4\,wt\,\%$; at higher levels methanol separates out as a different layer. 2.5 and 4 $wt\,\%$ methanol in cyclohexane mixtures were made and the caffeine and oxalic acid cocrystallisation experiment repeated on the SVC.

Caffeine and oxalic acid cocrystallisation was repeated in 2.5% and 4% methanol in cyclohexane using 8.2g (0.04 moles) and 3.8g (0.04 moles) of caffeine and oxalic acid, respectively, both gave postive results (Figs. 4.8 and 4.9) , as shown by the appearance of two peaks at about $2\theta \approx 10^{\circ}$, although caffeine and oxalic acid crystal peaks were also evident. The experiment was repeated with 2.5% methanol in a 250 ml flask and overhead stirrer and was positive for cocrystal formation. At 4% methanol in cyclohexane, solids were observed sticking to the SVC glass column (Fig. 4.10a) but at 2.5 $wt\,\%$ methanol in cyclohexane, mixing was fine and no solid sticking to the side of the glass column(Fig. 4.10b), so 4$wt\,\%$ methanol was not used in subsequent experiments.

SVC cocrystallisation of 0.04 moles caffeine and oxalic acid with 2.5 $wt\,\%$ chloroform in cyclohexane was carried out for comparison and the experiment showed no evidence of caffeine-oxalic acid cocrystallisation after 3 hrs, i.e the two peaks at about $2\theta \approx 10^{\circ}$ were absent (Fig. 4.11).

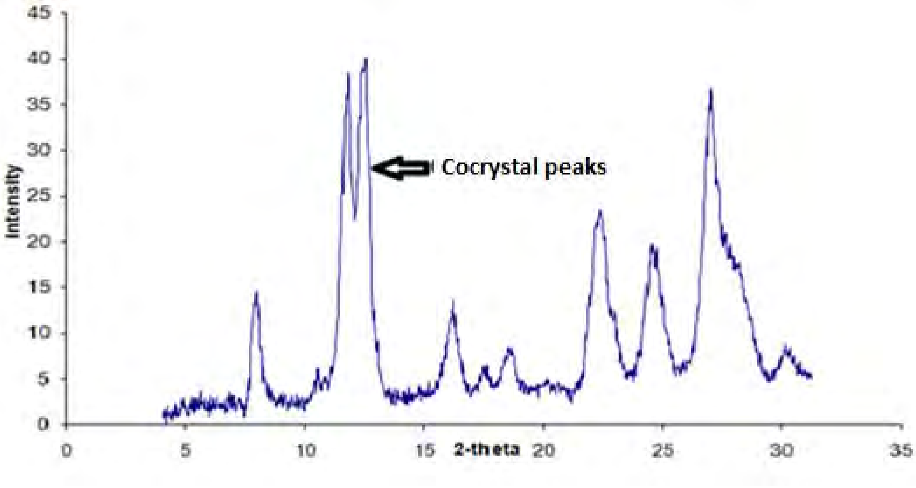

Fig. 4.8 PXRD analysis of caffeine and oxalic acid cocrystallisation in 4% methanol in cyclohexane mixture after 3hrs. PXRD shows two peaks confirming cocrystallisation.

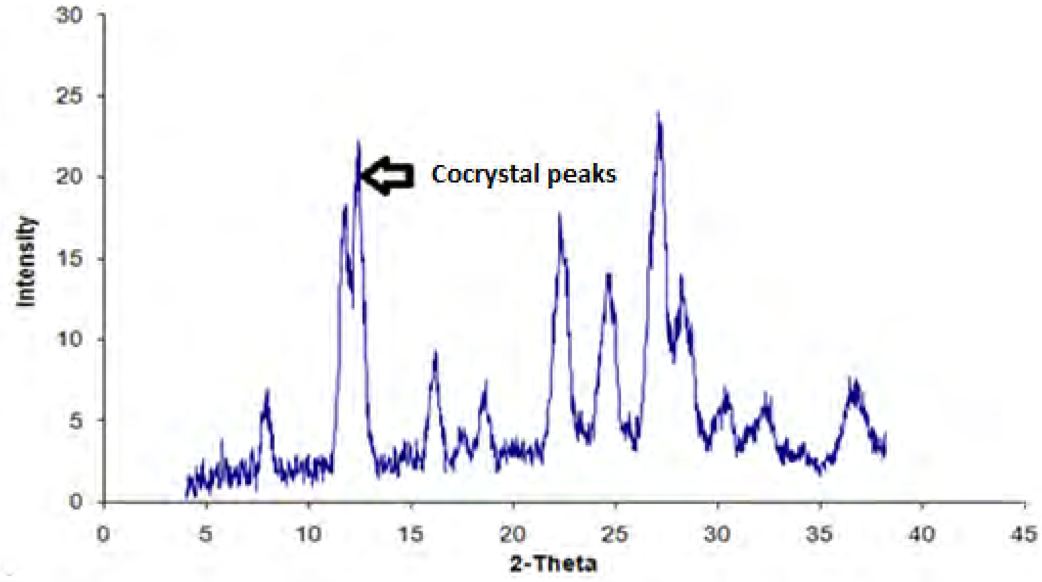

Fig. 4.9 PXRD analysis of caffeine and oxalic acid cocrystallisation in 2.5% methanol in cyclohexane mixture after 3hrs. PXRD shows two peaks confirming cocrystallisation.

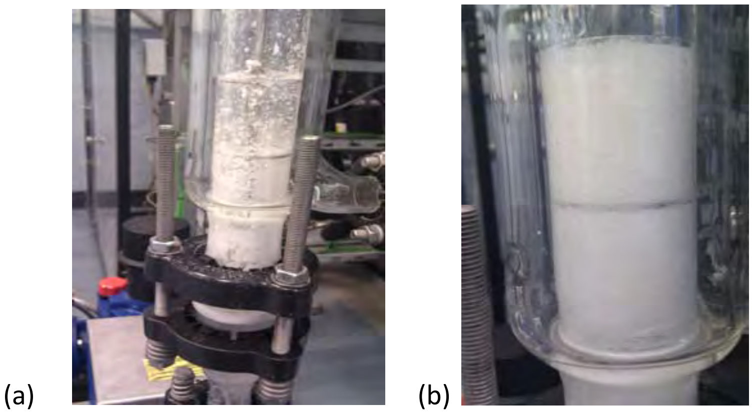

Fig. 4.10 (a) 4% methanol in cyclohexane cocrystallisation. (b) 2.5 % methanol in cyclohexane cocrystallisation respectively. Solids sticks to glass column in 4% experiment but good suspension in 2.5% experiment.

The SVC experimental results were compared with solubility data for the caffeine-oxalic acid cocrystal, caffeine and oxalic acid in chloroform and methanol (Table 4.1). Solubilities were determined in the laboratory by high performance liquid chromatography (HPLC), gravimetry method (see section 2) and from the literature. A trend was observed; in methanol in, which oxalic acid has high solubility but the caffeine solubility is low, the experiment was positive for cocrystallisation; in chloroform which has a low oxalic acid solubility[6,25] but high caffeine solubility, the experiment was negative for cocrystallisation. This aspect is further explored in section 4.3.2.

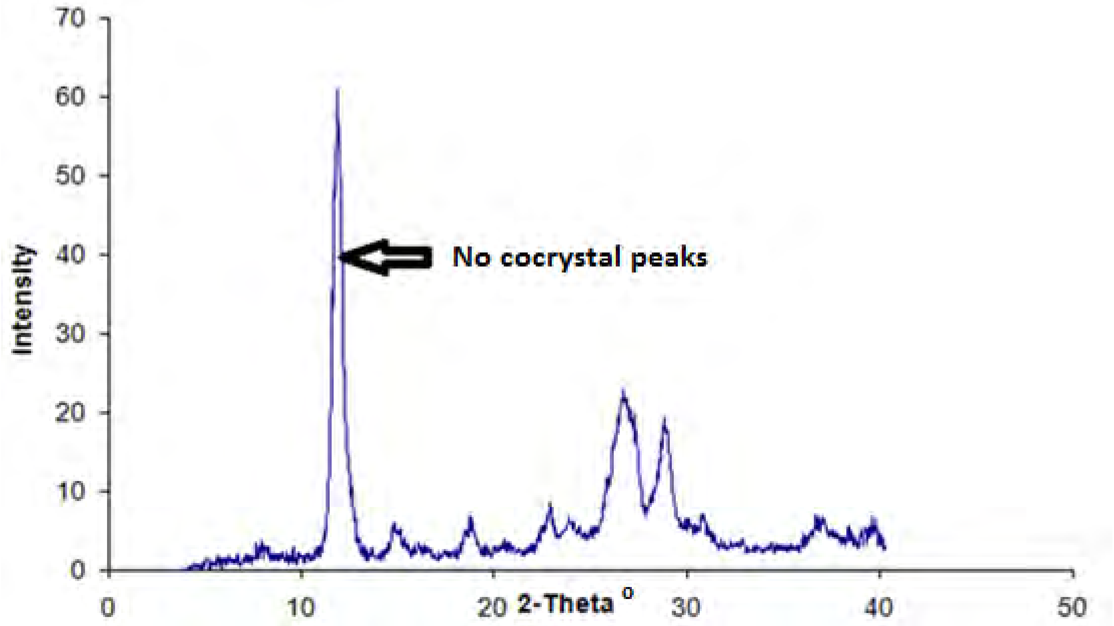

Fig. 4.11 PXRD analysis of caffeine and oxalic acid cocrystallisation in 2.5% chloroform in cyclohexane mixture after 3hrs. PXRD does not show the two peaks, so no cocrystallisation.

Describing the solubility of caffeine and oxalic acid in the mixed anti-solvent/solvent by their solubility in 100% solvent was adopted because initial experimental results showed no evidence of cocrystallisation in 100% cyclohexane making solubility of caffeine and oxalic acid in cyclohexane irrelevant in the overall scheme of cocrystallisation formation. In addition, the solubility of the cocrystal, oxalic acid and caffeine in cyclohexane with 2.2% methanol determined by HPLC were either very low or below the limit of detection (LOD) of the instrument (Table 4.1). Although 36.42% cocrystal yield (Table 4.4) was observed in 100% cyclohexane by solid state nuclear magnetic resonance analysis, this assumption is still considered valid because the focus of the investigation of the science of cocrystallisation in the anti-solvent/solvent mixture was on the influence of the presence of the organic solvent, and not the anti-solvent, in facilitating cocrystal formation in SVC experiments and determining the mechanims by which solvents facilitate cocrystal formation.

In experiments with different organic solvents in cyclohexane, variation in caffeine and oxalic acid solubility can be attributed to the organic solvent present. High performance liquid chromatography determination of cocrystal component solubility in cyclohexane (Table 4.2) shows up to 10^6 fold solubility difference for oxalic acid in cyclohexane and methanol, this difference in cocrystal component solubility in organic solvents and cyclohexane will vary but for consistency the assumption that the solvent is mainly responsible for the changes in the extent of cocrystal yield is adopted in all discussions.

Table 4.1 Solubility determination by HPLC for cocrystal, caffeine, and oxalic acid in anti-solvent/solvent mixture.

	Caffeine (mg/g)		Oxalic Acid (mg/g)	
Sample	**Average**	**S. E**	**Average**	**S.E**
Caffeine in 2.2% methanol in cyclohexane	0.171	0.001		
Oxalic acid in 2.2% methanol in cyclohexane			<LOD*	
Caffeine-oxalic acid cocrystal in 2.2% Methanol in Cyclohexane	<LOD*		<LOD*	

* HPLC method LOD = 0.001 mg/g.
S.E. = standard error.

Table 4.2 Solubility table for caffeine, oxalic acid and cocrystal in organic solvents

Solvent	Solubility in mg/g		
	Caffeine-oxalic cocrystal	Caffeine	Oxalic acid
Methanol	10.2 (8.28 g caffeine and 1.92 g oxalic acid)	13.3	1108.2
Chloroform	2.0 (1.62 g caffeine and 0.38 g oxalic acid)	122.6[a]	1.03
Cyclohexane	n.d	0.053[b]	<LOD[b]

[a] Merck index
[b] HPLC method LOD = 0.001 mg/g.
[c] Gravimetry

4.3.2 Investigating oxalic acid solubility in solvent/anti-solvent cocrystallisation.

To investigate the relationship between oxalic acid solubility and caffeine-oxalic acid cocrystallisation, the solubility of caffeine and oxalic acid was determined in different organic solvents. Cocrystallisation experiments with 2.2 wt % solvent in cyclohexane were carried out in the SVC using 0.042 moles fraction caffeine and 0.021 moles of oxalic acid. Samples were analysed by PXRD and two peaks at about $2\theta \approx 10^{o}$ used to confirm cocrystallisation. Similar results to previous ones were observed; solvents with high oxalic acid solubility were positive for cocrystallisation (i.e. methanol, butanol, acetonitrile, methyl tert-butyl ether and methyl acetate) but solvents with low oxalic acid solubility were negative for cocrystallisation (i.e. chloroform, toluene and dichloromethane) (Table 4.3). These results for caffeine-oxalic acid cocrystallisation points towards the fact that oxalic acid solubility plays a key role in the cocrystallisation reactions.

Oxalic acid is the more crystalline of the two caffeine-oxalic acid cocrystal components; caffeine hydrogen bonds weakly to itself and displays a disordered orientation in its crystal structure[26-28]. This difference in crystallinity could make the activation energy requirement for the solvation of oxalic acid higher than that for caffeine and may make the solvation of oxalic acid the rate determing step; so the solvents used in the cocrystallisation experiments influence the kinetics of reaction by lowering the activation barrier for cocrystallisation.

Ab initio lattice energy analysis for caffeine and oxalic acid[26] showed very little difference in their individual lattice energy and suggest that lattice energy may not play a role in the trend observed the cocrystallisation in the different solvents.

A simple design of experiment (DoE) cocrystallisation screen was done to test the influence of solvent ratio on cocrystallisation in the anti-solvent/solvent mixture using methanol as the solvent. The screen was done with 4 experiments; two experiments representing high and low values for methanol: 100% cyclohexane and 100% methanol and two replica experiments with intermediate methanol/cyclohexane level referred to as “centre points”. These centre points were used to test the reliability of the experimental design. The experiments were done on the SVC and lasted for 30 minutes. The order of the experiments was randomised by staggering the two centre point experiments to minimise experimental bias[29]. The number of moles of caffeine and oxalic acid used were 0.011 and 0.005, respectively, in all the experiments. The cocrystal yield value was determined using SSNMR.

Table 4.4 tabulates the results from the DoE screen. The cocrystal yield of 66.06% and 61.75% for the two centre point experiments are not too dissimilar, the standard deviation (s) and the coefficient of variance (CV) are 3.05% and 4.77% respectively. The coefficient of variance of 4.77% is less than 5% suggesting that the noise in the experimental design is low and that the cocrystal yields in the screen are reliable. The 100% methanol experiment gave ≈ 100% yield and 0% methanol experiment gave

36.42%, these results confirm that methanol actually influences cocrystal yield in the solvent/anti-solvent mixture.

Table 4.3 Solubility table for caffeine, oxalic acid and cocrystal in common organic solvents

Solvent	Solubility in mg/g		
	Caffeine-oxalic cocrystal	Caffeine	Oxalic acid
Toluene	0.4 (0.32 g caffeine and 0.08 g oxalic acid)	5.5	0.9
Dichloromethane	1.0 (0.81 g caffeine and 0.19 g oxalic acid)	65.1	0.5
Acetonitrile	4.01 (3.25 g caffeine and 0.76 g oxalic acid)	27.4	162.9
Tetrahydrofuran	6.6 (5.36 g caffeine and 1.24 g oxalic acid)	8.98	494.6
Methyl acetate	n.d	11.6	122.9
Butan-1-ol	n.d	4.3	164
Acetic acid	16.9 (8.28 g caffeine and 1.92 g oxalic acid)	23.9	77.5
Methyl tert-butyl ether	n.d	1.57	312.65

n.d = not determined.

Table 4.4 Design of experiment screen of caffeine-oxalic acid cocrystallisation.

Solvents	Cocrystal yield (%)
100% Methanol	100*
2.2% methanol in cyclohexane	66.06
2.2% methanol in cyclohexane	61.75
100% cyclohexane	36.42

*100% is an estimate based on the absence of caffeine and oxalic acid peak in the SSNMR spectra.

Three cocrystallisation experiments with methanol levels between the 0-3 % were carried out to further test the influence of methanol in the mixed solvent/anti-solvent mixture, 0.45, 1.34 and 2.21 *wt* % methanol in cyclohexane were used and the experiments monitored for 3 hrs. Samples were taken after 5 minutes and at the end of the experiment, the results are presented in Table 4.5 below.

Table 4.5 SVC cocrystallisation with three different solvent amounts.

wt/wt %	Cocrystal yield %	
	5 minutes	180 minutes
2.21	47.9	76.8
1.34	46.1	61.9
0.45	25.9	33.1

The methanol levels in the anti-solvent/solvent mixtures were plotted against the cocrystal yield observed after 5 and 180 minutes. The two scatter plots (Figs. 4.12 and 4.13) were analysed using statistical approach to test for interdependency between the level of methanol and cocrystal yield using correlation coefficient (r) analysis, while the significance of the experimental data were measured using the coefficient of determination (R^2).

The correlation coefficient (r) for the cocrystal yield after 5 and 180 minutes were 0.90 and 0.98, respectively, indicating a strong interdependence between the level of methanol and caffeine-oxalic acid cocrystal yield.

The coefficient of determination (R^2) measures the variance in the linear regression model. It measures how much of the response variable (cocrystal yield) is explained by the independent variable (methanol ratio). The disparity observed in the coefficient of determination for 5 minutes (0.81) and 180 minutes (0.97) could be due to inhomogeneity of the sample used for analysis; the samples taken after 180 minutes were taken at the end of experiments, after isolation of the solids and were more representative of the reaction slurry than the samples taken after 5 minutes, which consisted of 5 ml of slurry extracted from the SVC with a syringe from a 40 ml reaction (see section 2.1.1) so the samples may not be representative of the reaction slurry at that stage of the reaction; hence the higher coefficient of determination of 0.97 observed for the 180 minutes samples and 0.82 for 5 minutes sample.

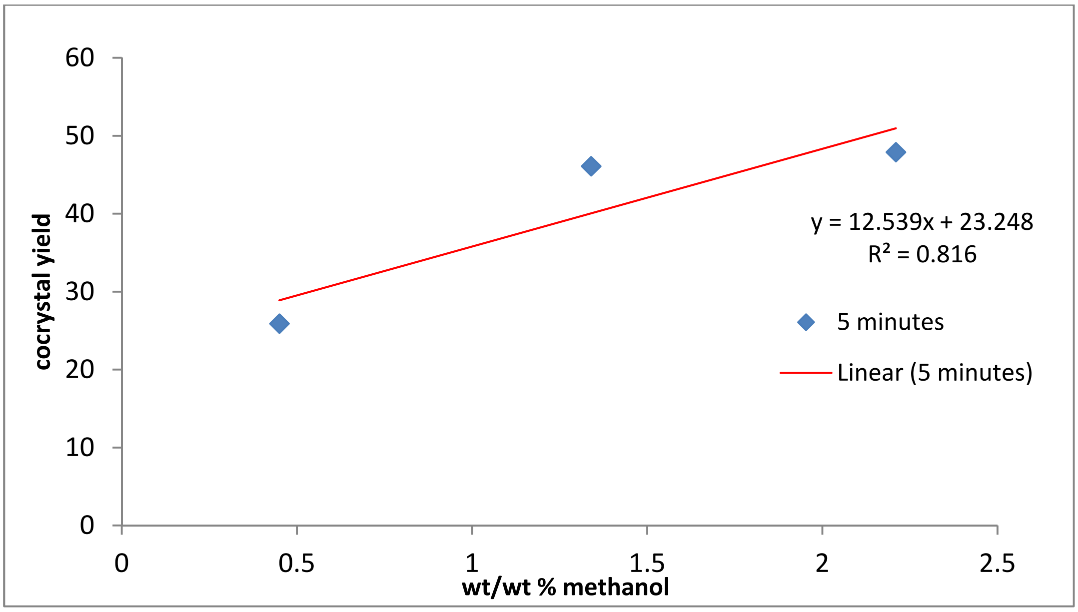

Fig. 4.12 Scatter plot of cocrystal yield against the different ratios of methanol for samples taken after 5 minutes SVC cocrystallisation of caffeine and oxalic acid.

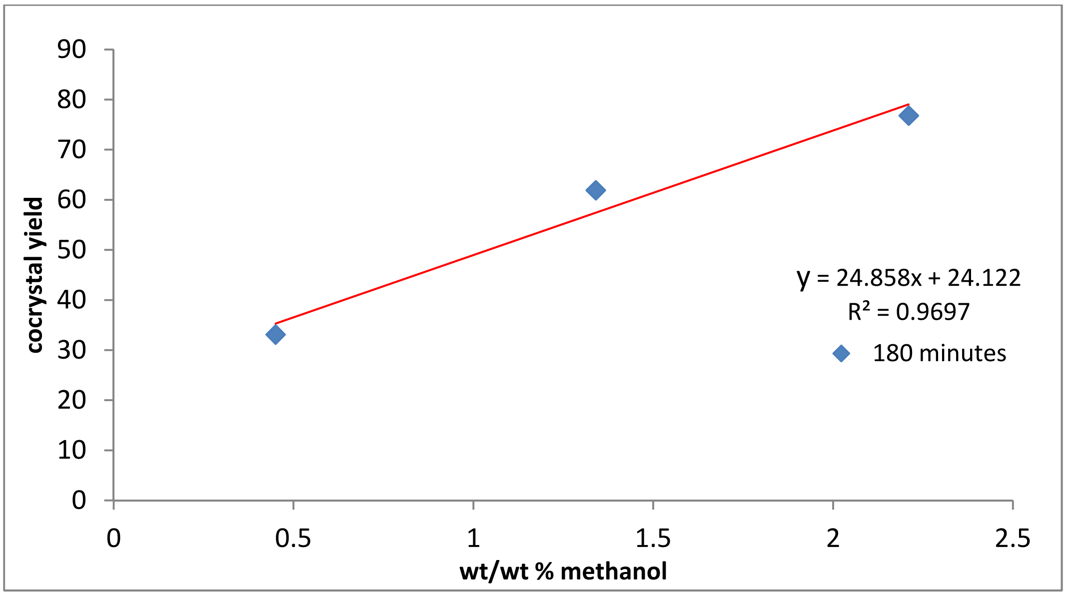

Fig. 4.13 Scatter plot of cocrystal yield against the different ratios of methanol for samples taken after 180 minutes SVC cocrystallisation of caffeine and oxalic acid.

The intercept values of 23.46% and 24.45% for the regression model (Figs. 4.12 and 4.13) are similar and represent the expected cocrystal yield when no methanol is present in the system. The intercept values are less than the yield of 36.42% observed for pure cyclohexane in the cocrystallisation screen (Table 4.4). However, the difference may be as a result of temperature variation during experiments; reaction temperatures were monitored during the screen (Table 4.4), but not for the experiments with different methanol ratios (Table 4.5). Temperature difference of up to 10 °C has been observed between experiments carried out early in the morning on a cold day and later in the day because the temperature in the solvent storage room falls to less than 5 °C overnight during the winter months.

4.3.3 Hansen solubility parameter in solvent/anti-solvent cocrystallisation.

Caffeine-oxalic acid cocrystal yield for five different solvents were quantified using the SSNMR. Each experiment lasted 30 minutes, with a solid loading of 7 wt % and 2.2 wt % of solvent in cyclohexane. The number of moles of oxalic acid and caffeine in the solid loadings were 0.006 and 0.011, respectively. The quantitative yield of caffeine-oxalic acid cocrystal was compared against oxalic acid solubility and presented in Table 4.6, the associated scatter plot is shown in Fig. 4.14.

The solubility of oxalic acid in the different solvents does not account for all the cocrystal yield observed in the experiments. Oxalic acid has the highest solubility in methanol and the highest cocrystal yield of 73% was attained in this solvent. However, the next highest cocrystal yield of 61.4% was observed in acetic acid system but oxalic acid solubility in acetic acid is lower than tetrahydrofuran and acetonitrile, where cocrystal yields were lower at 52.2% and 30.6%, respectively.

Table 4.6. Comparing cocrystal yield with oxalic acid and caffeine solubility.

Solvents	Oxalic acid solubility in mg/g	Caffeine solubility in mg/g	Cocrystal yield (%)
Methanol	1108.2	13.3	77.7
Acetic acid	77.5	23.9	61.4
Tetrahydrofuran	494.6	9.0	52.2
Acetonitrile	162.9	27.4	30.6
DCM	0.5	65.1	23.9

The scatter plot suggests a linear regression exists between caffeine-oxalic acid cocrystal yield and oxalic acid solubility with acetic acid looking like an outlier because of its considerable distance away from the regression line (Fig. 4.14). The coefficient of determination for the regression is low at R^2 ≈ 0.6 indicating that only 60% of cocrystal yield is explained by oxalic acid solubility in the experiments. When the data point for acetic acid is excluded, the coefficient of determination improves significantly to $R^2 \approx 0.99$ (Fig. 4.15) i.e. 99% of the cocrystal yield is explained by oxalic acid solubility.

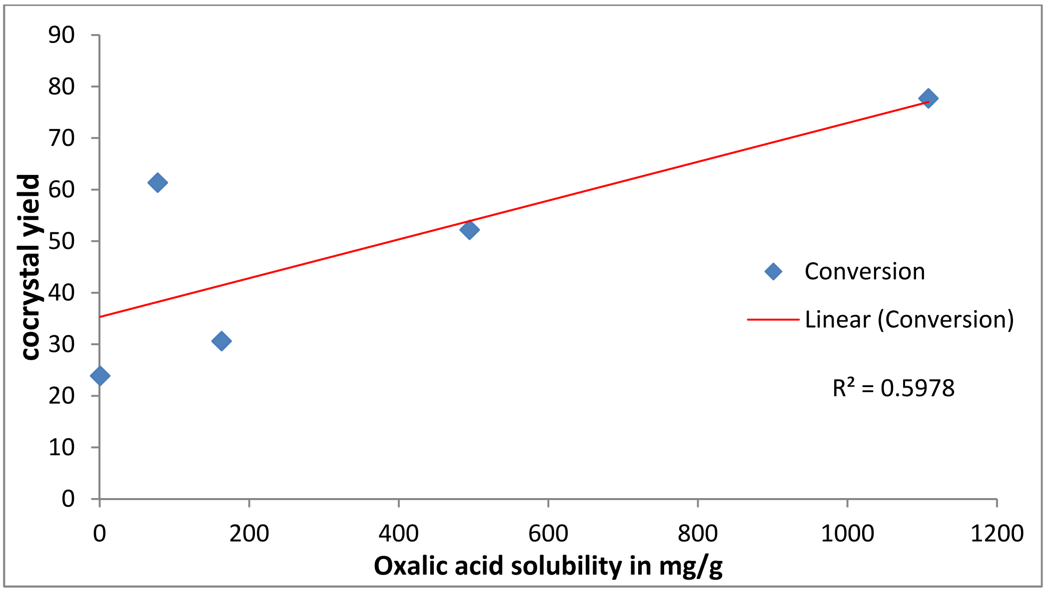

Fig. 4.14 Scatter plot of oxalic acid solubility vs. cocrystal yield for7 *wt* % loading.

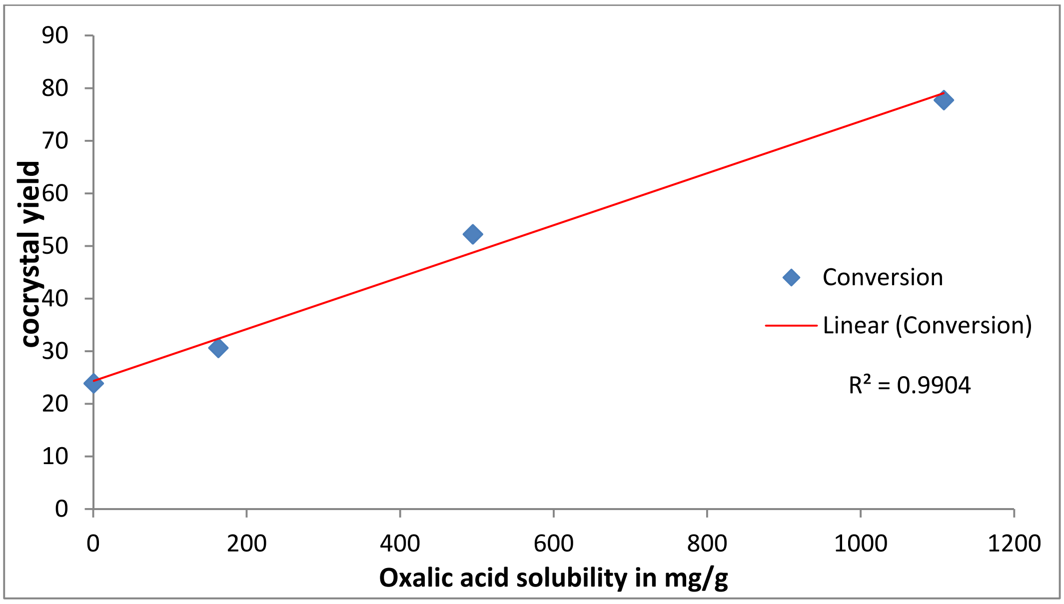

Fig. 4.15 Scatter plot of oxalic acid solubility vs. cocrystal yield without acetic acid data point and showing an improved coeffficient of determination of 99%.

The solubility of Oxalic acid in acetic acid was repeated and determined to be ≈74.37 mg/g, which is similar to the 77.5 mg/g value used in the scatter plot. Results from cocrystallisation experiment of 2.2 *wt* % acetic acid, tetrahydrofuran, methyl acetate and methanol in cyclohexane, with a higher solid loading of 23% instead of 7% *wt* are presented in Table 4.7. In the table, acetic acid still attains a higher than expected caffeine-oxalic acid cocrystal yield (53.46%) compared to tetrahydrofuran (39.24%)

and methyl acetate (35.27%) even though the oxalic acid solubility is lower in acetic acid (77.5 mg/g) than in tetrahydrofuran (494.6 mg/g) and methyl acetate (123.3 mg/g). Therefore, because the higher cocrystallisation yield was repeated in Table 4.7 acetic acid data were included in the subsequent investigations. The scatter plot of oxalic acid solubility and cocrystal yield for 23% wt loading experiments (Fig. 4.16) has a coefficient of determination of R^2 ≈0.61 which is similar to the R^2 value of 0.59 obtained for 7% wt experiments.

The scatter plot for caffeine solubility and cocrystal yield (Table 4.6) is presented in Fig. 4.17. The plot shows a negative regression exists between caffeine solubility and cocrystal yield. The coefficient of determination is $R^2 \approx 0.55$, showing that only 55% of the observed variation in caffeine-oxalic acid cocrystal yield is explained by caffeine solubility in the solvents investigated.

Table 4.7 Caffeine-oxalic acid cocrystallisation at 23% wt solid to liquid loading.

Solvents	Oxalic acid solubility in mg/g	Caffeine solubility in mg/g	Cocrystal yield (%)
Methanol	1108.2	13.3	76.8
Acetic acid	77.5	23.9	53.5
Tetrahydrofuran	494.6	9.0	39.2
Methyl acetate	123.3	11.8	35.3

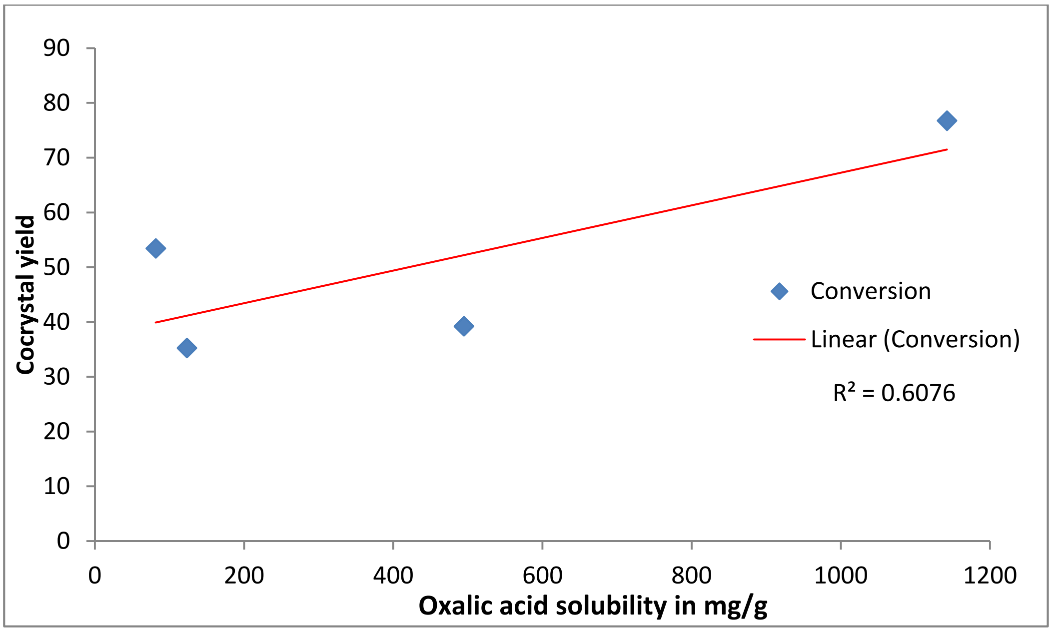

Fig. 4.16 Scatter plot of oxalic acid solubility vs. cocrystal yield for 23% wt loading.

The solubility of caffeine and oxalic acid were determined by high performance liquid chromatography in 2.2 wt % methanol, ethanol, isopropanol and THF in cyclohexane and the values compared against the observed caffeine-oxalic acid cocrystal yield in the SVC experiments to check for trends between cocrystal yield and cocrystal component solubility in the mixed anti-solvent/solvent (Table 4.7).

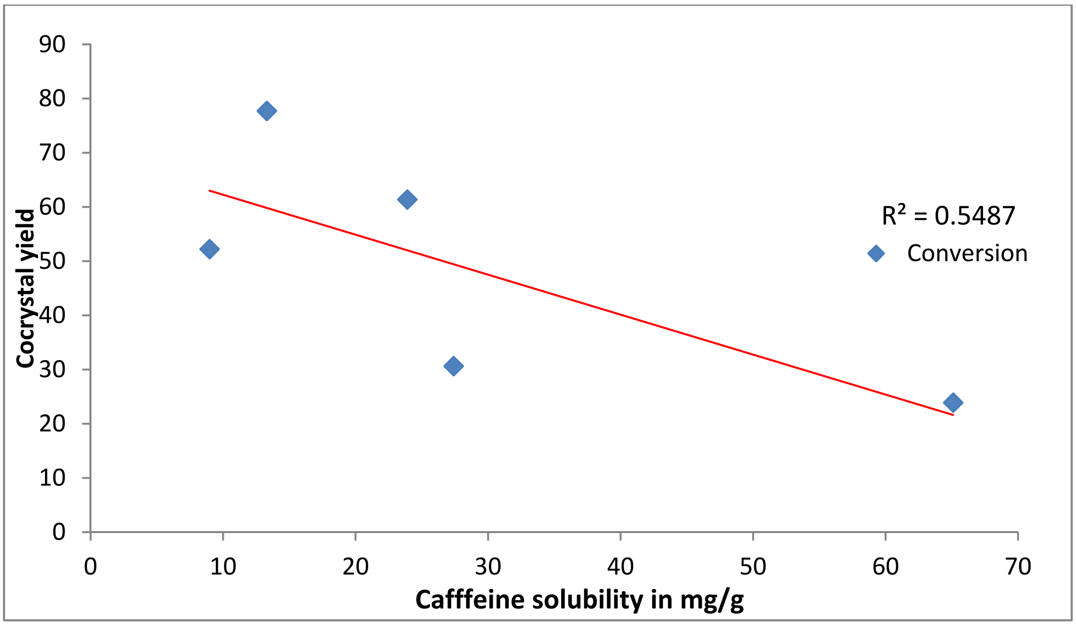

Fig. 4.17 Scatter plot of caffeine solubility vs. cocrystal yield for7% wt loading. Plot shows a negative relationship between caffeine solubility and cocrystal yield.

As would be expected, the solubility of oxalic acid and caffeine is reduced in the various anti-solvent/solvent mixture (Table 4.8) compared to the pure solvents (Table 4.6). Caffeine has the highest solubility of 0.222 mg/g in the ethanol/cyclohexane mixture but this does not give the highest caffeine-oxalic acid cocrystal yield. In addition, oxalic acid has the highest solubility of 0.408 mg/g in the isopropanol/cyclohexane mixture but this also does not also give the highest caffeine-oxalic acid cocrystal yield. Note that in some solubility tests, the oxalic acid solubility was not determined because the levels were below the limit of detection of the HPLC.

The caffeine solubility determined for four mixed anti-solvent/solvent mixture were plotted on a scatter plot against the observed caffeine-oxalic acid cocrystal yields in 7 wt % and 2.2 wt % solvent in cyclohexane SVC experiments (Fig. 4.14). A low coefficient of determination (R^2) of ≈0.097 was obtained, showing less than 10% of caffeine-oxalic acid cocrystal yield was explained by caffeine's solubility in the anti-solvent/solvent mixtures.

These results of statistical analysis of the relationships between caffeine/oxalic acid solubility data and observed caffeine-oxalic acid cocrystal yield in SVC experiments suggest that the cocrystal component solubility alone in either pure solvent or anti-solvent/solvent mixture are not sufficient to explain the role of the solvents in facilitating caffeine-oxalic acid cocrystal yield.

Table 4.8 HPLC solubility for caffeine, and oxalic acid in pure and anti-solvent/solvent mixture with observed cocrystal yield.

	Caffeine Solubility (mg/g)		Oxalic Acid Solubility (mg/g)		Cocrystal yield (%)
Sample	**Average**	**S. E**	**Average**	**S.E**	
2.2% methanol in cyclohexane	0.171	0.001	<LOD*		77.7
2.2% ethanol in cyclohexane	0.222	0.001	<LOD*		58.87
2.2% isopropanol in cyclohexane	0.183	0.001	0.408	0.09	55.3
2.2% THF in cyclohexane	0.075	0.001	<LOQ*		52.2

*HPLC method LOD = 0.001 mg/g
S.E. = standard error

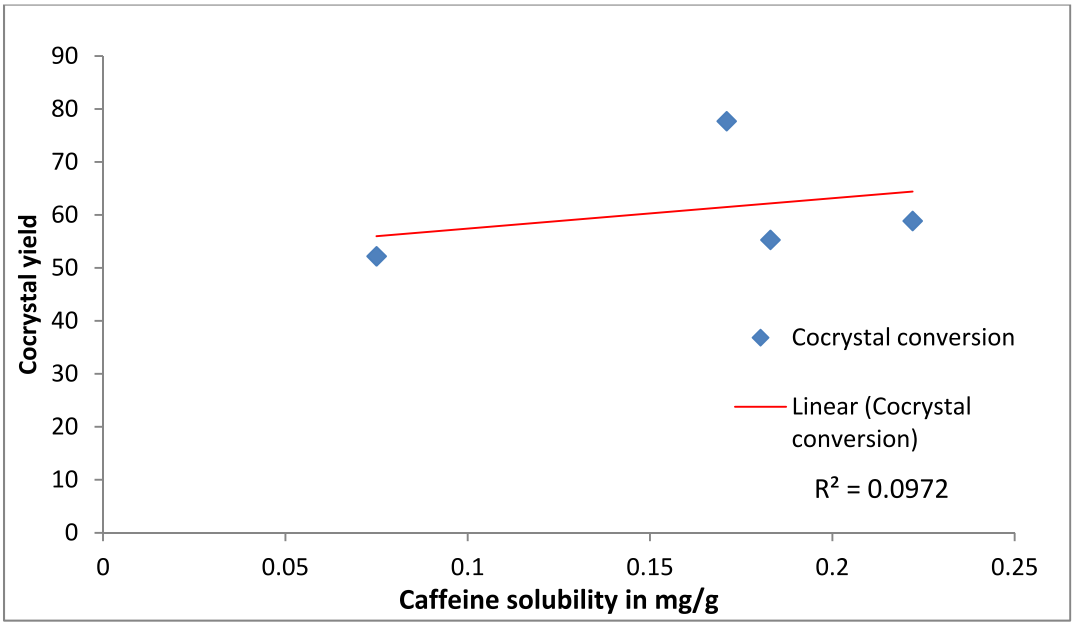

Fig. 4.18 Scatter plot of caffeine solubility in anti-solvent /solvent vs. cocrystal yield.

To determine whether the percentage of cocrystal yield could be explained by other factors, the solvent properties of the organic solvents likely to influence hydrogen bonding were investigated.The solvent properties selected were: number of hydrogen bond donors and acceptors present in solvent, Hansen solubility parameter (δ_D , δ_P , δ_H and δ_T) and dielectric constant (ε_r) of the solvents.

In Chapter 1, the Hansen solubility parameter was introduced as been derived from the Hildebrand solubility parameter (δ_T) (Eqn. 4.3), which is used in predicting solubility between substances based on the “like dissolves like” principle; substances with similar Hildebrand solubility parameters have high affinity for each other and a high probability of forming a solution with each other[30,31].

$$\delta_T = \left(\frac{E}{V}\right)^{\frac{1}{2}} \qquad \text{Eqn. 4.3}$$

where E = energy of vaporisation and V = molar volume, its unit is $\mathrm{Pa}^{\frac{1}{2}}$.

The Hansen solubility parameters are: dispersive (δ_D) referring to the non-polar atomic forces density, polarisability (δ_P) referring to permanent dipole-dipole intermolecular force density and hydrogen bonding (δ_H) referring to intermolecular hydrogen bonding force density[31,32]. These components have been used for predicting cocrystal formation[33].

$$\delta_{\mathrm{T}}^2 = \delta_D^2 + \delta_{\mathrm{P}}^2 + \delta_{\mathrm{H}}^2 \qquad \text{Eqn. 4.4}$$

Correlation analysis was used to test the significance of relationships between cocrystal yield and the selected organic solvent properties using the data from five organic solvents (Table 4.9). In correlation analysis, each variable considered is treated as an independent variable when testing for relationships.

Table 4.10 is the correlation table output for cocrystal yield and solvent properties. H-bonding and H-donor properties were excluded from the correlation table because H-donor and H-acceptor property of the solvent did not explain cocrystal yield in Table 4.8, e.g. methanol has one H-donor and H-acceptor but has a higher cocrystal yield than acetic acid with one H-donor and two H-acceptors. The solubility of caffeine and oxalic acid in pure solvents were included to broaden the test and check if any significant interdependency exists between caffeine and oxalic acid solubility and the other solvent properties.

The values in the cells in Table 4.10 are the correlation coefficient values (r) measuring the interdependency between the variable in the rows and columns. Moving from left to right along a row, the correlation coefficient value in each cell represents the interdependency between the variable at the start of the row and the variable at the top of the column of that cell. The row of interest is the last row labelled “yield”; it measures the correlation coefficient (r) between the cocrystal yield and different solvent properties. The highest correlation coefficient value (r) of 0.91 for cocrystal yield is observed for solvent H-bonding cohesive energy density (δ_H), indicating that the density of H-bonding (δ_H) has the strongest interdependence with cocrystal yield. The strong H-bonding density (δ_H) correlation coefficient with cocrystallisation was alluded to by Mohammed et. al.[33], stating that H-bonding (δ_H) was important for cocrystal formation. The next strongest interdependency is observed for oxalic acid solubility r = 0.77 and agrees with previous experimental results suggesting that oxalic acid solubility plays a significant role in the observed caffeine-oxalic acid cocrystal yield. The correlation table shows that caffeine solubility has an inverse relationship with cocrystal yield, which agrees with the scatter plot of caffeine solubility vs. cocrystal yield (Fig. 4.17).

Table 4.9 Comparison of cocrystal yield with solvent properties.

Solvent	H-Donor	H-Acceptor	Hansen solubility parameter			δ_T	ε_r	Cocrystal Yield (%)
			δ_D	δ_P	δ_H			
Methanol	1	1	15.1	12.3	22.3	29.6	32.6	77.7
Acetic acid	1	2	14.5	8	13.5	21.4	6.2	61.4
Tetrahydrofuran	0	1	16.8	5.7	8.0	19.4	7.5	52.2
Acetonitrile	0	1	15.3	18	6.1	24.4	36.0	30.6
DCM	0	0	18.2	6.3	6.1	20.3	8.9	23.9

The total cohesive energy density (δ_T) correlation coefficient (r) of 0.55 has the third strongest interdependency with cocrystal yield but not much can be attached to this value because the total cohesive energy density, which is equivalent to the Hildebrand energy density, is not good at explaining solubility in polar systems[30].

Table 4.10 Correlation table for SVC cocrystallisation experiments with 5 solvents.

	Caffeine	Oxalic acid	δ_D	δ_P	δ_H	δ_T	ε_r
Oxalic acid	-0.63						
δ_D	0.65	-0.29					
δ_P	-0.19	0.16	-0.53				
δ_H	-0.49	0.80	-0.57	0.09			
δ_T	-0.34	0.75	-0.54	0.65	0.77		
ε_r	-0.24	0.47	-0.41	0.92	0.30	0.83	
Yield	-0.74	0.77	-0.63	-0.06	0.91	0.55	0.10

The high value for δ_T may be just due to the H-bonding (δ_H) component of the total cohesive energy density (Eqn. 4.4) that has already been considered. The negative correlation coefficient values for polarisability (δ_P) = -0.06 and dispersive energy (δ_D)= -0.63 shows an inverse interdependency, similar to the value obtained for caffeine solubility, suggesting that these solvent properties do not facilitate caffeine-oxalic acid cocrystal yield. The dielectric constant (ε_r) correlation coefficient (r) = 0.1 suggests that solvent dielectrics influence on caffeine-oxalic acid cocrystal yield is not significant.

The correlation analysis was expanded to include 5 more solvents taking the total to ten (Table 4.11); the expansion of data was to improve the reliability of the correlation analysis and confirm if the correlation coefficients (r) obtained previously were reliable. The solvents added were: ethanol, butanol, isopropanol, methyl tert-butyl ether and diethyl ether.

Table 4.12 is the correlation output for the expanded test. Looking at the yield row, the highest correlation coefficient (r) value for caffeine-oxalic acid cocrystal yield is observed for solvent H-bonding cohesive energy density δ_H (r) = 0.81. Although the strength of the interdependency with caffeine-oxalic acid cocrystal yield drops compared with Table 4.10, the fact that it still has the strongest interdependency shows that it is the most significant factor amongst the properties being considered. The next strongest interdependency is oxalic acid solubility (r) = 0.75, followed by the total cohesive energy density (δ_T) r = 0.62. The trend in correlation coefficients (r) in Table 4.12 is similar to Table 4.10, confirming that the correlation coefficients (r) are reliable. The polarisability energy density correlation coefficient (δ_P) r = 0.19

changes slightly from a negative value of -0.06 to a positive value;, this shows the benefit of expanding the data set. A similar change is seen in the correlation coefficient (r) for the total cohesive energy density which increases from 0.55 to 0.62.

Still not all the caffeine-oxalic acid cocrystal yields are explained by just H-bonding cohesive density and oxalic acid solubility; acetic acid with a δ_H= 13.5 and oxalic acid solubility of 77.5 mg/g has a higher cocrystal yield (64.1%) than isopropanol (55.3%) which has a higher δ_H= 16.4 and oxalic acid solubility =360.68 mg/g. A similar scenario is observed when comparing the greater cocrystal yield rate of acetic acid compared to butanol. This trend cannot be explained using the total cohesive energy density (the next strongest correlation coefficient) but the polarisability energy density (δ_P) does seem to explain the trend. The polarisability energy densities (δ_P) for the three solvents are: 8, 6.1 and 5.7 for acetic acid, 2-propanol and butanol respectively, which agrees with the observed caffeine-oxalic acid cocrystal yield.

Table 4.11 Comparison of cocrystal yield with solvent properties for 10 solvents.

Solvent	Oxalic acid solubility (mg/g)	Caffeine solubility (mg/g)	Hansen solubility parameter			δ_T	ε_r	Cocrystal Yield (%)
			δ_D	δ_P	δ_H			
Methanol	1108.2	13.3	15.1	12.3	22.3	29.6	32.6	77.7
Ethanol	612	6.9	15.8	8.8	19.4	26.5	24.6	74.75
Acetic acid	77.5	23.9	14.5	8	13.5	21.4	6.2	61.4
2-propanol	360.68	5.1	15.8	6.1	16.4	23.5	18.3	55.3
Tetrahydrofuran	494.6	8.98	16.8	5.7	8.0	19.4	7.5	52.2
Methyl tert-butyl ether	343	1.6	13.7	3.5	5.1	15.1	2.6	37.0
Diethyl ether	337.5	0.8	14.5	2.9	5.1	15.8	4.3	35.06
Butanol	164	4.4	16	5.7	15.8	23.1	17.8	33.36
Acetonitrile	162.9	27.4	15.3	18	6.1	24.4	36.0	30.6
DCM	0.5	65.1	18.2	6.3	6.1	20.3	8.9	23.9

Table 4.12 Correlation table for SVC cocrystallisation experiments for 10 solvents.

	Caffeine	Oxalic acid	δ_D	δ_P	δ_H	δ_T	ε_r
Oxalic acid	-0.43						
δ_D	0.64	-0.20					
δ_P	0.27	0.19	0.01				
δ_H	-0.26	0.61	-0.01	0.23			
δ_T	0.08	0.52	0.19	0.69	0.83		
ε_r	0.03	0.43	0.07	0.87	0.53	0.87	
Yield	-0.36	0.75	-0.21	0.19	0.81	0.62	0.33

Both correlation analyses show that the solubility of the oxalic acid and the Hydrogen bonding Hansen solubility parameter are the two most important factors for cocrystallisation. Lee et al.[34] came to a similar conclusion, with the H-bonding property of organic solvents being the most significant factor when considering the level of cocrystallisation achieved in a screen of 23 solvents for the cocrystallisation of crown ether and ammonium nitrate. It has been shown that solvents with strong hydrogen bonding (δ_H) interact with the solute to favour intermolecular interaction over intramolecular interaction during crystallisation[35]. During nucleation, solutes associate in solution to form clusters that can grow or dissolve. If the clusters reach a critical nucleus size, then nucleation occurs. Samir et. al.[36] observed in the nucleation of isonicotinamide that the hydrogen bonding strength (δ_H) of the solvent used in crystallisation influences the way the solute associates together. Strong hydrogen bonding (δ_H) solvents like methanol were able to overcome the head-to-tail self-association chain tendency of isonicotinamide by hydrogen bonding to the pyridine group in isonicotinamide making it unavailable for head-to-tail chain interaction, thereby forcing the isonicotinamide to associate via a dimer motif with its amide group. Solvents with high H-bonding cohesive energy density (δ_H) can form strong hydrogen bonding association with the carboxylic acid group in oxalic acid and pyridine nitrogen in caffeine, thereby rendering them less likely to partake in homomeric self-association and so favouring heteromemeric association to form the cocrystal.

Developing a model capable of predicting the best solvent for the anti-solvent/solvent cocrystallisation, based on scientific approach would be useful. It would remove the need for carrying out solvent screens each time the cocrystallisation of a new system is required, reducing the time required for developing the process. This was the next goal that was embarked upon in this investigation.

The Hansen solubility parameter has been used in the polymer industry for selecting suitable solvents for polymers. This is done by using the square root of the sum of square differences between the substrates for the Hansen parameter (δ_H, δ_P and δ_D) shown in Eqn. 4.5. This gives a numerical value (Ra) for comparing compatibility between solvent and polymer.

$$\sqrt{\ } (\mathrm{Ra})^2 = \sqrt{4(\delta_{\mathrm{D2}}-\delta_{\mathrm{D1}})^2+(\delta_{\mathrm{P2}}-\delta_{\mathrm{P1}})^2+(\delta_{\mathrm{H2}}-\delta_{\mathrm{H1}})^2} \quad \text{Eqn. 4.5}$$

Ra is referred to as the Hansen solubility parameter distance, and is a measure of the affinity between the two substrates; the 1 and 2 subscripts refer to the Hansen solubility parameter value for the polymer substrate and solvent. The lower the Ra value, the better the affinity between the solvent and polymer and the higher probability of forming a solution between both, because the Hansen solubility differences between the polymer and solvent is squared, the Ra value is not affected by the order in which the subtraction is made. The calculated Ra values for oxalic acid and different solvents used in the screen are presented in Table 4.13.

In Table 4.13, the lowest Ra value of 4.3 is obtained for methanol and corresponds to the highest cocrystal yield (77.73%). The highest Ra value is obtained for methyl tert-butyl ether (21.11) but this does not correspond to the lowest cocrystal yield. The lowest cocrystal yield is observed in DCM (23.9%) with Ra value of 17.96, which is lower than methyl tert-butyl ether ($\mathrm{Ra} = 21.11$) and diethyl ether ($\mathrm{Ra} = 20.99$), both solvents having higher cocrystal yields of 37% and 35.06%, respectively.

In the selection of solvent, the holding capacity should also be considered. This is because sometimes using the Hansen solubility parameter distance (Ra) may be misleading for determining solvent suitability, as it will give a low Ra value but nevertheless turn out be a poor solvent [30]. The holding capacity in this case refers to the solubility of oxalic acid in the solvents, which has been shown to have the second strongest correlation coefficient with caffeine-oxalic acid cocrystal yield (Table 4.11), so combining them together should give a better selection criterion. The Ra value has an inverse relationship with caffeine-oxalic acid cocrystal yield because the lower the Ra value the higher the expected cocrystal yield (Table 4.13) but the oxalic acid solubility has a linear relationship with caffeine-oxalic acid cocrystal yield (Table 4.12), combining both together for predicting caffeine-oxalic acid cocrystal yield will require dividing the Ra values in Table 4.13 by the oxalic acid solubility, which is shown in Table 4.14.

Comparing the calculated $\frac{\mathrm{Ra}}{\mathrm{Oxalic\ acid}}$ values with caffeine-oxalic acid cocrystal yield shows good agreement (Table 4.14). The lowest $\frac{\mathrm{Ra}}{\mathrm{Oxalic\ acid}}$ value of < 0.001 is observed for methanol with the highest cocrystal yield and the highest $\frac{\mathrm{Ra}}{\mathrm{Oxalic\ acid}}$ value of 35.92 is observed in DCM with the lowest cocrystal yield. The only solvent that does not fit the trend is acetic acid. This means that other factors aside from oxalic acid solubility and solvent affinity may be responsible for the higher than expected caffeine-oxalic acid cocrystal yield for acetic acid. Oxalic acid and acetic acid both have the same carboxylic acid functionality and similar molar volume of 50.8 cm^3 and 57.1 cm^3, respectively, which suggests that acetic acid may be able to play a further role of lowering the activation energy of the caffeine-oxalic acid cocrystal intermediate and increasing caffeine-oxalic acid cocrystal yield.

The $\frac{\mathrm{Ra}}{\mathrm{Oxalic\ acid}}$ values show better precision than oxalic acid solubility for predicting solvent cocrystallisation strength. Looking at Table 4.11, the oxalic acid solubility for tetrahydrofuran and isopropanol are 494.6 mg/g and 360.68 mg/g, respectively, but their cocrystal yields are 52% and 55.3%, so despite the significantly higher oxalic acid solubility in tetrahydrofuran compared to isopropanol the cocrystal yield is reversed. However, the $\frac{\mathrm{Ra}}{\mathrm{Oxalic\ acid}}$ values for tetrahydrofuran and isopropanol are very similar at 0.3, which when combined with the fact that isopropanol has a higher δ_H value, would give isopropanol the higher cocrystal yield, as is observed. Plotting the $\frac{\mathrm{Ra}}{\mathrm{Oxalic\ acid}}$ values against cocrystal yield in Table 4.14 but leaving out the values for DCM (because the $\frac{\mathrm{Ra}}{\mathrm{Oxalic\ acid}}$ is very large compared to the others) and acetic acid (because it has been shown that other factors are involved), the plot (Fig. 4.19) gives a correlation of determination of R^2 = 0.89, showing that 89% of the variation in caffeine-oxalic acid cocrystal yield can be explained with the $\frac{\mathrm{Ra}}{\mathrm{Oxalic\ acid}}$ value, and a correlation coefficient (r) of -0.94, showing a strong inverse relationship between $\frac{\mathrm{Ra}}{\mathrm{Oxalic\ acid}}$ and caffeine-oxalic acid cocrystal yield.

This correlation coefficient (r) is better than the correlation coefficient obtained for δ_H (0.78) and oxalic acid solubility (0.88) when the same rules i.e. excluding data for the DCM and acetic acid systems, are applied, suggesting that the $\frac{\mathrm{Ra}}{\mathrm{Oxalic\ acid}}$ is a better model for selecting solvents to achieve high caffeine-oxalic acid cocrystal yield than either oxalic acid solubility or δ_H. Plotting the Ra values in Table 4.13 against cocrystal yield (Fig. 4.20) gives a correlation of determination of R^2 = 0.64, showing that 64% of the variation in caffeine-oxalic acid cocrystal yield can be explained with the Ra value, and a correlation coefficient (r) of -0.80, showing that although a strong inverse relationship between Ra value and caffeine-oxalic acid cocrystal yield, the relationship is not as strong as $\frac{\mathrm{Ra}}{\mathrm{Oxalic\ acid}}$.

Calculating the $\frac{\mathrm{Ra}}{\mathrm{Caffeine}}$ value for caffeine (Table 4.15) and plotting this against caffeine-oxalic acid cocrystal yield and applying the same rules of excluding DCM and acetic acid data (Fig.4.20), the plot gives a coefficient of determination (R^2) = 0.18 and a correlation coefficient (r) of -0.43, both values are low and further confirms the fact that caffeine solubility does not play a significant role in caffeine-oxalic acid cocrystal yield in the anti-solvent/solvent mixture.

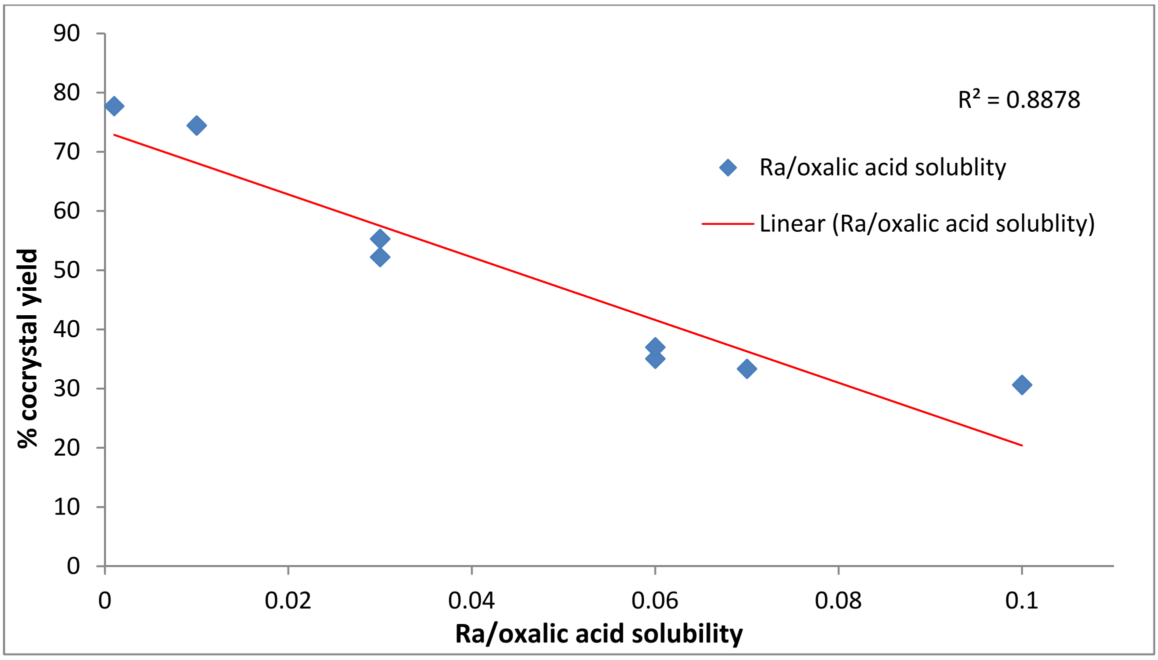

Fig. 4.19 Plot of Ra/oxalic acid solubility values against cocrystal yield.

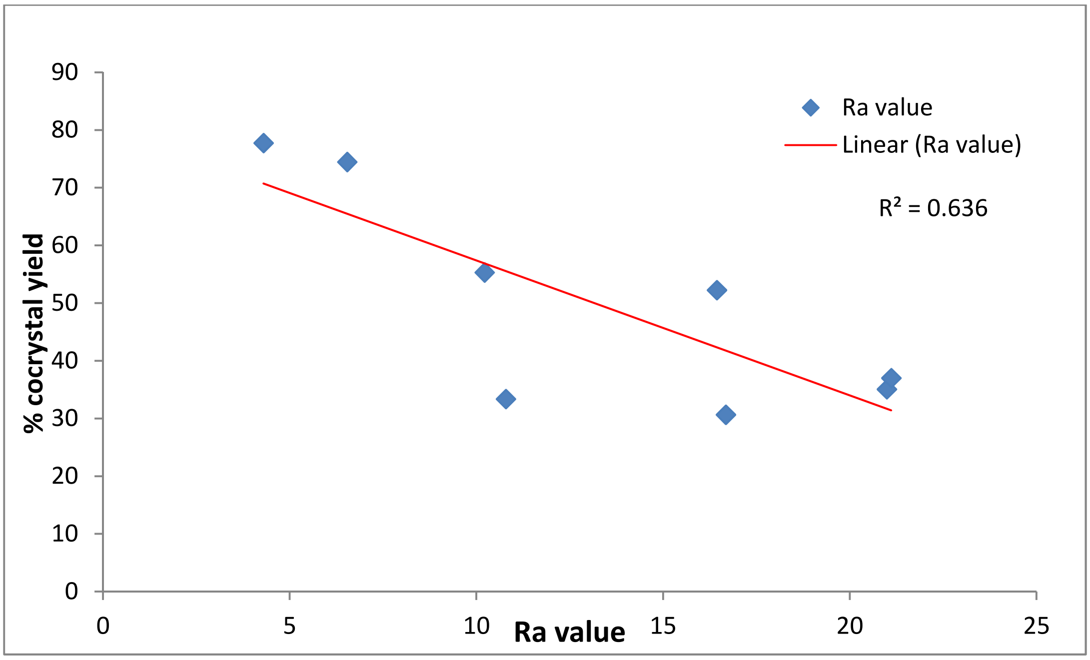

Fig. 4.20 Plot of Ra values against cocrystal yield.

Table 4.13 showing Ra values for oxalic acid and solvents.

Solvent	δ_D	δ_P	δ_H	$(\delta_{P2}-\delta_{P1})^2$	$(\delta_{H2}-\delta_{H1})^2$	$4(\delta_{D2}-\delta_{D1})^2$	Ra	Yield (%)
Methanol	15.1	12.3	22.3	4	0.09	14.44	4.30	77.73
Ethanol	15.8	8.8	19.4	30.25	6.76	5.76	6.54	74.45
Acetic acid	14.5	8	13.5	39.69	72.25	25	11.70	61.38
Isopropanol	15.8	6.1	16.4	67.24	31.36	5.76	10.22	55.3
Tetrahydrofuran	16.8	5.7	8	73.96	196	0.16	16.44	52.23
Methyl tert-butyl ether	13.7	3.5	5.1	116.64	285.61	43.56	21.11	37
Diethyl ether	14.5	2.9	5.1	129.96	285.61	25	20.99	35.06
Butanol	16	5.7	15.8	73.96	38.44	4	10.79	33.36
Acetonitrile	15.3	18	6.1	13.69	252.81	11.56	16.68	30.64
DCM	18.2	6.3	6.1	64	252.81	5.76	17.96	23.9
Oxalic acid	17	14.3	22					

Table 4.14 showing Ra/oxalic acid solubility values and for different solvents.

Solvent	Oxalic acid (mg/g)	δ_D	δ_P	δ_H	$(\delta_{P2} - \delta_{P1})^2$	$(\delta_{H2} - \delta_{H1})^2$	$4(\delta_{D2} - \delta_{D1})^2$	Ra	$\frac{\mathrm{Ra}}{\text{Oxalic acid}}$	Yield (%)
Methanol	1108.2	15.1	12.3	22.3	4	0.09	14.44	4.30	0.001	77.73
Ethanol	612	15.8	8.8	19.4	30.25	6.76	5.76	6.54	0.01	74.45
Acetic acid	77.5	14.5	8	13.5	39.69	72.25	25	11.70	0.15	61.38
Isopropanol	360.68	15.8	6.1	16.4	67.24	31.36	5.76	10.22	0.03	55.3
Tetrahydrofuran	494.6	16.8	5.7	8	73.96	196	0.16	16.44	0.03	52.23
Diethyl ether	337.5	14.5	2.9	5.1	129.96	285.61	25	20.99	0.06	35.06
Butanol	164	16	5.7	15.8	73.96	38.44	4	10.79	0.07	33.36
Acetonitrile	162.9	15.3	18	6.1	13.69	252.81	11.56	16.68	0.10	30.64
DCM	0.5	18.2	6.3	6.1	64	252.81	5.76	17.96	35.92	23.9
Oxalic acid		17	14.3	22						

Table 4.15 showing Ra/caffeine solubility values and for different solvents

Solvent	Caffeine (mg/g)	δ_D	δ_P	δ_H	$(\delta_{P2} - \delta_{P1})^2$	$(\delta_{H2} - \delta_{H1})^2$	$4(\delta_{D2} - \delta_{D1})^2$	$\frac{\mathrm{Ra}}{\mathrm{Caffeine}}$	Yield (%)
Methanol	13.3	15.1	12.3	22.3	19.36	86.49	77.44	1.02	77.73
Tetrahydrofuran	8.98	16.8	5.7	8	62.41	25	29.16	1.20	52.23
Acetonitrile	27.4	15.3	18	6.1	4.41	47.61	70.56	0.40	30.64
Acetic acid	23.9	14.5	8	13.5	14.44	0.25	100	0.45	61.38
DCM	65.1	18.2	6.3	6.1	1.69	47.61	6.76	0.12	23.9
Ethanol	6.9	15.8	8.8	19.4	19.36	40.96	54.76	1.55	74.45
Butanol	4.4	16	5.7	15.8	43.56	7.84	49	2.28	33.36
Methyl tert-butyl ether	1.6	13.7	3.5	5.1	51.84	62.41	134.56	9.86	37
Diethyl ether	0.8	14.5	2.9	5.1	16	62.41	100	16.70	35.06
Isopropanol	5.1	15.8	6.1	16.4	17.64	11.56	54.76	1.80	55.3
Caffeine		19.5	10.1	13					

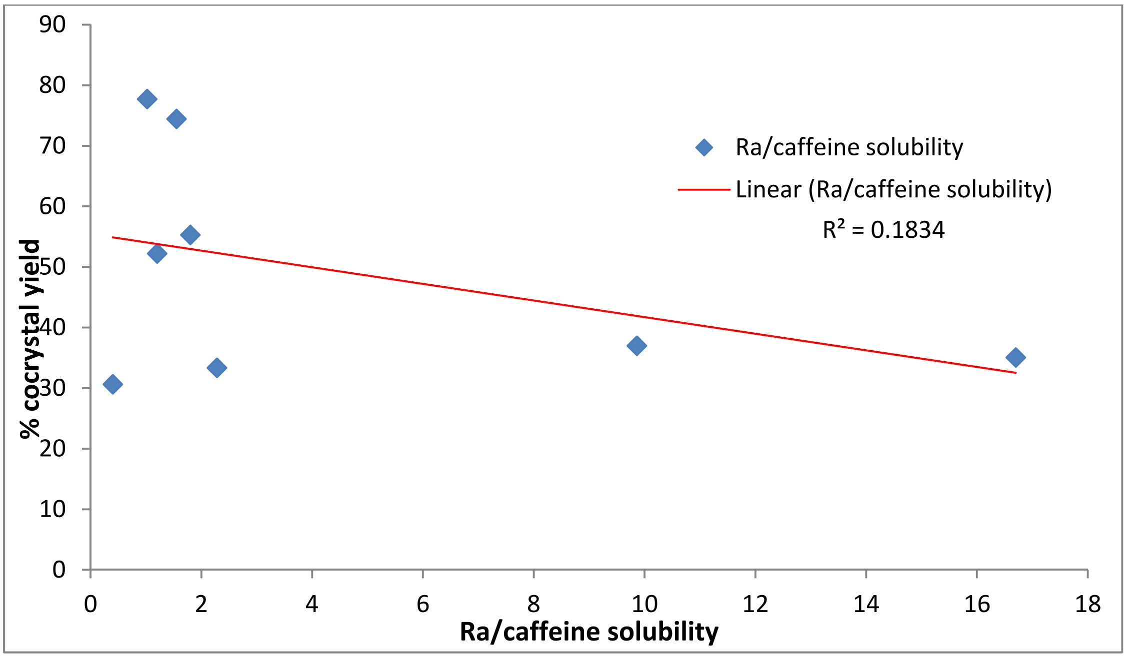

Fig. 4.21 Plot of Ra/caffeine solubility values against cocrystal yield.

Table 4.16 compares the correlation coefficient and coefficient of determinant for $\frac{\text{Ra}}{\text{Oxalic acid}}$, $\frac{\text{Ra}}{\text{Caffeine}}$, Ra , δ_H and oxalic acid solubility with cocrystal yield for anti-solvent/solvent cocrystallisation of caffeine-oxalic acid cocrystal. The $\frac{\text{Ra}}{\text{Oxalic acid}}$ parameter gives the highest correlation coefficient (r) of -0.94, and correlation of determination of R^2 = 0.89, of five parameters considered. The $\frac{\text{Ra}}{\text{Oxalic acid}}$ combines the oxalic acid solubility, Ra and δ_H into one parameter, which are the next three parameters of significance in terms of correlation coefficient and coefficient of determinant.

Table 4.16 Comparing statistical values for different models.

	$\frac{\text{Ra}}{\text{Oxalic acid}}$	$\frac{\text{Ra}}{\text{Caffeine}}$	Ra	δ_H	oxalic acid solubility
Correlation coefficient (r)	-0.94	-0.43	-0.80	0.78	0.88
Coefficient of determination (R^2)	0.89	0.18	0.64	0.61	0.78

For a solution-mediated cocrystallisation to occur between caffeine and oxalic acid; energy input is required to break the intermolecular bonding within caffeine and oxalic acid crystals and then the two solutes combine to form the cocrystal. This can be illustrated by the Eqns. 4.6 and 4.7. The square bracket implies the molecule is in solution.

$$A \rightleftharpoons [A] \quad \text{and} \quad B \rightleftharpoons [B] \text{ then} \quad \text{Eqn. 4.6}$$

$$[A] + [B] \leftrightharpoons AB \quad \text{Eqn. 4.7}$$

Favourable solvent-solute interaction will provide the required energy input for breaking the intermolecular bonds in caffeine and oxalic acid. Ra, the Hansen solubility parameter distance, is a measure of this. A low Ra between coformer/API and solvent anti-solvent/solvent mixture means good miscibility and more favourable solvent-solute interaction to compensate for the energy required to break the intermolecular bonds in the solid caffeine and oxalic acid. This will push the equilibrium in Eqn. 4.6 towards the right.

A solvent with high holding capacity will result in high levels of API or coformer solute in the system. This will push the equilibrium in Eqn. 4.7 towards the right, resulting in formation of cocrystal.

The free energy of solubilisation is give by Eqn. 4.8

$$\Delta G_{solution} = \Delta G_{lattice} + \Delta G_{solvation} \quad \text{Eqn. 4.8}$$

Solubility depends on $\Delta G_{lattice}$ of the solid to be dissolved. In the caffeine-oxalic acid cocrystal system, oxalic acid is more crystalline than caffeine, and so its dissolution would be expected to require more energy than that of the more amorphous caffeine, in which the intermolecular bonding is not optimised and so likely to be weaker. This explains why oxalic acid solubility has a stronger correlation with cocrystal yield than caffeine; and why $\frac{\mathrm{Ra}}{\mathrm{Oxalic\ acid}}$ has a stronger correlation than $\frac{\mathrm{Ra}}{\mathrm{Caffeine}}$.

4.3.4 Nucleation rate

The rates of nucleation observed in the anti-solvent/solvent mixture experiments were fast with ≈48% phase transformation observed after 5 minutes as determined by ^{13}C SSNMR (Table 4.4).This cocrystallisation rate is similar to that observed in solvent slurry cocrystallisation, where a new cocrystal phase was observed by PXRD after 1 minute[1] but faster than solution evaporation cocrystallisation, which can take hours or days to observe a new cocrystal phase[37]. The nucleation rate for crystallisation ($\mathcal{J}$) is related to the rate of attachment ($\mathcal{W}$) onto the critical nuclei and the concentration of critical nuclei $[n]$ of the crystallising species (Eqn. 4.9). $[n]$ is proportional to the concentration of the crystallising species in the solvent phase.

$$\mathcal{J} = \mathcal{W}[n]e^{\left(\frac{-\Delta G^*}{\mathrm{KT}}\right)} \qquad \text{Eqn. 4.9}$$

The Gibbs energy (ΔG^*) of nucleation can be expressed in terms of supersaturation ($\Delta\mu$) and the interfacial energy (γ) as shown in Eqn. 4.1. The relationship between the rate of nucleation ($\mathcal{J}$), the interfacial energy (γ) and supersaturation ($\Delta\mu$) is given by Eqn. 4.10.

$$\mathcal{J} = \mathcal{W}[n]e^{\left(\frac{-16\pi\gamma^3 v_c^2}{3\Delta\mu^2 \mathrm{KT}}\right)} \qquad \text{Eqn. 4.10}$$

From Eqn. 4.10, the nucleation rate $\mathcal{J}$ increases with increasing values of $[n]$, $\mathcal{W}$ and the exponential term ($e^{\left(\frac{-16\pi\gamma^3 v_c^2}{3\Delta\mu^2 \mathrm{KT}}\right)}$). The low solubility of the caffeine, the oxalic acid and the cocrystal in the anti-solvent/solvent mixture, determined by HPLC and shown in Tables 4.8 and 4.17, should result in a low $[n]$ value and hence a low nucleation rate ($\mathcal{J}$). However, if the solubility of the caffeine-oxalic acid cocrystal is lower than that of oxalic acid and caffeine, then a solution saturated in oxalic acid and caffeine, such as occurs in our slurry cocrystal experiments, would give a high degree of supersaturation ($\Delta\mu$) for the cocrystal, leading to a large exponential term and hence a higher nucleation rate ($\mathcal{J}$). Given that adding a small percentage of solvent to the cyclohexane anti-solvent has been shown to significantly increase the cocrystal yield rate (see Table 4.4), this suggests that the low solubility of the cocrystal components in the solvent/anti-solvent mixture is not seriously limiting the ability to obtain high cocrystal yield rates in reasonable timescales of minutes to hours.

Table 4.17 Solubility of cocrystal determined by monitoring caffeine and oxalic acid by HPLC.

	Caffeine (mg/g)		Oxalic Acid (mg/g)	
Sample	**Average**	**S. E**	**Average**	**S.E**
Caffeine/oxalic acid in 2.2% methanol in cyclohexane	<LOD*		<LOD*	
Caffeine/oxalic acid in 2.2% ethanol in cyclohexane	<LOD*		<LOD*	
Caffeine/oxalic acid in 2.2% IPA in cyclohexane	<LOD*		0.251	0.001

*Limit of detection (LOD) = 0.001 mg/g

In slurry cocrystallisation, there is also an increased probability of heterogeneous nucleation[38] occuring. Heterogeneous nucleation reduces the interfacial energy (γ) for nucleation and further increases the exponential term in Eqn. 4.10. Heterogeneous nucleation also results in the reduction of the critical nucleus size (r^*) for nucleation; the relationship between the critical nucleus size (r^*), interfacial energy (γ) and supersaturation (Δμ) is given by Eqn. 4.11.

$$r^* = \frac{2\gamma v_c}{\Delta\mu} \qquad \text{Eqn. 4.11}$$

The lowering of the interfacial energy of nucleation (γ) between heterogeneous and homogeneous nucleation is represented by the wetting factor ($\mathcal{F}(\theta)$) which varies between 0 (for perfect wetting) and 1 (for no wetting, i.e. heterogeneous nucleation doesn't occur, so the nucleation must be homogeneous, or occur on a different substrate with $\mathcal{F}(\theta) < 1$) as given in Eqn. 4.12.

$$\mathcal{F}(\theta) = \frac{2 - 3\cos\theta + \cos^3\theta}{4} \qquad \text{Eqn. 4.12}$$

where θ is the contact angle between the nucleus and substrate onto which it is adsorbed.

The rate of nucleation ($\mathcal{J}$) for a heterogeneous nucleation is given by

$$\mathcal{J} = \mathcal{W}[n]e^{\left(\frac{-16\pi\gamma^3 v_c^2 \mathcal{F}(\theta)}{3\Delta\mu^2 \mathrm{KT}}\right)} \qquad \text{Eqn. 4.13}$$

From Eqn. 4.13, a high supersaturation (Δμ) and a low value for the wetting function($\mathcal{F}(\theta)$) both increase the nucleation rate ($\mathcal{J}$). Given the large amount of solid interfacial area available in the slurry cocrystal experiments, it is highly likely that heterogeneous nucleation occurs. This, together with the likely high values for supersaturation, can sufficiently increase the value of the exponential term thereby compensating for the low value of $[n]$ expected.

4.3.5 Particle size distribution (PSD)

The caffeine-oxalic acid cocrystal particle sizes obtained from the anti-solvent/solvent mixture (Fig. 4.22) were smaller than crystal particle size obtained from slurry cocrystallisation in 100% methanol (Fig. 4.24) or from solution cocrystallisation (Fig. 4.26) from water, the difference in crystal particle sizes is likely to be due to a larger nucleation rate in the anti-solvent/solvent slurry cocrystallisation system due to a smaller critical nucleus size. The critical nucleus size for nucleation (r^*) is related to the supersaturation ($\Delta\mu$) by Eqn.4.8; the smaller particle size from the anti-solvent/solvent mixture can be as a result of the higher level of caffeine-oxalic acid cocrystal supersaturation ($\Delta\mu$) attained in the mixture compared to slurry cocrystallisation in 100% methanol or solution cocrystallisation in water. A high level of supersaturation results in a large number of precipitating nuclei which depletes the solution mass of solute necessary for crystal growth; hence nucleation is faster than crystal growth under the anti-solvent/solvent mixture compared to the two cocrystallisation approach.

Caffeine-oxalic acid cocrystal particles from the anti-solvent/solvent slurry cocrystallisation (Fig. 4.22) form agglomerates but the crystal particle size are much smaller than crystal particles obtained from slurry cocrystallisation in 100% methanol (Fig. 4.24) and solution cocrystallisation from water (Fig. 4.26). All three samples showed very high levels of cocrystallisation by SSNMR (Figs. 4.23, 4.25 and 4.27).

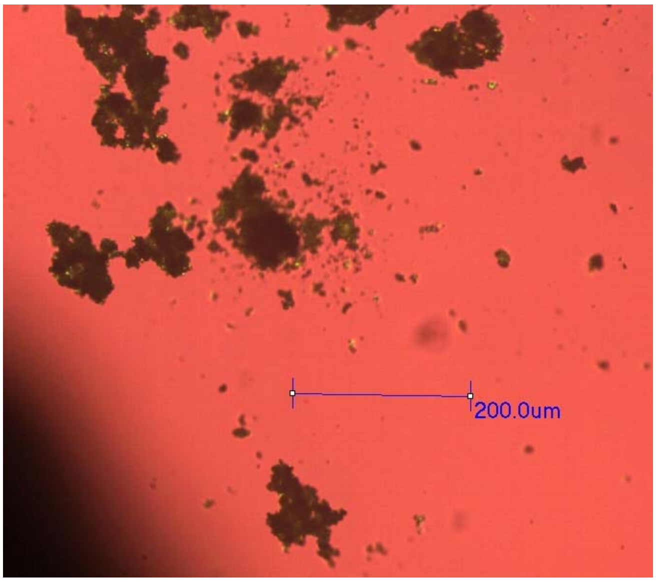

Fig. 4.22 Caffeine-oxalic acid cocrystal from 7% solid loading in 2.2 wt % methanol in cyclohexane.

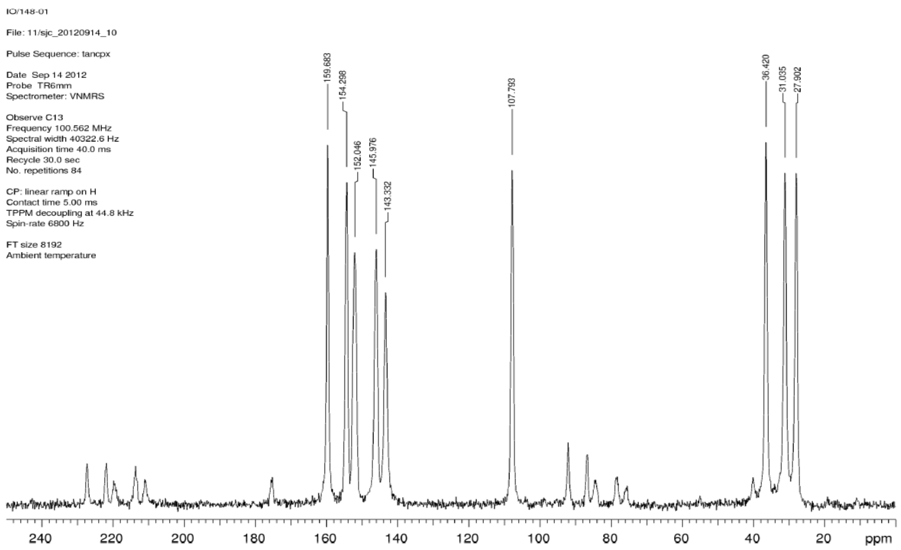

```
IO/148-01

File: 11/sjc_20120914_10

Pulse Sequence: tancpx

Date  Sep 14 2012
Probe  TR6mm
Spectrometer: VNMRS

Observe C13
Frequency 100.562 MHz
Spectral width 40322.6 Hz
Acquisition time 40.0 ms
Recycle 30.0 sec
No. repetitions 84

CP: linear ramp on H
Contact time 5.00 ms
TPPM decoupling at 44.8 kHz
Spin-rate 6800 Hz

FT size 8192
Ambient temperature
```

Fig. 4.23 SSNMR spectra of caffeine-oxalic acid cocrystal from 7% solid loading in 2.2 *wt* % methanol in cyclohexane.

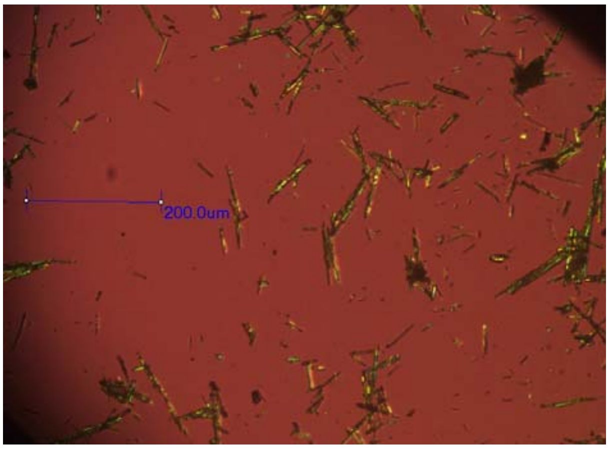

Fig. 4.24 Caffeine-oxalic acid cocrystal from 7% solid loading in 100% methanol.

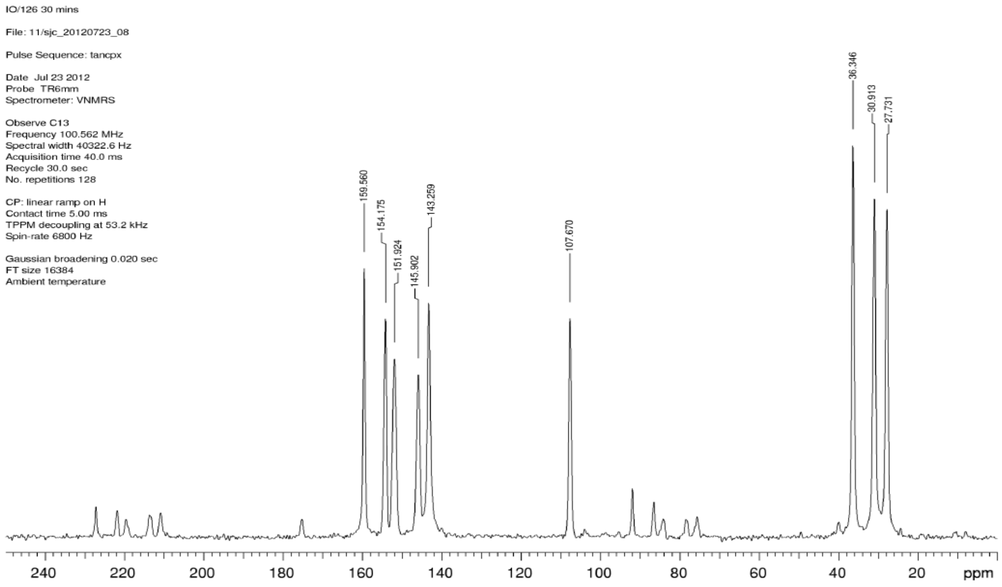

```
IO/126 30 mins

File: 11/sjc_20120723_08

Pulse Sequence: tancpx

Date  Jul 23 2012
Probe  TR6mm
Spectrometer: VNMRS

Observe C13
Frequency 100.562 MHz
Spectral width 40322.6 Hz
Acquisition time 40.0 ms
Recycle 30.0 sec
No. repetitions 128

CP: linear ramp on H
Contact time 5.00 ms
TPPM decoupling at 53.2 kHz
Spin-rate 6800 Hz

Gaussian broadening 0.020 sec
FT size 16384
Ambient temperature
```

Fig. 4.25 SSNMR of caffeine-oxalic acid cocrystal from 7% solid loading in 100% methanol.

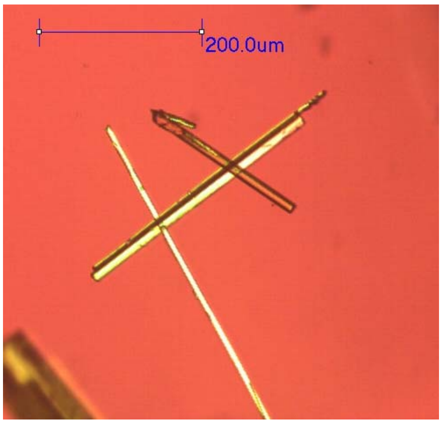

Fig. 4.26 Caffeine-oxalic acid cocrystal solution cocrystallisation from water.

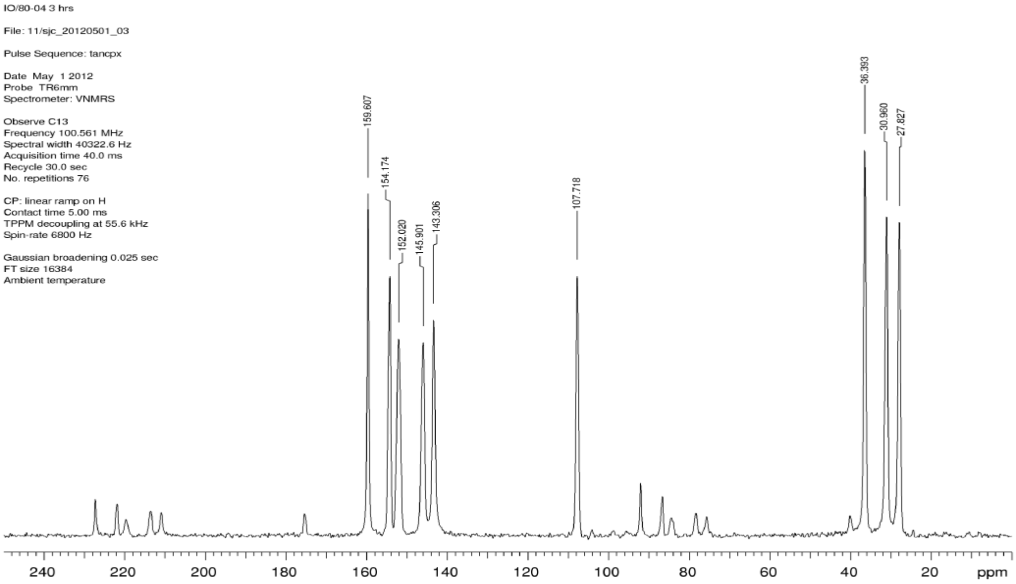

Fig. 4.27 SSNMR spectra of caffeine-oxalic acid cocrystal solution cocrystallisation from water.

A sieve test was used to determine the particle size distribution (PSD) for the caffeine-oxalic acid slurry cocrystallisation experiments in 100% methanol and 2.2 wt % methanol in cyclohexane (Table 4.18) and the PSD were compared using a histogram. The first set from the slurry caffeine-oxalic acid cocrystallisation (100% methanol and 2.2 wt % methanol in cyclohexane) was done using normal particle size caffeine and oxalic acid (Fig. 4.28), while the second set of caffeine-oxalic acid slurry cocrystallisation was done using caffeine and oxalic acid with particle sizes lower than 106 µm (both reagents were sieved through a 106 µm sieve prior to reaction). The second set of experiments was to eliminate the impact of variability in PSD that may be in the cocrystal components; the solid loadings for both experiments were the same (Fig. 4.29). In both histograms the PSD for the pure methanol cocrystallisation shows a higher proportion of large crystal sizes compared to the anti-solvent/solvent cocrystallisation.

The mean of the PSD's for the 4 experiments are shown in the last column of Table 4.19; the mean of each sieve test was determined by multiplying the median of each mesh range by the percent (%) compositions of each sieve test and summing this up, the lower and upper limit were used for the above 1 mm and below 105 µm range, respectively. The mean value for the slurry caffeine-oxalic acid cocrystallisation in 100% methanol is ≈2.3 times the mean value for experiments in 2.2 wt % methanol in cyclohexane.

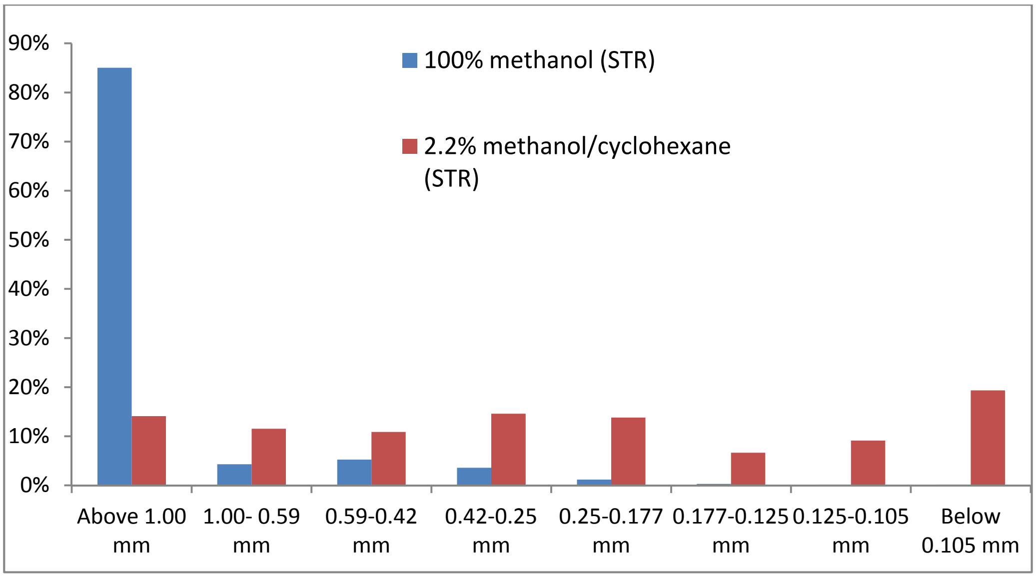

Fig. 4.28 Histogram of particle size distribution comparing methanol and cyclohexane/methanol cocrystallisation of caffeine-oxalic acid in STR.

Particle size distribution (PSD) is an important parameter in the pharmaceutical industry. Small particle size increases the surface area of an API thereby enhancing its dissolution rate[39,40], increase bioavailability[40,41] and reduces the API bulk density making it easier to handle. Consistent, reproducible particle size distribution is required for new drug registration with the food and drug administration (FDA) and needs to be controlled during large scale manufacture[42]. Failure to achieve the right particle size distribution results in the need for a secondary processing method e.g. crushing, milling etc., which may have a negative impact on the stability of the drug molecule. The Nernst-Brunner[40] (Eqn. 4.14) equation gives the relationship between surface area (S) and dissolution rate ($\frac{dC}{dt}$).

$$\frac{dC}{dt} = \frac{DS}{Vh}(C_s - C) \qquad \text{Eqn. 4.14}$$

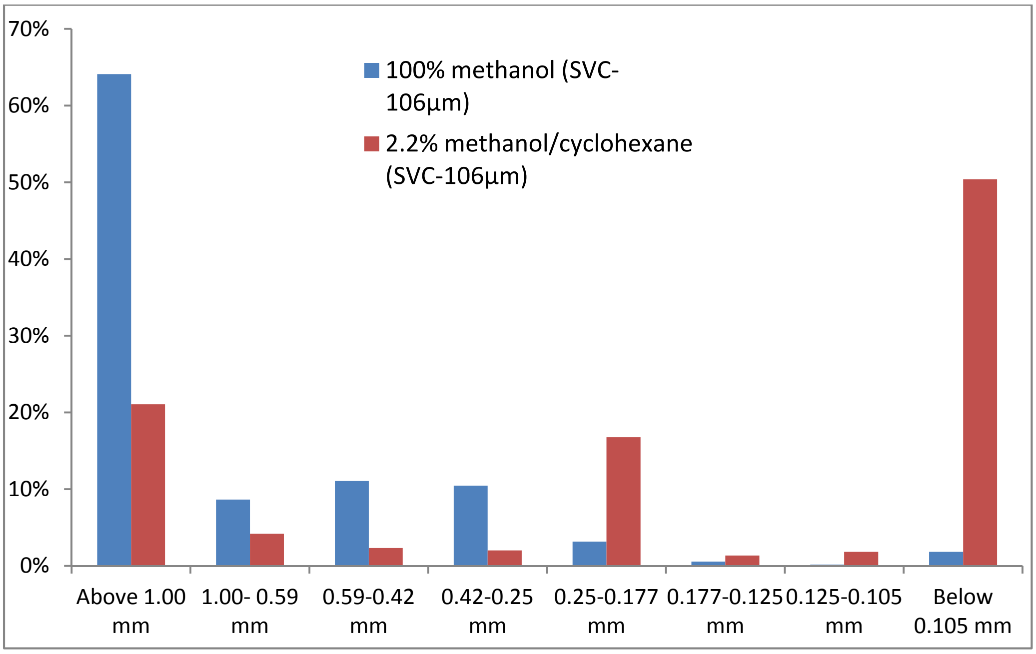

Fig. 4.29 Histogram of particle size distribution comparing methanol and cyclohexane/methanol cocrystallisation of caffeine-oxalic acid in SVC.

where D is the diffusion coefficient, V is the volume of the dissolution medium, h is the thickness of the diffusion layer on the surface of the solid, C_s is the saturation solubility of the solid and C is the instantaneous concentration of the solute.

Controlling particle size distribution during crystallisation is a challenge because it is influenced by many factors e.g. agglomeration, Ostwald ripening, depletion of supersaturation, hydrodynamics, viscosity, crystal attrition by stirrer blades etc.[43,44]. The use of an anti-solvent in crystallisation in the pharmaceutical industry is not new, but often the anti-solvent is added last[45,46] to induce supersaturation. An anti-solvent precipitation method is dependent on the efficiency of the mixing in the system, residence time, and supersaturation[46,47]. Mixing refers to the time it takes for the anti-solvent to be uniformly distributed in the solvent phase (τ_{mix}). Another factor relevant to anti-solvent precipitation is the time delay for precipitation to occur ($\tau_{precipitation}$) either via coagulation or condensation (crystal growth)[48]; the ratio of both these factors (Eqn. 4.15) is called the Damkohler number (Da)[43,44], which is dimensionless.

$$Da = \frac{\tau_{mix}}{\tau_{precipitation}} \qquad \text{Eqn. 4.15}$$

Table 4.18 Particle size distribution from sieve test.

	Above 1.00 mm	1.00- 0.59 mm	0.59-0.42 mm	0.42-0.25 mm	0.25-0.177 mm	0.177-0.125 mm	0.125-0.105 mm	Below 0.105 mm
100% methanol (STR)	85.02%	4.31%	5.25%	3.59%	1.17%	0.31%	0.18%	0.18%
100% methanol (SVC-106μm)	64.10%	8.65%	11.07%	10.46%	3.16%	0.56%	0.16%	1.84%
2.2% methanol/cyclohexane (STR)	14.10%	11.53%	10.87%	14.60%	13.81%	6.64%	9.12%	19.33%
2.2% methanol/cyclohexane (SVC-106μm)	21.07%	4.18%	2.34%	2.03%	16.77%	1.36%	1.84%	50.39%

Table 4.19 Calculating the average particle size for sieve test.

Median of sieve mesh	1 mm	0.795 mm	0.505 mm	0.335 mm	0.214 mm	0.151 mm	0.115 mm	0.105 mm	Total
100% methanol (STR)	0.8502	0.0343	0.0265	0.0120	0.0025	0.0005	0.0002	0.0002	0.9264
100% methanol (SVC-106μm)	0.6410	0.0688	0.0559	0.0350	0.0068	0.0008	0.0002	0.0019	0.8104
2.2% methanol/cyclohexane (STR)	0.1410	0.0917	0.0549	0.0489	0.0296	0.0100	0.0105	0.0203	0.4068
2.2% methanol/cyclohexane (SVC-106μm)	0.2107	0.0332	0.0118	0.0068	0.0359	0.0021	0.0021	0.0529	0.3555

Anti-solvent addition creates local regions of very high supersaturation and so the metastable zone is crossed quickly. Under this condition, nucleation is favoured over crystal growth, resulting in smaller particle sizes[49]; this condition is obtained for values of Da < 1 when the mixing time (nucleation) is less than the precipitation induction time (crystal growth). In a situation where the system mixing is inefficient and the anti-solvent takes time to become uniformly distributed, regions of high supersaturation are created by the anti-solvent resulting in localised nucleation leaving the system reasonably rich in solute; crystal growth becomes significant but unevenly dispersed, more concentrated in regions with low local nucleation and less in regions of high local nucleation, this distorts the particle size distribution of the isolated crystals and can affect down-stream processing of the solids. In addition, if too high local supersaturation values occur, the resulting crystals can be poorly crystalline and contain impurities, because the nucleation rate is so high that crystal growth is still favourable on defective and impure surfaces, so that these defective features are locked into the final crystal form. Consequently, anti-solvent addition, although it can provide small crystal sizes, can lead to a poorer crystal product.

In contrast, in the anti-solvent/solvent mixture slurry cocrystallisation method, the solvent mixing time τ_{mix}= 0 with regards to nucleation because the anti-solvent and solvent is completely mixed prior to the introduction of the API and coformer. Consequently, variations in the supersaturation level throughout the sample are reduced, Da < 1 is reproducible and τ_{mix} only depends on the rate of solid addition, which can be better controlled. When the anti-solvent is added post introduction of API and coformer as is usually the case, attaining τ_{mix} = 0 becomes a challenge and the value of Da is not easily reproducible unless with very efficient mixing. What this suggests is that variation in particle size distribution batch to batch should be minimal in the anti-solvent/solvent slurry cocrystallisation system.

4.3.5.1 Solvent influence on particle size distribution (PSD)

Four caffeine/oxalic acid SVC cocrystallisation experiments were carried out with different solvents and the crystals then sieved to determine the particle size distribution (PSD). The PSD for the samples are tabulated in Table 4.20 and represented as a histogram (Fig. 4.30).

Table 4.20 Sieve test results for particle size distribution

	Above 1.00 mm	1.00- 0.59 mm	0.59-0.42 mm	0.42-0.25 mm	0.25-0.177 mm	0.177- 0.125 mm	0.125-0.105 mm	Below 0.105 mm
SVC-Methanol in cyclohexane	24.40%	14.10%	11.20%	12.70%	9.20%	4.20%	4.70%	19.60%
SVC-Butanol in cyclohexane	13.80%	9.70%	9.00%	11.00%	11.20%	7.70%	6.10%	31.60%
SVC-DCM in cyclohexane	21.90%	10.70%	6.80%	9.50%	10.80%	6.20%	6.40%	27.80%

Table 4.21 Calculating the mean of the sieve test group distribution.

	Above 1.00 mm	1.00- 0.59 mm	0.59-0.42 mm	0.42-0.25 mm	0.25-0.177 mm	0.177- 0.125 mm	0.125-0.105 mm	Below 0.105 mm
Median of sieve mesh	1 mm	0.795 mm	0.505 mm	0.335 mm	0.214 mm	0.151 mm	0.115 mm	0.105 mm
SVC-Methanol in cyclohexane	0.244	0.112095	0.05656	0.042545	0.019688	0.006342	0.005405	0.02058
SVC-Butanol in cyclohexane	0.138	0.077115	0.04545	0.03685	0.023968	0.011627	0.007015	0.03318
SVC-DCM in cyclohexane	0.219	0.085065	0.03434	0.031825	0.023112	0.009362	0.00736	0.02919

The mean sieve mesh range, the standard deviation (s) and the coefficient of variance (CV) of the four experiments were calculated to check for reproducibility in particle size distribution, with a low coefficient of variance (CV) indicating good reproducibility of particle size. The mean of each sieve test was determined by multiplying the median of each mesh range by the % composition of each sieve test and summing this up (Table 4.21), the lower and upper limit were used for the above 1 mm and below 105 µm range, respectively. The standard deviation (s) and coefficient of variance (CV) were calculated using Eqn. 4.16 and 4.17. The calculations are illustrated in Tables 4.20, 4.21 and 4.22.

$$s = \sqrt{\frac{\sum(\mathcal{X}_{\mathrm{i}}-\bar{\mathcal{X}})^2}{n-1}} \qquad \text{Eqn. 4.16}$$

$$\mathrm{CV} = \frac{s}{\bar{x}} \times 100 \qquad \text{Eqn. 4.17}$$

In Table 4.22, $\mathcal{X}_{\mathrm{i}}$ denotes the mean for each sieve test and $\bar{\mathcal{X}}$ (0.44 mm) denotes the average of the means for the three sieve test. The standard deviation (s) of the three sieve test is 0.067 mm and the coefficient of variance (CV) = 15.23%; the coefficient of variance (CV) value of 15.23%, though greater than 10%, is not too much higher, suggesting that the reproducibility of particle size distribution although not precise is not too poor for the three solvents in the anti-solvent/solvent slurry cocrystallisation. The particle size distributions for the three cocrystallisation experiments are shown as a histogram in Fig. 4.30.

Table 4.22 Standard deviation calculation for three sieve test.

	$\mathcal{X}_{\mathrm{i}}$ (mm)	$(\mathcal{X}_{\mathrm{i}}-\bar{\mathcal{X}})^2$	s	CV
SVC-Methanol in cyclohexane	0.507	4.532E-03	0.067 mm	15.23%
SVC-Butanol in cyclohexane	0.373	4.447E-03		
SVC-DCM in cyclohexane	0.439	4.062E-07		
$\sum(\mathcal{X}_{\mathrm{i}}-\bar{\mathcal{X}})^2$		8.980E-03		

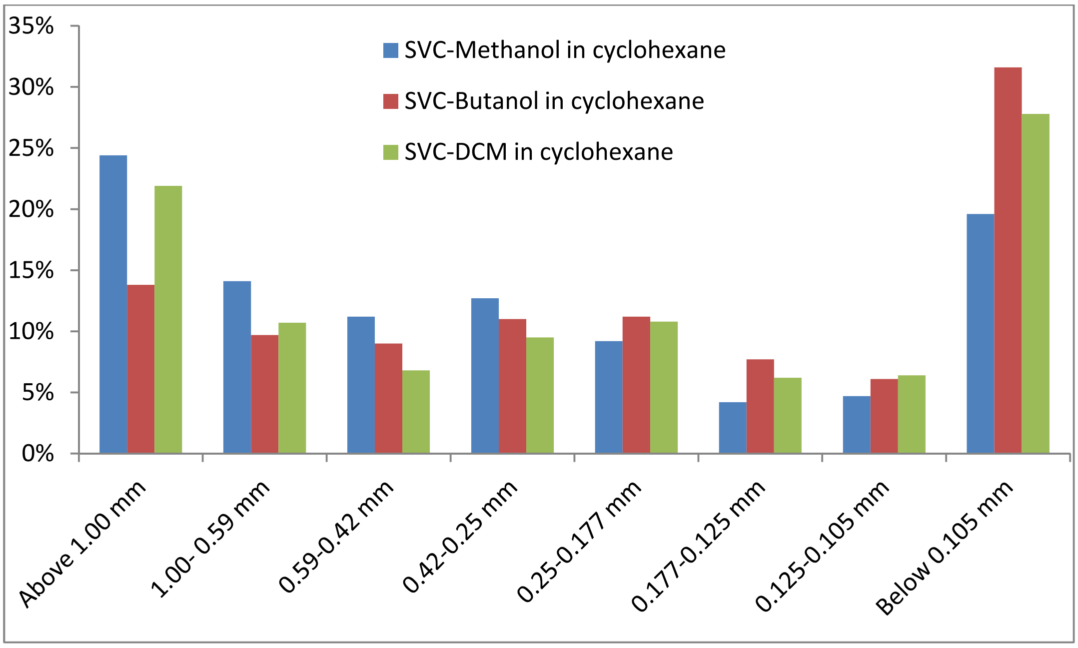

Fig 4.30 Histogram of particle size distribution for three different solvent in SVC caffeine-oxalic acid cocrystallisation experiments.

4.3.5.2 Effect of anti-solvent on particle size distribution (PSD)

Caffeine/oxalic acid cocrystallisation experiments with a solid loading of 23% were carried out in three different anti-solvents: cyclohexane, hexane and dodecane (Table 4.23). The isolated solids from the experiments were sieved to investigate the influence of anti-solvent on the PSD. Caffeine/oxalic acid cocrystallisation experiments were carried out with 2.2wt % methanol in the three different anti-solvents. The mean $\bar{X}$ = 0.642 mm, represents the average mean for the three sieve test. The standard deviation (s) = 0.106 mm and the coefficient of variance (CV) = 16.58% are shown in Table 4.24 and 4.25, while the histogram for the PSD of the three anti-solvent experiments is illustrated in Fig. 4.31.

The CV of 16.58% (Table 4.25) for the anti-solvent cocrystallisation is similar to the CV (15.23%) for the different solvent in cyclohexane (Table 4.22). The CV is higher than 10%, so the reproducibility of the particle size for the three anti-solvent experiments is poor.

The anti-solvent consists of a large proportion of the liquid phase in the slurry cocrystallisation experiments, whereas there is limited amount of the solvent (2.2 wt %). It would be of interest to investigate how changing the anti-solvent influences the PSD of the isolated solids. The caffeine-oxalic acid cocrystal yields for the three experiments were: 82%-methanol in hexane, 77%-methanol in cyclohexane and 57%-

methanol in dodecane. Looking at the mean particle size distributions for each experiment (Table 4.25), the trend observed is dodecane PSD > cyclohexane PSD > hexane PSD. The viscosity of the anti-solvent used in the cocrystallisation experiment was investigated using correlation analysis to check for any interdependency between viscosity and the observed mean particle size distribution (Table 4.26). The viscosities of the anti-solvents are: hexane = 0.292 mPa.s, cyclohexane = 0.898 mPa.s and dodecane = 1.34 mPa.s.

Table 4.23 PSD for 23% SVC cocrystallisation with three anti-solvent.

	Above 1 mm	1 mm-600 µm	600 -425 µm	425-106 µm	Below 106 µm
Methanol in cyclohexane	46.10%	10.90%	5.40%	33.90%	3.70%
Methanol in hexane	23.70%	14.00%	7.00%	50.50%	4.80%
Methanol in dodecane	53.20%	11.90%	5.90%	26.90%	2.20%

Table 4.24 Calculating the mean of the sieve test group distribution

	Above 1 mm	1 mm-600 µm	600 -425 µm	425-106 µm	Below 106 µm
Median	1.000	0.800	0.513	0.266	0.106
Methanol in cyclohexane	0.461	0.087	0.028	0.090	0.004
Methanol in hexane	0.237	0.112	0.036	0.134	0.005
Methanol in dodecane	0.532	0.095	0.030	0.072	0.002

Table 4.25 Standard deviation and RSD calculation for anti-solvent experiments.

	$\mathcal{X}_i$ (mm)	$(\mathcal{X}_i - \bar{\mathcal{X}})^2$	s (mm)	CV
Methanol in cyclohexane	0.670	0.0008	0.106	16.58%
Methanol in hexane	0.524	0.0138		
Methanol in dodecane	0.731	0.0080		
$\sum(\mathcal{X}_i - \bar{\mathcal{X}})^2$		0.0226		

Table 4.26 Coefficient of correlation for anti-solvent viscosity and PSD

Viscosity (mPa.s)	Mean (mm)	Correlation coefficient
0.292	0.524	0.99
0.898	0.67	
1.34	0.731	

The correlation coeffiecient (r) for the viscosity and mean particle size distribution = 0.99, this is very close to 1 and indicates that there exists a strong linear interdepency between the viscosity of the anti-solvent used in the cocrystallisation experiment and the mean particle size distribution obtained from the sieve test. Plotting a scatter plot of anti-solvent viscosity and mean particle size (Fig.4.32), a coefficient of determination (R^2) of 0.98 is obtained from the scatter plot and shows that 98% of the variability in particle size distribution is explained by the anti-solvent viscosity.

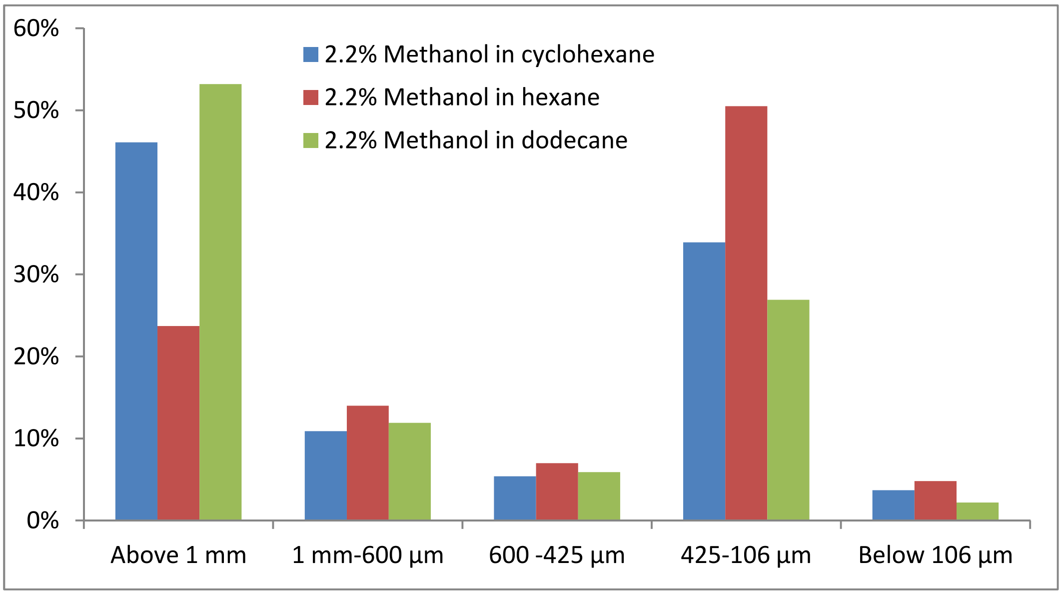

Fig. 4.31 Histogram of particle size distribution for different anti-solvent of caffeine-oxalic acid SVC cocrystallisation experiments.

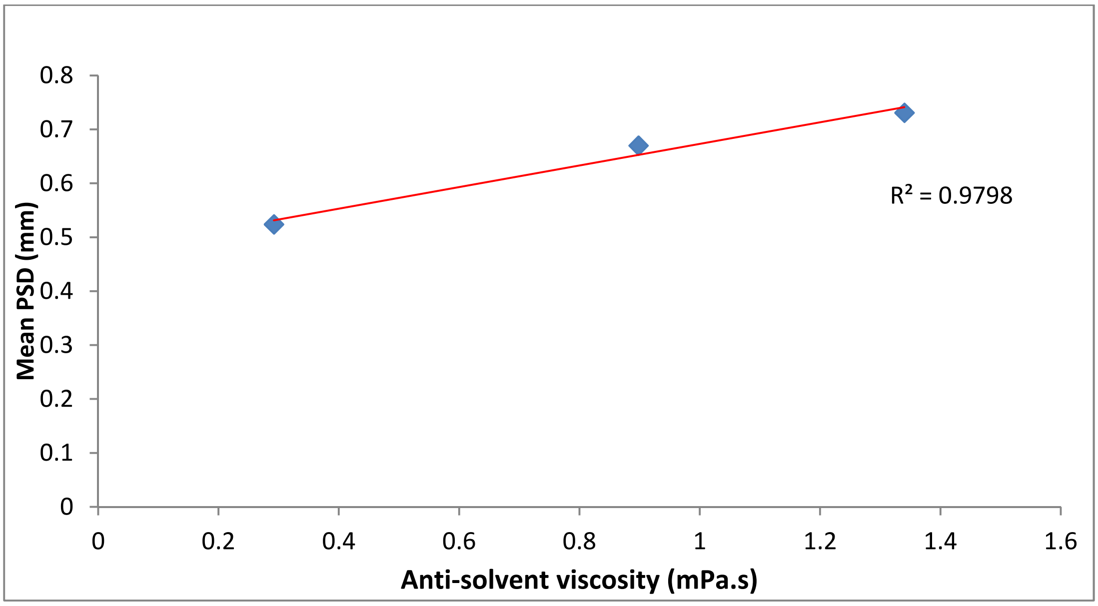

Fig. 4.32 Scatter plot of mean particle size distribution against viscosity of anti-solvent.

The rate of attachment of solute unto the growing cluster ($\mathcal{W}$) in crystal nucleation has an inverse relationship with the viscosity (η) of the liquid phase in which the solute are dissolved in. This relationship is shown in Eqn. 4.18, a higher viscosity of the medium results in a lower attachment rate of solute unto the growing cluster and so reduces the nucleation rate ($\mathcal{J}$) [35,50] (this is shown in Eqn. 4.9). This lower nucleation rate results in a larger crystal particle size because there are fewer nuclei available for crystal growth. The viscosity of the anti-solvent/solvent mixture is determined by the anti-solvent because it accounts for up to 97% of the mixture.

$$\mathcal{W} = \frac{\mathrm{kT}}{3\pi a_0^3 \eta} \qquad \text{Eqn. 4.18}$$

where η is the viscosity of the liquid phase, a_0 is the mean diameter of the diffusing solute, k is the Boltzmann constant and T is temperature.

The proportion of large particles should increase with increasing viscosity of the anti-solvent as predicted in Eqn. 4.18.

However, another possible explanation for the observed trend in particle size distribution (Table 4.26) may be the change in solubility of the caffeine-oxalic acid cocrystal and its components in the different anti-solvents used in the investigation, and so this was tested. The variation in solubility of caffeine in cyclohexane and dodecane was found to be very little, whilst the solubility of oxalic acid in cyclohexane and dodecane below the 0.001 mg/g limit of the detection (LOD) of the HPLC (Table 4.27). Consequently, the influence of change in solubility on PSD can be discounted, and the increase in PSD with viscosity can be linked with the lower rate of nucleation that arises.

Table 4.27 HplcSolubility determination by HPLC for caffeine, oxalic acid in cyclohexane and dodecane

	Caffeine (mg/g)		Oxalic Acid (mg/g)	
Anti-solvent	Average	S. E	Average	S.E
Cyclohexane	0.053	0.001	<LOD*	
Dodecane	0.072	0.001	<LOD*	

*Limit of detection (LOD) = 0.001 mg/g

4.4 Comparing the SVC and batch-stirred cocrystallisation reaction

One advantage for adopting the oscillatory baffle technology (SVC) for the cocrystallisation scale up is that scaling up of this process is linear and so the well-known challenges of replicating laboratory conditions for mixing and heat removal associated with batch stirred reactors are avoided in the oscillatory baffle reactor[51]. The SVC approach also provides an opportunity for continuous cocrystal manufacture, which is difficult to achieve with batch stirred reactors[52]. To assess whether there are other advantages of using the SVC compared to batch cocrystallisations, this section compares caffeine-oxalic acid cocrystallisation experiments carried out in the SVC and stirred batch reactor.

4.4.1 Cocrystallisation yield

The cocrystal yields for caffeine-oxalic acid slurry cocrystal experiments in methanol/cyclohexane mixture were compared for the batch stirred and SVC reactors. The comparisons included experiments at $23\,wt\,\%$ and $7\,wt\,\%$ solid loading, 0% - 2.2% methanol in cyclohexane content and 30 minutes and 180 minutes reaction time (Table 4.28). In 6 out of the 7 experiments considered, caffeine-oxalic acid cocrystal yields in the SVC experiments were better than in the corresponding batch stirred experiments. The observed higher yield in SVC experiments may be as a result of the better mixing that is achieved in the SVC, which aids better transportation of solute in the slurry.

Table 4.28. Cocrystallisation yield comparison for SVC and STR reactors.

Methanol in cyclohexane (%)	Time (mins)	Loading (%)	Cocrystal level in %	
			SVC	Batch stirred
1.76	180	23	80.5	67.3
1.32	180	23	61.9	63.8
2.2	180	23	76.77	56.78
2.2	30	7	73.04	66.06
2.2	30	7	77.73	61.75
0	30	7	49.07	36.42

The rate of nucleation ($\mathcal{J}$) during crystallisation is related to the rate of attachment ($\mathcal{W}$) of solute onto the critical nuclei and the concentration of critical nuclei [n] of the crystallising species (Eqn. 4.6). Good mixing within the reaction system results in the local environment around the growing nuclei and crystals being enriched with fresh solute more rapidly, thereby increasing the rate of attachment ($\mathcal{W}$) unto the nuclei and crystals and hence the crystallisation rate increases resulting in a higher cocrystal yield in a given time. The baffle orifice in the SVC reactor helps generate efficient turbulent mixing but in a batch stirred reaction the mixing is not as efficient because laminar flow mixing is generated[51,53] if baffles are not used in the reactor. This can lead to a locally lower solute concentration around the growing nucleus and hence a lower cocrystallisation rate.

4.5 Comparing the pure solvent and solvent/anti-solvent cocrystallisation reaction

Chemical transformation in a suitable solvent helps to improve selectivity and to lower the activation energy for reaction, the use of the anti-solvent/solvent negates this principle. This section compares cocrystallisation experimental variables in pure solvents and anti-solvent/solvent mixture, highlighting the benefits of using the anti-solvent-solvent cocrystallisation approach over the 100% solvent approach.

4.5.1 Solid recovery

The solid recovery refers to the amount of physical solid that is isolated after filtration and drying of the caffeine-oxalic acid cocrystal powder. It is determined as a percentage of the initial mass of cocrytal components used in the experiment. The mean ($\bar{\mathcal{X}}$), standard deviation (s) and the coefficient of variance (CV) were determined for both pure solvent and anti-solvent/solvent experiments. This was used to examine the reproducibility and benefits of both approaches for the caffeine-oxalic acid cocrystal system. Not all experiments had 100% cocrystal yield but since the amount of solid dissolved in the liquid phase depends on the saturation solubility of all the components in the solvent or solvent mixture, the amount of solid isolated should remain the same irrespective of the level of cocrystal yield.

For the 7% solid loading experiments in the SVC (Table 4.29) in the anti-solvent/solvent systems, the mean ($\bar{\mathcal{X}}$) solid recovery = 91.01%, the standard deviation (s) = 5.6% and the coefficient of variance (CV) = 6.15%. The coefficient of variance (CV) of 6.15% is close to 5% and less than 10% indicating good reproducibility of cocrystal solid recovery for the caffeine-oxalic acid cocrystal system. The mean of 91.01% is high and shows that good solid recoveries are achieved. This high solid recovery mean arises despite the low solid recovery of 75.74% (Table 4.29) for the SVC experiment using 106 µm particle size of caffeine and oxalic acid, which is atypical; excluding this entry, the mean solid recovery increases to 92.19%.

For the 23% solid loading experiments in the antisolvent/solvent systems (Table 4.30), the mean ($\bar{\mathcal{X}}$) solid recovery = 94.84%, the standard deviation (s) =2.96% and the coefficient of variance (CV) = 3.12%. As would be expected, the higher solid loading in these 23% loading experiments resulted in a higher mean ($\bar{\mathcal{X}}$), standard deviation (s) than in the 7% solid experiments. The coefficient of variance (CV) = 3.12% is less than 5% showing very good reproducibility in solid recovery.

For the 7% solid loading experiments in 100% solvents (methanol, methyl acetate and DCM) (Table 4.31), the mean ($\bar{\mathcal{X}}$) solid recovery = 72.55%, the standard deviation (s) =18.99% and the coefficient of variance (CV) = 26.18%. The mean solid recovery of 72.55% for the 100% solvent cocrystallisation is much lower than the mean solid recovery for both the 7% (91.01%) and 23% (94.84%) solid loading experiments. The standard deviation (s) and the coefficient of variance (CV) are also much higher.

The coefficient of variance (CV) for the 100% solvent cocrystallisation is approximately 4x and 8x higher than the coefficient of variance (CV) values for 7% and 23% loading experiments, respectively (Table 4.32). This shows that solid recovery reproducibility is very low when solvents are changed in the 100% solvent caffeine-oxalic acid cocrystallisation experiments. The CV improves from 26.18% to 4.13% (Table 4.32) when only the three 100% methanol experiments are considered but the mean solid recovery ($\bar{\mathcal{X}}$) for these three 100% methanol experiments (86.13%) is still lower than both the anti-solvent/solvent cocrystallisation experiments (Table 4.32).

When caffeine-oxalic acid cocrystallisation experiments in different anti-solvents (xylene and hexane) are considered (Table 4.33), the average ($\bar{\mathcal{X}}$) solid recovery = 95.72%, the standard deviation (s) =1.49 and the coefficient of variance (CV) = 1.55%,

Table 4.29 Solid recovery from antisolvent/solvent cocrystalllisation experiments (7% loading)

Experiment description	Reactor	Solid recovery	$(\mathcal{X}_{\mathrm{i}} - \bar{\mathcal{X}})^2$
Caffeine/oxalic acid, 7% loading 2.2% methanol in cyclohexane	SVC	91.84%	0.69
Caffeine/oxalic acid, 7% loading 2.2% ethanol in cyclohexane	SVC	87.16%	14.82
Caffeine/oxalic acid, 7% loading 2.2% butanol in cyclohexane	SVC	88.60%	5.81
Caffeine/oxalic acid, 7% loading 2.2% methanol in cyclohexane (106µm)	SVC	91.84%	0.69
Caffeine/oxalic acid, 7% loading 2.2% isoprppanol in cyclohexane	SVC	95.21%	17.64
Caffeine/oxalic acid, 7% loading 2.2% MTBE in cyclohexane	SVC	94.52%	12.32
Caffeine/oxalic acid, 7% loading 2.2% MeCN in cyclohexane	SVC	95.00%	15.92
Caffeine/oxalic acid, 7% loading 2.2% methanol in cyclohexane (106µm)	SVC	75.74%	233.17
Caffeine/oxalic acid, 7% loading 2.2% methanol in cyclohexane (106µm)	SVC	85.90%	26.11
Caffeine/oxalic acid, 7% loading 2.2% diethyl ether in cyclohexane	SVC	94.95%	15.52
Caffeine/oxalic acid, 7% loading 2.2% DCM in cyclohexane	SVC	94.40%	11.49
Caffeine/oxalic acid, 7% loading 2.2% isoprppanol in cyclohexane	SVC	95.51%	20.25
Caffeine/oxalic acid, 7% loading 2.2% THF in cyclohexane	SVC	95.80%	22.94
Caffeine/oxalic acid, 7% loading 2.2% ethanol in cyclohexane	SVC	87.70%	10.96
$\sum(\mathcal{X}_{\mathrm{i}} - \bar{\mathcal{X}})^2$			408.34

Table 4.30 Solid recovery from antisolvent/solvent cocrystalllisation experiments (23% loading)

Experiment description	Reactor	Solid recovery	$(\mathcal{X}_\mathrm{i} - \bar{\mathcal{X}})^2$
Caffeine/oxalic acid, 23% loading 2.2% acetic acid in cyclohexane	SVC	93.05%	3.20
Caffeine/oxalic acid, 23% loading 2.2% methanol in heptane	SVC	91.87%	8.82
Caffeine/oxalic acid, 23% loading 2.2% methanol in cyclohexane	SVC	93.70%	1.30
Caffeine/oxalic acid, 23% loading 1.95% methanol in cyclohexane	SVC	99.67%	23.33
Caffeine/oxalic acid, 23% loading 2.2% methanol in cyclohexane	SVC	94.38%	0.21
Caffeine/oxalic acid, 23% loading 2.2% methanol in cyclohexane	SVC	98.30%	11.97
Caffeine/oxalic acid, 23% loading 2.2% methyl acetate in cyclohexane	SVC	92.91%	3.72
$\sum(\mathcal{X}_\mathrm{i} - \bar{\mathcal{X}})^2$			52.56

Table 4.31 Solid recovery from pure solvent cocrystalllisation experiments.

Experiment description	Reactor	Solid recovery	$(\mathcal{X}_{\mathrm{i}} - \bar{\mathcal{X}})^2$
Caffeine/oxalic acid, 7% loading 100% methanol	STR	88.40%	251.22
Caffeine/oxalic acid, 7% loading 100% methyl acetate	STR	55.10%	304.50
Caffeine/oxalic acid, 7% loading 100% DCM	STR	49.23%	543.82
Caffeine/oxalic acid, 7% loading 100% methanol	SVC	80.90%	69.72
Caffeine/oxalic acid, 7% loading 100% methanol	STR	89.10%	273.90
$\sum(\mathcal{X}_{\mathrm{i}} - \bar{\mathcal{X}})^2$			1443.17

this coefficient of variance value is very low and shows very good, reproducible solid recovery.

The higher variability in the solid recovery for the 100% solvent cocrystallisation experiments may be because the variation in solubility of the cocrystal and its component in the pure solvents are higher than in the anti-solvent/solvent mixture comprising, which comprises mainly of the anti-solvent. This result shows that solvents may be changed in the anti-solvent/solvent approach without adversely affecting the amount and reproducibility of cocrystal recovery, whereas in the cocrystallisation with 100% solvent, the cocrystal recovery can be seriously affected.

Table 4.32 Summary of statistical analysis of solid recovery.

	7% solid loading	23% solid loading	7% loading (100% solvent)	7% loading (100% methanol)
$\bar{X}$	91.07%	94.84%	72.55%	86.13%
S	5.6%	2.96%	18.99%	4.55%
CV	5.16%	3.12%	26.18%	5.28%

Table 4.33 Solid recovery for cocrystallisation in different anti-solvent

Experiment description	Reactor	Solid recovery
Caffeine/oxalic acid, 7% loading 2.2% methanol in xylene	STR	93.70%
Caffeine/oxalic acid, 7% loading 3.86% methanol in xylene	STR	95.51%
Caffeine/oxalic acid, 7% loading 2.2% methanol in xylene	STR	96.77%
Caffeine/oxalic acid, 7% loading 4% methanol in hexane	STR	96.90%

4.6 Conclusion

Cocrystallisation of caffeine and oxalic acid using the anti-solvent/solvent approach was shown to proceed via a solution-mediated process and not due to attrition of the solids. The solvent used in the cocrystallisation process has a direct influence on the level of caffeine-oxalic acid cocrystal yield observed.

Using correlation analysis, it was shown that the hydrogen bonding Hansen solubility parameter (δ_H) and oxalic acid solubility, in the solvent selected had the strongest correlation with caffeine-oxalic acid cocrystal yield. The yield was higher when a solvent with high δ_H and oxalic acid solubility was selected.

The increased crystallinity in oxalic acid compared to caffeine was suggested as the reason for a stronger correlation between cocrystal yield and oxalic acid solubility. This increased crystallinity in oxalic acid means the $\Delta G_{lattice}$ of dissolution is higher.

A parameter for selecting solvents to use in cocrystallisation experiments was suggested. The model ($\frac{\text{Ra}}{\text{Oxalic acid}}$) incorporates both the δ_H value and coformer solubility, and was shown to have a better correlation coefficient than both the individual δ_H value and coformer solubility.

The anti-solvent/solvent cocrystallisation approach produces smaller crystal particle sizes and higher solid recovery compared to pure solvent slurry cocrystallisation because of the higher level of supersaturation achieved. The mixing of the anti-solvent and solvent prior to the introduction of API and coformer helps improve consistency in PSD. The anti-solvent/solvent cocrystallisation system also displayed a higher solid recovery tolerance to solvent change when compared to pure solvents.

References

(1) Bucar, D.; Henry, R. F.; Lou, X.; Duerst, R. W.; MacGillivray, L. R.; Zhang, G. Z. *Cryst. Growth Des.* **2009**, *9*, 1932.

(2) Zhang, G.; Henry, R. F.; Borchardt, T. B.; Lou, X. *Journal of Pharmacutical Sciences* **2007**, *96*, 990.

(3) Friscic, T.; Childs, S. L.; Rizvi, S. A. A.; Jones, W. *Crystengcomm* **2009**, *11*, 418.

(4) *Pharmaceutical salts and co-crystals*; RSC Publishing, **2012.**

(5) L.Q, J.; Haitao, Z.; Alejandro, A.; James, E.; M.S, A.; L.T, B. *Cryst. Growth Des.* **2012**, *12*, 3036.

(6) Zhang, S.,*Physical Properties and Crystallization of Theophylline Co-crystals*,KTH Royal Institute of Technology, **2010**.

(7) Rager, T.; Hilfiker, R. *Zeitschrift Fur Physikalische Chemie* **2009**, *223*, 793.

(8) Rager, T.; Hilfiker, R. In *Pharmaceutical Salts and Co-crystal*; Wouters, J., Quere, L., Eds.; Royal Society of Chemistry: **2012,** 280.

(9) Timo, R.; Rolf, H. *Cryst. Growth Des.* **2010**, *10*, 3237.

(10) Childs, S. L.; Rodríguez-Hornedo, N.; Reddy, L. S.; Jayasankar, A.; Maheshwari, C.; McCausland, L.; Shipplett, R.; Stahly, B. C. *Crystengcomm* **2008**, *10*, 856.

(11) Schultheiss, N.; Newman, A. *Cryst. Growth Des.* **2009**, *9*, 2950.

(12) Braga, D.; Grepioni, F. *Making crystals by design : methods, techniques and applications*; Wiley-VCH: Weinheim, **2007**

(13) Shattock, T. R.; Arora, K. K.; Vishweshwar, P.; Zaworotko, M. J. *Cryst. Growth Des.* **2008**, *8*, 4533.

(14) Bruno, I. J.; Cole, J. C.; Edgington, P. R.; Kessler, M.; Macrae, C. F.; McCabe, P.; Pearson, J.; Taylor, R. *Acta Cryst., B58,* **2002**, 389.

(15) Pirttimaki, J.; Laine, E.; Ketolainen, J.; Paronen, P. *International Journal of Pharmaceutics* **1993**, *95*, 93.

(16) Derissen, J. L.; Smit, P. H. *Acta Crystallographica Section B-Structural Crystallography and Crystal Chemistry* **1974**, *30*, 2240.

(17) Nobeli, I.; Price, S. L. *A Journal of Physical Chemistry A,* **1999**, *103*, 6448.

(18) Aakeroy, C. B.; Beatty, A. M.; Helfrich, B. A.; Nieuwenhuyzen, M. *Cryst. Growth Des.* **2003**, *3*, 159.

(19) Daniele Musumeci, C. A. H., Rafel Prohens, Serena Scuderia and James F. McCabe *Chemical Science,* **2011**, *2*, 883.

(20) Trask, A. V.; Motherwell, W. D. S.; Jones, W. *Cryst. Growth Des.* **2005**, *5*, 1013.

(21) Bolton, S.; Null, G. *Orthomolecular Psychiatry,* **1981**, *10*, 202.

(22) Nkondjock, A. *Cancer Letters* **2009**, *277*, 121.

(23) A. Delori; T. Friscic; W. Jones *Crystengcomm* **2012**, *14*, 2350.

(24) Macrae, C. F.; Bruno, I. J.; Chisholm, J. A.; Edgington, P. R.; McCabe, P.; Pidcock, E.; Rodriguez-Monge, L.; Taylor, R.; van de Streek, J.; Wood, P. A. *J. Appl. Cryst.* **2008** *41*, 466.

(25) Zhanga, S.; Rasmuson, A. C. *Crystengcomm* **2012**, *14*, 4644.

(26) Issa, N.; Karamertzanis, G. P.; Welch, G. W. A.; Price, S. L. *Cryst. Growth Des.* **2009**, *9*, 442.

(27) Lehmann, C. W.; Stowasser, F. *Chemistry - a European Journal* **2007**, *13*, 2908.

(28) Derollez, P.; Correia, N. T.; Danède, F.; Capet, F.; Affouard, F.; Lefebvre, J.; Descamps, M. *Acta Crystallographica Section B Structural Science* **2005**, *B61*, 329.

(29) Aggarwal, V. K.; Staubitz, A. C.; Owen, M. *Organic Process Research & Development* **2006**, *10*, 64.

(30) Hansen, C. M. *Hansen Solubility Parameter: A User's Handbook*; CRC Press, **2007.**

(31) Greenhalgh, D. J.; Williams, A. C.; Timmins, P.; York, P. *Journal of Pharmaceutical Sciences,* **1999**, *88*, 1182.

(32) Hancock, B. C.; York, P.; Rowe, R. C. *International Journal of Pharmaceutics* **1997**, *148*, 1.

(33) Mohammad, M. A.; Alhalaweh, A.; Velaga, S. P. *International Journal of Pharmaceutics* **2011**, *407*, 63.

(34) Lee, T.; Chena, J. W.; Lee, H. L.; Lin, T. Y.; Tsai, Y. C.; Cheng, S. L.; Lee, S. W.; Hu, J. C.; Chen, L. T. *Chemical Engineering Journal,* **2013**, *225*, 809.

(35) Rohani, S. *Organic Process Research & Development*, **2005**, *9*, 858.

(36) Samir, K.; McGarrity, E.; Hugo, M.; Joop, H. *Chemical Commununication* **2012**, *48*, 4983.

(37) Aakeroy, C. B.; Hussain, I.; Desper, J. *Cryst. Growth Des.* **2006**, *6*, 474.

(38) E. Gagniere , D. M., F.Puel , A.Rivoire , O.Monnier , E.Garcia , J.P.Klein, *Journal of Crystal Growth* **2009**, *311*, 2689.

(39) Mansour Mansouri, M.; Pouretedal, H. R.; Vosoughi, V. *The Open Conference Proceedings Journal,* **2011**, *2*, 88.

(40) Dokoumetzidis, A.; Macheras, P. *International Journal of Pharmaceutics* **2006**, *321*, 1.

(41) Liversidge, G. G.; Cundy, K. C. *International Journal of Pharmaceutics* **1995**, *125*, 91.

(42) Department of Health and Human Services; US Food and Drug administration: **2001**.

(43) Dalvi, S. V.; Dave, R. N. *Industrial and Engineering Chemistry Research,* **2009**, *48*, 7581.

(44) Sameer, D.; Rajesh, D. *Ind. Eng. Chem. Res.* **2009**, *48*, 7581.

(45) Jian-Feng, C.; Ji-Yao, Z.; Zhi-Gang, S.; Jie, Z.; Jimmy, Y. *Ind. Eng. Chem. Res.* **2006**, *45*, 8723.

(46) Alvarez, A. J.; Myerson, A. S. *Cryst. Growth Des.* **2010**, *10*, 2219.

(47) Ó'Ciardhá, C. T.; Hutton, K. W.; Mitchell, N. A.; Frawley, P. J. *Cryst. Growth Des.* **2012**, *12*, 5247.

(48) Matteucci, M. E.; Hotze, M. A.; Johnston, K. P.; Williams, R. O. *Langmuir* **2006**, *22*, 8951.

(49) Khan, S.; Matas, M.; Zhang, J.; Anwar, J. *Cryst. Growth Des.* **2013**, 7, 2766.

(50) Gonzalez-Oliver, C. J. R.; Johnson, P. S.; James, P. F. *Journal of Materials Science* **1979**, *14*, 1159.

(51) Ni, X. *The Chemical Engineering Journal* **1993**, *52*, 107.

(52) Harvey, A. P.; M. R. Mackley, M. R.; Stonestreet, P. *Industrial & Engineering Chemistry Research* **2001**, *40*, 5371.

(53) Ni, X.; Mackley, M. R.; Harvey, A. P.; Stonestreet, P.; Baird, M. H. I.; Rama Rao, N. V. *Trans IChemE* **2003**, *81*, 373.

Chapter 5 Process evaluation

5.1 Introduction

The process parameters of the anti-solvent/solvent cocrystallisation were investigated in chapter 4 using caffeine-oxalic acid cocrystal system as a model. Chapter 5 focuses on the application of the anti-solvent/solvent process to make cocrystals and a salt using different active pharmaceutical ingredients (API) and coformers.

The importance of cocrystals to the pharmaceutical industry and the similarity between cocrystals and salts has been stated in Chapter 1. Salt formulation of drug molecules is the most used technique in the pharmaceutical industry for improving the solubility of drugs[1-3]. Large scale manufacture of salts is done by precipitating from a suitable solvent[2]. This process can result in the formation of unwanted hydrates or solvate and reduction in yield due to losses in the mother liquor as a result of high solubility in the solvent. Salt formation may require high energy input for solvent evaporation or cooling to bring about supersaturation[1,2]; the anti-solvent/solvent process can help avoid these disadvantages associated with normal salt formation because it is done at ambient temperature; requires low solvent level minimising the chance of forming solvates or hydrates but supersaturation is still achieved as a result of the low solubility of the salt in the anti-solvent/solvent mixture.

This chapter is divided into two sections:

1. Small scale cocrystallisation and salt formation in the single vertical column (SVC) or stirred tank reactor (STR) and
2. Pilot scale cocrystallisation in the particulate processing unit (PPU).

No process optimisation work was carried out during the validation of the cocrystal and salt systems; the aim of the process validation was to test if the anti-solvent/solvent cocrystallisation process could be applied to cocrystallisation of systems aside from caffeine-oxalic acid cocrystal and salt formation. The validation also afforded the opportunity to verify if the presence of the solvent in the anti-solvent/solvent mixture facilitates cocrystallisation.

5.2 SVC and STR experiments.

The experimental conditions used are stated in chapter 2, all experiments were performed using methanol as the solvent and cyclohexane as the anti-solvent. No comparison was made between experiments conducted in stirred tank reactor (STR) or the single vertical column (SVC) because of time constraints and the primary focus being validation of the slurry anti-solvent/solvent cocrystallisation process for different systems rather than an optimisation and then comparison between the different systems.

5.2.1 Caffeine-salicylic cocrystal

The caffeine-salicylic acid cocrystal system (Fig. 5.1) was used in the cocrystal validation process. The bonding motif in caffeine-salicylic acid cocrystal consists of the carboxylic acid /N-heterocyclic hydrogen bonding present in caffeine-oxalic acid cocrystal. Changing from caffeine/oxalic acid to caffeine /salicylic acid allowed for a stepwise change of coformer using the same API. The caffeine-salicylic acid cocrystal has two entries in Cambridge Structural Database (XOBCAT[4] and XOBCAT01[5]) with both powder x-ray pattern (Fig. 5.2) being similar but with different space groups $P2_1/n$ and $P2_1/c$.

Salicylic acid has anti-pyretic properties used for the treatment of fever. Its acetyl derivative acetylsalicylic acid, known as "Aspirin", is a high volume drug with more than 40,000 metric tonne consumed annually[6]. Aspirin is used in the treatment of inflammatory conditions like: arthritis, as an analgesic for treating mild pain and anti-pyretic in the treatment of fever. A commercial sample of salicylic acid was analysed by PXRD (Fig. 5.3) (note there are no diffraction peaks below $2\theta=10^o$), FTIR (Figs. 5.5 and 5.6) and DSC (Fig. 5.7), which showed an onset melting point of 158.12 ^oC, close to the reported melting point of 159 ^oC[7]. A commercial sample of caffeine was analysed by PXRD (Fig. 5.3) (note there is only one small peak below $2\theta=10^o$ at $2\theta=8.18^o$), FTIR (Figs. 5.5 and 5.6) and DSC (Fig. 5.7), which showed an onset melting point of 235.6 ^oC. The availability of a reference PXRD pattern for caffeine-salicylic acid cocrystal makes it an ideal system to study because cocrystal formation can be easily verified.

Caffeine and salicylic acid were mixed in a 1:1 molar ratio and added to the 2.2 wt % methanol in cyclohexane in the SVC. After 30 minutes of oscillatory mixing, the slurry was filtered, dried and the powder analysed by PXRD. The solid loading for the experiment was 8.9 wt % and the solid recovery after drying was 88.9%. Overlaying the caffeine and salicylic acid pattern on the reference PXRD shows a distinguishing peak at 2θ = 6.7° for the cocrystal (Fig. 5.3).

The PXRD of the SVC experiment sample (Fig. 5.4) shows the presence of the new peak at 2θ = 6.7°. The FTIR analysis of the SVC caffeine-salicylic acid sample was compared with that of its components (Fig. 5.5 and 5.6). The comparison shows the presence of two broad bands at 1850 cm^{-1} and 2350 cm^{-1} that are absent in both salicylic acid and caffeine. These peaks are evidences of un-ionised O-H hydrogen bonding stretching of the carboxylic acid[7,8]. The DSC analysis (Fig. 5.7) shows a new onset melting point of 138.3 °C, which is close to reported melting point of 142°C and is lower than the onset melting points[4] of salicylic acid (158.12°C) and caffeine (235.58°C).

A comparison of the PXRD pattern of the SVC sample and the reference spectrum from Mercury (Fig. 5.8) shows evidence of a low level of residual salicylic acid in the sample indicated by the peak at 2θ=11°. Despite this the pattern of the SVC sample is a good patternl match with the reference spectrum from Mercury. The successful cocrystallisation of caffeine and salicylic acid using the anti-solvent/solvent mixture has been confirmed by FTIR, PXRD and DSC.

Next, the impact of the solvent methanol in the cocrystallisation of caffeine-salicylic acid was investigated. Two stirred tank reactor cocrystallisation experiments of caffeine and salicylic acid were carried out for one hour each; one experiment was in 100% cyclohexane (without methanol) and the second experiment was in 2.2 wt % methanol in cyclohexane. The isolated solids from both experiments were analysed by PXRD.

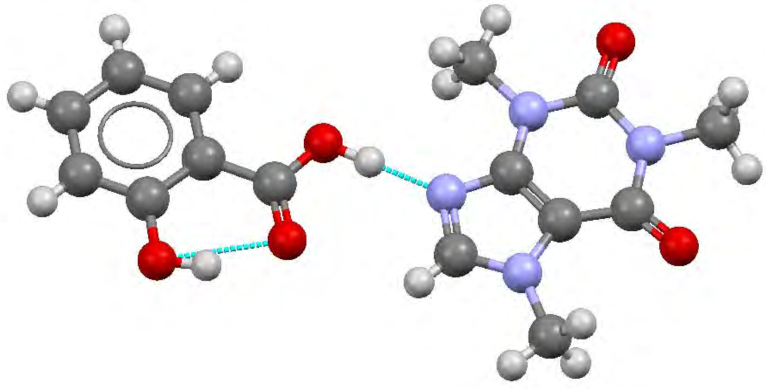

Fig. 5.1 Building motif of the caffeine-salicylic acid cocrystal visualised using Mercury.

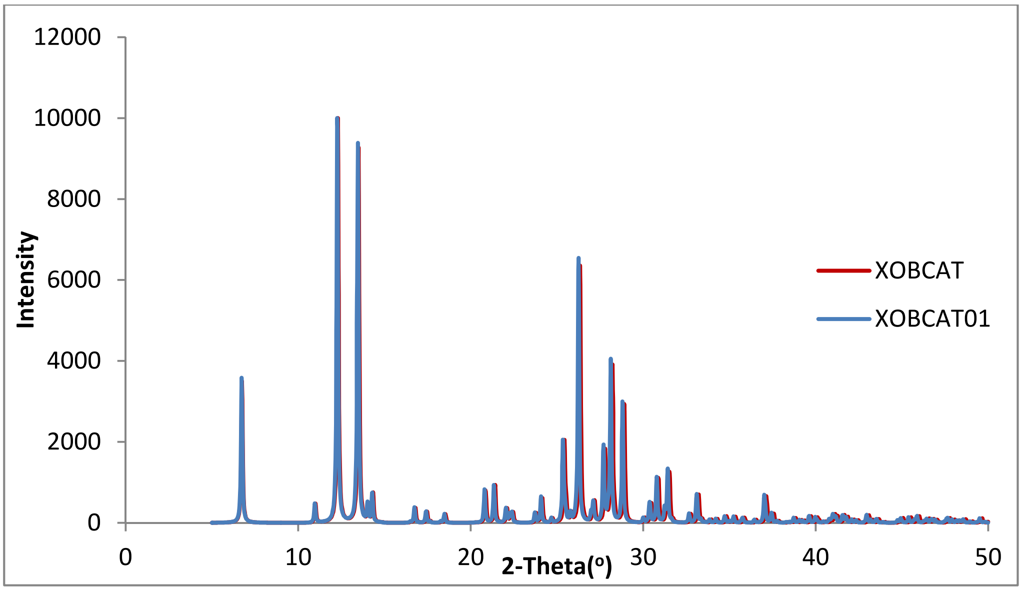

Fig. 5.2 PXRD pattern of caffeine-salicylic acid cocrystal (XOBCAT and XOBCAT01).

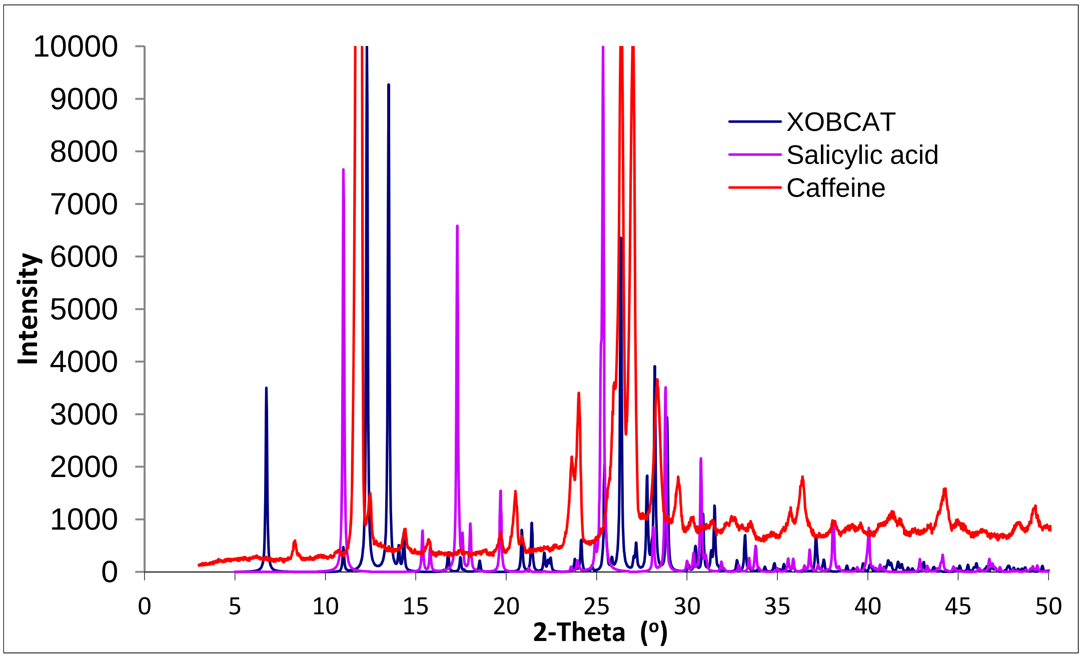

Fig. 5.3 Comparing powder pattern for caffeine, salicylic acid and caffeine-salicylic acid cocrystal reference pattern.

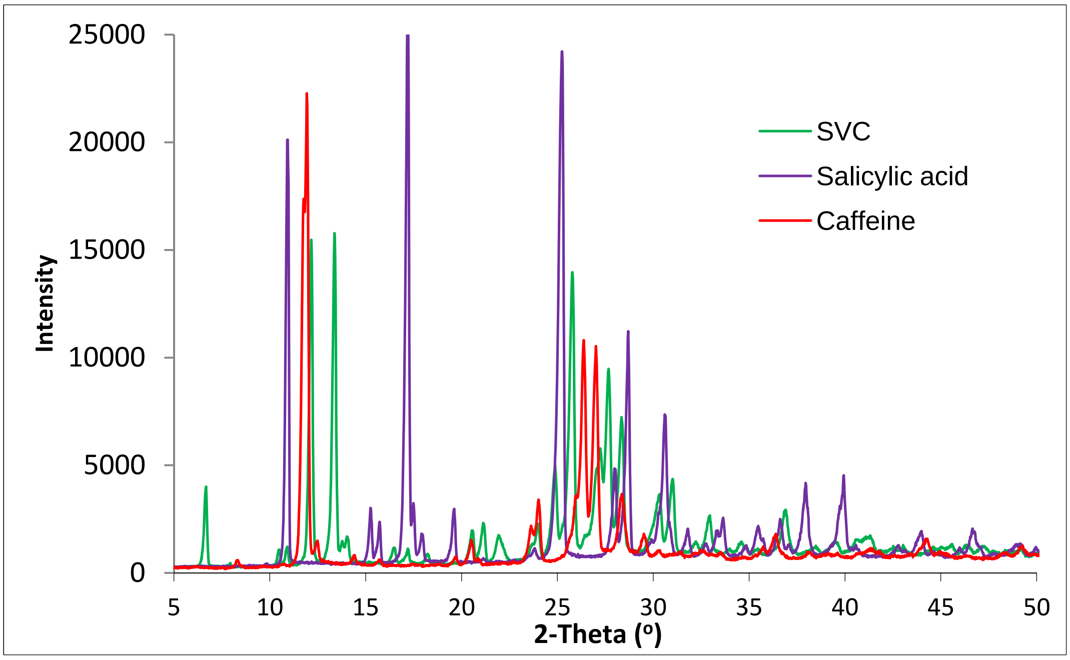

Fig. 5.4 PXRD pattern of caffeine-salicylic acid cocrystal sample from SVC and its component.

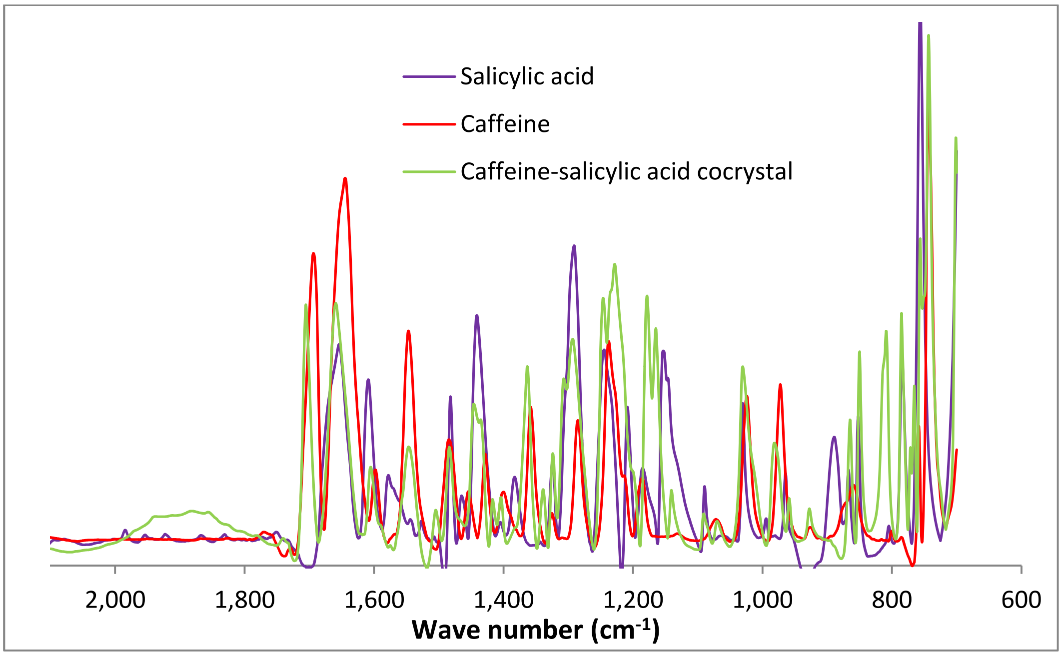

Fig. 5.5 Comparing FTIR spectrum for caffeine-salicylic acid cocrystallisation between the 600- 2,100 cm^{-1} region.

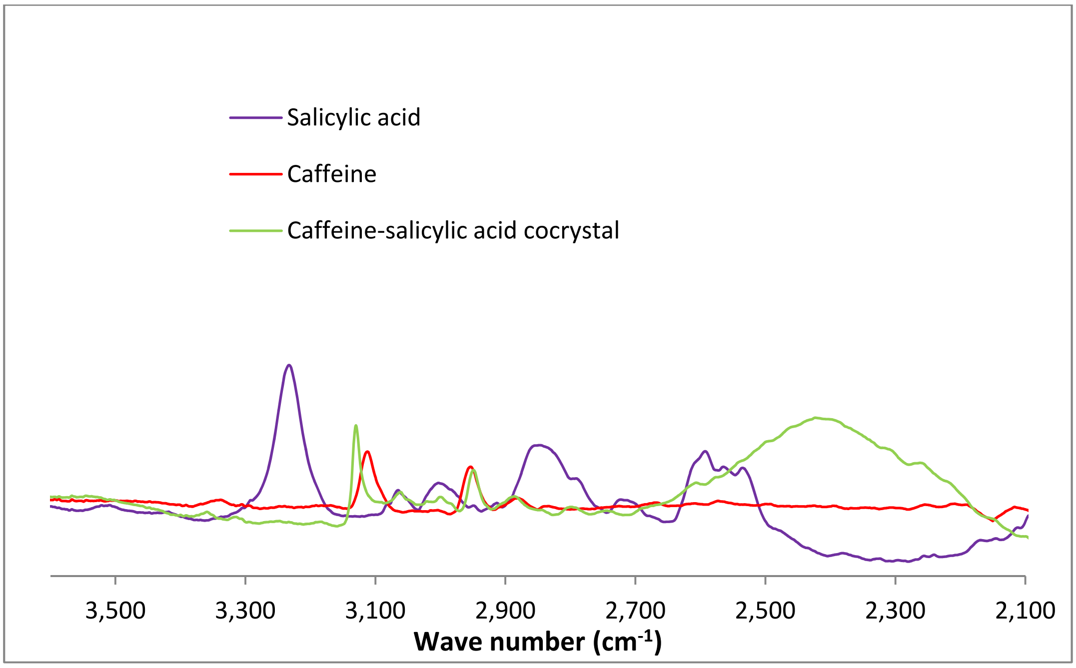

Fig. 5.6 Comparing FTIR spectra for caffeine-salicylic acid cocrystallisation between the 2,100 - 3,600 cm^{-1} region.

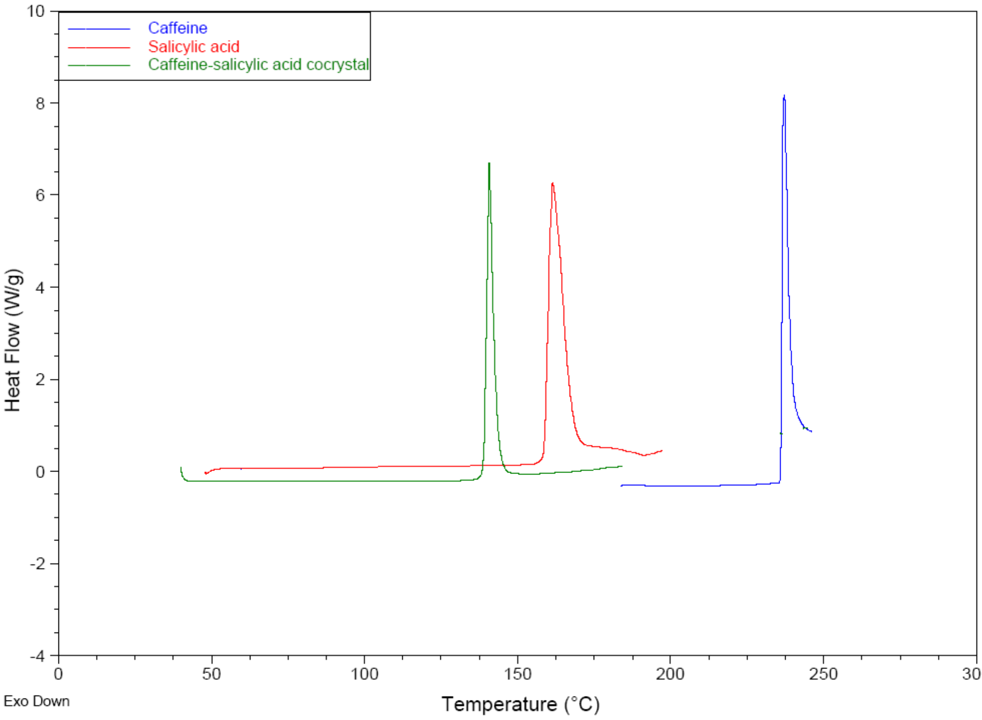

Fig. 5.7 DSC thermogram of caffeine-salicylic cocrystal overlaid with cocrystal components.

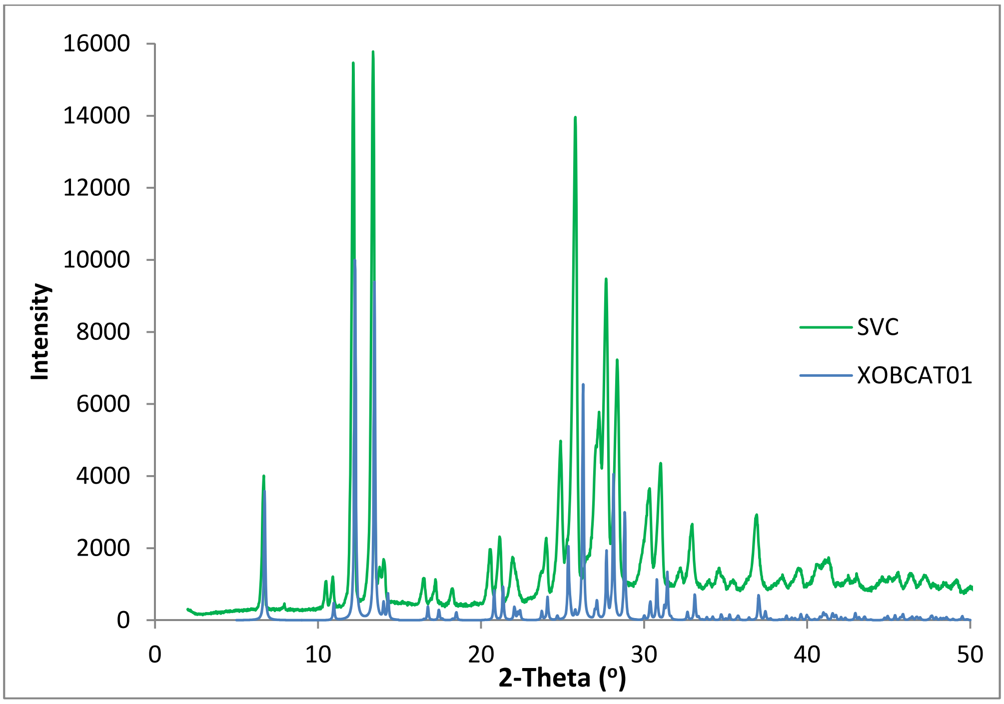

Fig. 5.8 Comparing PXRD pattern for SVC sample and reference.

The powder patterns for caffeine/salicylic acid cocrystallisation experiments with methanol and without methanol were compared (Fig. 5.9) and the comparison shows that in the experiment without methanol, the residual amount of salicylic acid ($2\theta \approx 10$ and 17, Fig. 5.9) in the sample is much higher than in the experiment with methanol. Both experiments use the same source of starting reagents, the same reaction time and the same stirrer speed; the only difference was that methanol was added in one experiment and not the other. The presence of a higher level of residual salicylic acid in the experiment without methanol confirms that the methanol solvent facilitates the cocrystallisation of caffeine/salicylic acid, agreeing with the observation made in Chapter 4 on the effect of the solvent methanol in caffeine/oxalic acid cocrystallisation, that the presence of methanol enhances the caffeine-oxalic acid cocrystal yield.

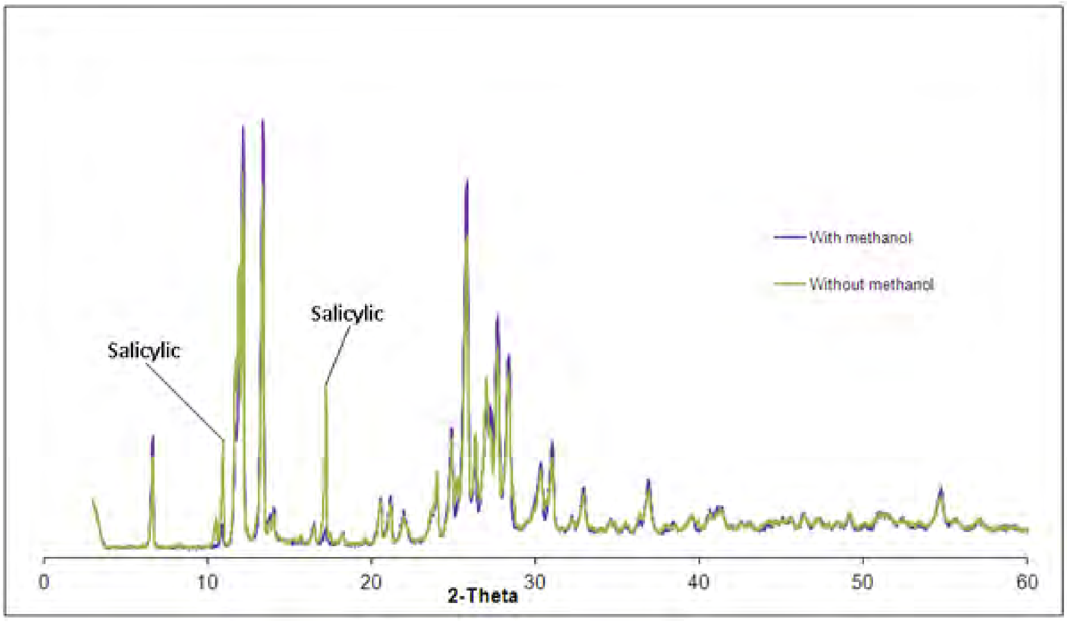

Fig. 5.9 PXRD comparison of stirred tank reactor (STR) cocrystallisation of caffeine/salicylic acid with and without methanol. The analysis shows that the level of residual salicylic acid in the experiment without methanol is higher than in the experiment with methanol.

5.2.2 Carbamazepine-nicotinamide cocrystal

Carbamazepine-nicotinamide cocrystal system was the second system used for validating the anti-solvent/solvent process on a small scale. Carbamazepine is an anti-convulsant used in the treatment of epilepsy. Carbamazepine exhibits polymorphism and has a poor bio-availability[9-11]. Nicotinamide has six entries in Mercury[12], five of these entries have similar PXRD patterns. Carbamazepine forms a 1:1 cocrystal with nicotinamide[11] (Fig. 5.10) and its entry name in Cambridge Structural Database is UNEZES, the PXRD powder pattern is available (Fig. 5.11). The carbamazepine-nicotinamide cocrystal system presents a good challenge for process validation because this system has a different API and coformer from previous cocrystal systems investigated in the anti-solvent/solvent mixture process; the amide/amide bonding motifs in carbamazepine-nicotinamide cocrystal system (Fig. 5.10) are different from the carboxylic acid/amine bonding motif in previous cocrystal systems.

The solubility of carbamazepine or nicotinamide in 2.2 wt % methanol in cyclohexane was not determined and no comparison was made with the previous cocrystal systems investigated. A commercial sample of carbamazepine was analysed by PXRD (Fig. 5.12), which shows no diffraction peak below $2\theta=10^{o}$, ATR-FTIR (Figs. 5.15 and

5.16) and DSC (Fig. 5.18), with the latter showing two endotherms at 171.2 °C and 187.9 °C. This DSC profile is consistent with the presence of Form I and III polymorphs of carbamazepine[9,13]. Nicotinamide was analysed by PXRD (Fig. 5.12) showing no diffraction peak below 2θ=10°, ATR-FTIR (Figs. 5.15 and 5.16) and DSC (Fig. 5.18), with the DSC showing a melt endotherm with an onset temperature of 127.2 °C close to the reported melting point of 124.6°C[14].

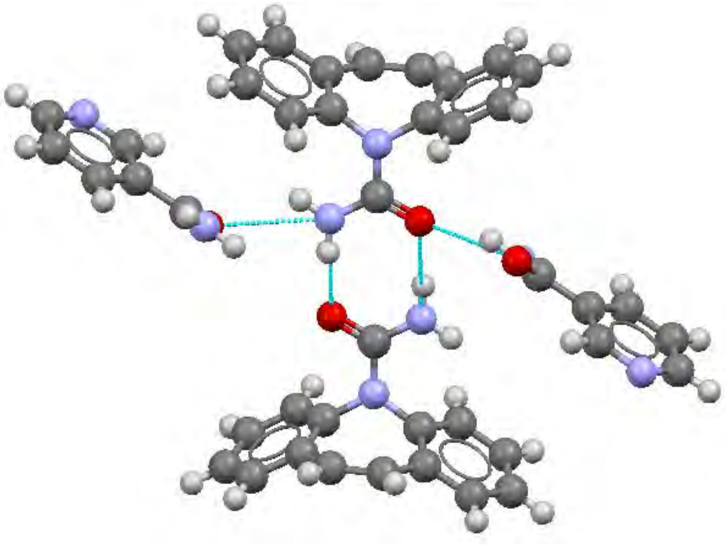

Fig. 5.10 Building motif of the carbamazepine-nicotinamide cocrystal (UNEZES).

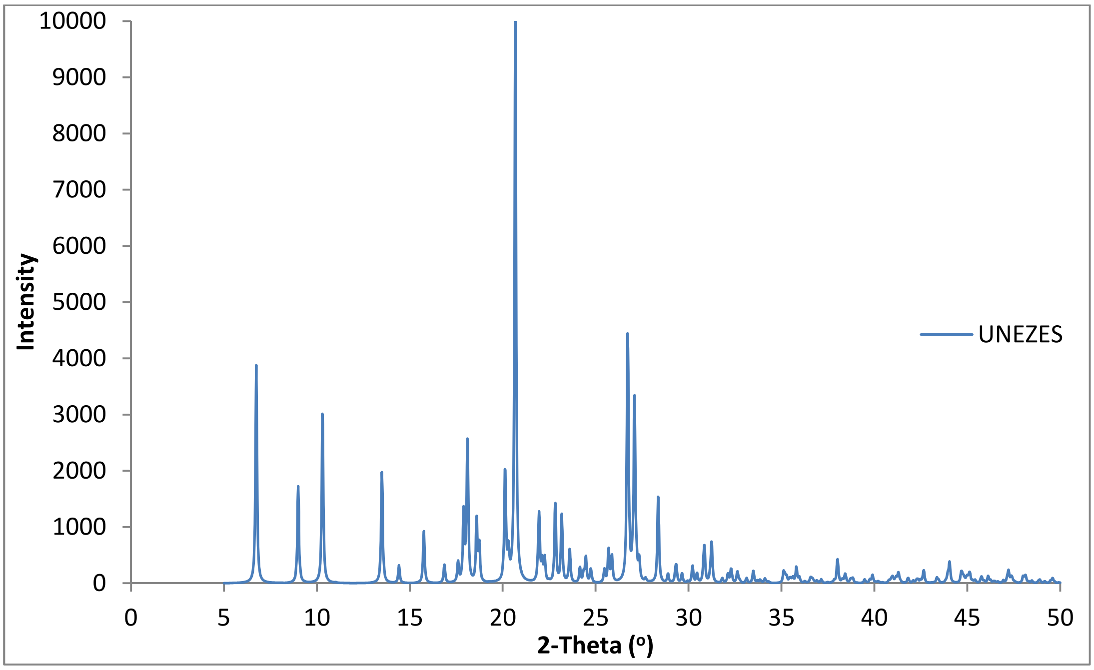

Fig. 5.11 PXRD pattern for carbamazepine-nicotinamide cocrystal.

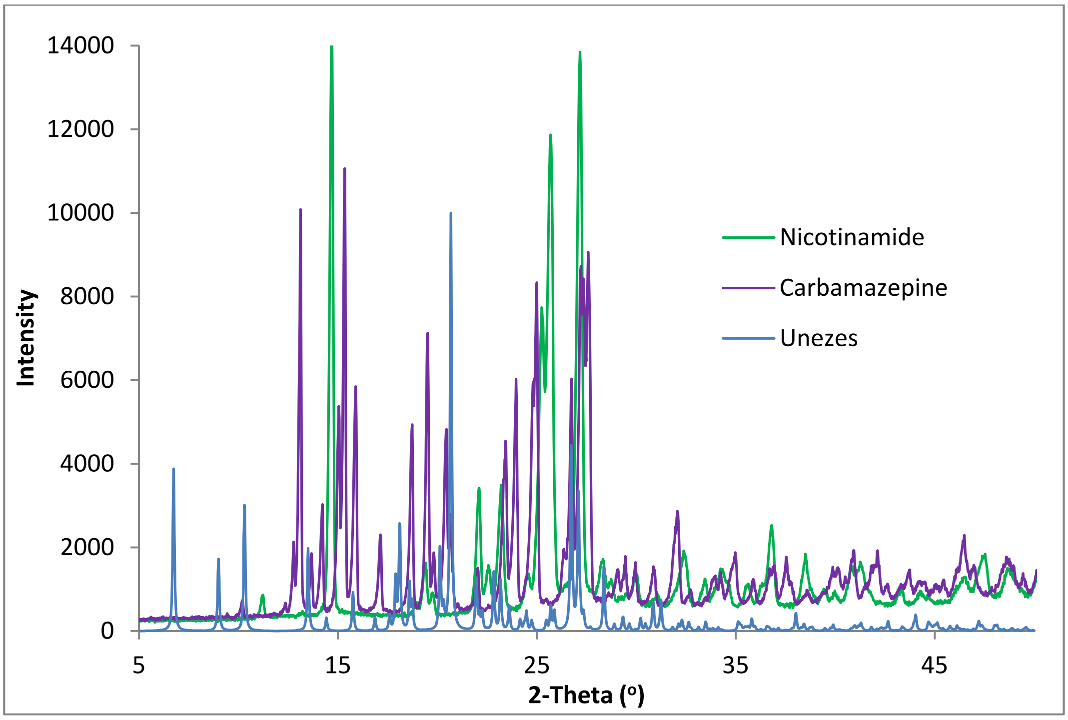

Fig. 5.12 Comparing pxrd for carbamazepine, nicotinamide and carbamazepine-nicotinamide cocrystal reference pattern.

Carbamazepine and nicotinamide were mixed in 1:1 molar ratio and added to the 2.2 *wt* % methanol in cyclohexane in a STR, after 30 minutes of mixing with a paddle stirrer, the slurry was filtered, dried and the powder analysed by PXRD (Fig. 5.13). The solid loading for the experiment was 8.6 *wt* % and the solid recovery after drying was 95.12 % of the initial reagents. A comparison of the powder pattern from the STR experiment and reference spectrum (Fig. 5.14) shows that both patterns are a good match. The ATR-FTIR spectra of the cocrystallisation sample (Figs. 5.15 and 5.16) was overlaid with the spectra of its components, focusing on the 1600 to 1700 cm^{-1} region (Fig. 5.17) where the C=O amide hydrogen stretching is observed[13,15]; the peaks observed in the carbamazepine-nicotinamide cocrystal spectra at 1660 cm^{-1} and 1680 cm^{-1} are shifts in the corresponding C=O amide stretching in nicotinamide (1675 cm^{-1}) and carbamazepine (1670 cm^{-1})[16]. The NH-vibrations at 3355 cm^{-1} in nicotinamide and 3463 cm^{-1} in carbamazepine shifts to 3382 cm^{-1} and 3440 cm^{-1} respectively; in carbamazepine-nicotinamide cocrystal (Fig. 5.16)[16]. The DSC thermogram of the carbamazepine-nicotinamide cocrystal (Fig 5-18) shows a melt endotherm at 156.47°C, which is within the 151-161°C carbamazepine-nicotinamide cocrystal melting point range reported, the cocrystal also has an intermediate melting point when overlaid with its component[7] (Fig. 5.18).

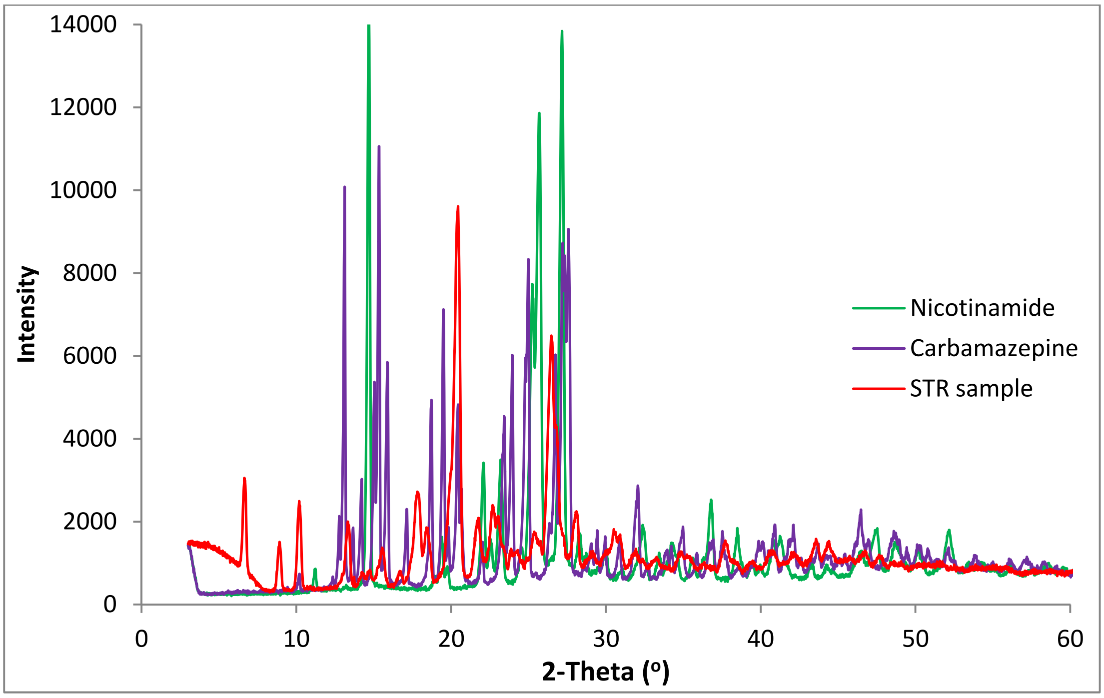

Fig. 5.13 PXRD pattern of carbamazepine-nicotinamide cocrystal for anti-solvent/solvent cocrystallisation from stirred tank reactor.

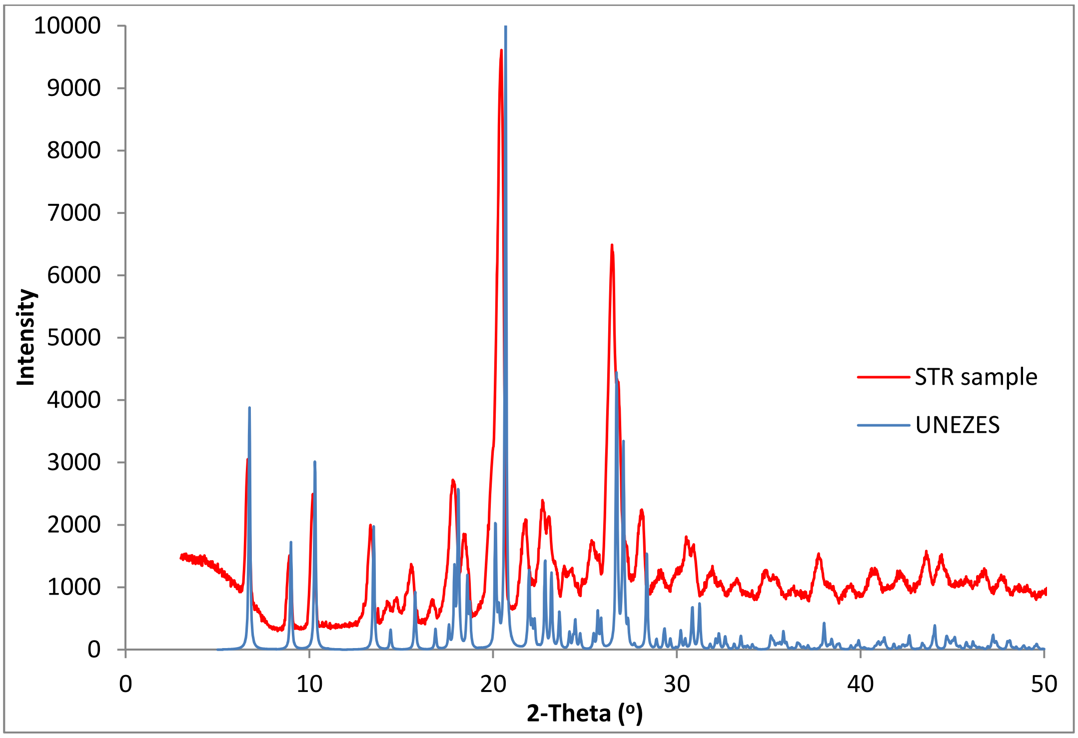

Fig. 5.14 Comparing PXRD pattern for carbamazepine-nicotinamide cocrystal from STR experiment with reference (UNEZES).

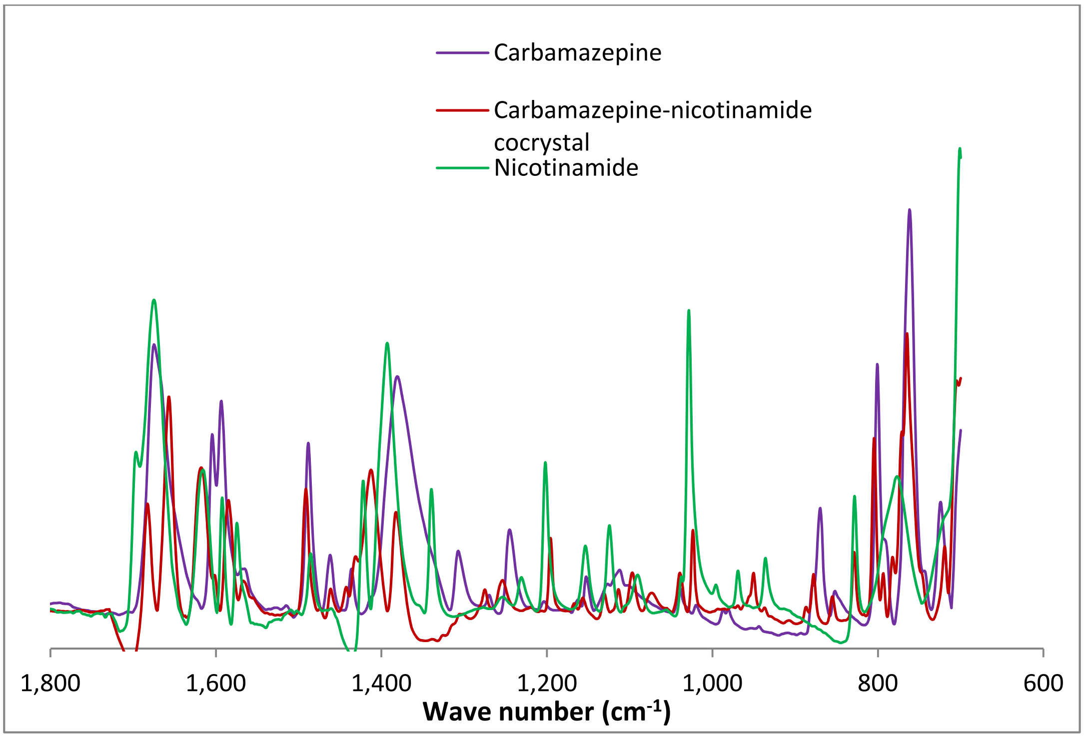

Fig. 5.15 ATR-FTIR spectrum for carbamazepine-nicotinamide cocrystal and component for region between 600- 1,800 cm^{-1}.

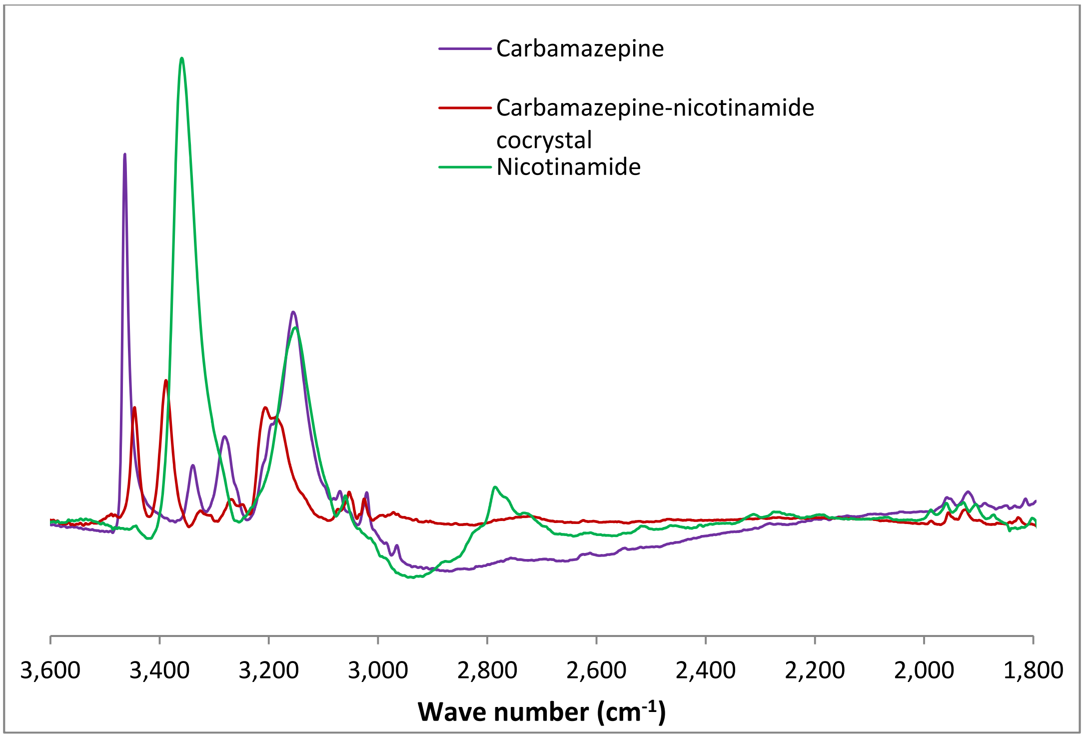

Fig. 5.16 ATR-FTIR spectrum for carbamazepine-nicotinamide cocrystal and component for region between 1,800 - 3,600 cm^{-1}.

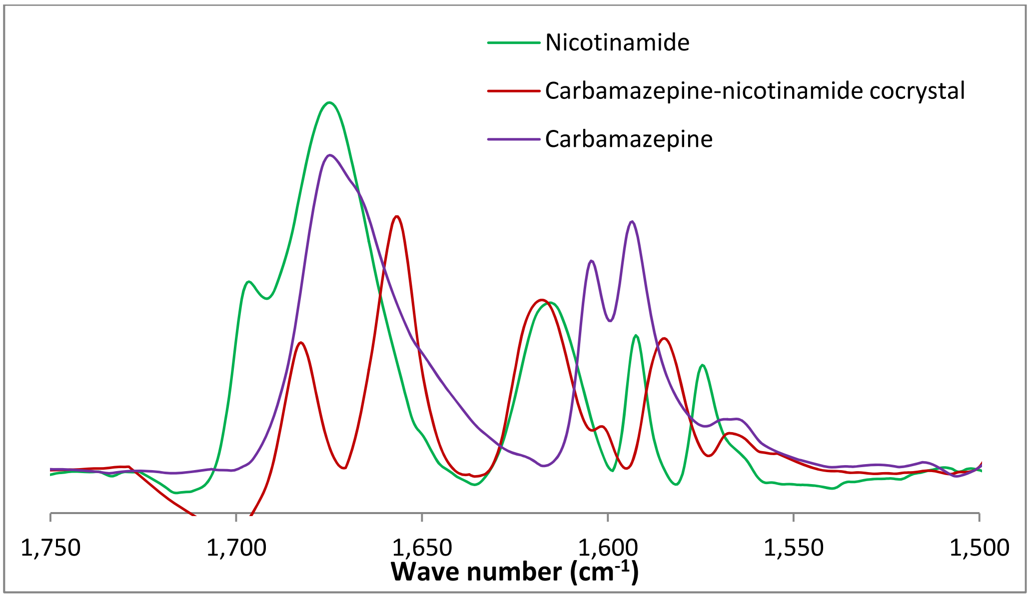

Fig. 5.17 ATR-FTIR spectrum for carbamazepine-nicotinamide cocrystal and component for region between 1500 – 1750 cm^{-1}.

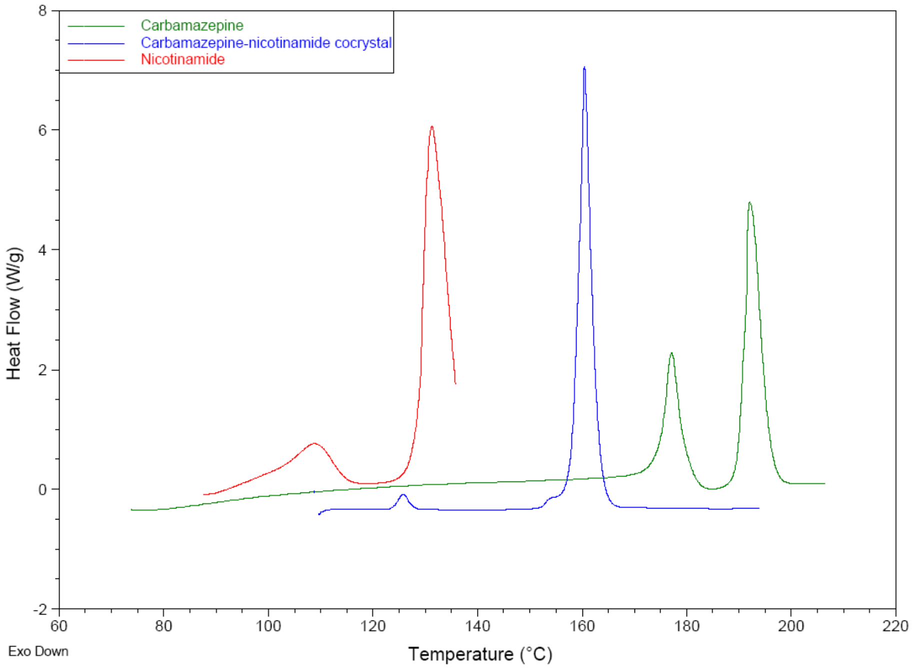

Fig. 5.18 DSC thermogram of carbamazepine-nicotinamide cocrystal and components.

These analytical results confirm the successful cocrystallisation of carbamazepine-nicotinamide cocrystal system and that the anti-solvent/solvent cocrystallisation approach can be used with different H-bonding motifs and not just carboxylic acid/amine H-bonding motif.

5.2.3 2-Aminopyrimidine-salicylic acid salt

Cocrystal and salts are both multi-component crystals differing in the position of the hydrogen bridge atom in the final multi-component crystal molecule; the hydrogen atom position depends on the pKa difference between the components in the multi-component crystal. Validating the anti-solvent/solvent process with an API salt molecule will increase the scope of applications for this process.

The salt system selected was 2-aminopyrimidine-salicylic acid salt. The bonding motif in the 2-aminopyrimidine-salicylic acid salt is the carboxylic acid/amine (Fig. 5.19) similar to the caffeine-salicylic acid cocrystal and the caffeine-oxalic acid cocrystal system bonding motif. 2-aminopyrimidine is a derivative of pyrimidine family, which shows biological activities used in anti-tumour therapies; derivatives of 2-aminopyrimidine are marketed as anti-cancer drugs[17].

2-Aminopyrimidine and salicylic acid forms a 1:1 salt and has an entry name of LEWROU[12] with an available reference PXRD pattern (Fig. 5.20) that was used to confirm formation of the salt. A commercial sample of 2-aminopyrimidine was analysed by PXRD (Fig. 5.21) showing no diffraction peak below $2\theta = 10^{o}$, ATR-FTIR (Figs. 5.24 and 5.25) and DSC (Fig. 5.26) showing an onset melt temperature of 121.5 ^{o}C, which is close to the reported melting point range of 122-126^{o}C. Salicylic acid has been discussed in section 5.2.1.

2-aminopyrimidine and salicylic acid were mixed in a 1:1 molar ratio and added to the 2.2 wt % methanol in cyclohexane in the SVC. After 30 minutes of oscillatory mixing, the slurry was filtered, dried and the powder analysed by PXRD (Fig. 5.22). The solid loading was 6.4 wt % and the solid recovery after drying was 90.6 %.

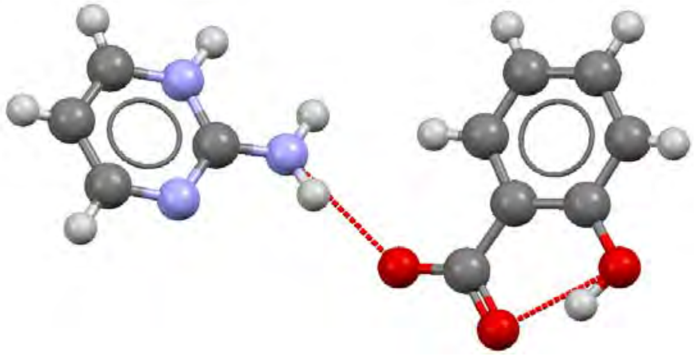

Fig. 5.19 Bonding motif of 2-aminopyrimidine-salicylic acid salt (LEWROU)[12].

A comparison of the powder pattern from the SVC salt formation experiment and the reference salt spectrum (Fig. 5.23) shows a good match between both pattern. The SVC sample was analysed by ATR-FTIR and overlaid with the pattern of 2-aminopyrimidine and salicylic acid (Figs. 5.24 and 5.25). The FTIR comparison in the region between 2000 to 4000 cm^{-1} (Fig. 5.25), shows the disappearance of the strong

2-aminopyrimidine peaks at 3156.9 cm^{-1} corresponding to the NH_2 stretch band and emergence of a broad peak between 2200 cm^{-1} and 2500 cm^{-1} for the corresponding NH stretch in the ammonium (NH^+) group[18,19] in the ring. The DSC analysis of the SVC sample is shown in Fig. 5.26 with an onset melting point of 92.3 ^{o}C and shows that 2-aminopyrimidine-salicylic acid salt has a lower melting point than both components.

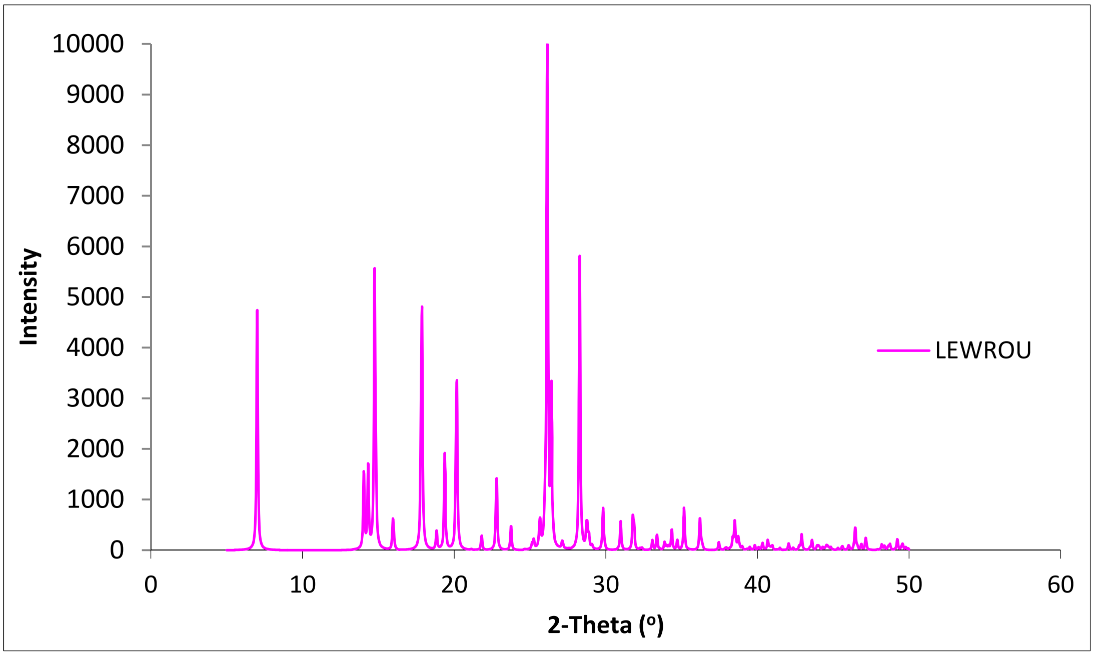

Fig. 5.20 PXRD pattern for 2-aminopyrimidine-salicylic acid salt (LEWROU[12]).

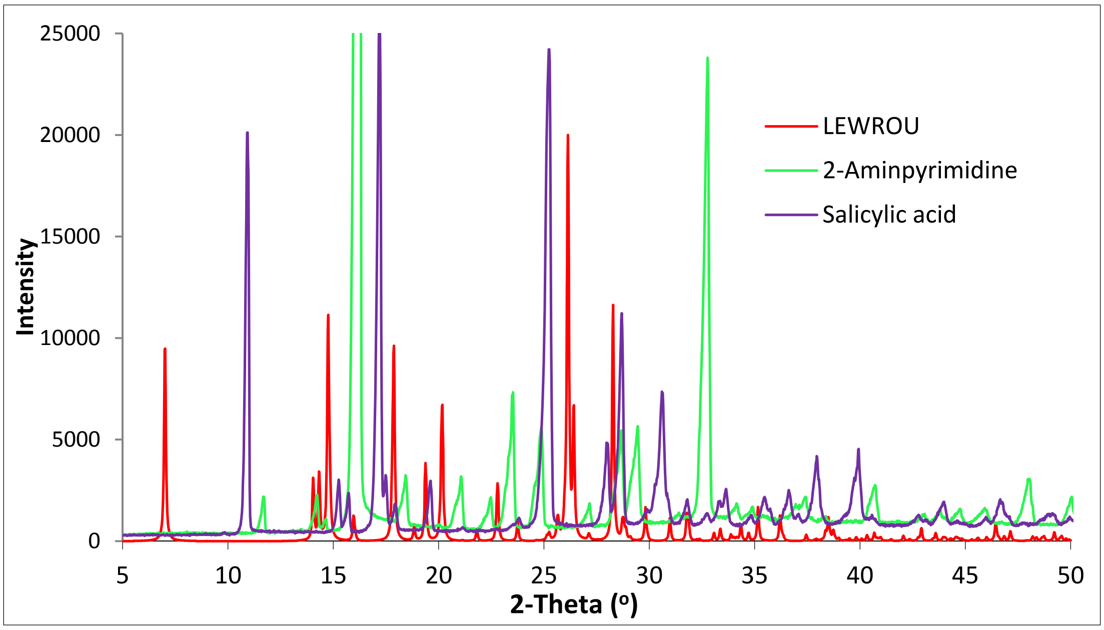

Fig. 5.21 Comparing powder pattern for 2-aminopyrimidine, salicylic acid and 2-aminopyrimidine-salicylic acid salt reference pattern.

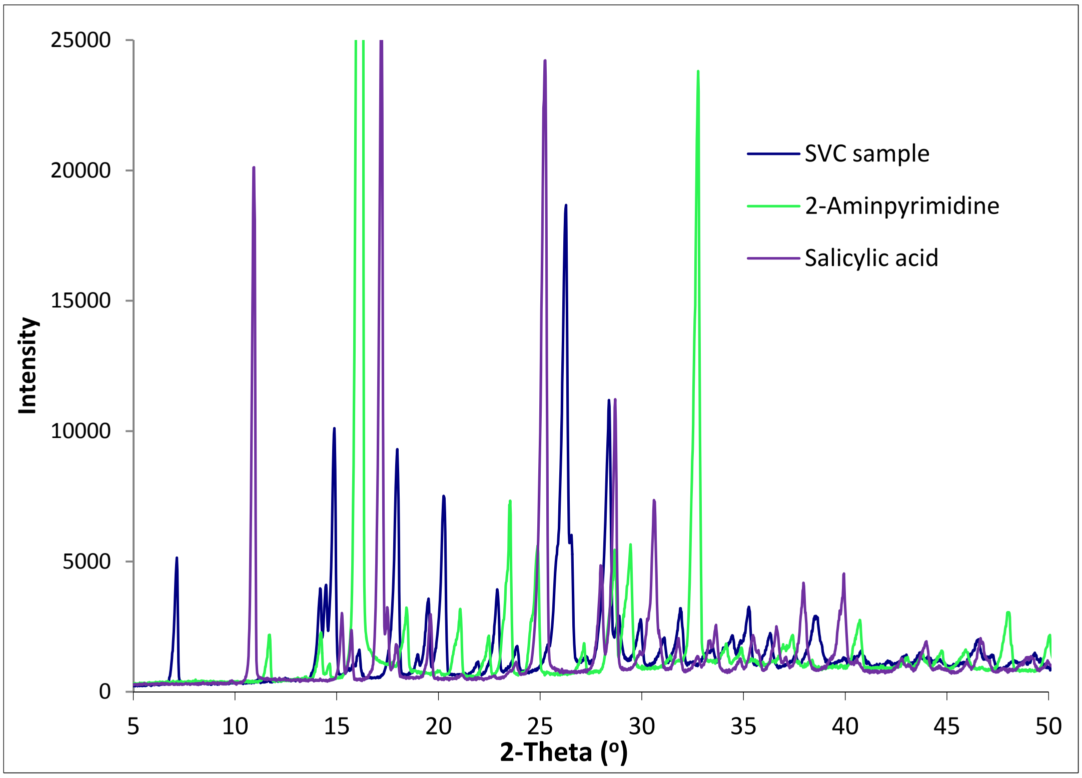

Fig. 5.22 PXRD pattern for 2-aminopyrimidine-salicylic acid salt from SVC experiment.

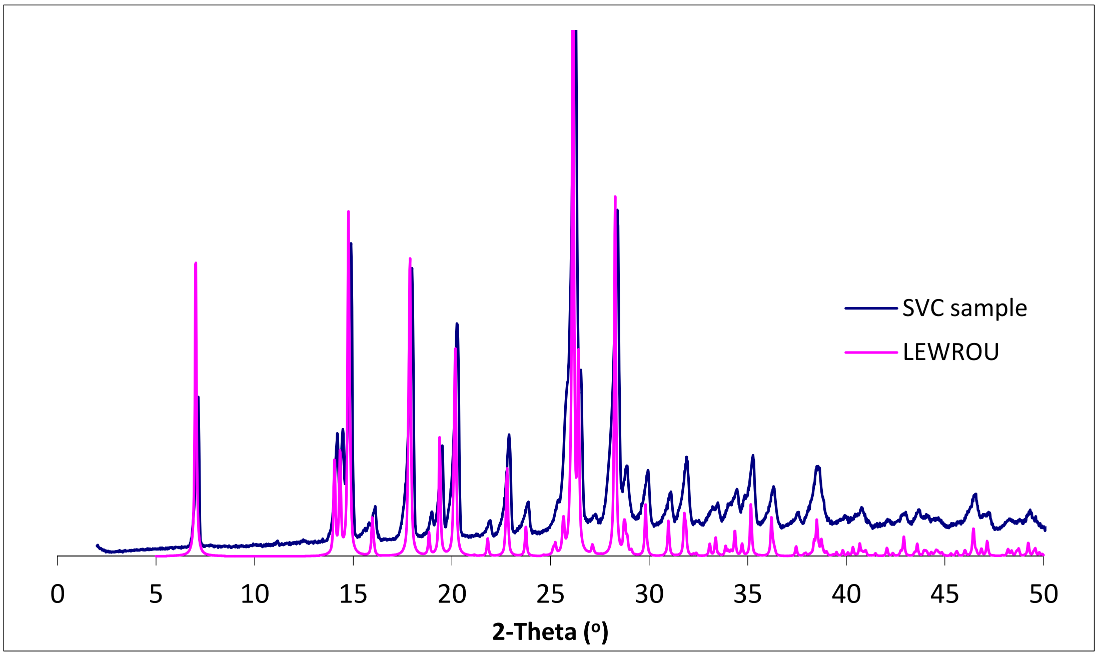

Fig. 5.23 Comparing powder pattern of SVC sample and reference pattern.

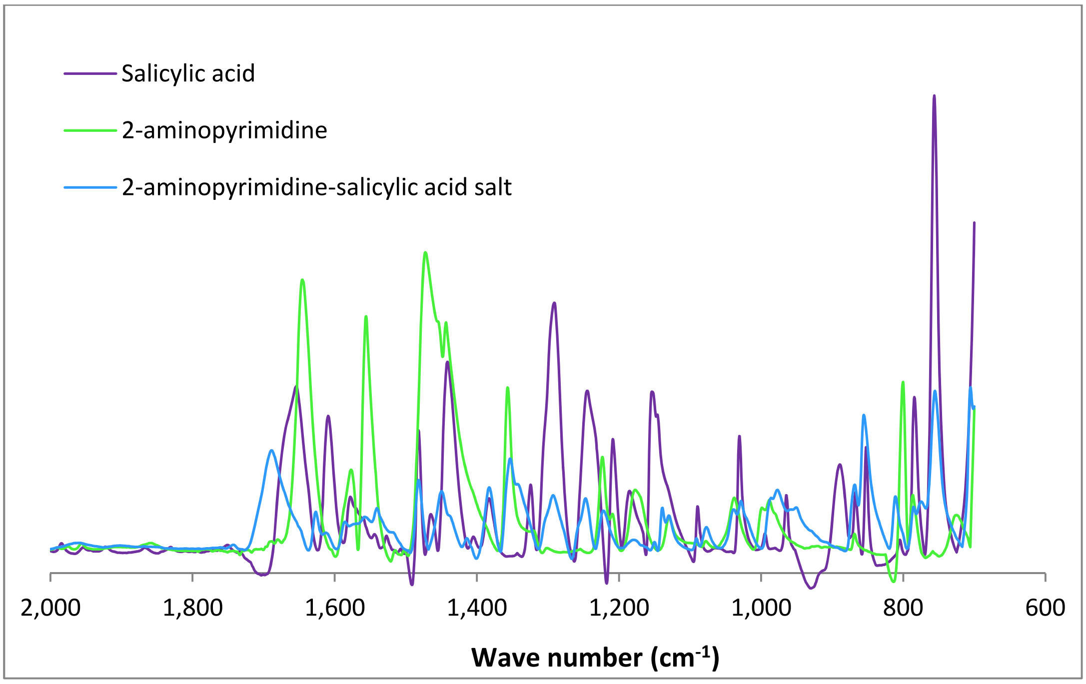

Fig. 5.24 Comparing FTIR spectra for 2-aminopyrimidine-salicylic acid salt between 600 – 2000 cm^{-1} region.

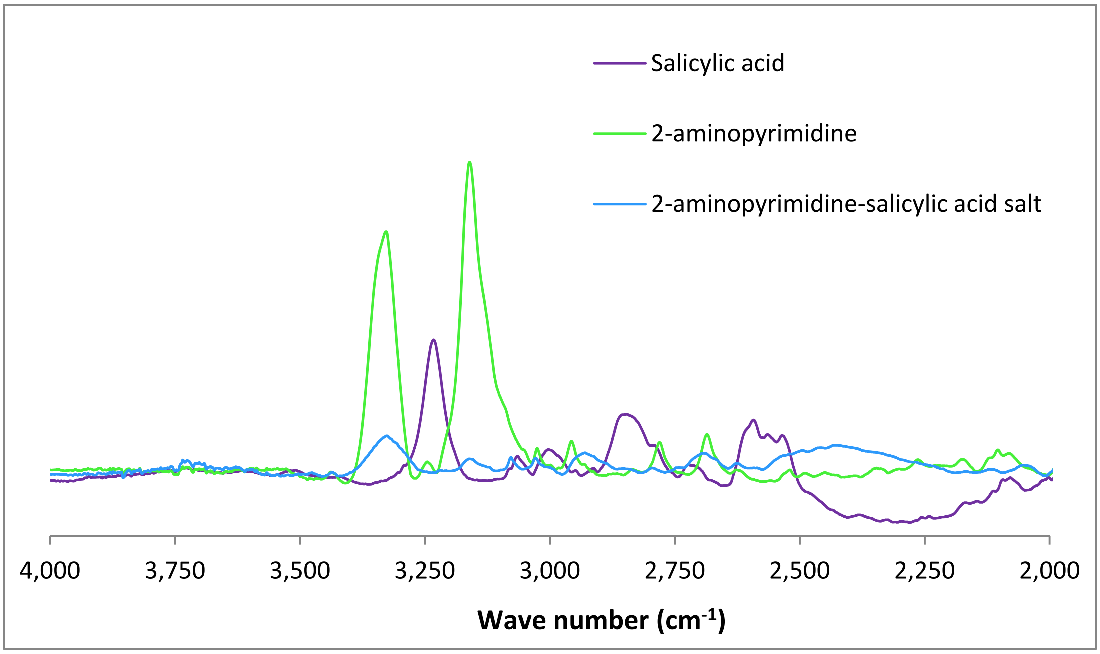

Fig. 5.25 Comparing FTIR spectra for 2-aminopyrimidine-salicylic acid salt between 2000-4000cm^{-1} region.

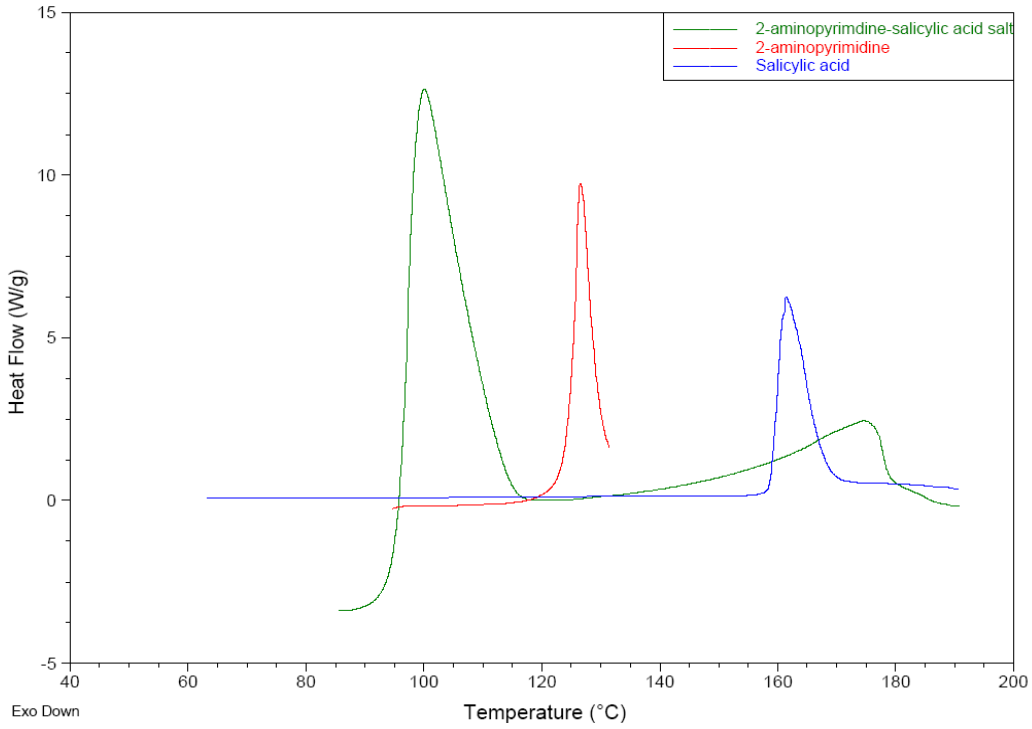

Fig. 5.26 DSC thermogram of laboratory sample of 2-aminopyrimidine-salicylic acid salt overlaid with components.

These results confirm the successful formation of 2-aminopyrimidine-salicylic acid salt using the anti-solvent/solvent mixture and expand the scope of application of this approach from cocrystal to salt formation.

5.3 Particulate processing unit (PPU)

This attempt to scale up the anti-solvent/solvent cocrystallisation in the particulate processing unit (PPU) with the oscillatory baffle technology, represents to the best of the author’s knowledge, the first attempt at trying to introduce a slurry into a static baffle reactor system on a large scale for continuous cocrystallisation; other attempts at scaling up cocrystallisation using static mixing baffle technology have introduced the cocrystal components as a solution dissolved in a suitable solvent and initiate cocrystallisation by cooling[20], or introduction of an anti-solvent or seeding[21].

A picture of the PPU is shown in chapter 2. The PPU experiments were done by making up 2 x 7 litre slurries of the cocrystal component with solid loadings between 2.5-5 wt %.The frequency of the oscillation pump was set at 2 Hz and the delay between slurry dosing from the pneumatic valves was set between 10 and 20 seconds (see section 2.1.2).

5.3.1 Caffeine-oxalic acid cocrystal

The caffeine-oxalic acid cocrystal system was used for optimising the anti-solvent/solvent cocrystallisation process in chapter 4. This system was a challenge to scale-up in the PPU because of the high density of oxalic acid (1.9 g/cm^3), which makes oxalic acid crystals prone to settling in the PPU reactor system, causing blockage in the pumps. Also the caffeine-oxalic acid system required stoichiometric dousing of caffeine and oxalic acid in a 2:1 mol ratio (Fig. 5.27), which was not easy to achieve with good precision. A reference powder pattern of caffeine-oxalic acid cocrystal system (Fig. 5.28) was obtained from the literature using single crystal x-ray diffraction data and used to check for cocrystal formation in the PPU sample.

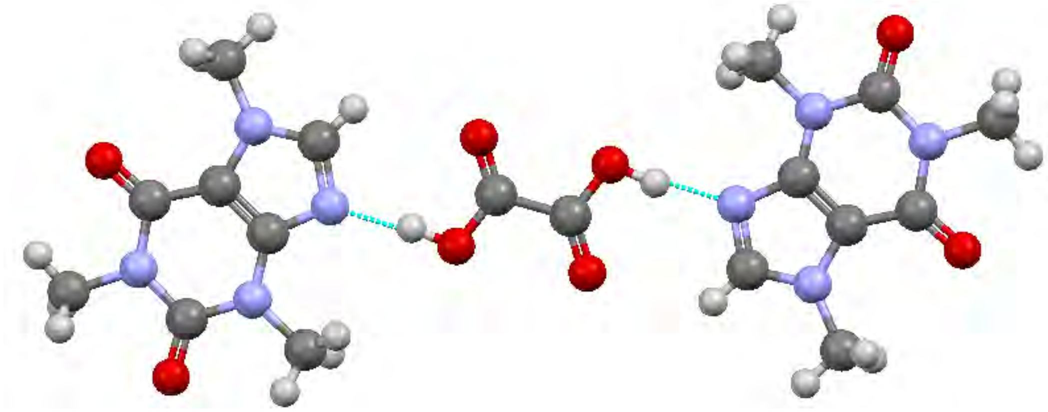

Fig. 5.27 Building motif of caffeine-oxalic acid cocrystal visualised using Mercury.

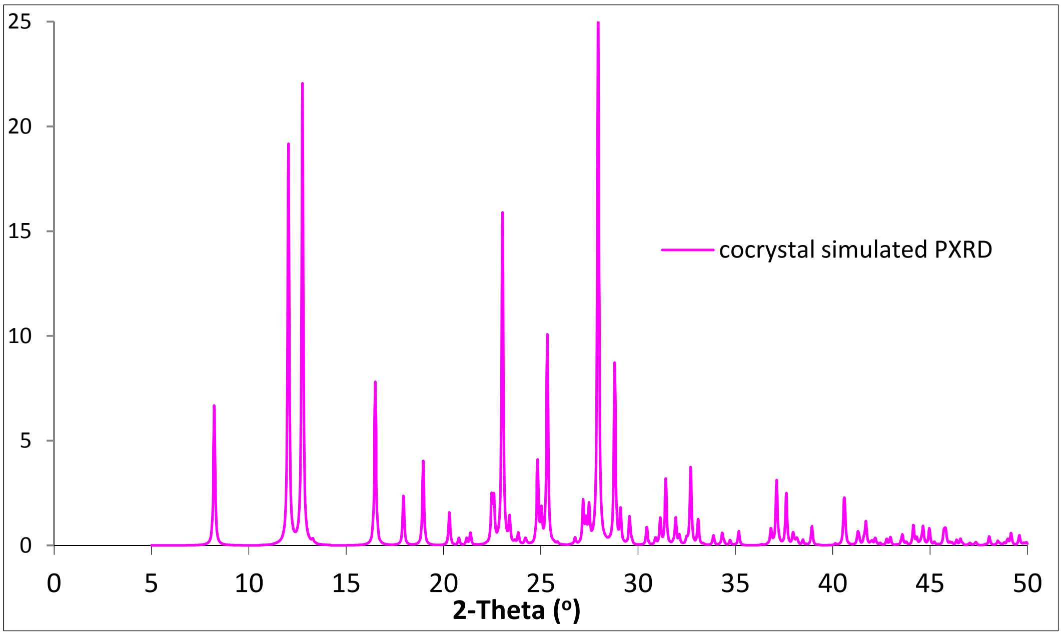

Fig. 5.28 Powder pattern for caffeine-oxalic acid cocrystal simulated from single crystal analysis.

A commercial sample of oxalic acid was analysed by PXRD (Fig. 5.29) and shows no diffraction peak below 2θ=14°; ATR-FTIR (Figs. 5.32 and 5.33) and DSC (Fig. 5.34) showing two onset melt temperature, the first small peak at 95.17°C corresponding to oxalic acid dihydrate[22] and the second larger peak at 186.93°C corresponding to anhydrous oxalic acid, indicating the sample had a small amount of oxalic acid dihydrate impurity in it. Caffeine analysis has been discussed in section 5.2.1.

To keep the oxalic acid in suspension, a low solid loading of 2.5 *wt* % was used .The PPU sample from the caffeine/oxalic acid cocrystallisation was analysed by PXRD (Fig. 5.30) and compared with reference spectrum (Fig. 5.31) which was a good match but showed some amount of residual caffeine in the sample. The FTIR spectra for caffeine-oxalic acid cocrystallisation spectrum was overlaid with the FTIR spectra of its components (Figs. 5.32 and 5.33), the region between 1800 cm^{-1} to 3600 cm^{-1} shows two broad peaks at about 1900 cm^{-1} and 2350 cm^{-1} present in the caffeine-oxalic acid cocrystal, which are characteristics of strong un-ionised O-H stretching for carboxylic acids[8].

The DSC analysis of the PPU cocrystallisation sample (Fig. 5.34) shows two onset melting point, the first peak at 206.5 °C for the cocrystal and the second peak at 235.5 °C corresponding to caffeine, when the thermogram is overlaid with the thermogram for its components, the cocrystal has an intermediate melting point[23].

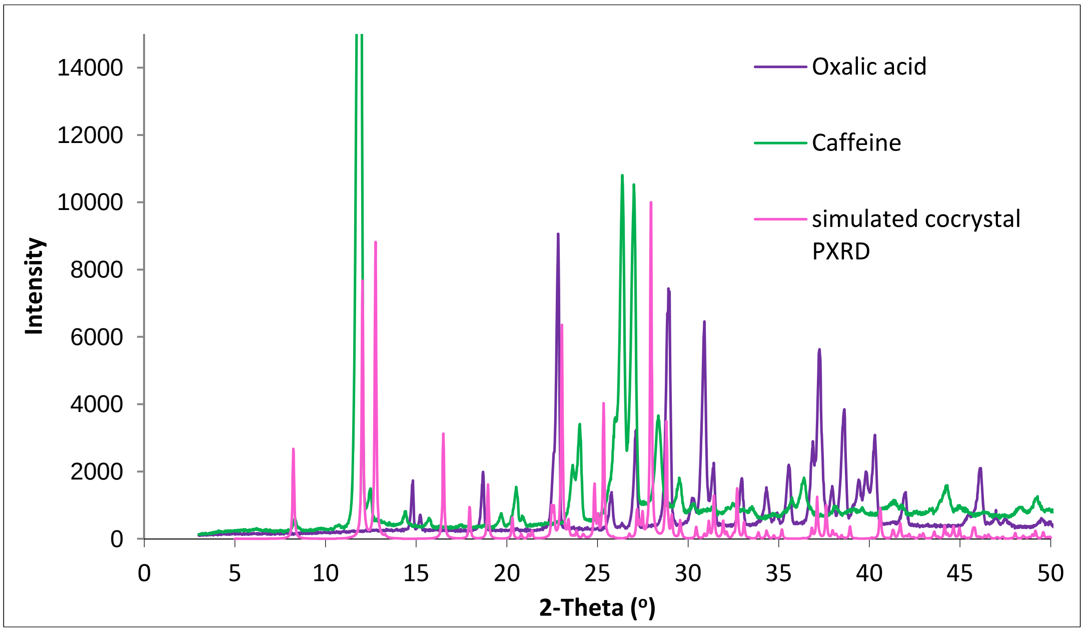

Fig. 5.29 PXRD pattern for commercial sample of oxalic acid, caffeine and caffeine-oxalic acid cocrystal (simulated pattern).

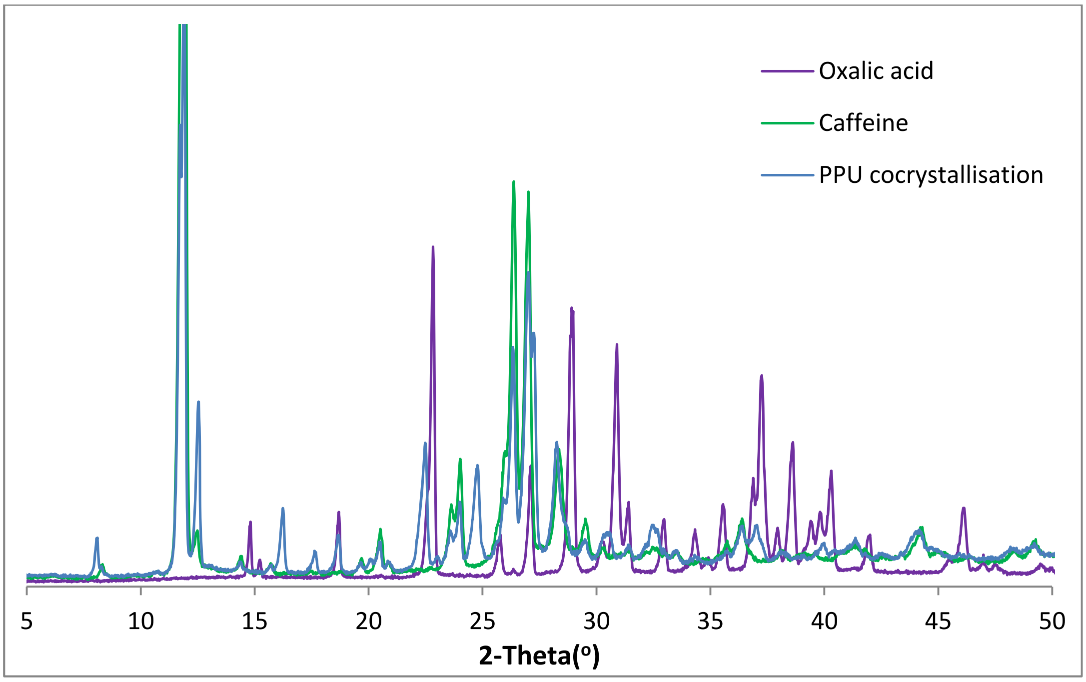

Fig.5.30 PXRD pattern of PPU sample of caffeine/oxalic acid cocrystallisation experiment.

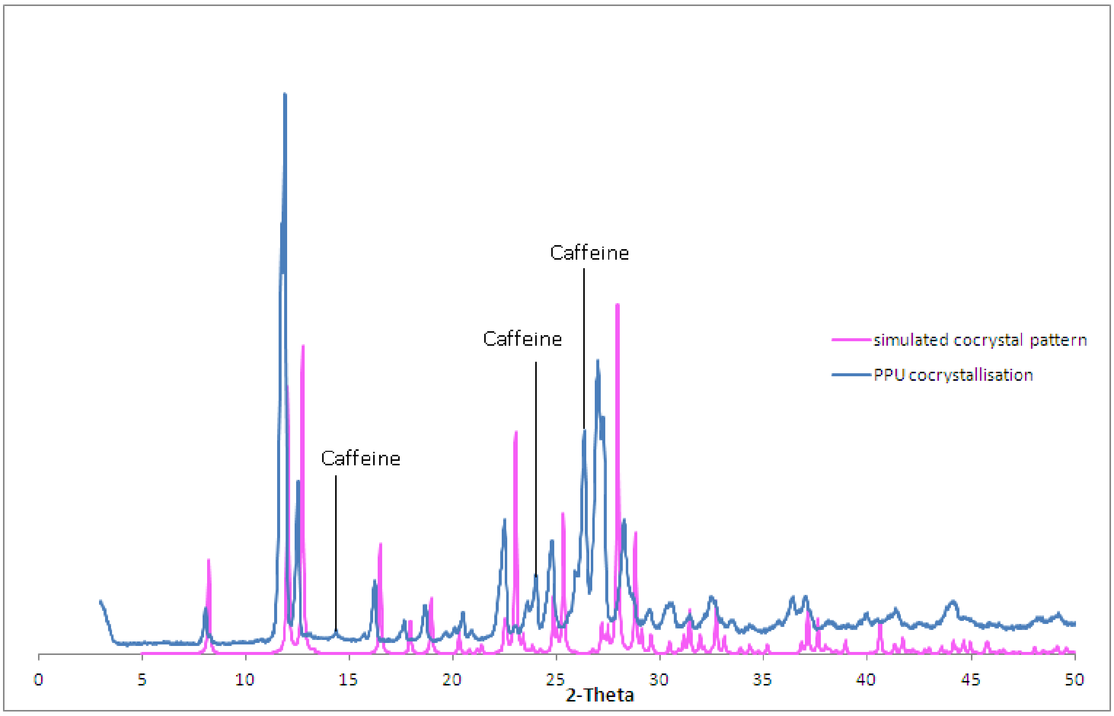

Fig. 5.31 Comparing PPU and for caffeine-oxalic acid cocrystal reference spectrum.

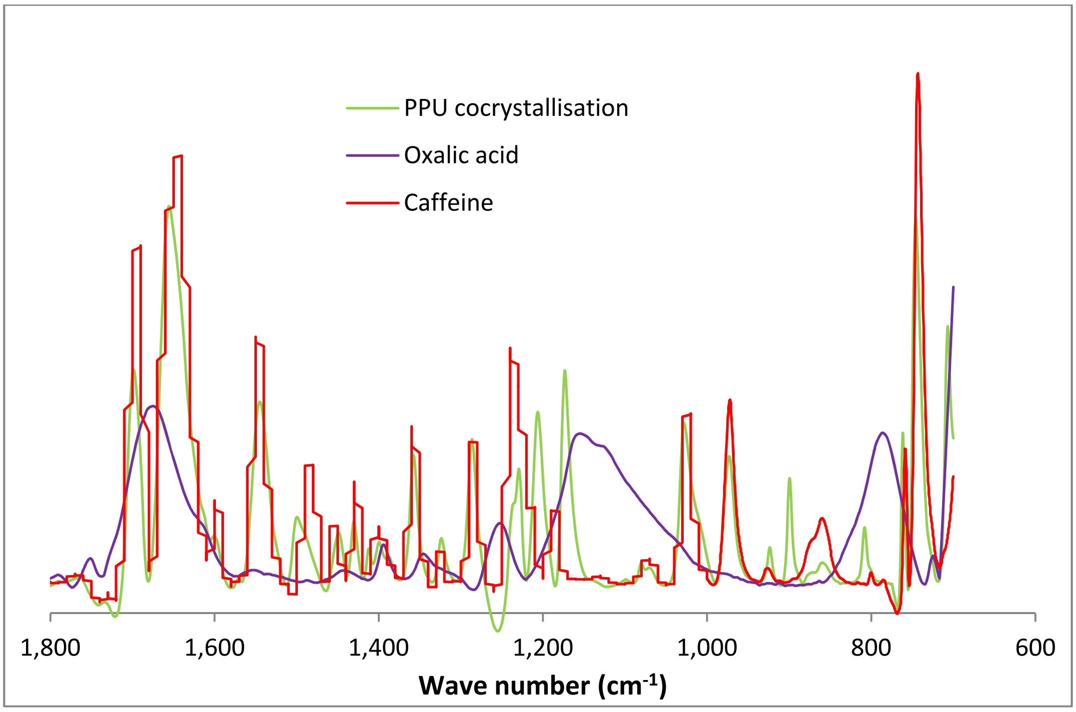

Fig. 5.32 Comparing FTIR pattern for caffeine-oxalic acid cocrystallisation 600-1,800cm^{-1} region.

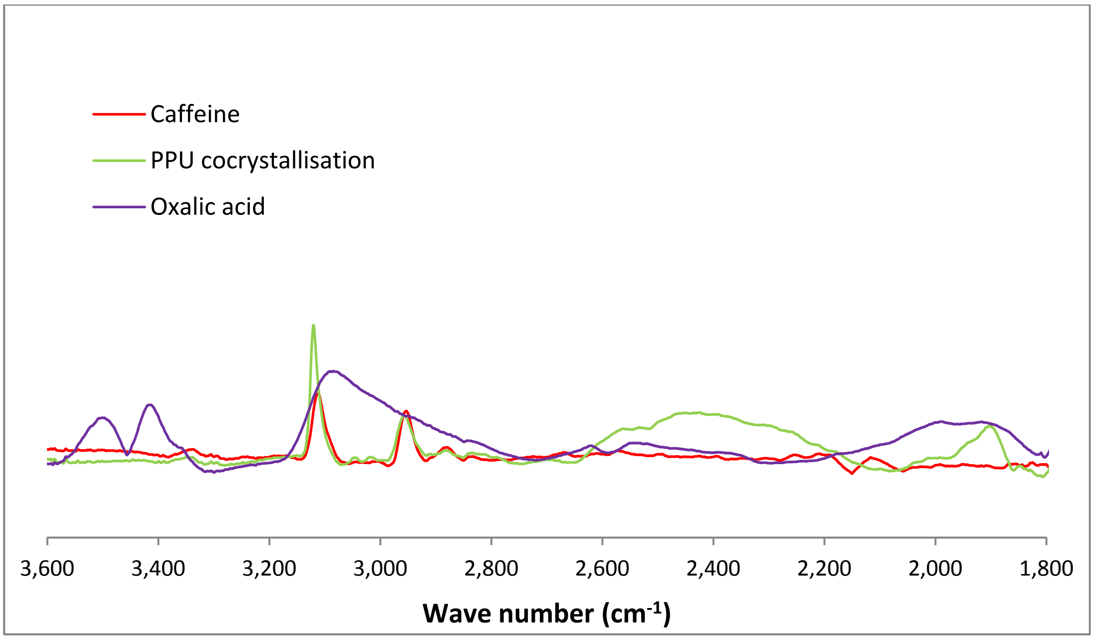

Fig. 5.33 Comparing FTIR spectra for caffeine-oxalic acid cocrystallisation 1800-3600cm^{-1} region.

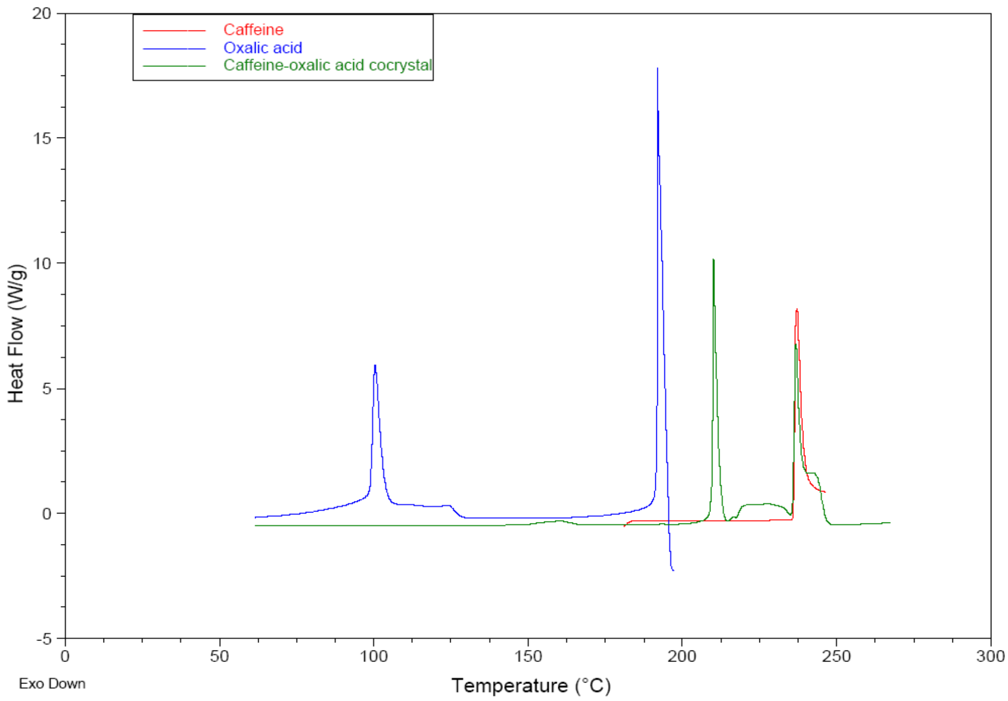

Fig. 5.34 DSC thermogram of caffeine-oxalic acid cocrystal overlaid with components.

These results confirm the cocrystallisation of caffeine-oxalic acid cocrystal in the PPU.

5.3.2 Caffeine-salicylic acid cocrystal

The caffeine-salicylic cocrystal system was scaled up in the PPU. The PPU experiment also examined the effect of methanol. Two PPU experiments were carried out and samples taken and analysed by PXRD. The first experiment was with only cyclohexane and the second experiment was in 2.2 *wt* % methanol in cyclohexane mixture. The powder patterns for both experiments were compared (Fig. 5.35). The powder pattern for the experiment in cyclohexane has a higher level of residual salicylic acid than in the sample from the experiment with methanol agreeing with the result obtained on the small scale caffeine-salicylic acid cocrystallisation. This shows that the role of methanol (solvent) in facilitating cocrystallisation is carried through to the large scale. The PXRD pattern from the experiment with methanol was compared with a reference spectrum of caffeine-salicylic acid (Fig. 5.36) and shown to be a good match. The FTIR spectrum of the PPU sample and DSC thermogram were the same as for the SVC experiment shown in section 5.2.1.

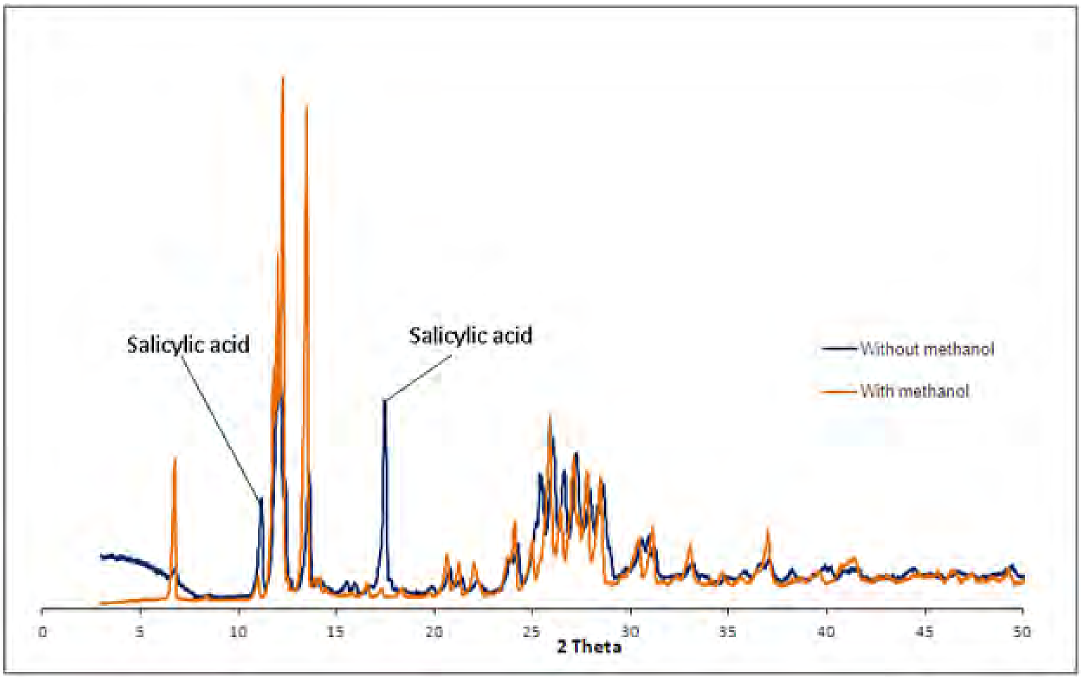

Fig. 5.35 Comparing powder pattern for two caffeine-salicylic acid PPU experiment.

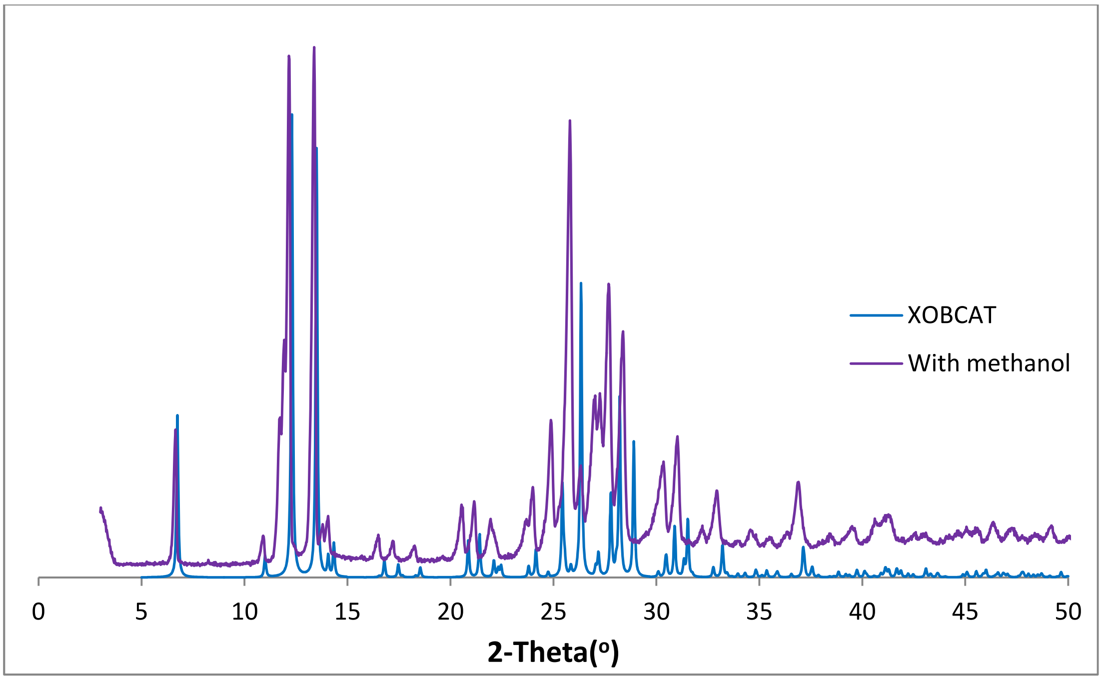

Fig. 5.36 PXRD of PPU cocrystallisation of caffeine-salicylic acid sample and reference spectrum (XOBCAT).

5.3.2 Theophylline-salicylic acid cocrystal

Theophylline belongs to the xanthine family, the same as caffeine, and is also known as methylxantine. Theophylline is used in the treatment of asthma. Theophylline forms a 1:1 cocrystal with salicylic acid (Fig. 5.37) and has an entry name KIGLES[18] in CDS. A reference powder pattern of theophylline-salicylic acid cocrystal (Fig. 5.38) was obtained and used for confirming the formation of the cocrystal. Theophylline monohydrate has two entry in Mercury with the same PXRD (Fig. 5.39) which showed no diffraction peak below 2θ=8.9^{o}, ATR-FTIR (Figs. 5.43 and 5.44) and DSC (Fig. 5.45), with the latter showing two endothermic peaks, the first being a small peak at 59.8 ^{o}C corresponding to dehydration of theophylline monohydrate and the second being at 270.78^{o}C and corresponding to theophylline melting.

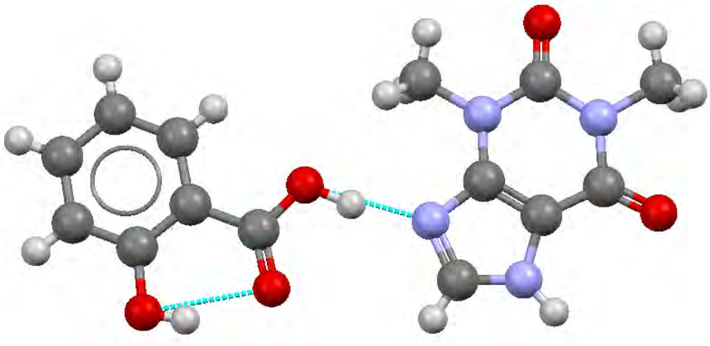

Fig. 5.37 Bonding motif of theophylline-salicylic acid cocrystal.

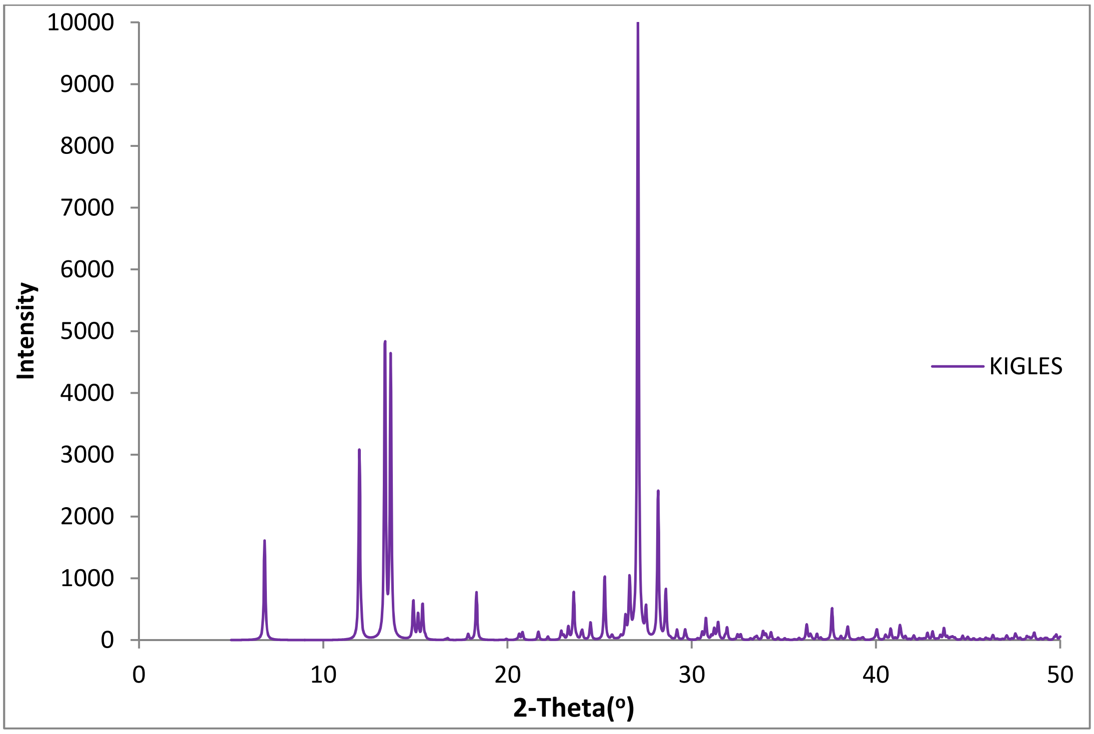

Fig. 5.38 PXRD pattern for theophylline-salicylic acid cocrystal (KIGLES).

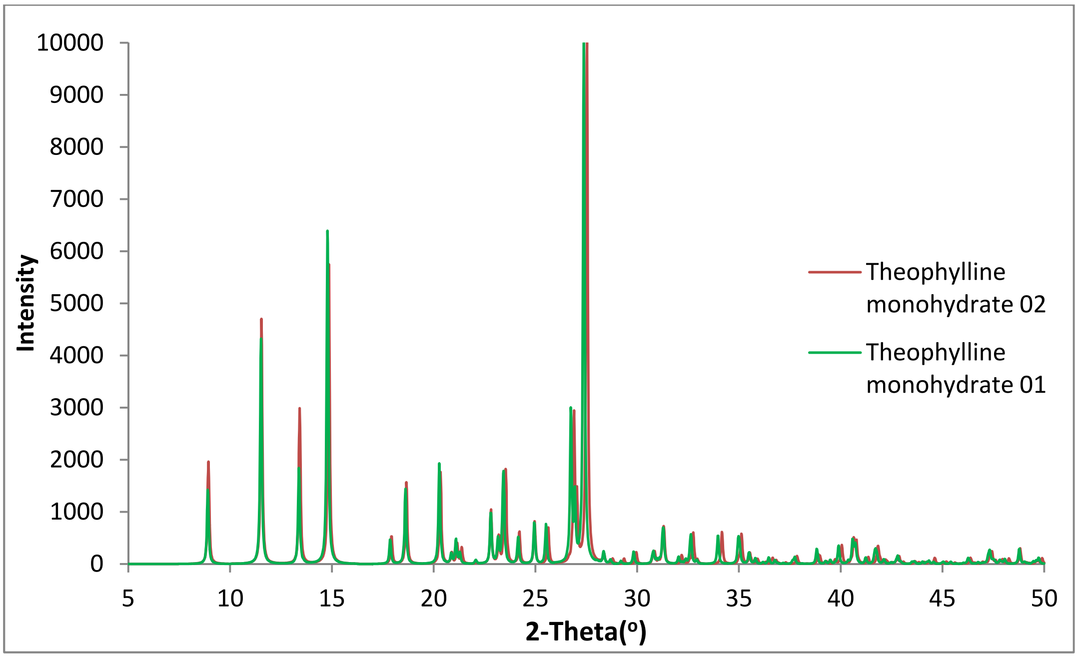

Fig. 5.39 Reference pxrd pattern of theophylline monohydrate.

Similar to the previous PPU validation process, two theophylline-salicylic acid cocrystallisation experiments were carried out and samples taken and analysed by PXRD. The first experiment was with only cyclohexane and the second experiment was in 1 $wt\,\%$ methanol in cyclohexane mixture. The powder pattern for both experiments were compared (Fig. 5.40), the powder pattern for the experiment in cyclohexane had a higher level of residual salicylic acid than in the sample from the experiment with methanol, agreeing with the previous observation for caffeine-salicylic acid cocrystal and caffeine-oxalic acid cocrystal, further confirming the role of the methanol (solvent) in facilitating cocrystallisation. The PXRD patterns from both experiments were compared with a reference spectrum of caffeine-salicylic acid (Figs. 5.41 and 5.42) and the experiment in methanol found to be a better match than the experiment in only cyclohexane.

The FTIR spectrum for theophylline-salicylic acid cocrystallisation PPU experiment with methanol was overlaid with the spectra of its component (Figs. 5.43 and 5.44), focusing on the region between 1750 cm^{-1} and 3600 cm^{-1}, it shows a broad peak at about 1900 cm^{-1}, which is characteristic of O-H stretching of un-ionised strong hydrogen bonding[7,8] and is not present in theophylline monohydrate. The broad peak at 3384 cm^{-1} that corresponds to the NH stretching band[18] in theophylline monohydrate disappears and a new broad peak appears at 3170 cm^{-1} corresponding to the new N---OH hydrogen bonding[22]. The DSC analysis (Fig. 5.45) shows an onset melting point of 184.0 °C, which is relatively close to the reported melting point of 189 °C[4]. When this thermogram is overlaid with those from its components, the theophylline-salicylic acid cocrystal is seen to have an intermediate melting point.

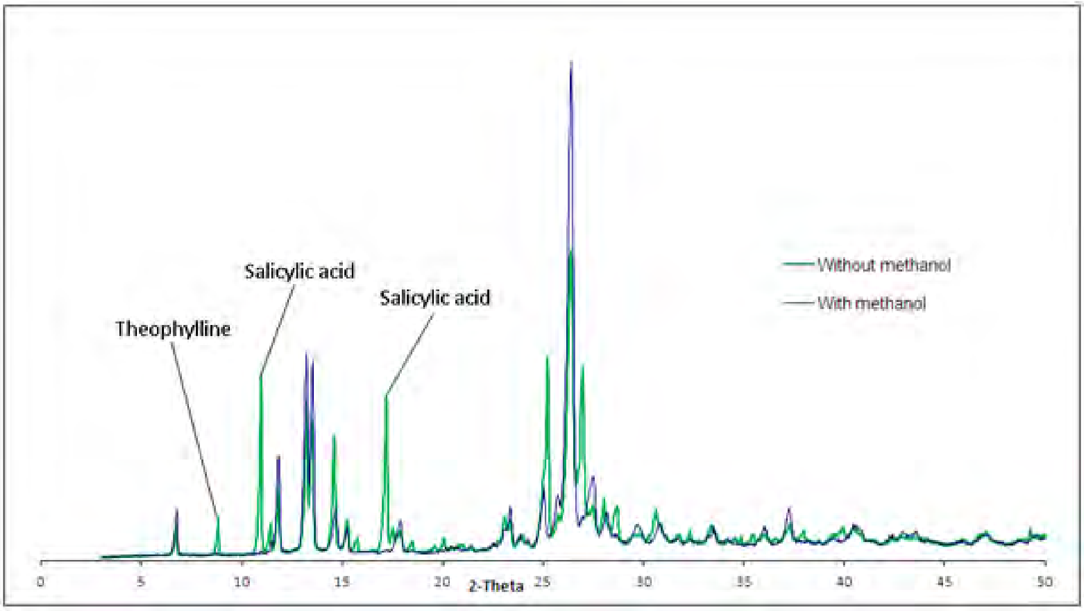

Fig. 5.40 Comparing powder pattern from both PPU experiments.

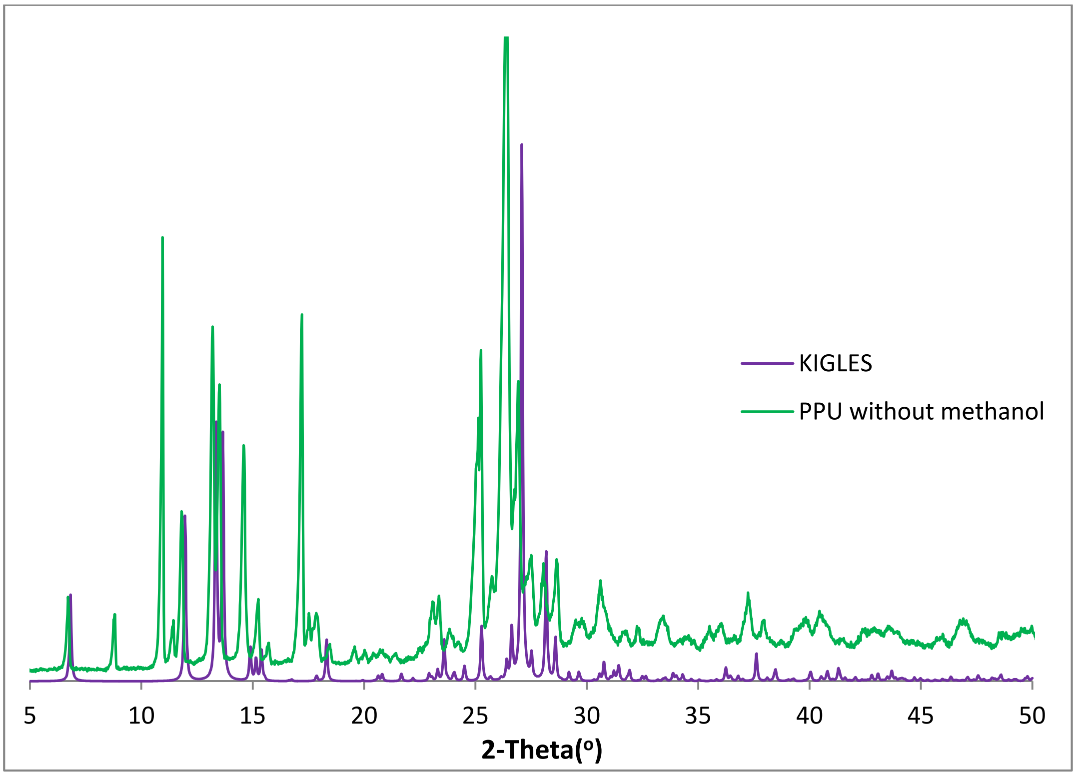

Fig. 5.41 A comparison of PPU cocrystallisation of theophylline-salicylic acid cocrystal without methanol and reference (KIGLES).

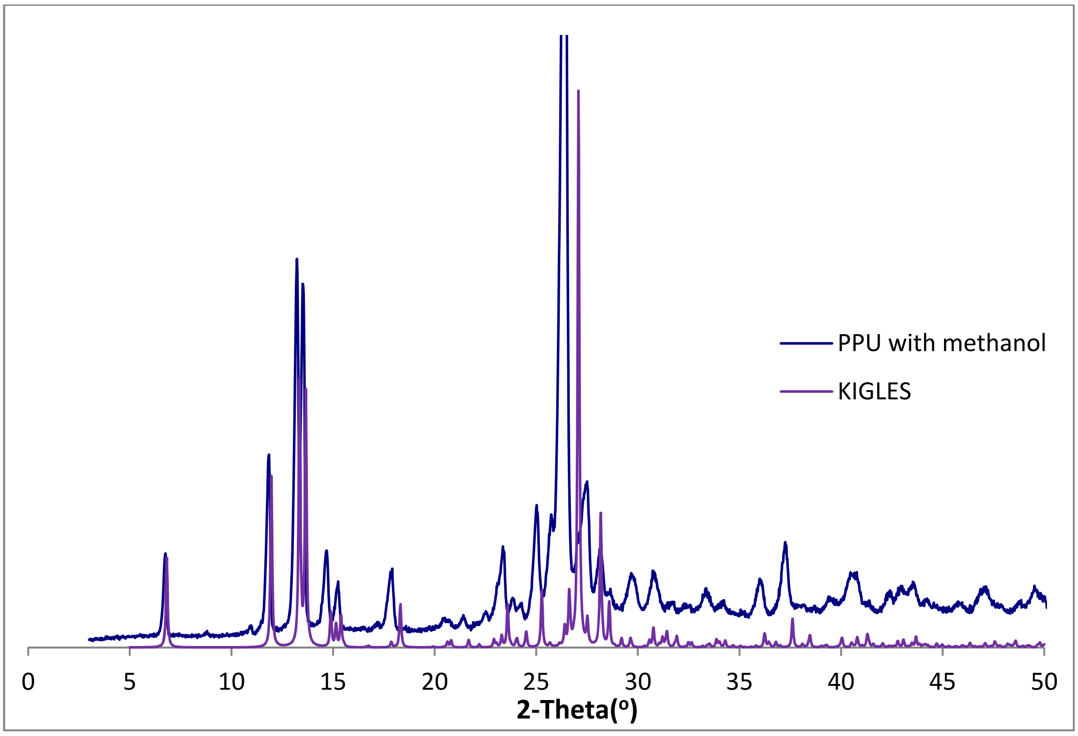

Fig. 5.42 PXRD comparison of PPU cocrystallisation with methanol sample and Mercury.

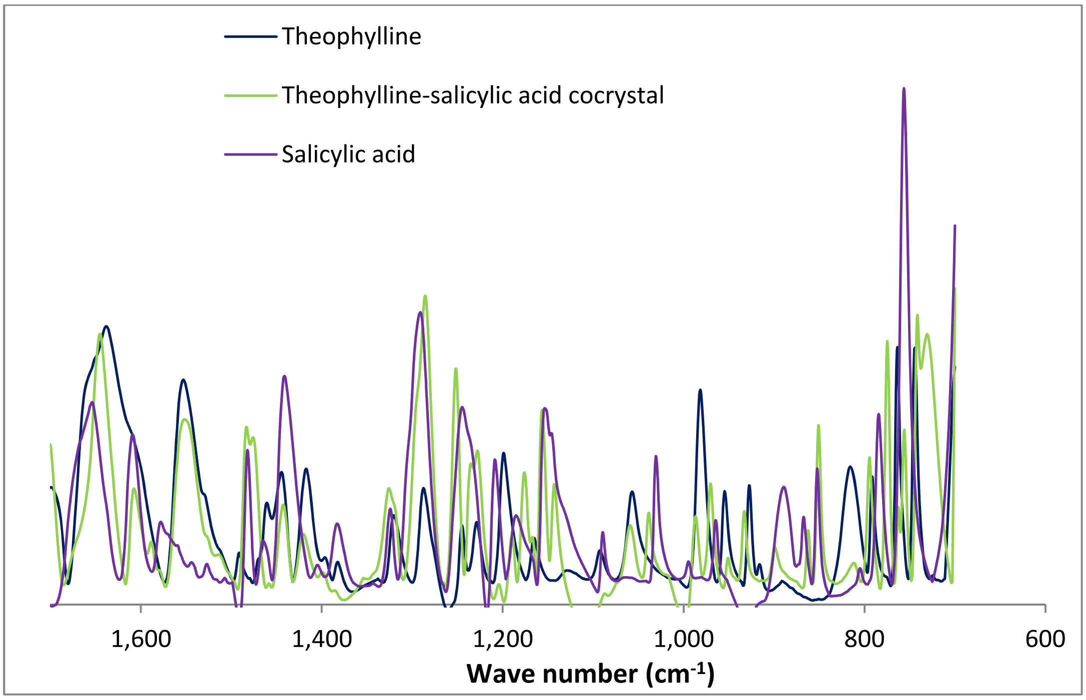

Fig. 5.43 Theophylline-salicylic acid cocrystallisation FTIR spectra comparison between 600 – 1,700 cm^{-1} region.

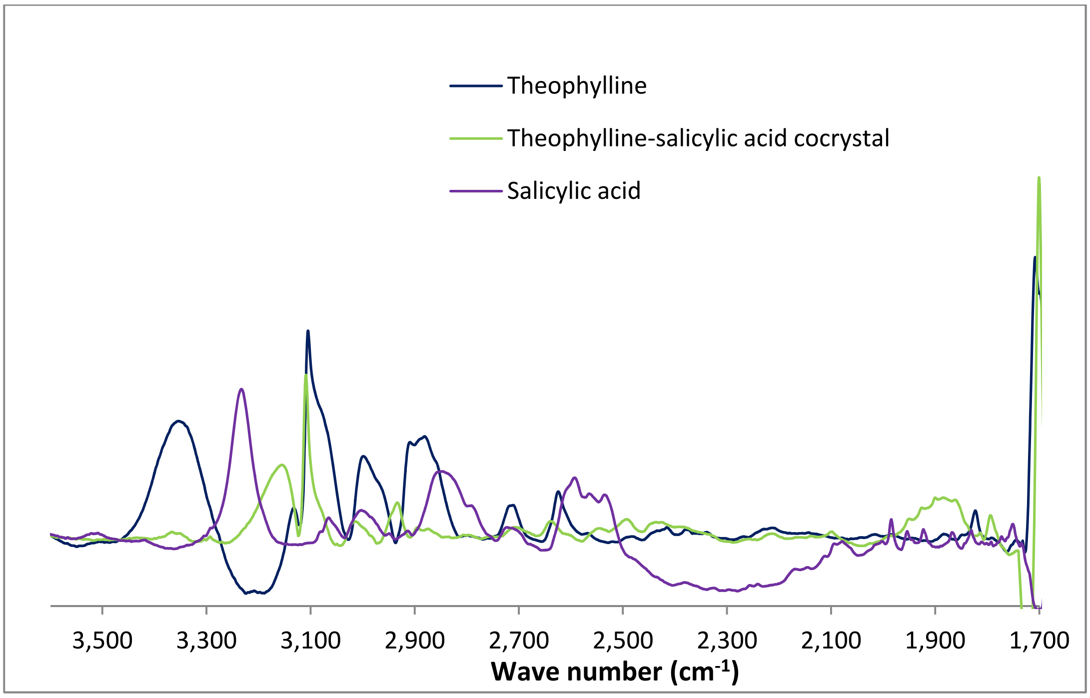

Fig. 5.44 Theophylline-salicylic acid cocrystallisation FTIR comparison between 1700 - 3600 cm^{-1} region.

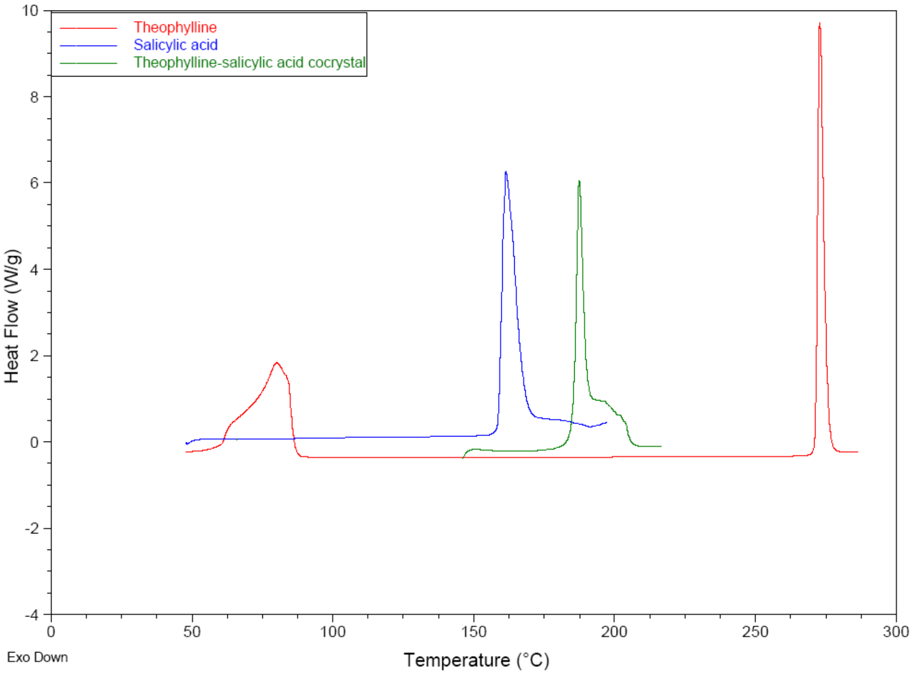

Fig. 5.45 DSC thermogram of theophylline-salicylic acid cocrystal overlaid with components.

5.4 Conclusion

In this chapter, four cocrystals systems and one salt system, namely: caffeine-salicylic acid cocrystal, caffeine-oxalic acid cocrystal, carbamazepine-nicotinamide cocrystal, theophylline-salicylic acid cocrystal and 2-aminopyrimidine-salicylic acid salt, were crystallised using the anti-solvent/solvent approach with methanol as the solvent and cyclohexane as the anti-solvent. Salt formation and cocrystallisation were confirmed by the different analytical techniques: DSC, FTIR and PXRD.

The role of methanol in the cocrystallisation of caffeine-salicylic acid on small scale in the SVC and large scale in the PPU was investigated by comparing PXRD analysis of experiments carried out with and without methanol. For caffeine-salicylic acid cocrystal system, the level of residual salicylic acid in the isolated solid were higher in both the SVC and PPU experiments without methanol; the same result was also observed in the PPU cocrystallisation of theophylline-salicylic acid. These results show that the presence of the methanol facilitates cocrystallisation on both the small and large scale. This observation rules out a purely solid state cocrystallisation process arising from solid particles grinding together. Instead, at least one of the coformer components must be in the solute state for the cocrystallisation to proceed at a reasonable rate.

The successful salt formation of 2-aminopyrimidine-salicylic salt increases the scope of the application of the anti-solvent/solvent approach which may provide some advantages over the traditional method of adding anti-solvent to a solution of the salt component.

The technology described in this chapter and its application in cocrystal and salt formation has been patented by CPI (patent filing number: GB1222287.3), the industrial partner in this research.

References

(1) Serajuddin, A. T. M. *Advanced Drug Delivery Reviews* **2007**, *59*, 603.

(2) Hoff, C.; Lee, S. *Handbook of Pharmaceutical salts: Properties, Selection and Use*; Stahl, P. H., Wermuth, C. G., Eds.; Wiley-VCH: Switzerland, 2002, p 191.

(3) Stahl, P. H.; Wermuth, C. G. In *Handbook of Pharmaceutical salts: Properties, Selection and Use*; Stahl, P. H., Wermuth, C. G., Eds.; Wiley-VCH: Switzerland, 2002, p 1.

(4) Enxian, L.; Rodríguez-Hornedo, N.; Raj, S. *Crystengcomm* **2008**, *10*, 665.

(5) Bucar, D.; Henry, R. F.; Lou, X.; Duerst, R. W.; MacGillivray, L. R.; Zhang, G. Z. *Cryst. Growth Des.* **2009**, *9*, 1932.

(6) Warner, T. D.; Mitchell, J. A. *Proceedings from the National Academy of Sciences of the United State of America* **2002**, *99* 13371.

(7) Schultheiss, N.; Newman, A. *Cryst. Growth Des.* **2009**, *9*, 2950.

(8) Johnson, S. L.; Rumon, K. A. *Thc Journal of Physical Chemistry* **1965**, *69*, 74.

(9) Grzesiak, A. L.; Lang, M.; Kim, K.; Matzger, A. J. *Journal of Pharmaceutical Sciences* **2003**, *92*, 2260.

(10) Scott L. Childs; Peter A. Wood; Naı´r Rodrı´guez-Hornedo; L. Sreenivas Reddy; Hardcastle, K. I. *Cryst. Growth Des.* **2009**, *9*, 1869.

(11) Fleischman, S. G.; Kuduva, S. S.; McMahon, J. A.; Moulton, B.; Walsh, R. B.; Rodrı´guez-Hornedo, N.; Zaworotko, M. J. *Cryst. Growth Des.* **2003**, *6*, 909.

(12) Macrae, C. F.; Bruno, I. J.; Chisholm, J. A.; Edgington, P. R.; McCabe, P.; Pidcock, E.; Rodriguez-Monge, L.; Taylor, R.; van de Streek, J.; Wood, P. A. *J. Appl. Cryst.* **2008** *41*, 466.

(13) Wang, I.; Lee, M.; Sim, S.; Kim, W.; Chun, N.; Choie, G. J. *International Journal of Pharmaceutics* **2013**, *450*, 311.

(14) Li, J.; Bourne, S. A.; Caira, M. R. *Chemical Communications* **2011**, *47*, 1530.

(15) Kong, J.; Yu, S. *Acta Biochimica et Biophysica Sinica* **2007**, *39*, 549.

(16) Rahman, Z.; Agarabi, C.; Zidan, A. S.; Khan, S. R.; Khan, M. A. *AAPS PharmSciTech* **2011**, *12*, 693.

(17) Matthew, W. M. et.al. *Journal of Medicinal Chemistry* **2006**, *49*, 4981.

(18) Childs, S. L.; Stahly, G. P.; Park, A. *Molecular Pharmaceutics* **2007**, *4*, 323.

(19) Lynch, D. E.; Smith, G.; Freney, D.; Byriel, K. A.; Kennard, C. *Australian Journal of Chemistry* **1994**, *47*, 1097.

(20) Florence, A. In *Practical Continuous Flow Technology* Munich, Germany, **2013**.

(21) Lee, T.; Chen, H. R.; Lin, H. Y.; Lee, H. L. *Cryst. Growth Des.* **2012**, *12*, 5897−5907.

(22) Zhang, S., KTH Royal Institute of Technology, **2010**.

(23) Daurio, D.; Medina, C.; Saw, R.; Nagapudi, K.; Alvarez-Núñez, F. *Pharmaceutics* **2011**, *3*, 582.

Chapter 6 2-aminopyrimidine-glutaric acid cocrystal system

6.1 Polymorphism in cocrystals

Polymorphism is an important factor to consider in drug processing. This chapter looks at the possibility of controlling cocrystal polymorphism in the SVC, by investigating the effect of different solvent systems. The new 2-aminopyrimidine-glutaric acid cocrystal polymorphs were used as model systems.

Polymorphism is the ability of a compound to crystallise in different and distinct crystal structures. Polymorphic consideration is important because the process of scaling-up drug manufacture can trigger polymorphism due to differences in process conditions like temperature, solvents etc. Polymorphism impacts drug bioavailability. Two cases that led to drug recall are: carbamazepine[1] used as an anti-convulsant and ritonavir[2] used as an HIV protease inhibitor. In both cases, the recall was because a more stable polymorph with poor bioavailability was generated during storage.

Polymorphism is important in solid-state chemistry because it influences the physio-chemical properties of crystals[3] e.g. colour, solubility, melting point, dissolution rate of pharmaceutical drugs[1,4] etc. Polymorphism in cocrystals, however, is rarely reported. In 2010 there were about 50 characterised cocrystal polymorphs, accounting for about 1.4% of the characterised cocrystals[1,5]. The low number of cocrystal polymorphs compared to single-component crystals could be due to the advanced stage of polymorph screening techniques employed in single-component crystals compared to polymorphic screening in cocrystals, which is in its infancy stage[1] still and the difficulty of predicting the structures of multi-component cocrystal molecules compared to single component crystals.

This chapter reports the successful solution cocrystallisation of three new 2-aminopyrimidine-glutaric acid cocrystals and one new 2-pyrimidine-glutaric acid cocrystal-salt hybrid using three different solvents: 100% acetonitrile, 100% methanol and 50:50 $wt\%$ of methanol and chloroform mixture. 2-aminopyrimidine-glutaric cocrystallisation experiments were carried out in the single vertical column (SVC) and stirred tank reactor (STR) using slurry cocrystallisation in 100% methanol, 100% chloroform, 100% acetonitrile, 50:50 $wt\%$ of methanol and chloroform mixture and 2.2 $wt\%$ methanol in a cyclohexane mixture. The results were compared with a solution cocrystallisation approach, to see which approach was more selective, as the cocrystallisation method can influence the polymorph synthesised[6,7]. Reagents used were commercial grade and obtained from Aldrich UK.

2- aminopyrimidine and glutaric acid in 1:1 ratio were ground together for 10 minutes. Portions from the bulk solid mix were taken and dissolved completely in acetonitrile, methanol and 50:50 $wt\,\%$ mixture of methanol/chloroform. The solutions were allowed to evaporate slowly over 3 days to obtain crystals suitable for single crystal X-ray diffraction analysis. . The single crystal X-ray diffraction data for the new multicomponent crystals are presented in Table 6.1.

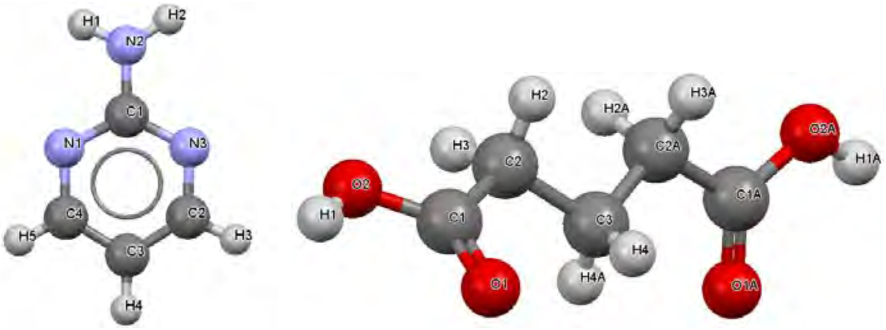

Fig.6.1 Chemical structure of 2-aminopyrimidine and glutaric acid.

6.2 2-aminopyrimidine

2 aminopyrimidine has two reported polymorphic forms crystallising in Pbca (AMPYRM01) and Pcab (AMPYRM10) space groups[8]. The AMPYRM01 unit cell consists of a the hydrogen bond forming motif, M1, with a graph set $R_2^2(8)$ and a motif M2 with a graph set $C_1^1(4)$ (Fig. 6.2). See section 1.3.2 on graph set for further information. The N3⋯N2 hydrogen bond length in motif M1 is 3.051 Å and the N1⋯N2 bond length in motif M2 is 3.077 Å.

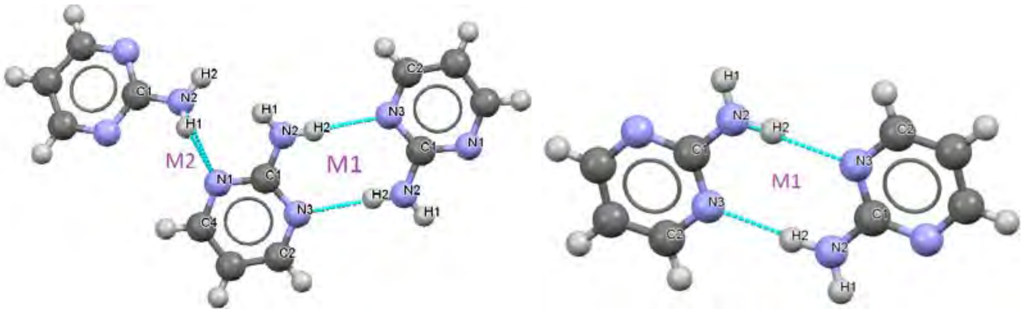

Fig. 6.2 Bonding motifs in the crystal structure of 2-aminopyrimidine[8].

A commercial sample of 2-aminopyrimidine was analysed by PXRD (Fig.6.3), which showed that the lowest diffraction peak occurred at 2θ =11.6°, FTIR (Fig. 6.4) and DSC (Fig. 6.5) with the latter giving an onset melting point of 122.4 °C and a peak maximum temperature of 126.5 °C.

Table 6.1 Single crystal X-ray diffraction data for the new multicomponent crystals

	A	**B**	**C**	**D**
Empirical formula	$C_4H_5N_3$ x $C_5H_8O_4$	$C_4H_5N_3$ x $C_5H_8O_4$	2 $C_4H_5N_3$ x $C_5H_8O_4$	$2[C_4H_6N_3]^+$ x $[C_5H_6O_4]^{2-}$ x $2[C_5H_8O_4]$
Formula weight g mol^{-1}	227.22	227.22	322.33	586.56
Crystal system	orthorhombic	triclinic	monoclinic	triclinic
Space group	Pbcm	P-1	$P2_1/n$	P-1
a/Å	4.1667(4)	6.0184(4)	10.2625(4)	5.4848(3)
b/Å	12.6657(11)	7.4714(5)	15.0558(6)	11.1944(5)
c/Å	20.3238(18)	12.0911(7)	11.1755(4)	22.9123(11)
α/°	90	84.3710(10)	90	91.7810(10)
β/°	90	89.9060(10)	113.0320(10)	92.3710(10)
γ/°	90	76.094(2)	90	103.0110(10)
Volume/Å^3	1072.57(17)	525.07(6)	1589.08(11)	1368.32(12)
Z	4	2	4	2
ρ_{calc}mg/mm^3	1.407	1.437	1.347	1.424
m/mm^{-1}	0.112	0.114	0.103	0.116
Temperature/K	120	120	120	120
2Θ data range	4 to 59°	3.38 to 58°	4.58 to 59°	3.74 to 59°
Reflections collected	9365	12033	12296	15931
Independent reflections	1525	2794	4412	7579
Data/restraints/parameters	1525/0/105	2794/0/197	4412/0/280	7579/0/506
Goodness-of-fit on F^2	1.061	1.035	0.99	1.053
R1	0.0665	0.0510	0.0642	0.0488
wR2	0.149	0.1258	0.1232	0.1105
Largest diff. peak/hole / e Å^{-3}	0.38/-0.31	0.35/-0.26	0.31/-0.27	0.41/-0.22

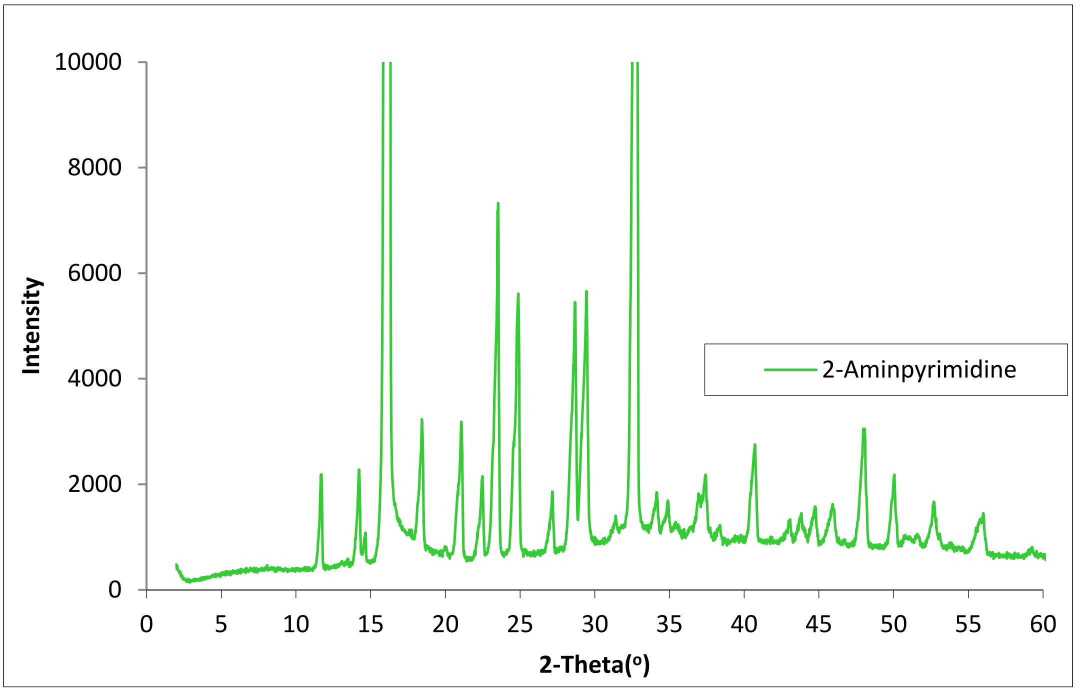

Fig. 6.3 PXRD pattern for commercial sample of 2-aminopyrimidine.

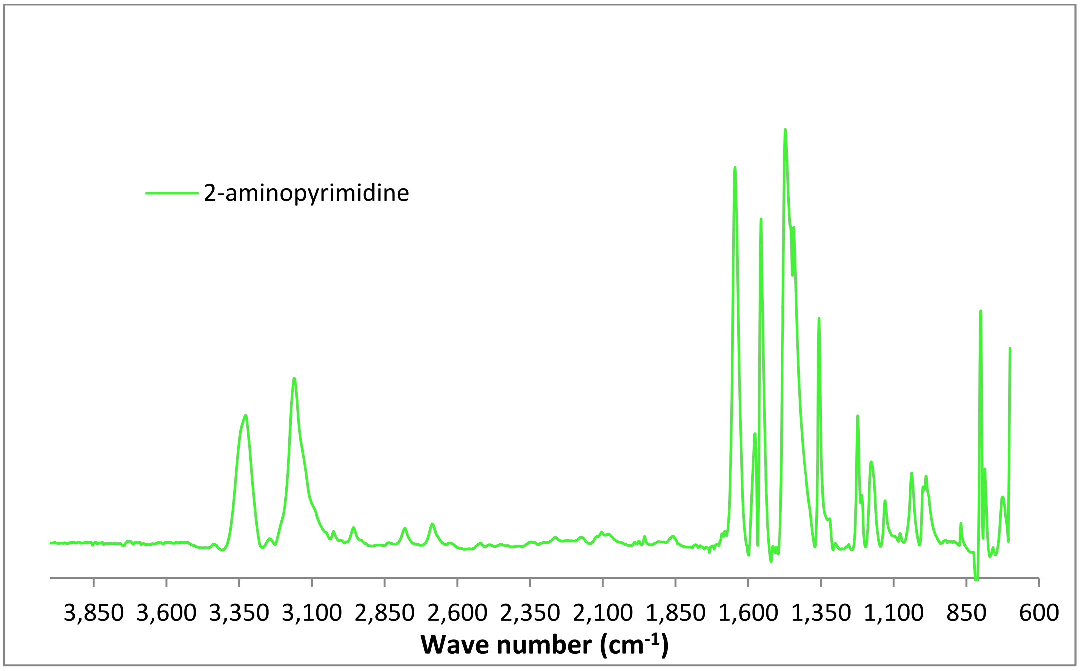

Fig. 6.4 ATR-FTIR spectrum of commercial sample of 2-aminopyrimidine.

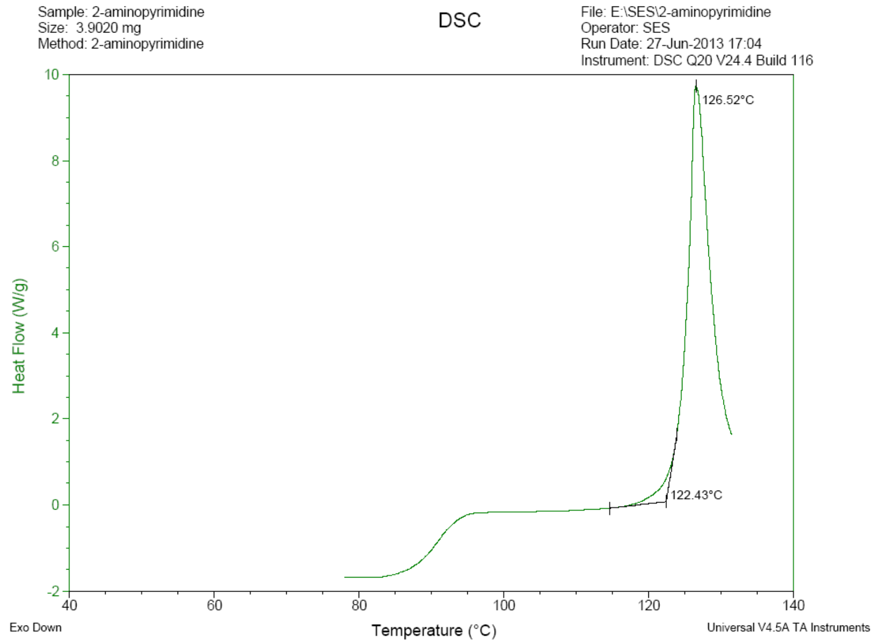

Fig. 6.5 DSC thermogram of commercial sample of 2-aminopyrimidine.

6.3 Glutaric acid

Glutaric acid (GLURAC03) has only one neutral molecule in its asymmetric unit; it has a monoclinic crystal system and space group C2/c[8]. The two carboxylic groups in glutaric acid do not reside in the same plane; the angle between their planes is 63.0^{o}[9]. The hydrogen bonding interaction forms a glutaric acid dimer with motifs M3 and M4. The motif M3 has a graph set of $R_2^2(8)$ and has hydrogen bonds that are of similar length at 2.664 Å. The motif M4 has a graph set $D_1^1(2)$ with an O2····O2 bond length of 2.934 Å,[10] forming a 2D chain network between adjacent chains (Fig. 6.6).

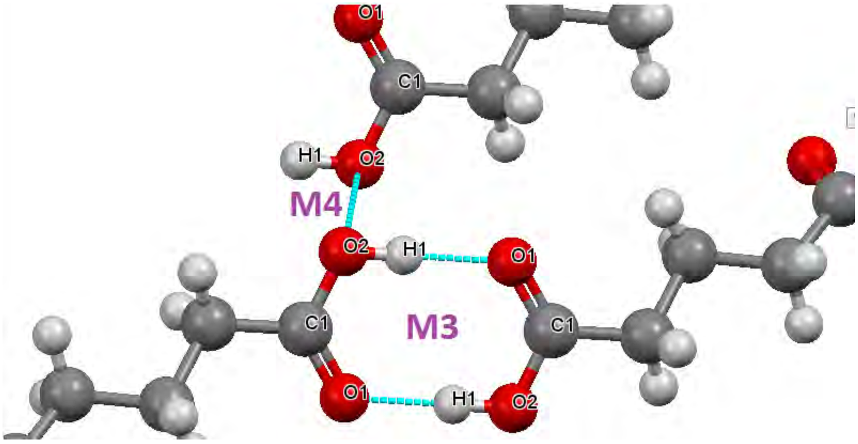

Fig. 6.6 Dimer and chain motifs in the glutaric acid crystal structure.

A commercial sample of glutaric acid was analysed by PXRD (Fig. 6.7), showing that the lowest diffraction peak is at 2θ=13.89^{o}, FTIR (Fig.6.8) and DSC (Fig.6.9), with the latter revealing two endothermic peaks with onset temperatures of 74.5 °C and 93.5 °C[11].

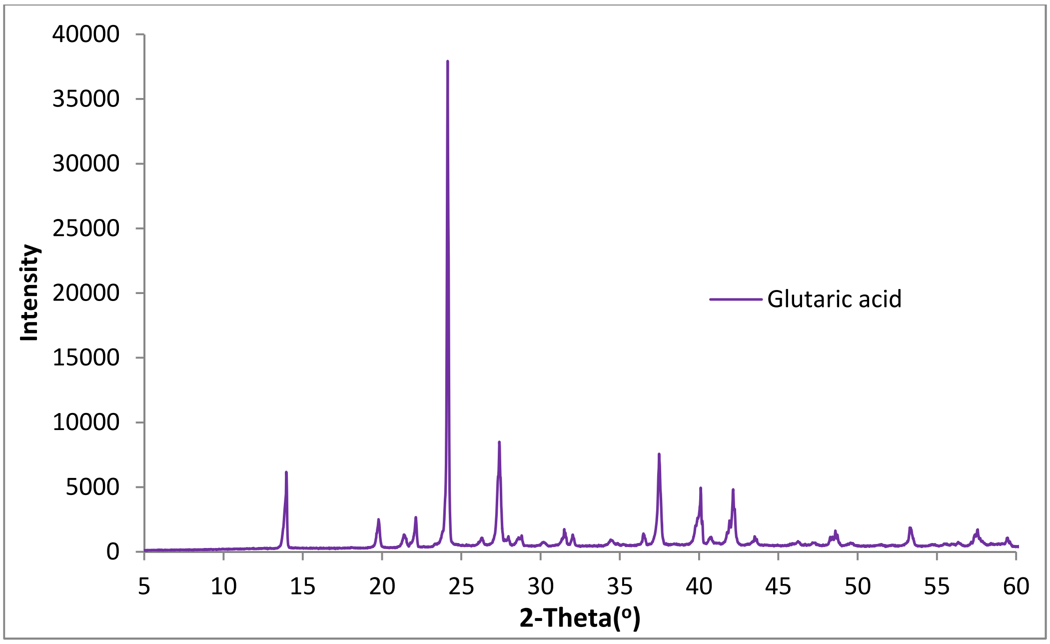

Fig. 6.7 PXRD pattern for commercial sample of glutaric acid.

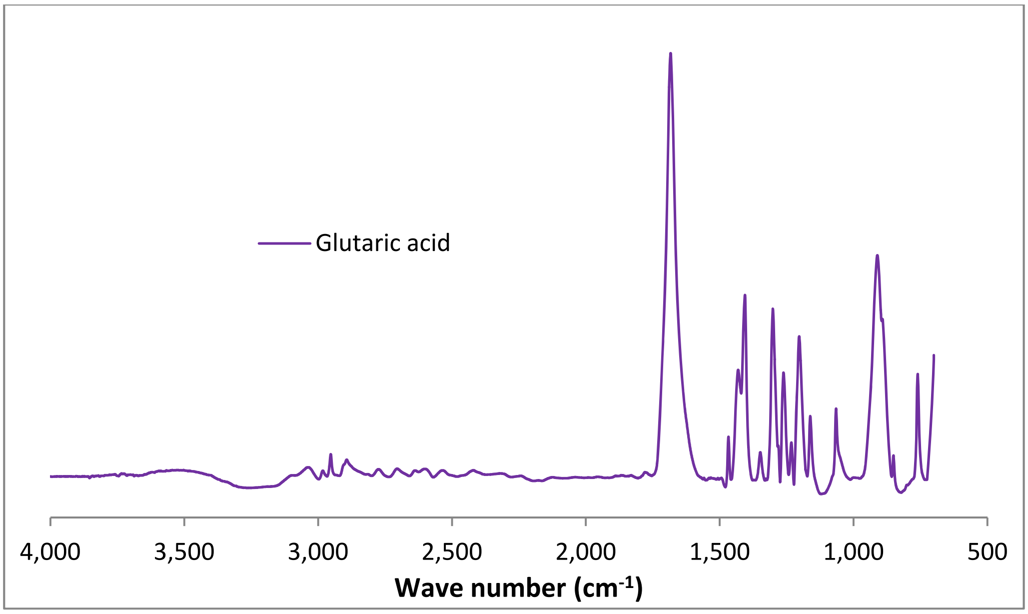

Fig. 6.8 ATR-FTIR of commercial sample of glutaric acid.

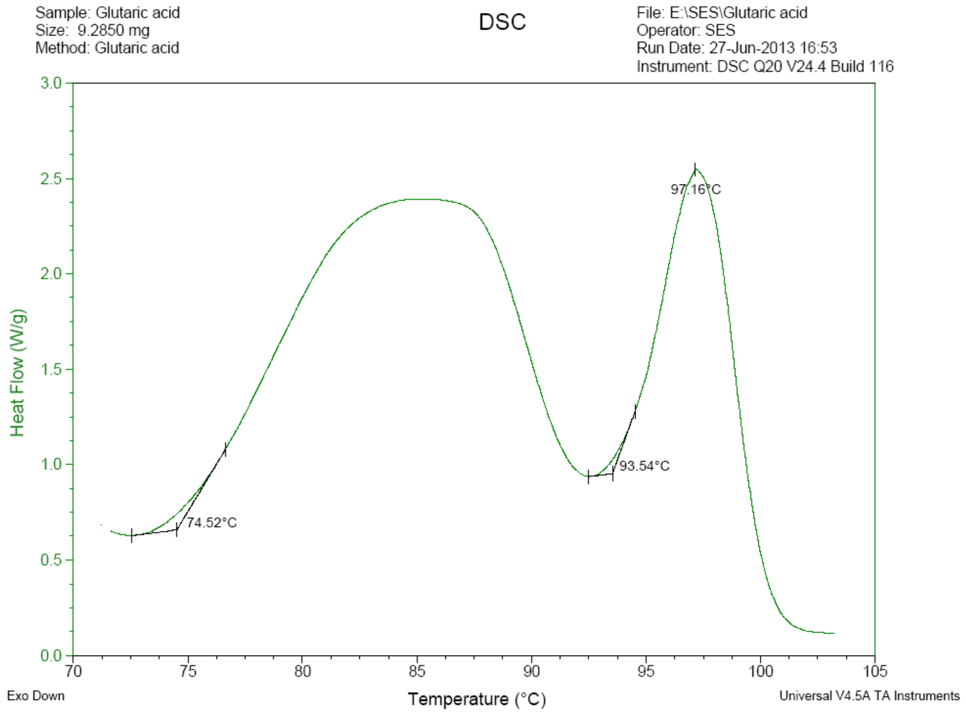

Fig. 6.9 DSC of Glutaric acid showing two endotherm peaks.

6.4 1:1 2-aminopyrimidine-glutaric acid cocrystal (A)

A was obtained from solution cocrystallisation in acetonitrile with 1:1 molar mixture of 2-aminopyrimidine and glutaric acid. **A** crystallises as white, flat plates (Figs. 6.10a and 6.10b). The asymmetric unit of **A** consists of one neutral molecule of 2-aminopyrimidine and one neutral molecule of glutaric acid (Fig.6.11). The crystal system is orthorhombic and the space group is Pbcm (Table 6.1). The cocrystal components interact through the COOH·····N_{atom} hydrogen bonding motif M5 with graph set R_2^2(8). The distance of the N1-H1A·····O2 bond is 2.94 Å (bond angle 172.62^{o}) and the N2····H1-O1 bond length is 2.68 Å (bond angle 169.72^{o}), corresponding to a moderately strong hydrogen bond interaction[12,13] (see section 1.3.1 for hydrogen bond strength classification based on A·····H·····B angle and length). These hydrogen bond lengths in **A** of 2.68 Å and 2.94 Å are shorter than those in 2-aminopyrimidine (3.051Å and 3.077Å) but similar to those in glutaric acid (2.664 Å).

In the carboxylic acid group, the C-O (C4-O1) bond length is 1.323(2) Å, the C=O (C4—O2) bond length is 1.213(2) Å and C1-N2-C2 bond angle in 2-aminopyrimidine is 117.18^{o}. The difference in length between C-O and C=O bond confirms that hydrogen atom transfer has not occurred in the hydrogen bonding in **A**[14], supporting the neutral nature of the hydrogen bonding[10,15].

The C-N-C bond angle in pyridine type molecules referred to as the ipso (α) angle differs substantially between neutral pyridine (≈117°) and ionic pyridinium (≈122°), by up to 4° and can be used to determine the ionic state of the molecule[16]. In pyridinium (N^+) cation, the hydrogen atom is pulled close to nitrogen, this increases the electronegativity of nitrogen, resulting in the deformation (enlargement) of the C-N-C bond angle.

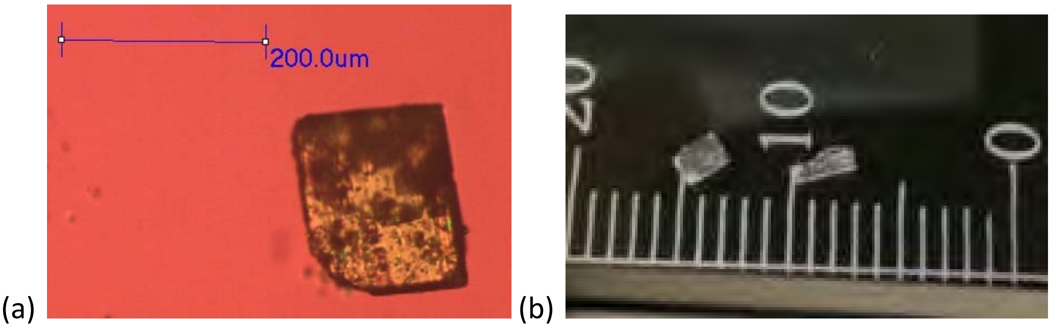

Fig. 6.10 (a). Microscopic view of flat plates of **A**. (b). White crystals of **A** (scale in mm).

In **A**, the non-planar nature of the chain network is due to the glutaric acid molecule, which is twisted around the middle CH_2 group by about 116.30°, resulting in a non-planar chain of alternating 2-aminopyrimidine and glutaric acid molecules (Fig.6.12). When the unit cell of **A** is viewed along the z-axis, the chain patterns become superimposable and the orientation of adjacent chains are rotated through 180° (Fig.6.13).

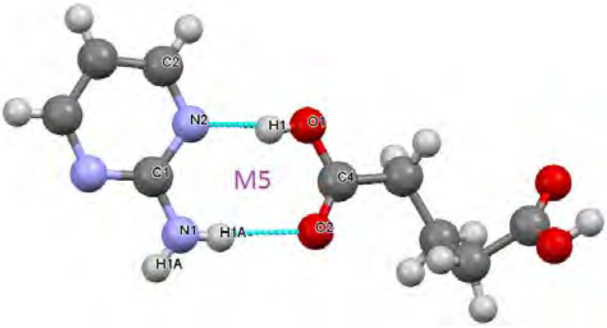

Fig. 6.11 Asymmetric unit of **A** showing hydrogen bonding motif.

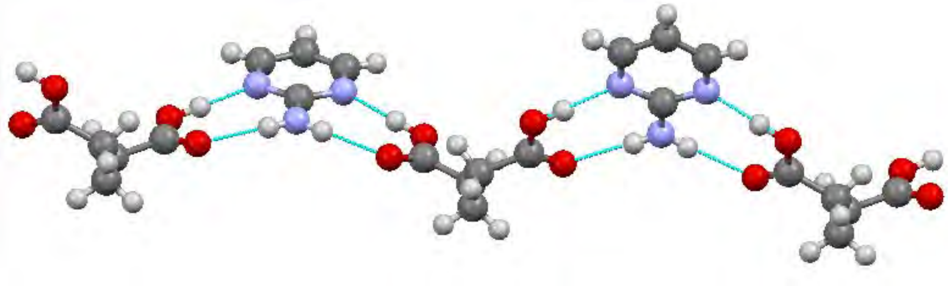

Fig. 6.12 Alternating 2-aminopyrimidine/glutaric acid chain pattern in **A**.

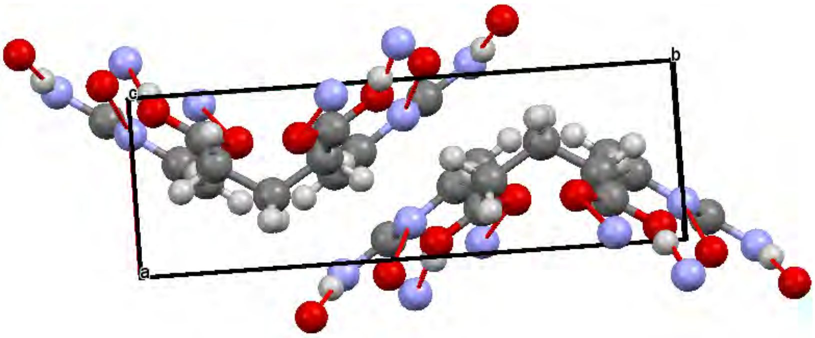

Fig. 6.13 super-imposable orientation of adjacent chains in **A**.

The simulated powder pattern for **A** was obtained from the single crystal X-ray diffraction analysis and overlaid with that of glutaric acid and 2-aminopyrimidine (Fig. 6.14), the diffraction peaks at 2θ = 11.61^{o}, 18.31^{o} and 32.93^{o} in 2-aminopyrimidine and in glutaric acid at 23.55^{o}, 37.5^{o} and 42.07^{o} are absent in **A**; the new peaks in **A** are: 25.6^{o}, 25.9^{o}, 38.1^{o}, 38.38^{o} and 17.46^{o}. **A** was also analysed by ATR-FTIR and overlaid with the spectra for 2-aminopyrimidine and glutaric acid (Fig. 6.15), the region between 1750 cm^{-1} and 4000 cm^{-1} (Fig. 6.16) shows two new broad peaks in the spectrum of **A** at 1900 cm^{-1} and 2350 cm^{-1}, which are absent in glutaric acid spectrum and are characteristic of un-ionised O-H hydrogen bonding stretching of the carboxylic acid[7,17,18]. The DSC analysis of **A** (Fig. 6.17) shows two endotherm peaks. The first peak has an onset temperature of 65.2 ^{o}C and a peak maximum of 73.4 ^{o}C, while the second peak has an onset temperature of 96.6 ^{o}C and peak maximum of 98.6 ^{o}C. Both onset temperatures and peak maximums are different from those observed for 2-aminopyrimidine (122.4 ^{o}C and 126.5 ^{o}C) and glutaric acid (93.5 ^{o}C and 97.2 ^{o}C); with **A** having a higher melting point than glutaric acid. The enthalpy of phase transitions e.g. melting, are unique for the different crystal forms. The enthalpies of the phase transitions in glutaric acid thermogram determined by DSC are 30.73 J/g and 84.23 J/g, while the enthalpies in **A** are 8.77 J/g and 159.4 J/g (Fig. 6.17). The low phase transition enthalpy of the first endotherm in **A** is a quarter of the first endotherm in glutaric acid and the second endotherm in **A** is twice the corresponding endotherm in glutaric acid, confirming that the endothermic peaks in **A** are not from glutaric acid. The first endotherm peak at 73.4 ^{o}C in **A** could be a solid-solid transition in which the two polymorphs are quite closely related so that the transformation requires relatively little energy input; this will be discussed later in section 6.8.1.

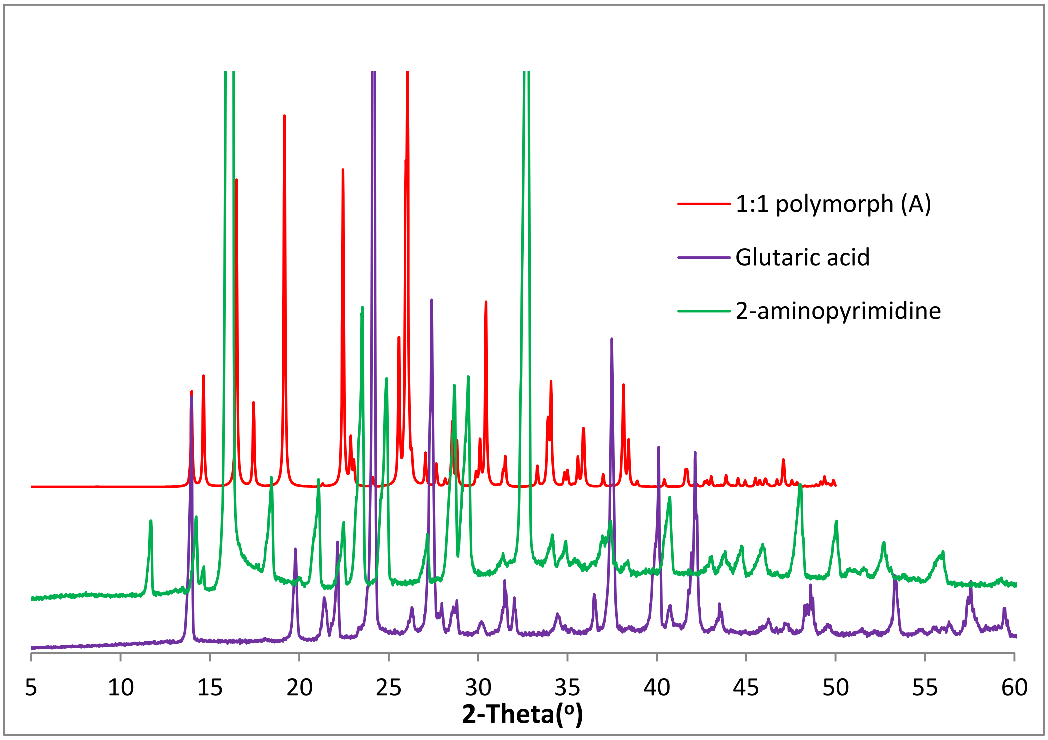

Fig. 6.14 Comparing the simulated PXRD for **A** with glutaric acid and 2-aminopyrimidine.

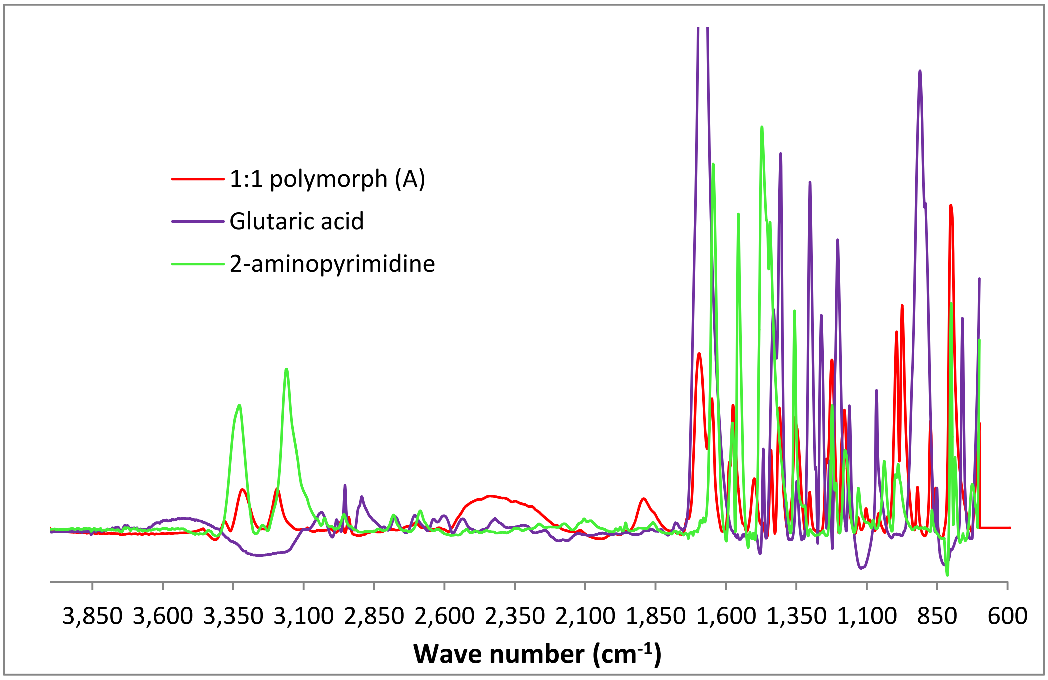

Fig. 6.15 Comparing FTIR spectra for **A** with glutaric acid and 2-aminopyrimidine.

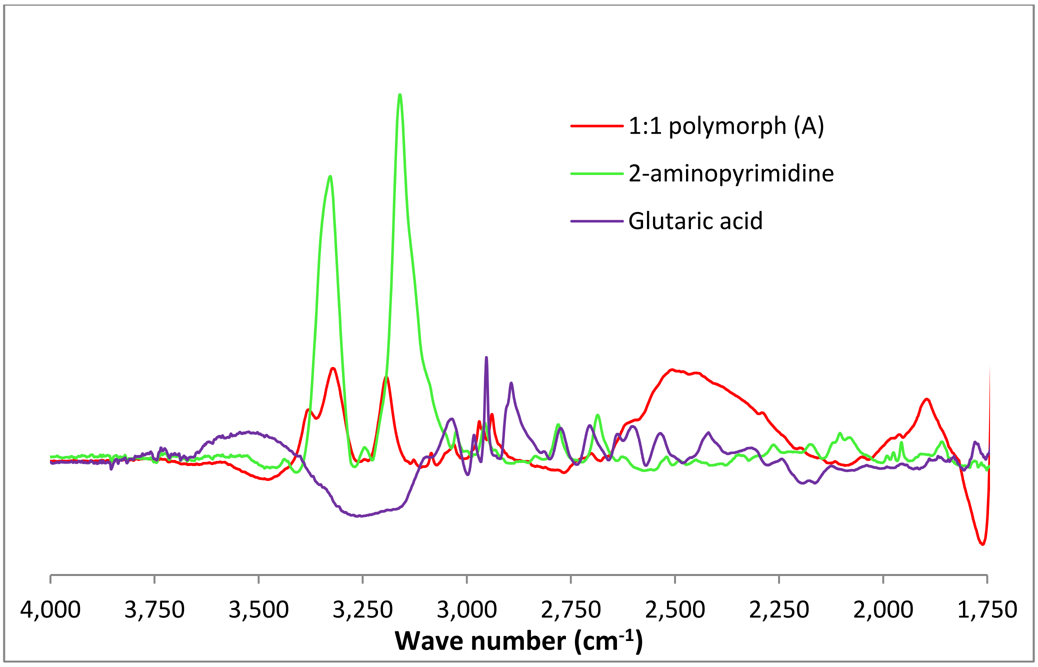

Fig. 6.16 FTIR comparison between 1750 cm^{-1} and 4000 cm^{-1} region for **A** and cocrystal components.

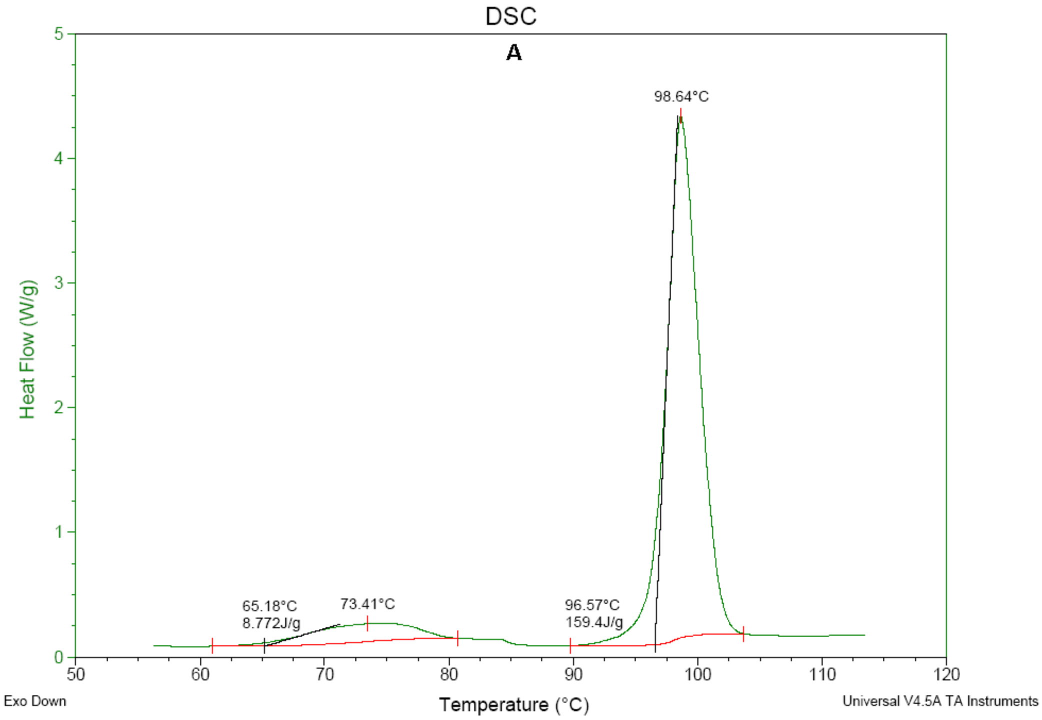

Fig. 6.17 DSC thermogram of **A** showing two endotherm peaks.

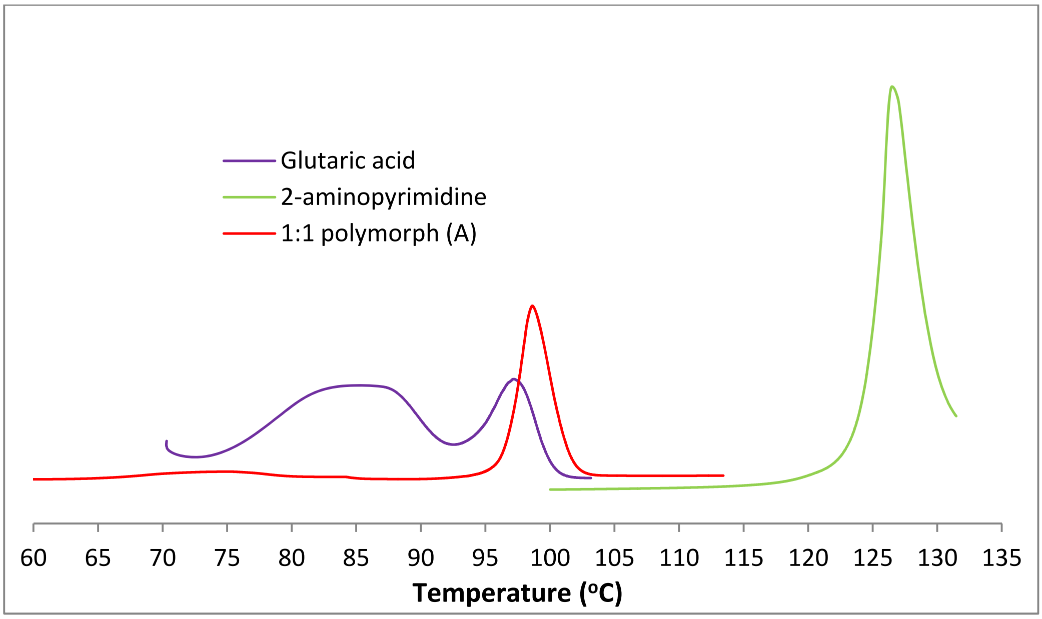

Fig. 6.18 Comparing DSC thermogram of **A** and its cocrystal components, showing A with an intermediate melting point.

6.5 1:1 2-aminopyrimidine-glutaric acid cocrystal (B)

B was obtained from solution cocrystallisation in 50:50 wt % of methanol and chloroform mixture with 1:1 molar mixture of 2-aminopyrimidine and glutaric acid. **A** and **B** are cocrystal polymorphs. **B** crystallises as peach orange, flat plate crystals (Fig. 6.19a and 6.19b). The asymmetric unit of **B** consists of one neutral molecule of 2-aminopyrimidine and one neutral molecule of glutaric acid. The crystal system is triclinic and the space group P-1 (Table 6.1). The cocrystal components interact through three different hydrogen bonding motifs, two M5 motifs with graph set R_2^2(8), an M6 motif with graph set D_1^1(2) and an M7 motif with graph set R_6^3(8) (Fig. 6.20).

Motifs M5 hydrogen bonding distances are N1-H1B····O4 = 2.894 Å with bond angle of 176.03° and the N2····H3-O3 bond = 2.677 Å with bond angle 166.16°, corresponding to a moderately strong hydrogen bond interaction[12,13]. The carboxylic acid group bond lengths in M5 are: C-O (C25-O3) = 1.305(1) Å, C=O (C25—O4) = 1.226(1) Å and the C1-N2-C2 bond angle in 2-aminopyrimidine is 117.06°, supporting the neutral nature of the hydrogen bonding[10,15,16]. The difference in bond length between the C-O and C=O bonds confirm that hydrogen atom transfer has not occurred in the hydrogen bonding[14].

The N1-H1⋯O bond length in A of 2.94 Å is longer than B of 2.894 Å. These lengths indicate that the hydrogen bonding in B is stronger than that in A. In the second hydrogen bonding N2⋯H-O in M5, the bond lengths of 2.68 Å and 2.677 Å in A and B respectively are very similar. Overall in M5, the hydrogen bonding in A is weaker than that in B, suggesting that B may be the more stable polymorph.

The M6 motif hydrogen bond distance for the N3⋯H1-O1 bond is 2.666 Å (bond angle 178.06°. The carboxylic acid groups bond lengths in M6 are: C-O (C21-O1) = 1.327(1) Å, the C=O (C21—O2) = 1.206(1) Å, C-O (C25-O3) = 1.305(1) Å, and C=O (C25—O4) = 1.226(1) Å; The C1-N3-C4 bond angle in 2-aminopyrimidine are 117.29°, supporting the neutral nature of the hydrogen bonding[10,15,16] in motif M6.

Motif M7 hydrogen bonding distances are: N1-H1A⋯O4 = 2.930 Å (bond angle 139.88°) and N1-H1B⋯O4 = 2.894 Å (bond angle 176.03°), which correspond to moderately strong hydrogen bond interactions[12,13].

The chain network in **B** is planar (Fig. 6.21). The difference between the twisted conformation in **A** (Fig. 6.12) and the planar conformation in **B** is as a consequence of the conformation of the linking glutaric acid molecule in the crystal lattice.

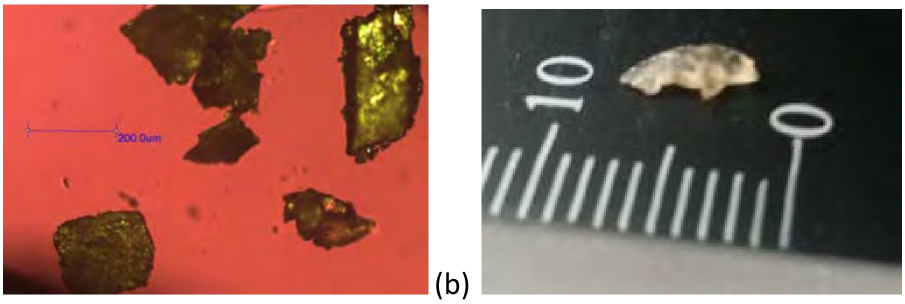

(a) (b)

Fig. 6.19 (a). Microscopic view of **B**. (b). Peach orange coloured crystals of **B** (scale in mm).

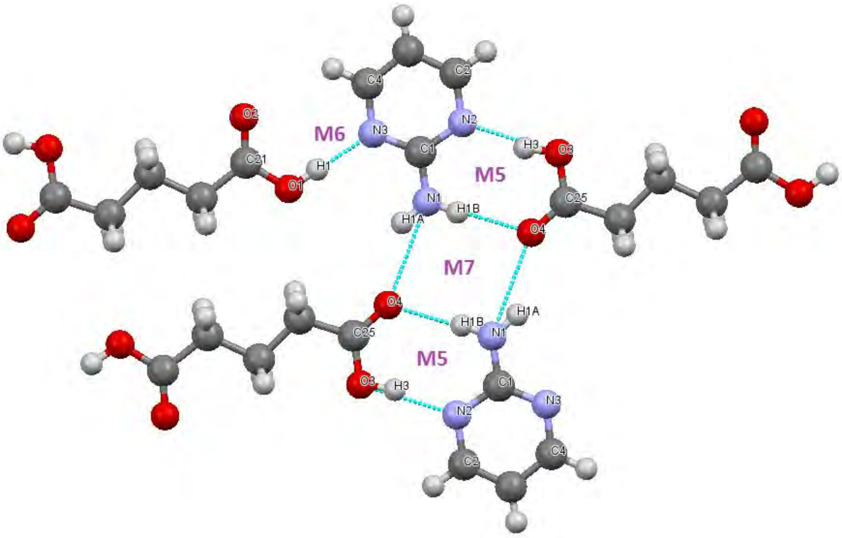

Fig. 6.20 Asymmetric unit of **B** showing hydrogen bonding motifs M5, M6 and M7.

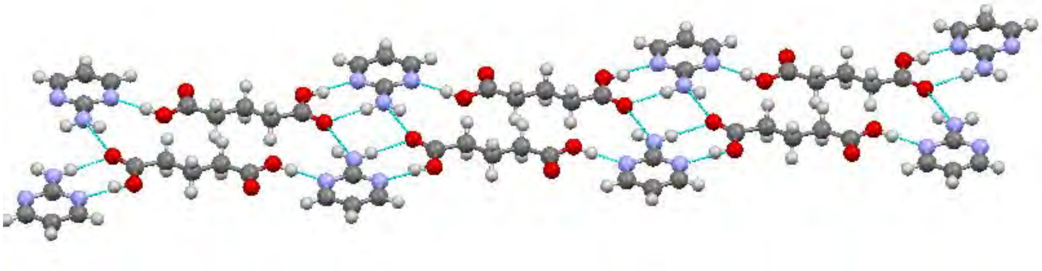

Fig. 6.21 Planar chain pattern of 2-aminopyrimidine/glutaric acid cocrystal.

The simulated powder pattern for **B** was obtained from the single crystal analysis. When the **B** pattern is overlaid with that of glutaric acid and 2-aminopyrimidine (Fig. 6.22), the diffraction peak at 2θ= 11.61°, 14.16°, 16.44°, 32.93° and 48.11° in 2-aminopyrimidine and the peaks at 13.78°, 19.87°, 24.06° and 41.86° in glutaric acid are completely absent in the cocrystal. The new peaks in **B** are: 15.12°, 16.64° and 16.8°. **B** was analysed by FTIR, overlaying this with the spectra for 2-aminopyrimidine and glutaric acid (Fig. 6.23), the region between 1750 cm^{-1} and 4000 cm^{-1} (Fig. 6.24) shows two new broad peaks in the spectrum of **B** at 1900 cm^{-1} and 2350 cm^{-1}, which are absent in glutaric acid and 2-aminopyrimidine. These peaks are characteristics of un-ionised O-H hydrogen bonding stretching of the carboxylic acid[7,17,18]. In addition, there is a weak double peak at 3300 cm^{-1} that is absent in both 2-aminopyrimidine and glutaric acid, which can be attributed to a shift in primary N-H bending signal in 2-aminopyrimidine due to hydrogen bonding. The DSC analysis of **B** (Fig. 6.25) shows an endothermic peak with a shoulder, an onset temperature of 85.1 °C and peak maximum of 98.7 °C. The onset temperature and peak maximum are different from those observed for 2-aminopyrimidine (122.4 °C and 126.5 °C) and glutaric acid (93.5 °C and 97.2 °C). When the thermograms are overlaid (Fig. 6.26), **B** has a slightly higher melting point than glutaric acid. The enthalpies of the phase transitions in the glutaric acid thermogram are 30.73 J/g and 84.23 J/g while the one in **B** is 202.3 J/g, which is 2.5 times the value for glutaric acid, confirming that the endotherm in **B** is not from glutaric acid despite their peaks occurring at similar temperatures.

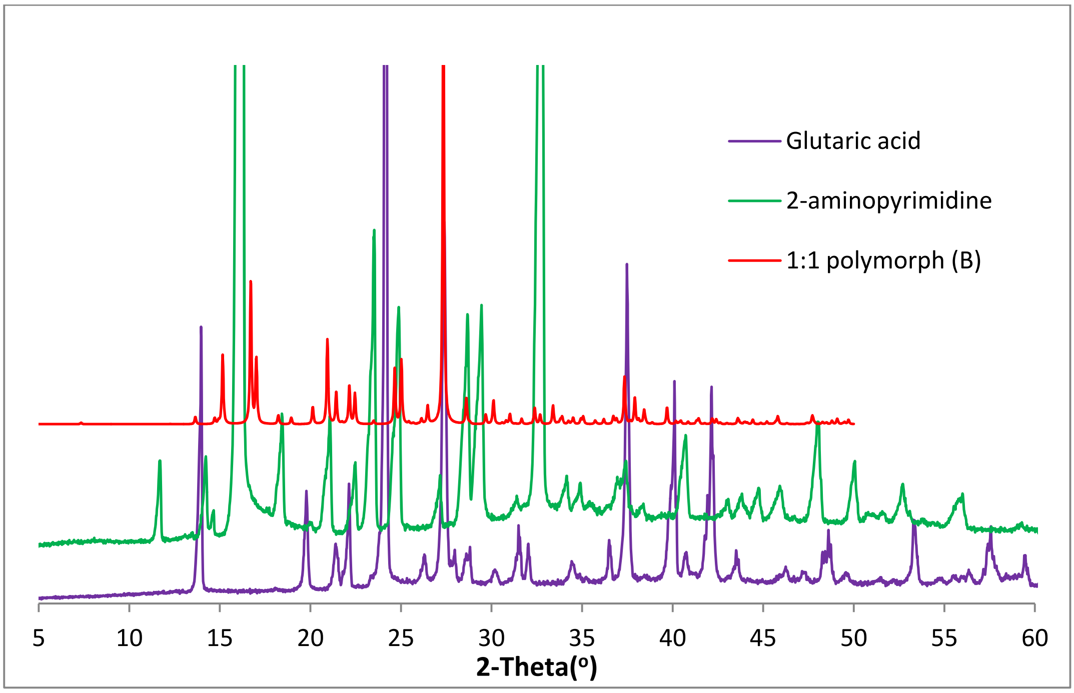

Fig. 6.22 Comparing simulated PXRD for **B** with glutaric acid and 2-aminiopyrimidine.

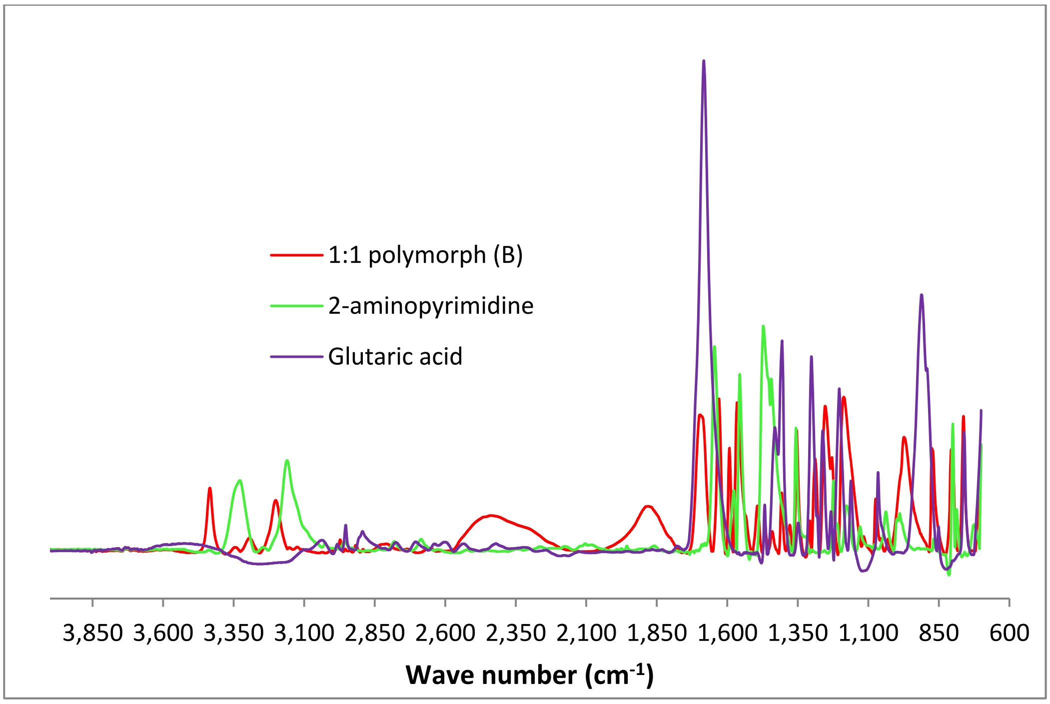

Fig. 6.23 Comparing FTIR spectra for **B** and its cocrystal components.

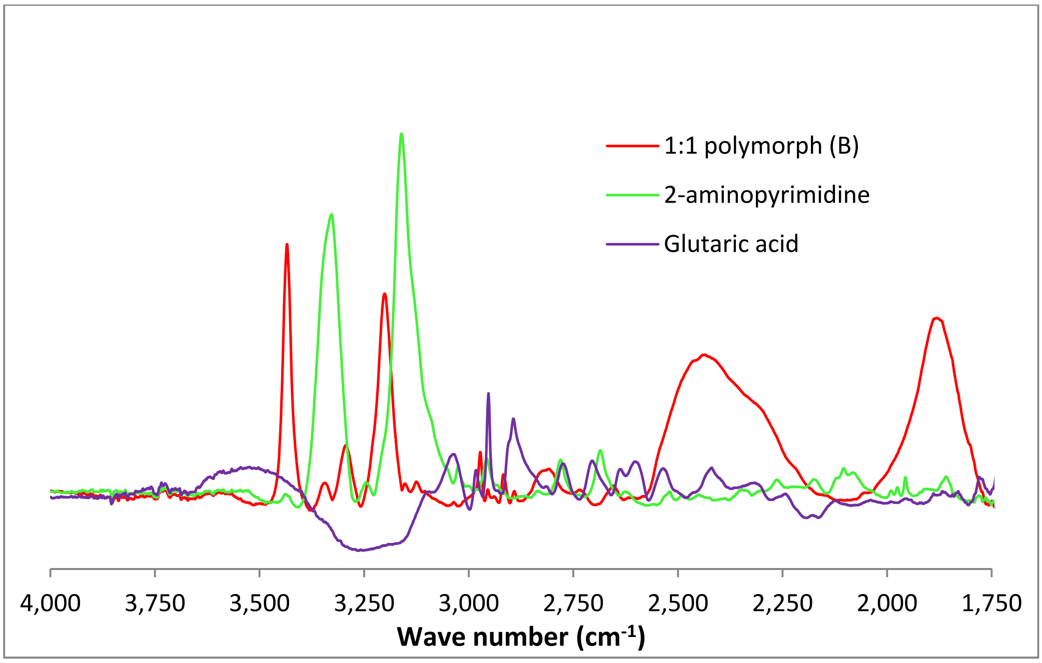

Fig. 6.24 FTIR comparison between 1750 cm^{-1} and 4000 cm^{-1} region for B and its cocrystal components.

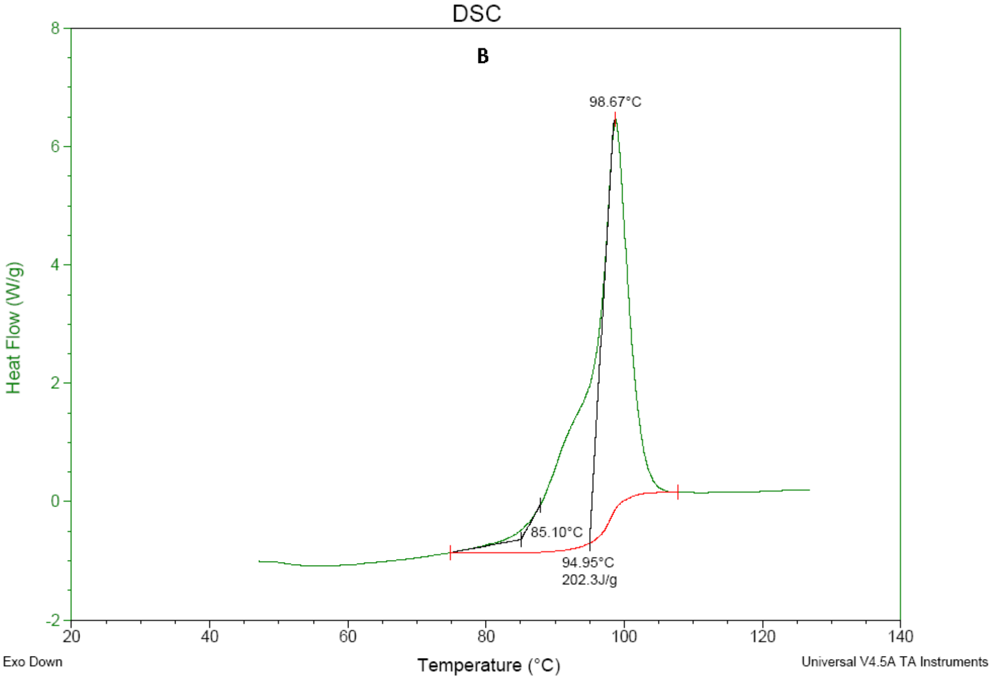

Fig.6.25 DSC thermogram of B showing one endotherm with a shoulder.

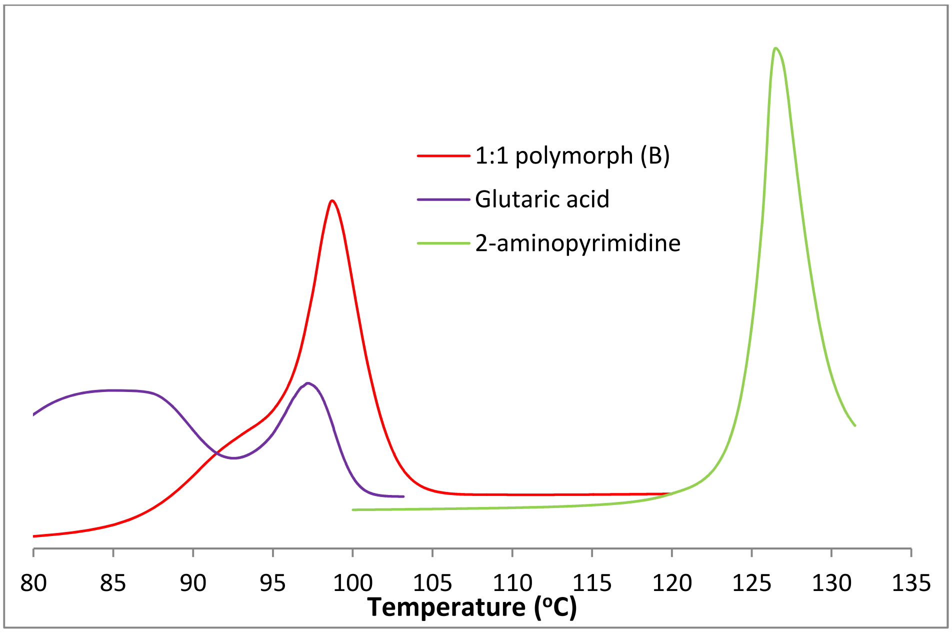

Fig.6.26 Comparing DSC thermogram of B with that of its components.

6.6 2:1 2-aminopyrimidine-glutaric acid cocrystal (C)

C was obtained from solution cocrystallisation in methanol with a 1:1 molar mixture of 2-aminopyrimidine and glutaric acid**. C** crystallises as rose coloured elongated cubes (Fig. 6.27a and 6.27b). The asymmetric unit of **C** consists of neutral molecules of 2-aminopyrimidine (two) and glutaric acid (one) (Fig. 6.28). The crystal system is monoclinic and the space group $P2_1/n$ (Table 6.1). **C** has two motifs in its hydrogen bonding network; the first motif, M1, involves two 2-aminopyrimidine molecules forming a dimer with graph set $R_2^2(8)$; this dimer is also present in 2-aminopyrimidine (Fig. 6.2). The second motif, M5, is a COOH·····N_{atom} bond type and the graph set $R_2^2(8)$ is also present in cocrystals **A** and **B**.

In motif M1, the hydrogen bond distance of the two bonds (N21·····H21B—N23) is 2.999 Å; this is shorter than the M1 dimer motif in 2-aminopyrimidine (3.051Å). The bond angles are both 174.65°. 2-aminopyrimidine interacts with one glutaric acid to form the M5 motif comprising of N21—H21A·····O4 hydrogen bond with a length of 2.884 Å and an angle of 175.11°, and O3—H3·····N22 with a length of 2.652 Å and bond angle of 173.95°. All bond lengths and angles correspond to moderate hydrogen bond strengths[12,13].

Comparing the cocrystal structure C with that of 2-aminopyrimidine, which has motifs M1 and M2, glutaric acid seems to displace the less strongly held 2-aminopyrimidine in motif M2 (Fig. 6.2), forming a much stronger interaction. In particular, the M2 motif in 2-aminopyrimidine has a hydrogen bond length of 3.077 Å compared to values of 2.884 Å and 2.652 Å in motif M5 of C. In M1, the C-O (C35-O3) bond length is 1.324(1) Å, the C=O (C35—O4) bond length is 1.217(1) Å; the C-N-C bond angles for C24-N23-C21 and C21-N22-C22 are 116.74° and 117.15° respectively, supporting a neutral hydrogen bond[10,15,16]. **C** extends to reveals a sequence of 2-aminopyrimidine dimers linked by one glutaric acid. This network results in sheets of planar chains (Fig. 6.29).

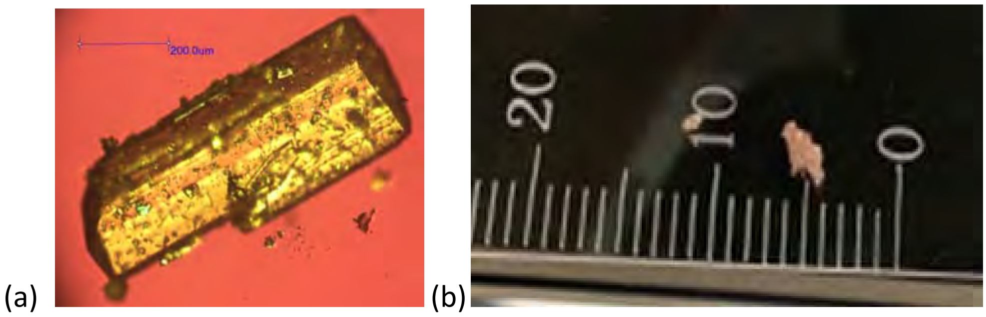

Fig. 6.27 (a). Microscopic view of **C** elongated cubes. (b). Rose coloured crystals of **C** (scale in mm).

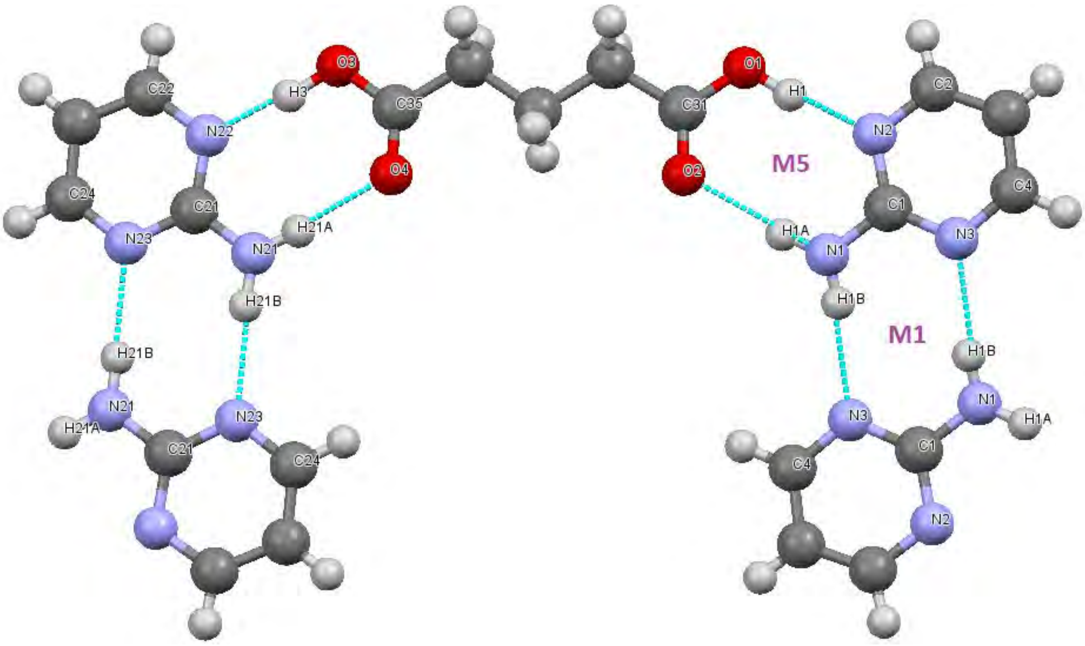

Fig. 6.28 Asymmetric unit of **C** showing hydrogen bonding motif M1 and M5.

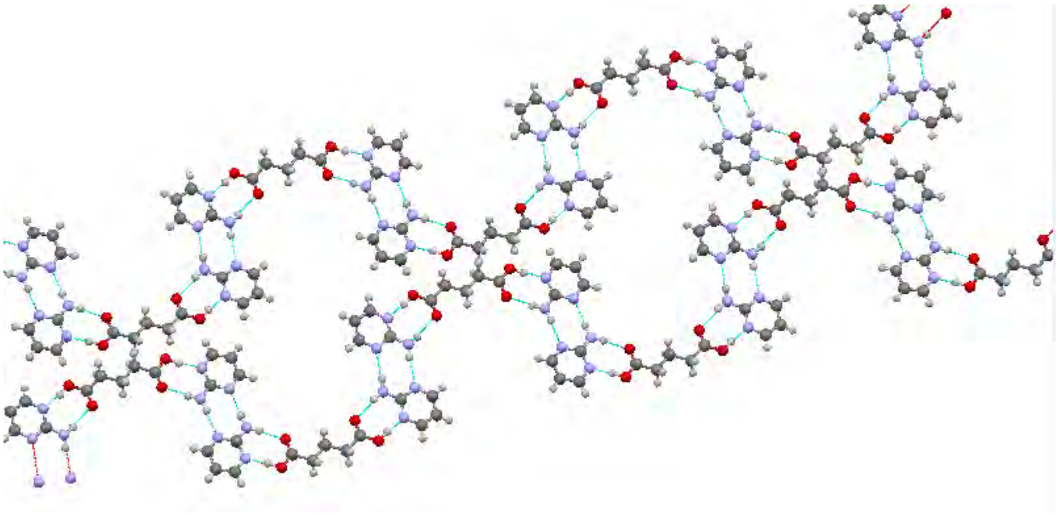

Fig. 6.29 Planar chain pattern of **C.**

The simulated powder pattern for **C** was obtained from the single crystal analysis and overlaid with the pattern of glutaric acid and 2-aminopyrimidine (Fig. 6.30), the diffraction peaks at $2\theta = 11.61^o$, 28.55^o, 32.93^o and 47.83^o in 2-aminopyrimidine and those at 13.78^o, 22.03^o and 18.82^o in glutaric acid are completely absent in the cocrystal. The new peaks in **C** are: 20.59^o and 26.08^o. **C** was analysed by ATR-FTIR and overlaid with the spectra for 2-aminopyrimidine and glutaric acid (Fig. 6.31), the region between 1750 cm^{-1} and 4000 cm^{-1} (Fig. 6.32) shows two new broad peaks in the spectrum of **C** at 1900 cm^{-1} and 2350 cm^{-1}, which are absent in glutaric acid and 2-aminopyrimidine. These peaks are characteristic of un-ionised O-H hydrogen bonding stretching of the carboxylic acid[7,17,18]. DSC analysis of **C** (Fig. 6.33) shows two endothermic peaks with onset temperatures of 83.0 ^oC and 96.1 ^oC, and peak maximums of 89.3 ^oC and 98.3 ^oC. The onset temperature and peak maximums are different from those observed for 2-aminopyrimidine (122.4 ^oC and 126.5 ^oC) and glutaric acid (93.5 ^oC and 97.2 ^oC). When the thermograms are overlaid (Fig. 6.34), **C** can be seen to have a slightly higher melting point than glutaric acid. The enthalpies of the phase transitions in the glutaric acid thermogram are 30.73 J/g and 84.23 J/g, while the enthalpies in **C** are 13.00 J/g and 151.2 J/g, the first endotherm in **C** is half the corresponding endotherm in glutaric acid and the second endotherm in **C** is twice the corresponding endotherm in glutaric acid, confirming that the endotherm in **C** is not from glutaric acid. The first endothermic peak at 83.0 ^oC in **C** could be evidence of a solid-solid co-crystal transition or the melting of residual crystals of glutaric acid, though the latter is unlikely given the absence of prominent glutaric acid peaks in the XRD.

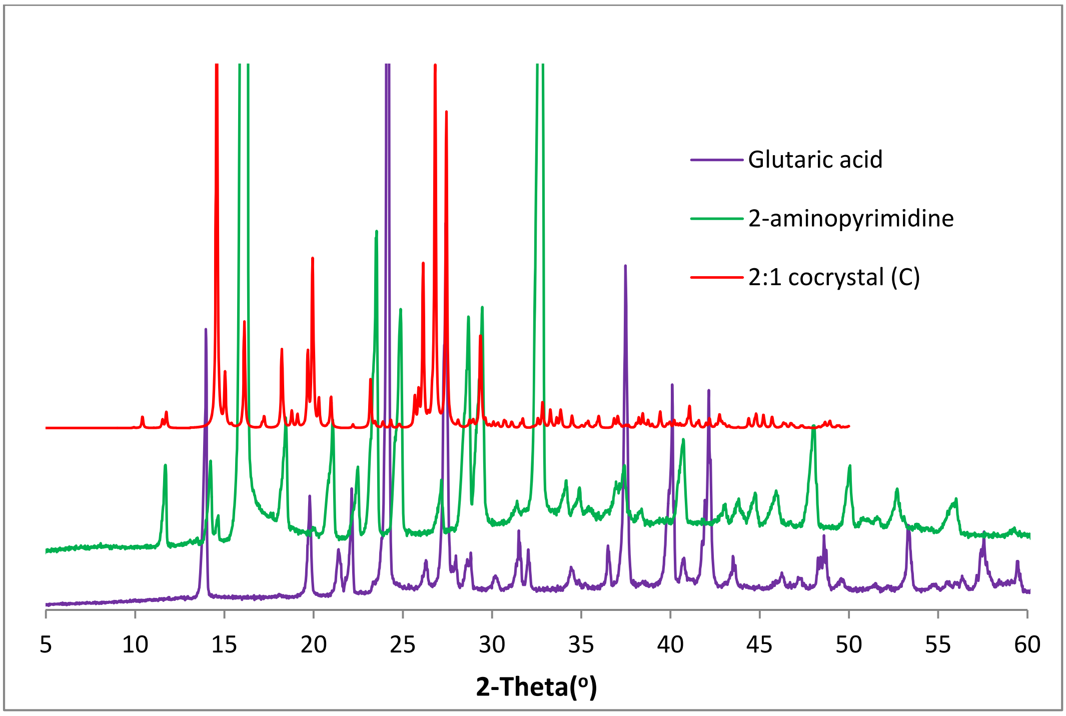

Fig. 6.30 Comparing simulated PXRD for **C** with 2-aminopyrimidine and glutaric acid.

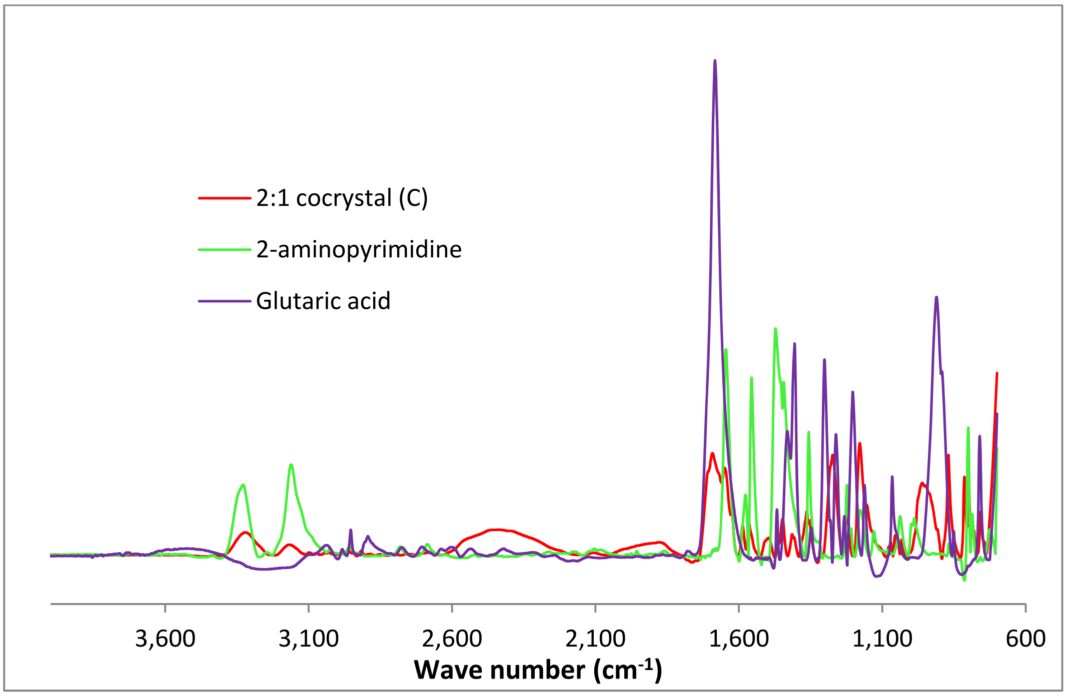

Fig. 6.31 Comparing FTIR spectra for **C** with that of its components.

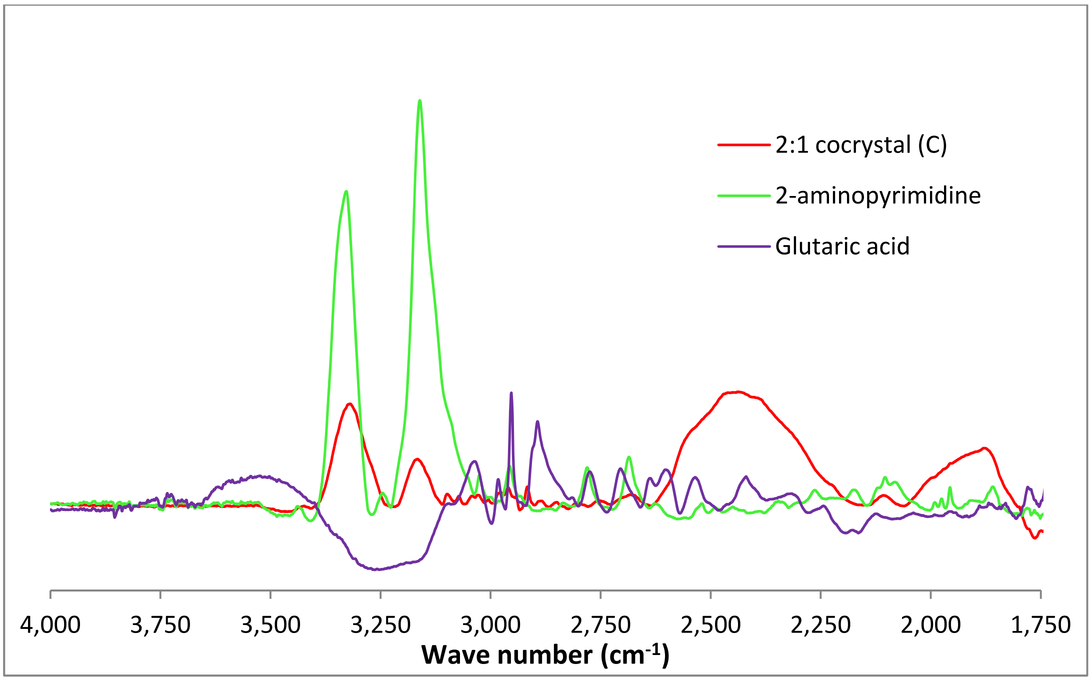

Fig. 6.32 FTIR comparison between 1750 cm^{-1} and 4000 cm^{-1} region for **C** and its components.

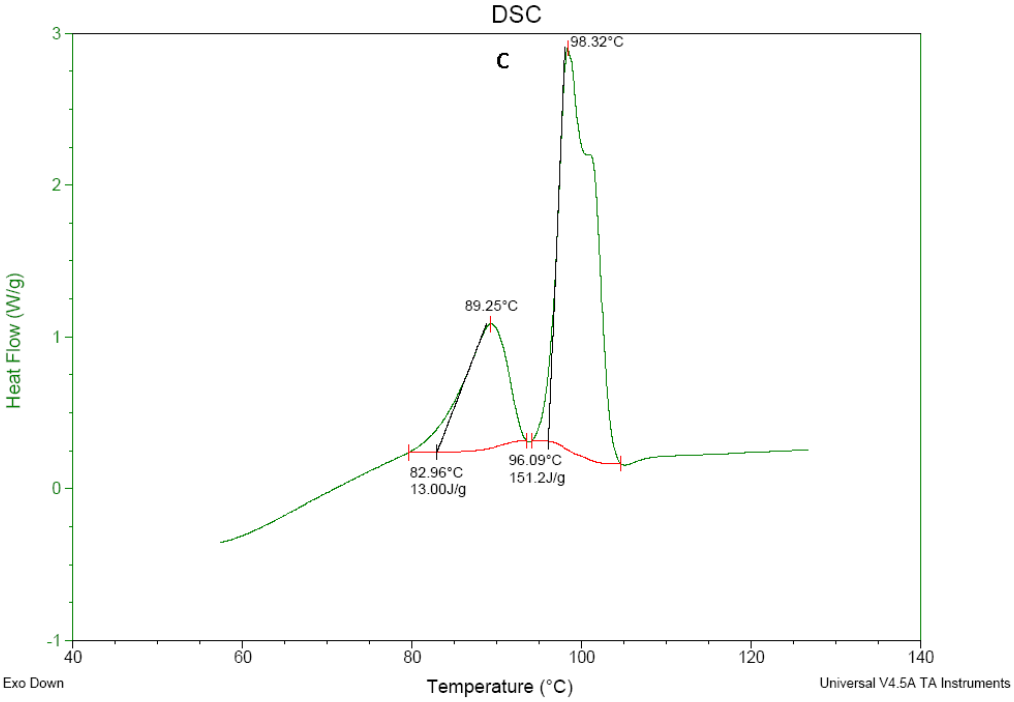

Fig. 6.33 DSC thermogram of **C** showing two endothermic peaks.

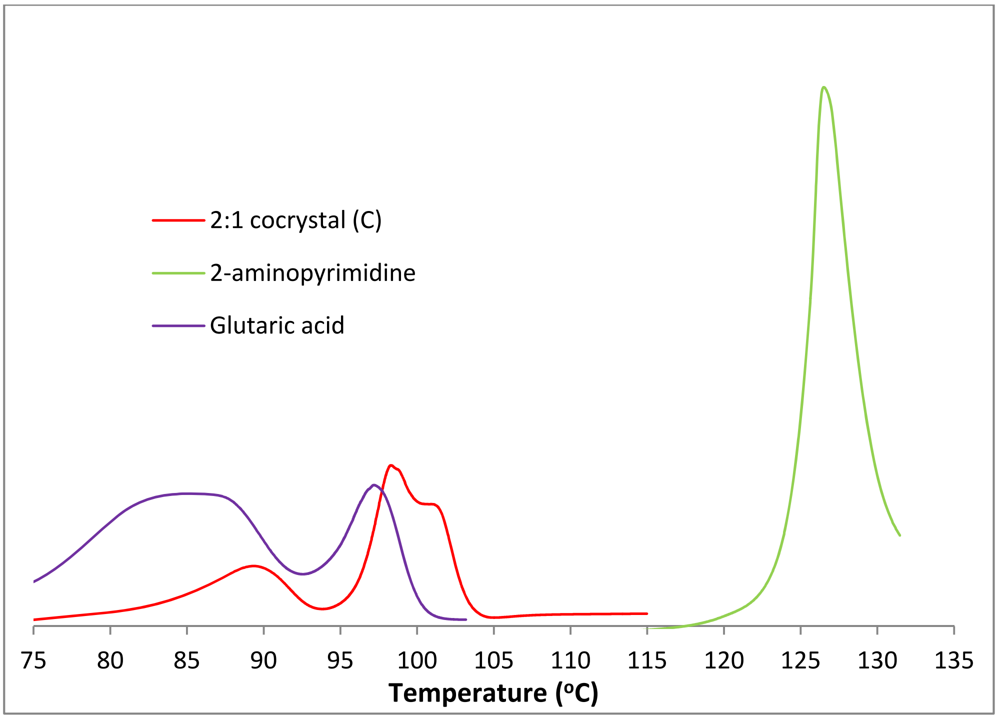

Fig. 6.34 Comparing DSC thermogram of **C** and it’s cocrystal components.

6.7 3:2 2-aminopyrimidine-glutaric acid cocrystal-salt hybrid (D)

D was obtained from solution cocrystallisation in a 50:50 wt % of methanol and chloroform mixture and 1:1 molar mixture of 2-aminopyrimidine and glutaric acid**. D** crystallises as gold coloured elongated cubes (Fig. 6.35a and 6.35b). The asymmetric unit of the **D** consists of five molecules: two 2-aminopyrimidinium cations, one glutaric acid dianion and two neutral glutaric acids (Fig. 6.36). The crystal system is triclinic and space group is P-1 (Table 6.1). In **D,** four different bonding motifs are present: M8, M1, M9 and M10. The crystal structure consists of both the planar and twisted conformation of glutaric acid observed in **A** and **B**, respectively.

Motif M8 with graph set $R_2^2(8)$ appears twice in the crystal structure of **D**. This motif involves one glutaric dianion molecule with a twisted conformation; the carboxylate groups are oriented in planes that are approximately perpendicular to one another. The dianion hydrogen bonds with two 2-aminopyrimidinium cation. The bond lengths between the carboxylate groups and 2-aminopyrimidinium cation are: 1.275(1) Å (C45—O44), 1.252(1) Å (C45—O43), 1.253(1) Å (C41—O41) and 1.277(1) Å (C41—O42) (Fig. 6.42).The similarity in bond lengths between the C—O’s support the ionic nature of the carboxylate groups[14,15]. The C-N-C bond angles in the 2-aminopyrimidium cations in M8 are 121.03° (C22-N22-C21) and 120.79° (C1-N3-C4), supporting an ionic bond[15,16]. The hydrogen bonding lengths in the M8 motif are

2.585 Å (N22$^{(+)}$-H22·····O44$^{(-)}$), 2.602 Å (N3$^{(+)}$-H3·····O42$^{(-)}$), 2.924 Å (N21-H21A·····O43$^{(-)}$) and 2.832 Å (N1-H1A·····O41$^{(-)}$), which are within the range of lengths expected for moderately strong hydrogen bonds[14].

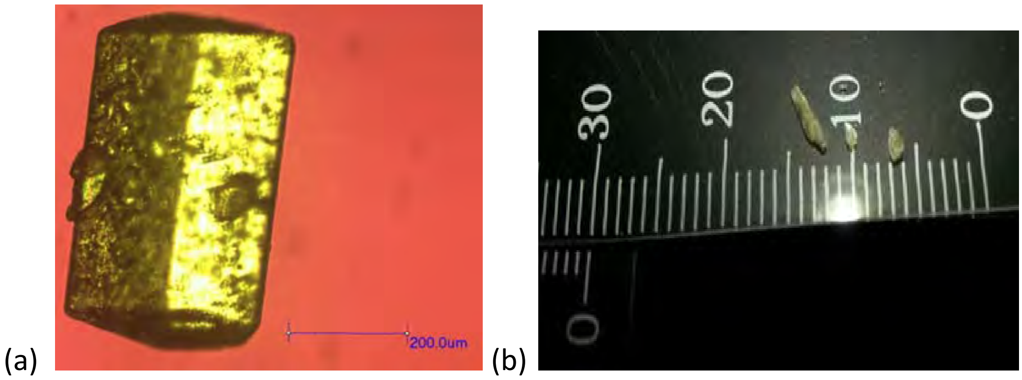

Fig. 6.35 (a). Microscopic view of **D** elongated cubes. (b). Gold coloured crystals of **D** (scale in mm).

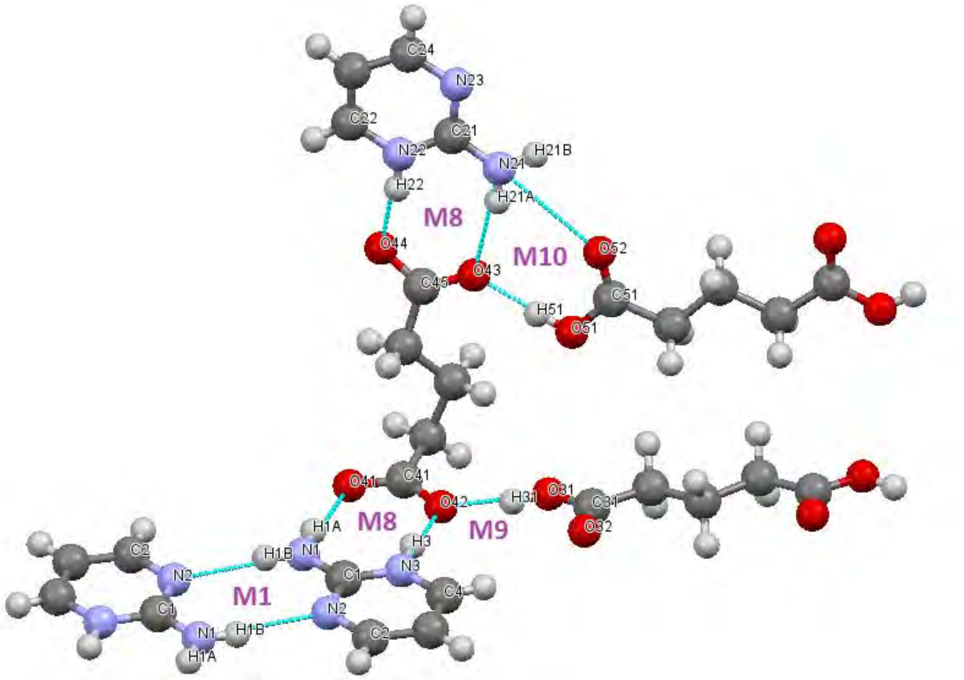

Fig. 6.36 Hydrogen bonding motifs in **D** showing motifs M1, M8, M9 and M10.

The second motif, M1, has the graph set $R_2^2(8)$ and involves two planar 2-aminopyrimidinium cations forming a dimer; this dimer motif is similar to the one present in 2-aminopyrimidine. The C-N-C bond angles in M1 are the same at 117.28° supporting the neutral nature of the nitrogen atoms involved[10,15,16], the two hydrogen bonding lengths are also the same at 3.092 Å and similar to the hydrogen bond length in 2-aminopyrimidine (3.051 Å).

Motif M9 has the graph set $D_1^1(2)$; it involves a neutral glutaric acid molecules hydrogen bonding to the carboxylate ion. The hydrogen bond length in the M9 motif is 2.609 Å for the O31-H31·····O42$^{(-)}$ bond and is within the hydrogen bonding range expected for moderately strong hydrogen bonds[14].

Motif M10 has the graph set $R_3^2(8)$; it comprises of a neutral glutaric acid molecule, a carboxylate ion and the amino group in 2-aminopyrimidine. The hydrogen bond lengths in the M10 motif are: 2.590 Å for the O51-H51·····O43$^{(-)}$ bond, 2.924 Å for the N21-H21A·····O43$^{(-)}$ and 3.038 Å for the N21-H21B·····O52. In this motif, the C-O (C51-O51) bond length is 1.319 Å, the C=O (C51—O52) bond length is 1.210 Å, the difference in bond lengths between C-O and C=O bond confirms the neutral nature of this carboxylic acid group[14].

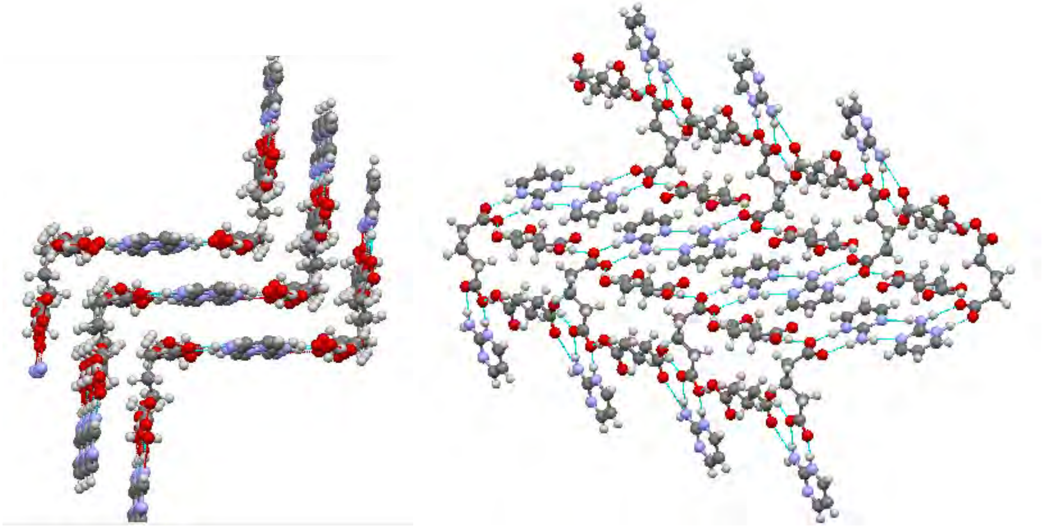

Fig. 6.37 Chair orientation of crystal chain network in **D**.

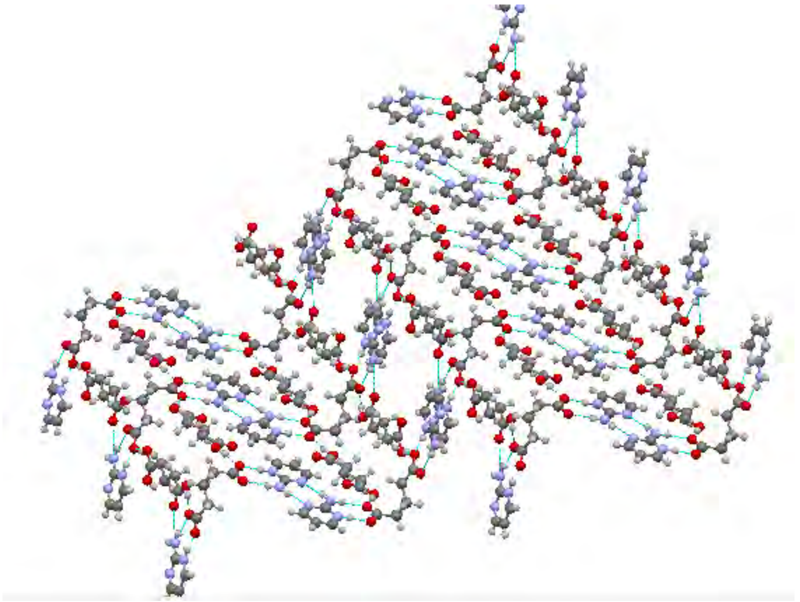

Fig. 6.38 Chain network in **D**.

The chain network in **D** forms a chair conformation (Fig.6.37) that extends out along the b-axis. The hanging 2-aminopyrimidinium molecule sits in the space between the 2-aminiopyrimidium cations in the next sheet of the network below (Fig. 6.38).

The simulated powder pattern for **D** was obtained from the single crystal analysis, when overlaid with that of glutaric acid and 2-aminopyrimidine (Fig. 6.39), the diffraction peaks at 2θ= 11.61°, 16.44°, 32.93° and 47.83° in 2-aminopyrimidine and those at 13.78°, 27.23° and 37.37° in glutaric acid are absent in **D**. The new peaks in **D** are: 8.06°, 8.86°, 9.18°, 16.82°, 17.26° and 17.78°. **D** was analysed by ATR-FTIR, overlaying the FTIR spectrum of **D** with the spectra for 2-aminopyrimidine and glutaric acid (Fig. 6.40), in the region between 1750 cm^{-1} and 4000 cm^{-1} (Fig. 6.41) this shows two new broad peaks in the spectrum of **D** at 1900 cm^{-1} and 2350 cm^{-1} that are absent in glutaric acid and 2-aminopyrimidine. These peaks are characteristic of un-ionised O-H hydrogen bonding stretching of the carboxylic acid[7,17,18]. There is a weak double peak at 3300 cm^{-1} that is absent in both 2-aminopyrimidine and glutaric acid, which can be attributed to a shift in the primary N-H bending signal in 2-aminopyrimidine due to hydrogen bonding. The DSC analysis of **D** (Fig. 6.42) shows two endothermic peaks with onset temperatures of 81.2 °C and 95.1 °C; and peak maximums of 83.5 °C and 98.2 °C. The onset temperatures and peak maximums are different from those observed for 2-aminopyrimidine (122.4 °C and 126.5 °C) and glutaric acid (93.5 °C and 97.2 °C). When the thermograms are overlaid (Fig. 6.43), **D** has a slightly higher melting point than glutaric acid. The enthalpies of the phase transitions in the glutaric acid thermogram are 30.73 J/g and 84.23 J/g while the enthalpies in **D** are 4.69 J/g and 163.7 J/g (Fig. 6.42). The first endotherm in **D** is one-seventh the corresponding endotherm in glutaric acid and the second endotherm in **D** is twice the corresponding endotherm in glutaric acid, confirming that the endotherm in **D** is not from glutaric acid.

A comparison of the TGA and DSC thermogram of **D** (Fig. 6.48), shows no significant weight loss is observed below the melting point. This suggests that the first endotherm peak at 83.5 °C in **D** could be due to energy absorption to vaporise residual solvents or evidence of a solid-solid transition in which the two forms are closely related given the relatively low enthalpy value of 4.69 J/g. This will be discussed further in section 6.8.2.

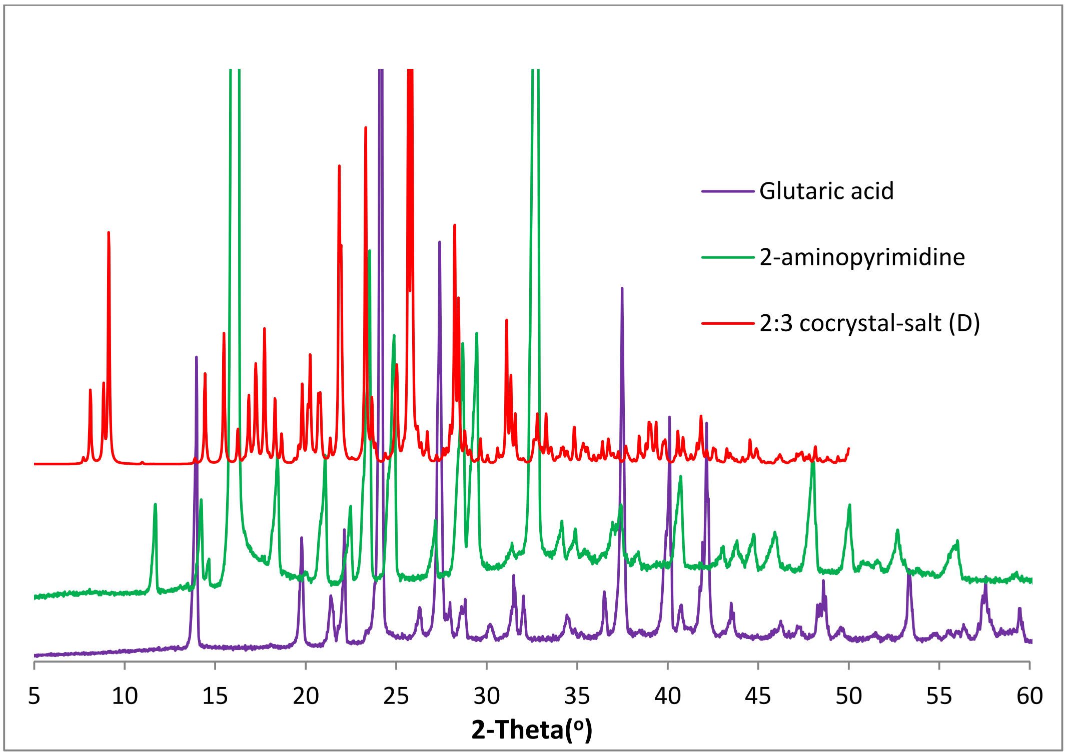

Fig. 6.39 Comparing simulated PXRD for **D** with its components.

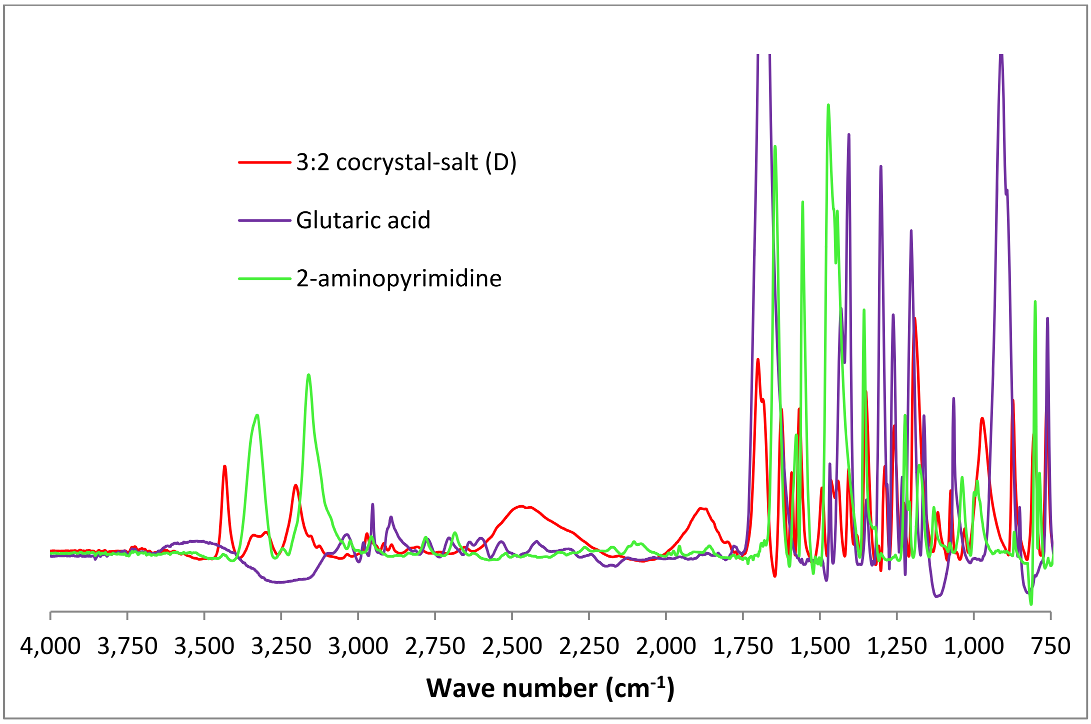

Fig. 6.40 Comparing FTIR spectra of **D**, with its components.

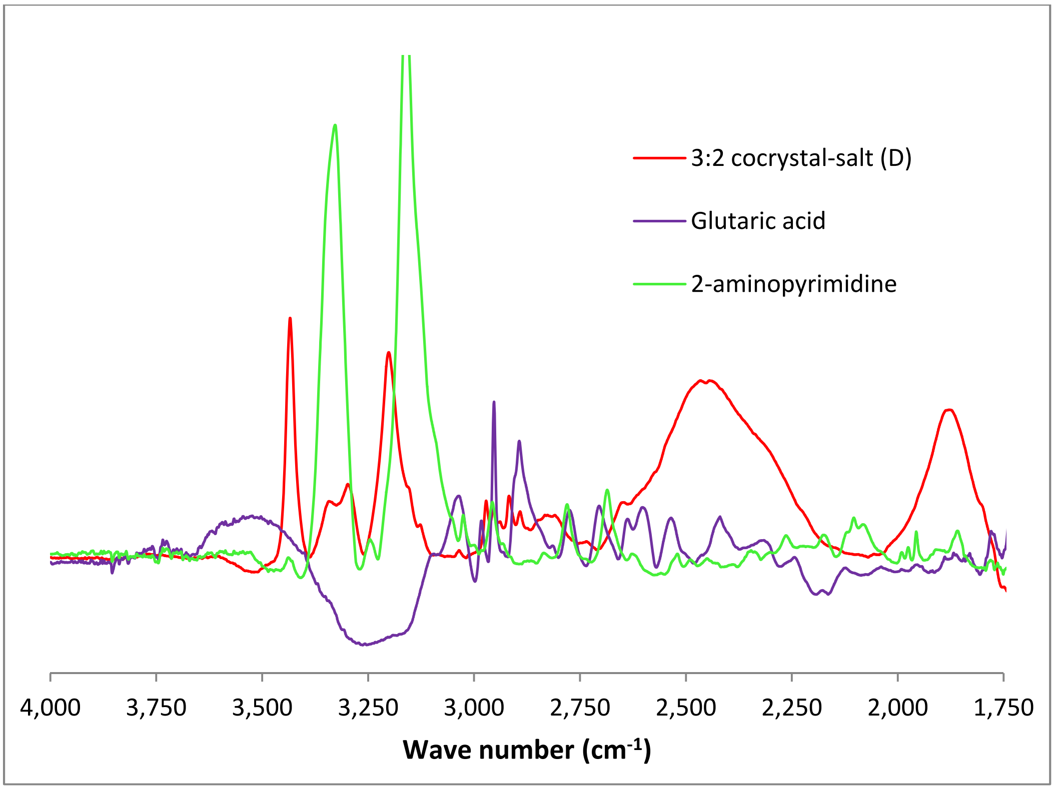

Fig. 6.41 FTIR comparison for **D** with its components between 1750 cm^{-1} and 4000 cm^{-1} region.

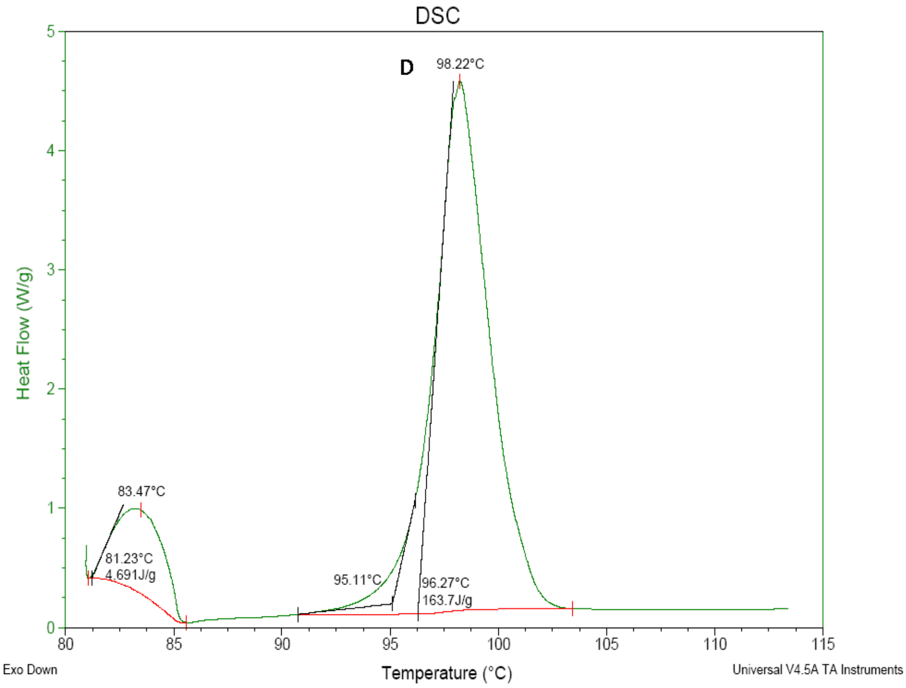

Fig. 6.42 DSC thermogram of D.

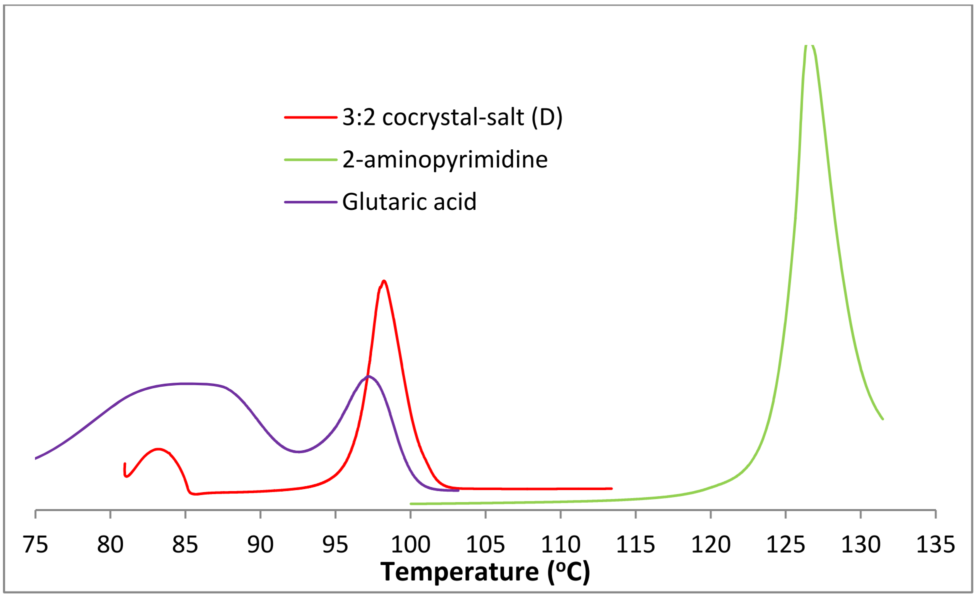

Fig.6.43 Comparing DSC thermogram of **D** with its components.

6.8 Discussion on 2-aminopyrimidine-glutaric acid new multicomponent crystals.

A comparison of the PXRD pattern of the four new multi-component crystals of 2-aminopyrimidine/glutaric cocrystals, 2-aminopyrimidine and glutaric acid (Fig. 6.44) shows that they are all different. A comparison of the FTIR spectra of the 4 new multicomponent crystals (Fig. 6.45) shows the spectrum having two new broad peaks at about 1900 cm^{-1} and 2350 cm^{-1} characteristic of un-ionised O-H hydrogen bonding stretching of the carboxylic acid[7,17,18]. A double peak at about 3300 cm^{-1} (Fig. 6.46) is observed in crystals **A**, **B** and **D** but absent in **C**. This peak is attributed to a shift in the primary N-H bending signal in 2-aminopyrimidine due to hydrogen bonding. The M1 motif in **C** results in a 2-aminopyrimidine dimer, which can lock the primary amine and prevent bending. The DSC thermograms of the cocrystals (Fig. 6.47) show late endothermic peaks between 96.7 ^{o}C and 98.5 ^{o}C. The shouldering observed on the peaks may be a result of non-uniform heating across the sample, which is pronounced when intact crystals are used for DSC analysis[8], or it may be an inherent feature of the sample. In particular, the shouldering may be due to overlap between 2 endothermic peaks caused by a solid-solid transformation closely followed by melting, or due to overlap between an endothermic peak, exothermic peak and final endothermic peak, due to melting of one polymorph, re-crystallization into another and finally melting of this new polymorph.

The TGA analysis (Fig. 6.48) shows less than 5% mass loss before the melt transitions of all for crystal, suggesting loss of residual surface-adsorbed solvent may be responsible for some of the DSC endothermic transitions before melting. The crystals' solubility in diethyl ether is presented in Table 6.2.

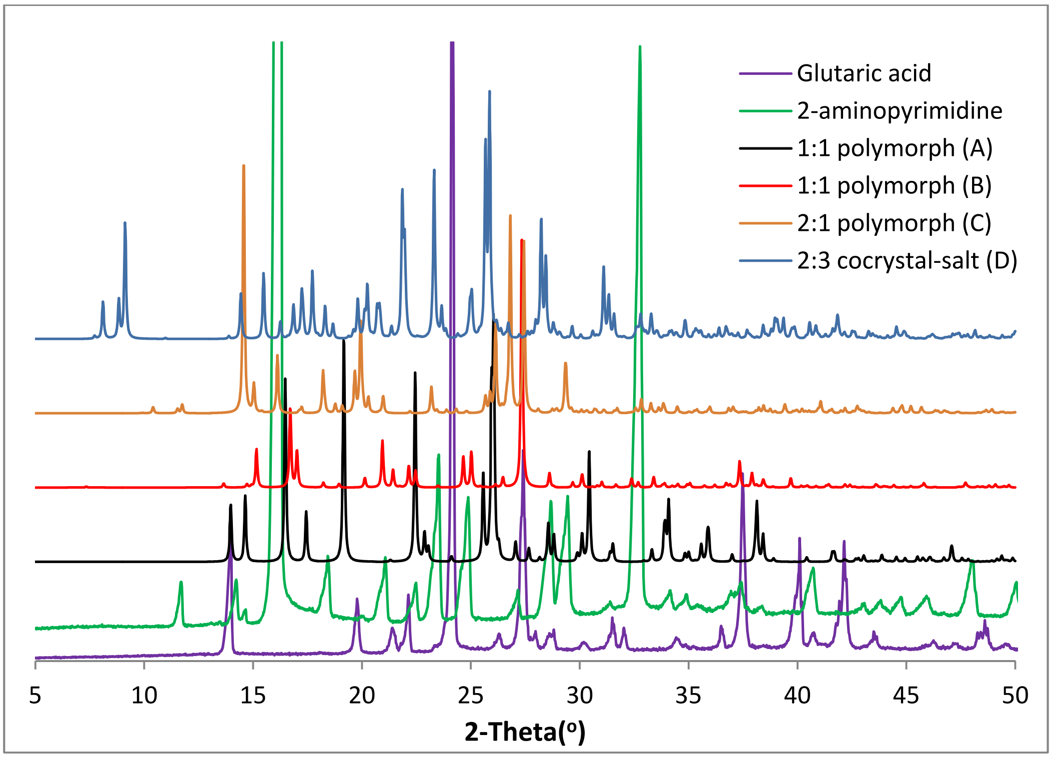

Fig.6.44 Simulated PXRD patterns for the 4 new crystal forms of 2-aminopyrimidine-glutaric acid, glutaric acid and 2-aminopyrimidine.

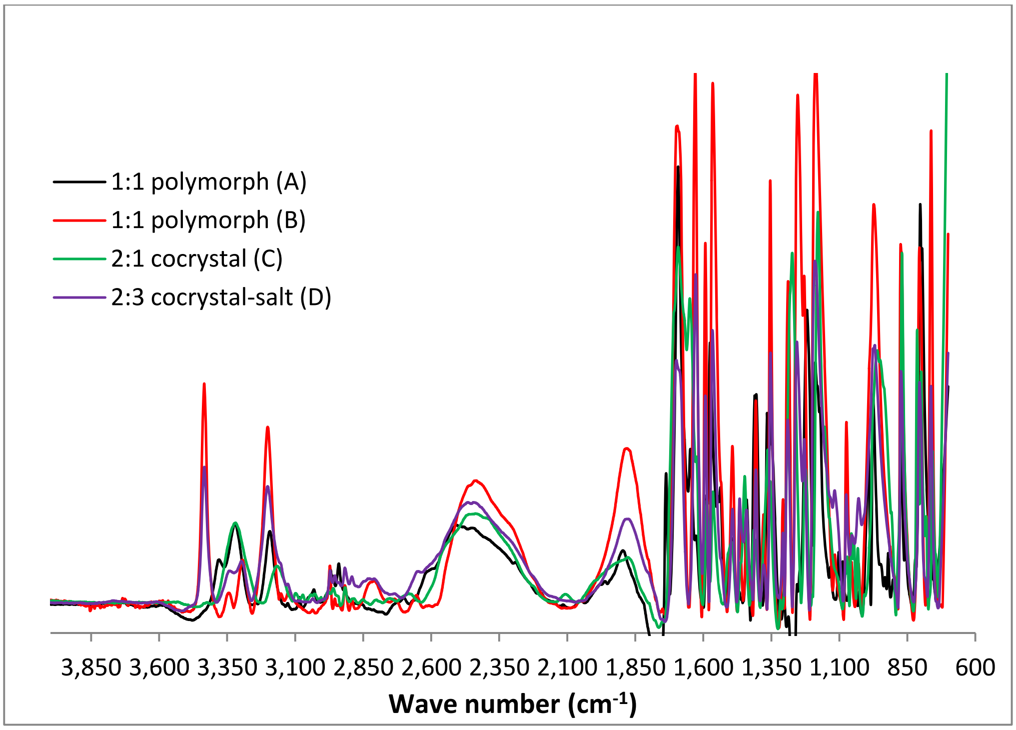

Fig. 6.45 FTIR spectra of all 2-aminopyrimidine-glutaric acid cocrystals.

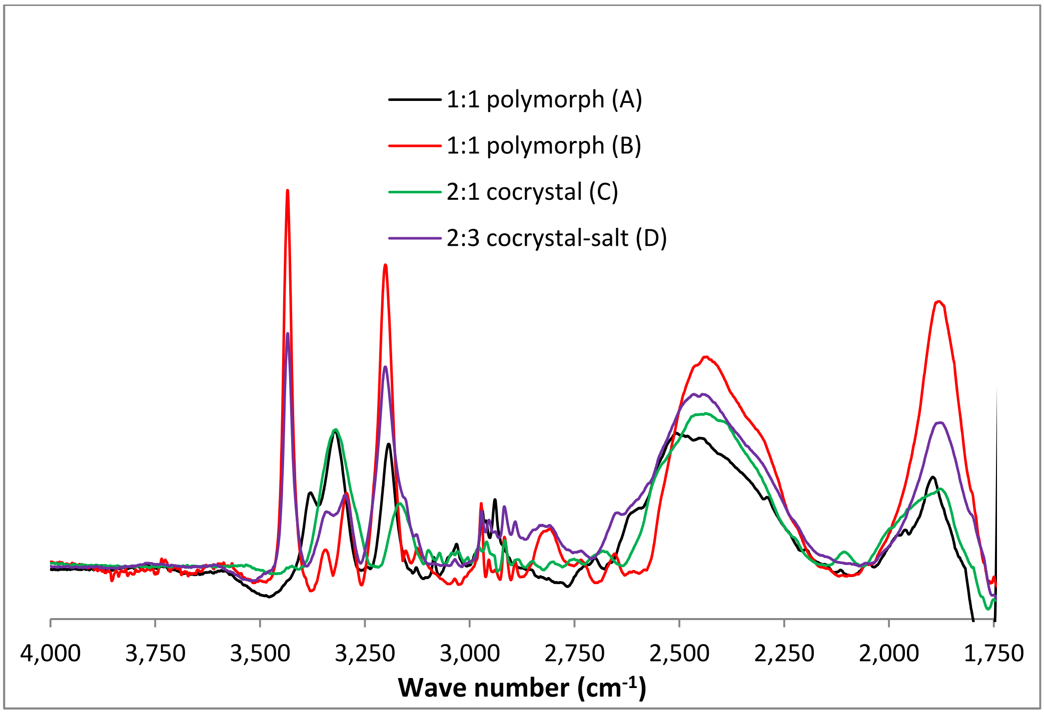

Fig. 6.46. FTIR comparison between 1750 cm^{-1} and 4000 cm^{-1} region.

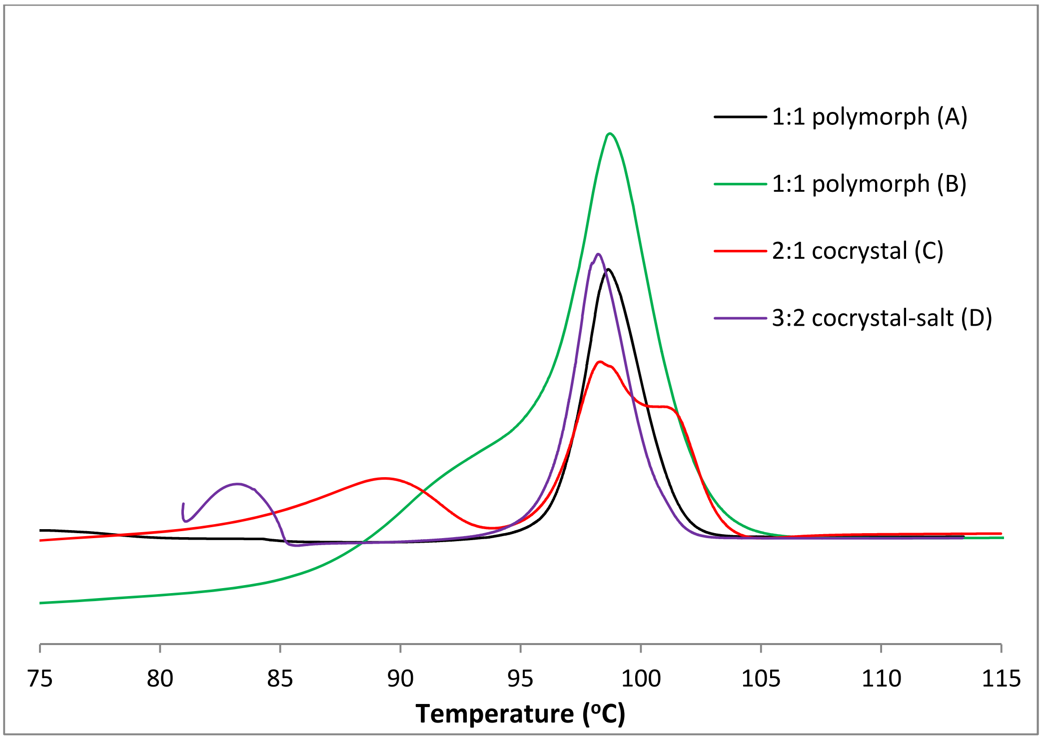

Fig. 6.47 DSC thermogram of all 2-aminopyrimidine-glutaric acid cocrystals.

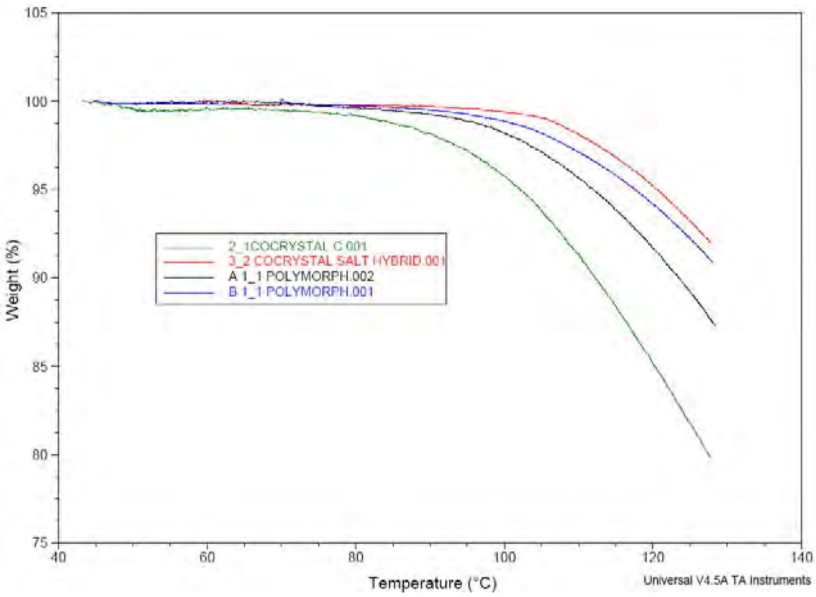

Fig. 6.48 TGA thermogram of all 2-aminopyrimidine-glutaric acid cocrystals.

6.8.1 Conformational polymorphism

Crystals **A** and **B** are 1:1 polymorphs of 2-aminopyrimidine-glutaric acid cocrystal. A comparison of their PXRD pattern (Fig. 6.49) shows considerable difference in their simulated powder pattern. Diffraction peaks at 13.96°, 14.66° and 30.48° in **A** are absent in **B**; and diffraction peaks: 15.2°, 20.9° and 27.26° present in **B** but not in **A**.

A comparison of the FTIR spectra for both **A** and **B** in the region between 1750 cm^{-1} and 4000 cm^{-1} (Fig. 6.50) shows two peaks at 2805 cm^{-1} and 3431 cm^{-1} present in **B** are absent in **A**. Overlaying the DSC thermogram of **A** and **B** (Fig. 6.51) shows two endothermic transitions in **A** but a single transition in **B**. The peak maximums for the two larger endothermic peaks are very close at 98.6 °C and 98.8 °C, respectively, suggesting that the two forms melting at this temperature may be the same. The heat of transition rule states that if any endothermic transition is observed below the melting point of a polymorph that is the most stable at ambient temperature, then it can be assumed that a solid-solid transition exists below this point and both polymorphs are enantiotropically related[8-11]. Consequently, the peak endotherm at 73.4 °C in the thermogram of **A** may suggest that **A** and **B** are enantiotropic polymorphs, with **A** the stable form below 73.4 °C converting to B at 73.4 °C.

Table 6.2 Cocrystal solubility (mg/g) in Diethyl ether

A	B	C	D
7.3	6.8	11.4	5.7

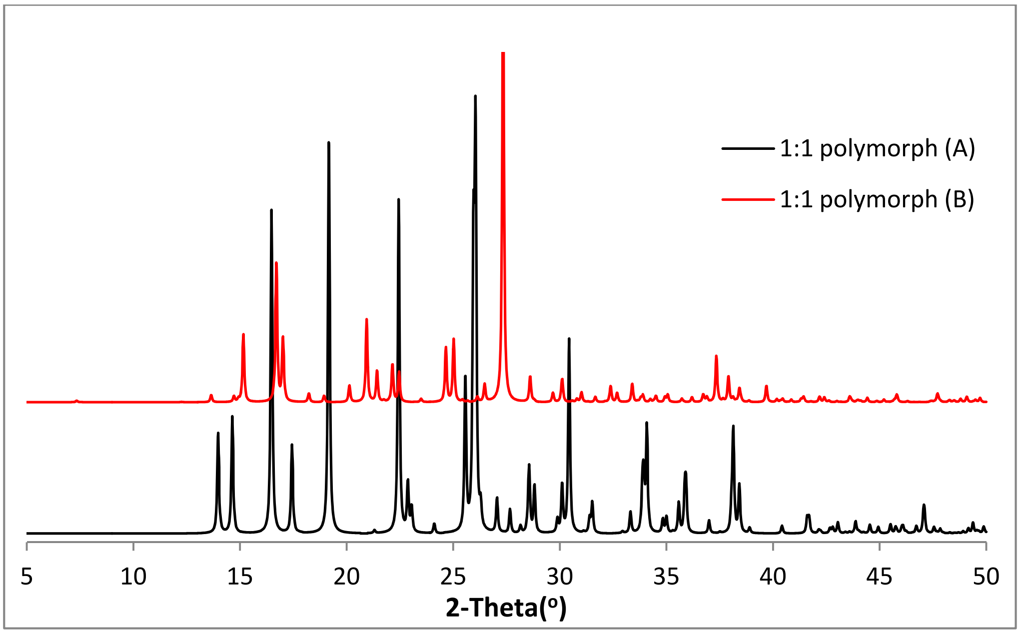

Fig. 6.49 Simulated PXRD pattern for 1:1 polymorph of 2-aminopyrimidine-glutaric acid cocrystal.

To verify the latter, a sample of **A** was heated and the PXRD measured at temperatures of 80 °C, 90 °C and 30 °C after cooling (Fig 6.52). The sample used was grounded gently to reduce particle size to help minimise the effect of preferred orientation but avoid inducing polymorphic transformation. The simulated PXRD at 25°C was used in the comparison. It can be seen that although the sample still shows preferred orientation, with many peaks missing that are present in the simulated PXRD, at 80 °C, 90 °C and 30 °C after cooling, the PXRD shows new broad peaks at $2\theta = 24.3^o$ and 26.8^o. These new peaks are consistent with **B** and not **A**. In addition, the intense A peak at 16.5° has disappeared, confirming that at elevated temperature **A** converts to **B**.

Crystals of **A** were heated on a microscope stage and then monitored for phase transition (Fig. 6.53). The microscope pictures show that at about 73 °C, crystals of **A** lose their brightness and become dark without going through a melt phase. This further suggests that **A** undergoes a solid-solid polymorphic transition to **B**.

A similar experiment was carried out at 25 °C and 90 °C with **B** (Fig. 6.54). The PXRD at 90 °C is similar to that at 25 °C, showing no phase transition occurs.

Combining the variable PXRD results for **A** and **B** and microscope thermal analysis of **A**, shows that A undergoes a solid-solid state polymorphic transition to **B** around 73.4 °C. The PXRD for **A** that has been heated and transformed to B remains the same at

30 °C after slow cooling, showing that it remains in the B polymorphic state. This is more consistent with a monotropic and not enantiotropic polymorphic relationship, between **A** and **B**, i.e. that **A** is the metastable polymorph and **B** is the stable one at all temperatures.

The proposed stability between polymorphs **A** or **B** is supported by the density rule, which states that if a particular form has a lower density then at absolute zero it can be assumed that this will be less stable form[8-10,12]. The density of **A** is 1.407 g cm^{-3} and **B** is 1.437 g cm^{-3} (Table 6.1). Applying the density rule means that **B** is the more stable than **A**. Although the application of the density rule to cocrystals may not be completely error free because hydrogen bonding may compensate for a weaker van der Waals attraction[13], it does suggest that **A** is the metastable form and **B** is the stable form. Also consideration of the hydrogen bond lengths in motif M5 (section 6.4) present in **A** and **B**, indicates the bonding in **B** is stronger than that of **A**. The room temperature solubility of **A** and **B** in diethyl ether was determined by gravimetric method, to be 7.3 mg/g and 6.8 mg/g respectively. These results show **A** has a higher solubility than **B** (but the values are close) again suggesting that **A** is the metastable polymorph and **B** is the stable polymorph. Consequently, the observed crystallisation of **A** from acetonitrile with a 1:1 molar mixture of 2-aminopyrimidine and glutaric acid shows that the crystallisation is under kinetic control, obeying Ostwald's rule of stages.

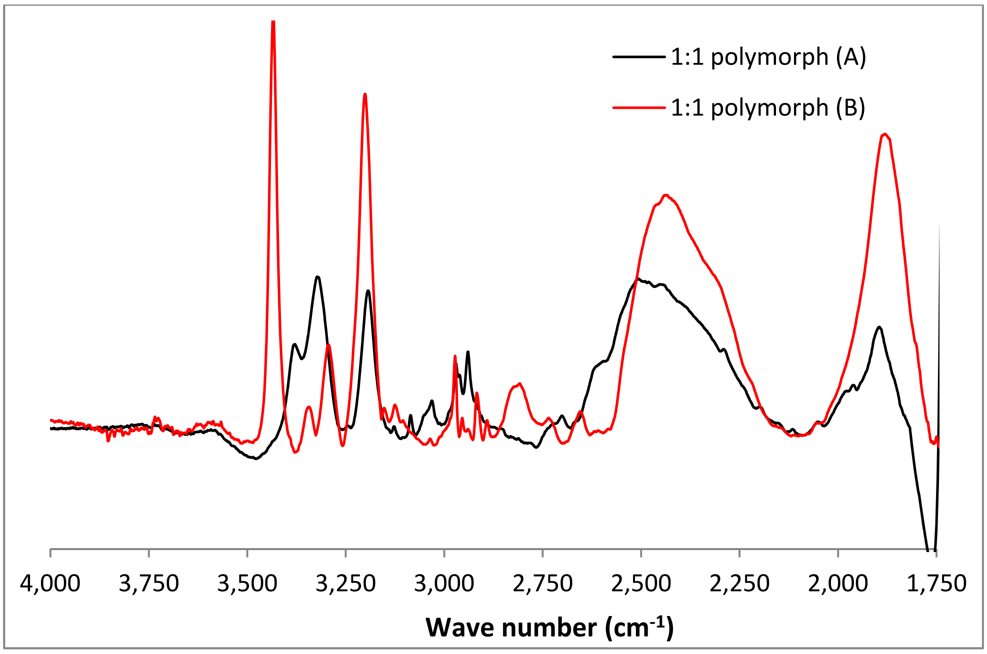

Fig. 6.50 FTIR comparison between 1750 cm^{-1} and 4000 cm^{-1} region for 1:1 polymorphs.

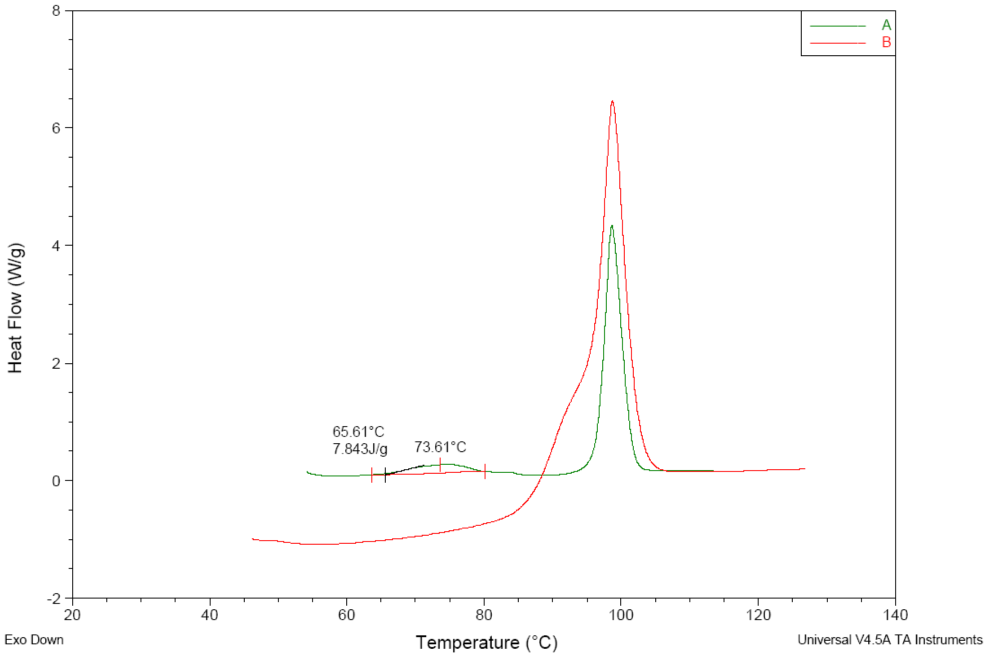

Fig. 6.51 DSC thermogram for 1:1 polymorph of 2-aminopyrimidine-glutaric acid cocrystal.

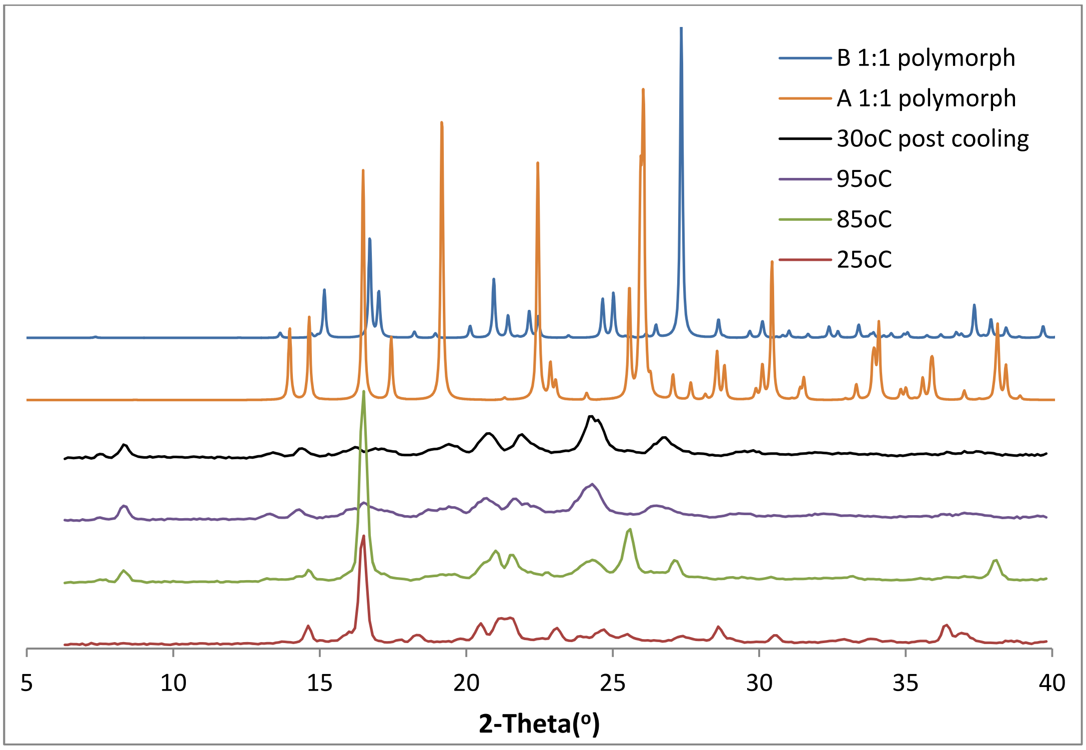

Fig. 6.52 PXRD of 1:1 polymorph (**A**) of 2-aminopyrimidine-glutaric acid cocrystal collected at three different temperatures: 25 °C, 80 °C, 90 °C and 30 °C after cooling, compared with the Simulated PXRD of **A** and **B**. The PXRD shows a possible phase transition of **A** to **B**.

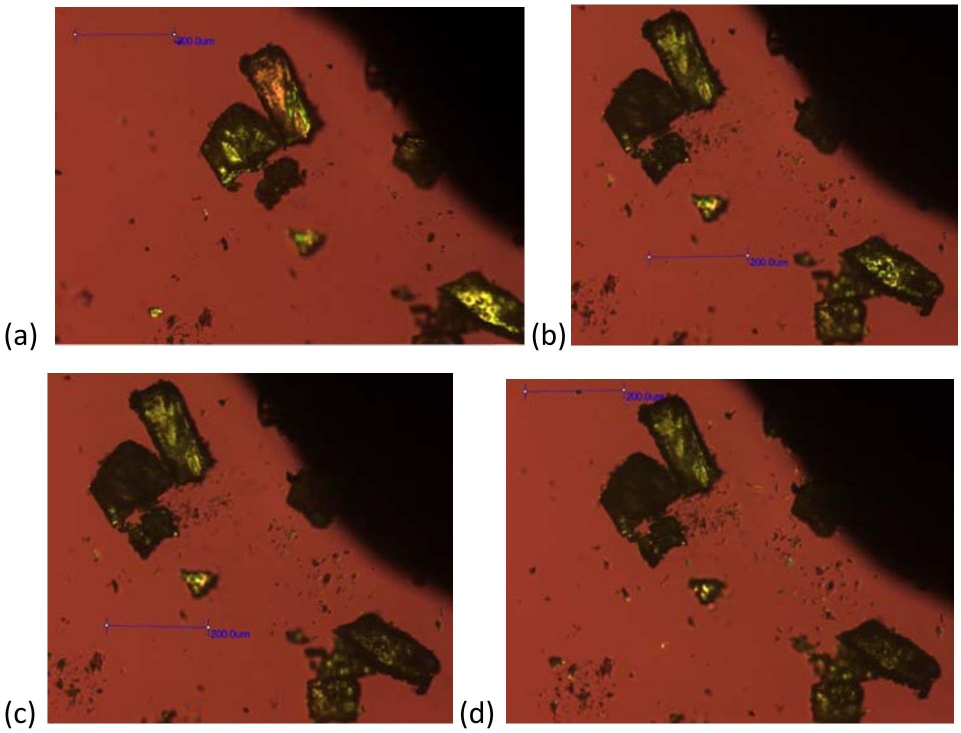

Fig. 6.53 Microscope images of 1:1 polymorph (**A**) of 2-aminopyrimidine-glutaric acid cocrystal. (a) at 25°C, (b) at 73.2°C, (c) at 73.8°C and (d) at 79°C. Pictures show crystals of **A**, at the top and bottom of the picture goes from bright to a dark crystals as temperature is increased. **A** transformation at elevated temperature does not go through a melt stage.

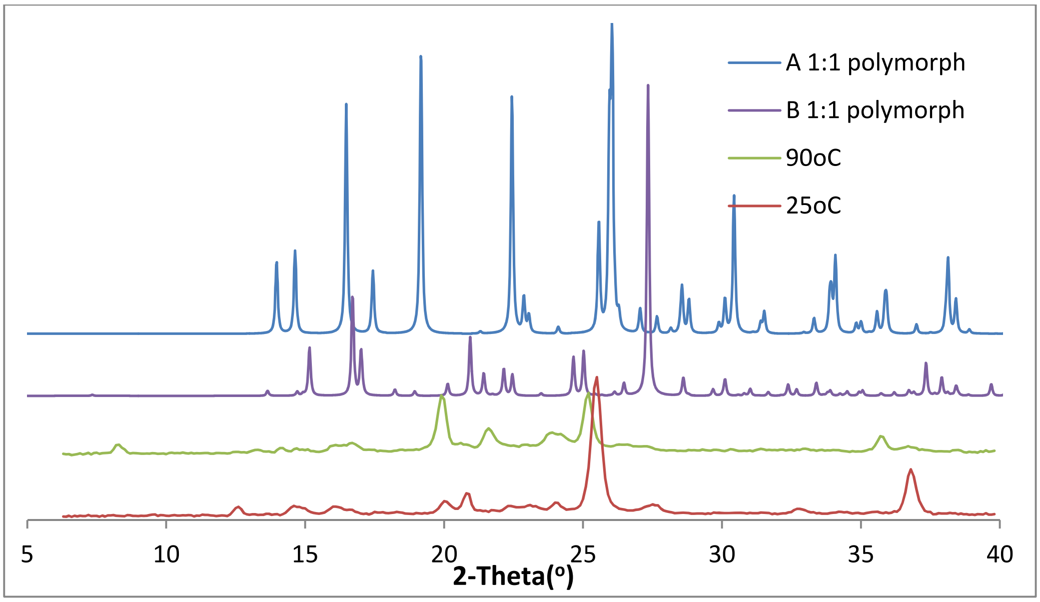

Fig. 6.54 PXRD of 1:1 polymorph (**B**) of 2-aminopyrimidine-glutaric acid cocrystal collected at two different temperatures: 25 °C and 90 °C, compared with the Simulated PXRD **A** and **B**. The PXRD shows no phase transition occurs at elevated temperature.

Glutaric acid displays cocrystal polymorphism as a coformer due to its torsional flexibility[23]. Glutaric acid has a preference for the twisted (α) over the planar (β) conformation[3]. The energy barrier between typical torsional conformations could be as low as 1-2 Kcal/mol [24]. The solid-solid transition in the thermogram of **A** has an enthalpy of 8.8 J/g ≈ 0.5 Kcal/mol, which is half the suggested value for a torsional conformation change, again supporting the idea that **A** transforms to **B** at 73 °C. The torsional flexibility in glutaric acid is due to the twisting of the carboxylic acid groups[25].

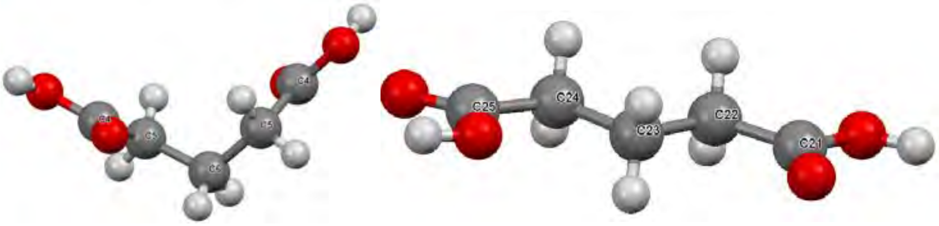

Fig. 6.55 Twisted and linear conformation of glutaric acid.

In particular, in cocrystal **A**, the glutaric acid torsion angle in C4-C5-C6-C5 = -74.9 ° (Fig. 6.55) and gives a twisted conformation but in **B**, the glutaric acid torsion angle in C22-C23-C24-C25 = -179.14 ° and C21-C22-C23-C24 = 179.45 ° and so gives a planar conformation.

6.8.2 Stability of cocrystal vs. salt

1:1 2-aminopyrimidine-glutaric acid cocrystal (**B**) and 2:3 2-aminopyrimidine-glutaric acid cocrystal-salt hybrid (**D**) were both made from solution cocrystallisation in 50:50 wt % of methanol and chloroform. A stability experiment was carried out to determine which multi-component crystal was more stable. A 1:1 solution of aminopyrimidine and glutaric acid was allowed to evaporate over 3 months; and the crystal isolated from this experiment analysed by single crystal analysis and found to be 1:1 2-aminopyrimidine-glutaric acid cocrystal (**B**). A very slow crystallisation is more likely to achieve the thermodynamically more stable form under the imposed conditions of temperature, pressure and composition. This is because the system spends sufficient time at low concentrations where either only the most stable form is supersaturated, or the metastable form is barely supersaturated and so cannot nucleate, that the most stable form has time to nucleate and grow. However, this strategy of employing slow evaporation can still sometimes produce a metastable form rather than the most stable one. This is particularly the case if the most stable form has a high nucleation barrier, and/or the metastable form is only slightly less stable and hence has a similar solubility as the most stable form. In addition, dimers/aggregates may occur in some solvents, which then favour a specific crystal form containing that dimer/aggregate. This means that of the two cocrystals **B** and **D** obtained in 50:50 *wt* % of methanol and chloroform solution cocrystallisation using a 1:1 solution of aminopyrimidine and glutaric acid, **B** is the thermodynamically favoured cocrystal form and **D** is kinetically favoured. The thermogram of **D** shows a solid-solid transformation requiring only a lower enthalpy of 4.69 J/g occurs at 83.5 ^{o}C followed by melting at 98.2 ^{o}C. The question arises as to what is the structure of the final melting species in **D**. To answer this, a sample of **D** was heated and the PXRD measured at temperatures of 25 ^{o}C, 97 ^{o}C and 25 ^{o}C after cooling (Fig. 6.56). The problem of preferred orientation of sample was encountered because minimal grinding was done to avoid a phase transition. The PXRD at 97 ^{o}C and 25 ^{o}C after slow cooling shows the disappearance of the peak at 2θ = 26^{o} and appearance of two broad peaks at 2θ = 25.1^{o}. These changes are consistent with at least some of **D** converting to **B** at elevated temperature.

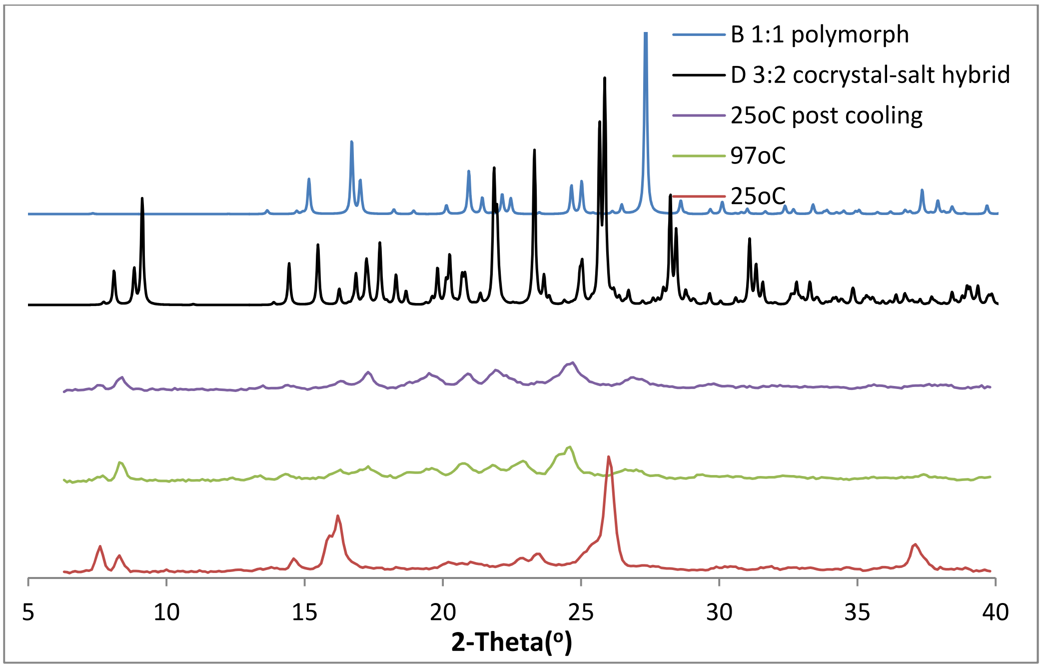

Fig. 6.56 PXRD of **D** collected at five different temperatures: 25 ^{o}C, 97 ^{o}C and 25 ^{o}C after cooling compared with the Simlated PXRD of **D** and **B**. The PXRD shows a likely phase transition from **D** to **B**.

6.8.3 The salt - cocrystal continuum

Salts and cocrystals differ in the position of the hydrogen atom in the final supramolecules. A complete transfer of the hydrogen atom to the hydrogen acceptor (HA) gives a salt but non-transfer of the hydrogen gives a cocrystal.

The ΔpKa can be used for predicting cocrystal formation (section 1.3.3). Childs et al.'s[18] review of the cocrystal-salt continuum with 2-aminopyrimidine and carboxylic acids, which included fumaric and succinic dicarboxylic acids, suggests that between ΔpKa 0-3 the cocrystal or salt prediction reliability drops because at equilibrium the ratio of ionised and unionised species in solution is relatively close to 1 and so other factors can influence the type of multicomponent crystal formed.

The ΔpKa values for 2-aminopyrimidine (3.86)[18] and glutaric acid (4.32 and 5.42)[19] are -0.46 and -1.56. Both values are negative and so the formation of a cocrystal is expected only[18]. Instead, cocrystal (**B**) and cocrystal-salt hybrid (**D**) were obtained in the 50:50 wt % of methanol and chloroform solvent system. -0.46 is close to zero where ΔpKa prediction reliability drops. In fact, using ΔpKa =-0.46 in equation 1.21 from Chapter 1, we see that the ratio of neutral to charged species is 0.35:1, showing that similar quantities of both the charged and neutral species are present in solution. The same solvent system was used, so a specific solvent effect can be eliminated. One factor that was not controlled was the rate of solvent evaporation. Quick solvent evaporation could prevent the crystallised metastable form re-dissolving and precipitating as a more stable form.

Other likely factors affecting the crystallisation outcome will include the relative stability of the salt vs. cocrystal, the nucleation energy barriers for the crystallisation of the two forms, and their relative crystal growth rates. Given that an ionic species will have a significantly different interaction with the surrounding solvent than a neutral one, it is highly possible that the nucleation pathways and barriers (and their crystal growth rates) can differ significantly between cocrystal and salt forms, particularly in the absence of complexation in solution.

6.8.4 Cocrystal colour

Cocrystal **B, C** and **D** crystals are peach-orange, rose and gold in colour, respectively, while crystals of **A** are white. 2-aminopyrimidine acts as a chromophore because of its electron rich aromatic ring, enabling the crystals to absorb light in the visible region of the electromagnetic spectrum; absorption in this region is responsible for imparting colour in matter. The orientation of the chromophore in organic molecules have been shown to impact colour properties[10]. In cocrystal forms **B, C** and **D,** the 2-aminopyrimidine ring has a planar orientation because of the planar conformation of the glutaric acid molecule hydrogen-bonded to it; but in **A**, the 2-aminopyrimidine molecule is not planar because of the twisted glutaric acid molecule.

Cocrystal **B, C** and **D** have different colours; hydrogen bonding can also influence the colour intensity of organic molecules. When a strong dipole-dipole effect is induced by hydrogen bonding in a molecule with a chromophore, absorption in the electromagnetic spectrum is shifted to longer wavelengths resulting in a bathochromic shift (red colour shift)[20,21] and higher colour intensity[22].

2-aminopyrimidine is light yellow in colour, the hydrogen bonding distance in motif M2 in 2-aminopyrimidine is 3.077 Å (Fig. 6.2). This length is longer than the hydrogen bonding distance in motifs M5, which are present in **B** and **C**, and M8 in **D**. These motifs involve hydrogen bonding between 2-aminopyrimidine and glutaric acid. Considering **B**, the hydrogen bond distances are: N1-H1B·····O4 = 2.894 Å and N2····H3-O3 bond = 2.677 Å**.** In **C** the bonding distances are: N21—H21A·····O4 = 2.884 Å and O3—H3·····N22 = 2.652 Å. In **D**, motif M8 the hydrogen bonding distances are: N22$^{(+)}$-H22·····O44$^{(-)}$ = 2.585 Å, N3$^{(+)}$-H3·····O42$^{(-)}$ =2.602 Å , N21-H21A·····O43$^{(-)}$ =2.924 Å and N1-H1A·····O41$^{(-)}$ =2.832 Å between the glutaric acid dianion and 2-aminopyrimidine cation in **D.**

The shorter hydrogen bond lengths observed in **B**, **C** and **D** indicates stronger hydrogen bonding and hence a stronger dipole-dipole effect exists in **B**, **C** and **D** compared to 2-aminopyrimidine. Consequently, the strong dipole-dipole effect shifts absorption to longer wavelengths (bathochromic shift to red colour) in **B**, **C** and **D** compared to 2-aminopyrimidine.

6.9 SVC and STR slurry cocrystallisation.

The importance of controlling polymorphism during API manufacture has already been stated. The control of polymorphism in the 2-aminopyrimidine-glutaric acid cocrystal system was investigated. Slurry cocrystallisation of 2-aminopyrimidine and glutaric were carried out in the SVC and STR to determine their capability in controlling polymorphism. The solvent systems used were 2.2 wt% methanol in cyclohexane (SVC), 100% methanol (STR), 100% chloroform (STR), 100% acetonitrile (STR) and 50:50 wt % of methanol and chloroform (STR). Note that the STR experiments using methanol, chloroform and acetonitrile could not be repeated on the SVC because the elastic membrane (Section 2.1.1) broke due to incompatibility with the solvents.

6.9.1 SVC slurry cocrystallisation in 2.2 wt % methanol in cyclohexane.

2-aminopyrimidine-glutaric acid cocrystallisation was done in the SVC using 34.15 g of 2.2 wt % methanol in cyclohexane, 0.01 mole of 2-aminopyrimidine and 0.01 mole of glutaric acid; the solid loading was 6.2%. After 30 minutes of oscillatory mixing, the slurry was filtered, dried and a light yellow powder (Fig. 6.57) was isolated. The weight of solid recovered was 1.93 g (85.02%). Cocrystal yield was not determined because of lack of time.

Fig. 6.57 Picture of SVC sample light yellow powder.

The sample was analysed by PXRD. Overlaying the PXRD pattern of the SVC sample with 2-aminopyrimidine and glutaric acid (Fig. 6.58) shows that the intense diffraction peaks at 2θ= 11.61°, 16. 44° and 32.93° in 2-aminopyrimidine and 24.07° and 37.37° in glutaric acid are absent in the sample suggesting a cocrystal has formed. The new peaks in the cocrystal are: 8.16°, 9.18° , 25.43° and 25.59°. The PXRD pattern of the SVC sample was compared with the four new 2-aminopyrimidine-glutaric acid cocrystals (Fig. 6.59).The new peaks at 8.16° and 9.18° in the SVC sample matches the peaks at 8.06°, 8.86° and 9.18° in **D**, with these diffraction peaks only being in **D** (2:3 2-aminopyrimidine-glutaric acid cocrystal-salt hybrid). However, the peaks at 13.9° and 26.7° in the SVC sample are absent in **D** (Fig. 6.59). These peaks are close to the peaks at 13.78° and 27.3° in glutaric acid (Fig. 6.58) suggesting residual glutaric acid could be present in the SVC sample, though given the absence of the intense glutaric acid peaks at 24.07° and 37.37°; this seems unlikely unless sample orientation is responsible for the apparent absence of these peaks. Alternatively, the sample may also contain 2:1 cocrystal **C**, which was previously obtained in the methanol solution cocrystallisation, or the SVC sample cocrystal may differ from **A**, **B**, **C** and **D**.

The SVC sample was analysed by ATR-FTIR. Overlaying the SVC FTIR spectrum with that for 2-aminopyrimidine and glutaric acid (Fig. 6.60), the region between 1750 cm^{-1} and 4000 cm^{-1} (Fig. 6.61) shows two new broad peaks in the SVC sample at 1900 cm^{-1} and 2350 cm^{-1} absent in glutaric acid and 2-aminopyrimidine; these peaks are characteristic of un-ionised O-H hydrogen bonding stretching of the carboxylic acid[7,17,18]. A comparison of the FTIR spectrum of the SVC sample with **C** and **D** (Fig. 6.62) shows that it has a closer match with **C** than **D** spectrum.

The DSC analysis (Fig. 6.63) shows three endotherm peaks; the first has an onset temperature of 78.7 ^{o}C, peak maximum of 82.1 ^{o}C and enthalpy of 9.64 J/g. The second endotherm has an onset temperature of 89.4 ^{o}C, peak maximum of 91.4 ^{o}C and enthalpy of 10.7 J/g. The last endotherm has an onset temperature of 95 ^{o}C, peak maximum of 97.3 ^{o}C and transition enthalpy of 156.0 J/g. 2-aminopyrimidine (122.4 ^{o}C and 126.5 ^{o}C) and glutaric acid (93.5 ^{o}C and 97.2 ^{o}C). When the thermograms are overlaid (Fig. 6.64), the SVC sample has only a slightly higher melting point than glutaric acid. However, the enthalpy of fusion in glutaric acid is 84.23 J/g while that of the SVC samples is 156.0 J/g (Fig. 6.63); this is twice that in glutaric acid. Despite this transition overlap, the difference in enthalpies of fusion confirms that the SVC sample is not glutaric acid.

The first endotherm in the SVC sample overlaps with the boiling point for cyclohexane (80.74^{o}C), so is likely to be the desolvation of cyclohexane from the sample. A comparison of the thermogram of **D** and the SVC sample was done (Fig.6.65) because of the similarity in their PXRD. The melt transition for **D** is slightly higher than that for the SVC sample. The enthalpy of fusion in the SVC sample (156.0 J/g) is similar to that in **D** (151.8 J/g).

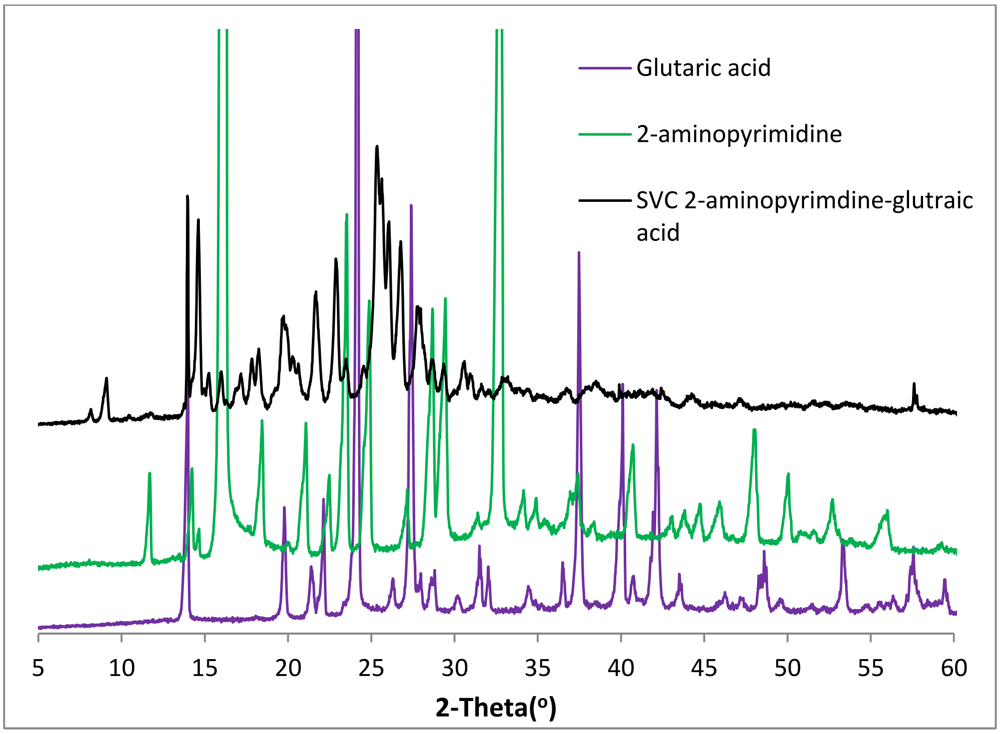

Fig. 6.58 A comparison of PXRD for SVC sample of 2-aminopyriminde-glutaric acid cocrystal and component.

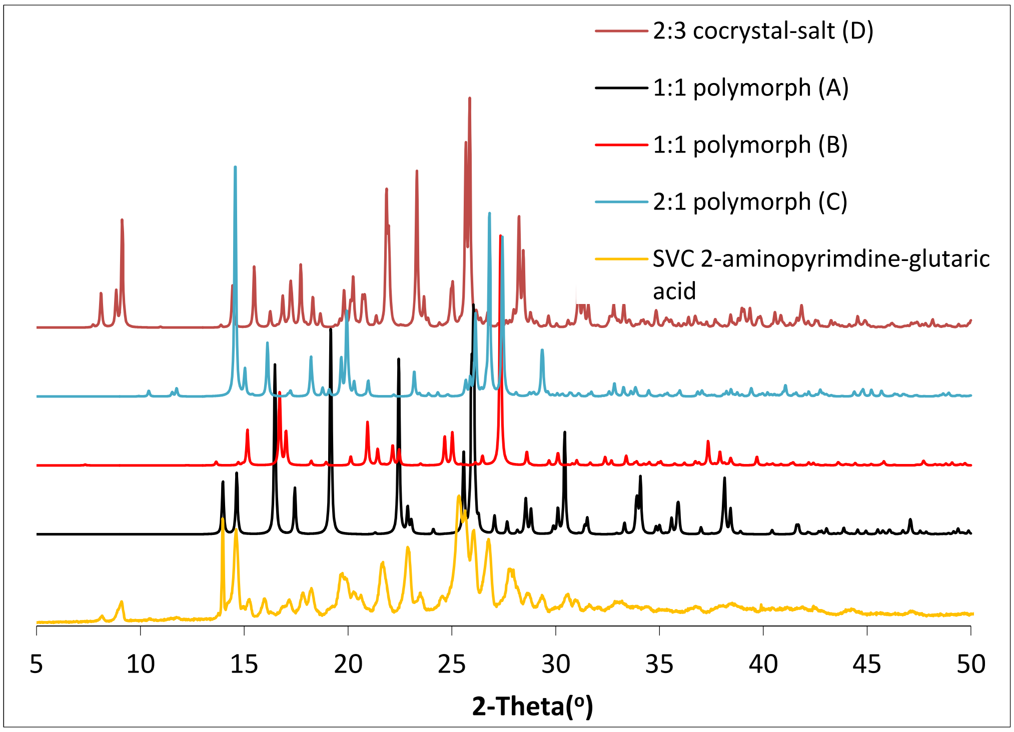

Fig. 6.59 A comparison of PXRD for SVC sample and simulated patterns of 2-aminopyrimidine-glutaric acid cocrystals.

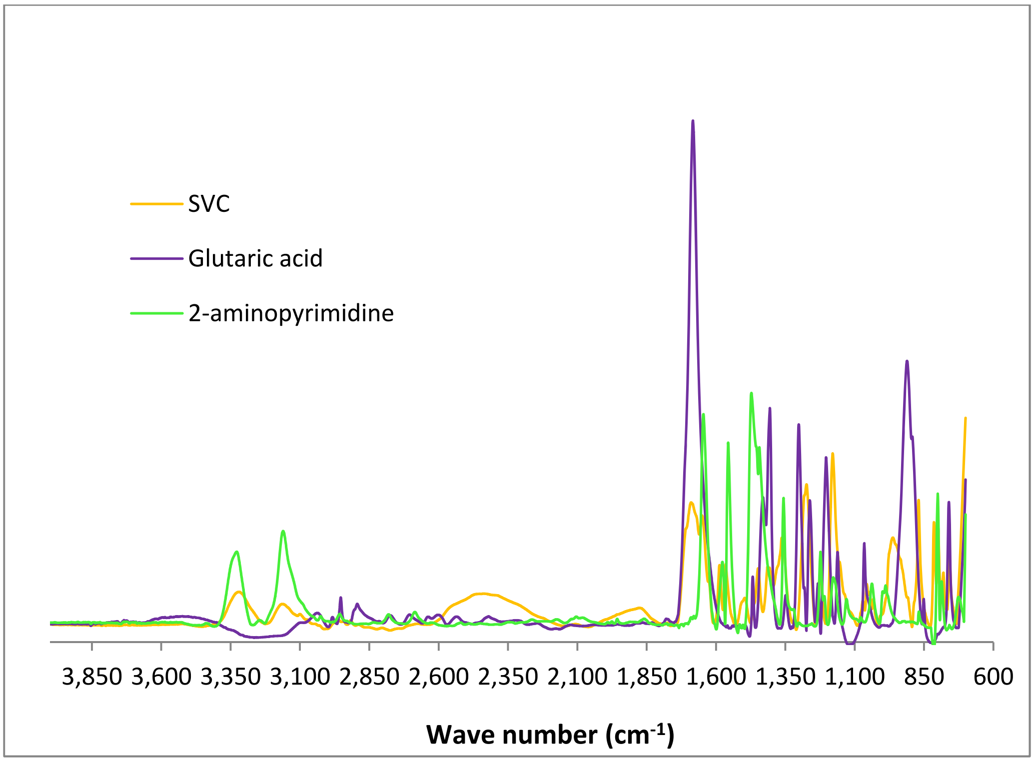

Fig. 6.60 A comparison of FTIR spectrum for SVC sample of 2-aminopyriminde-glutaric acid cocrystal and components.

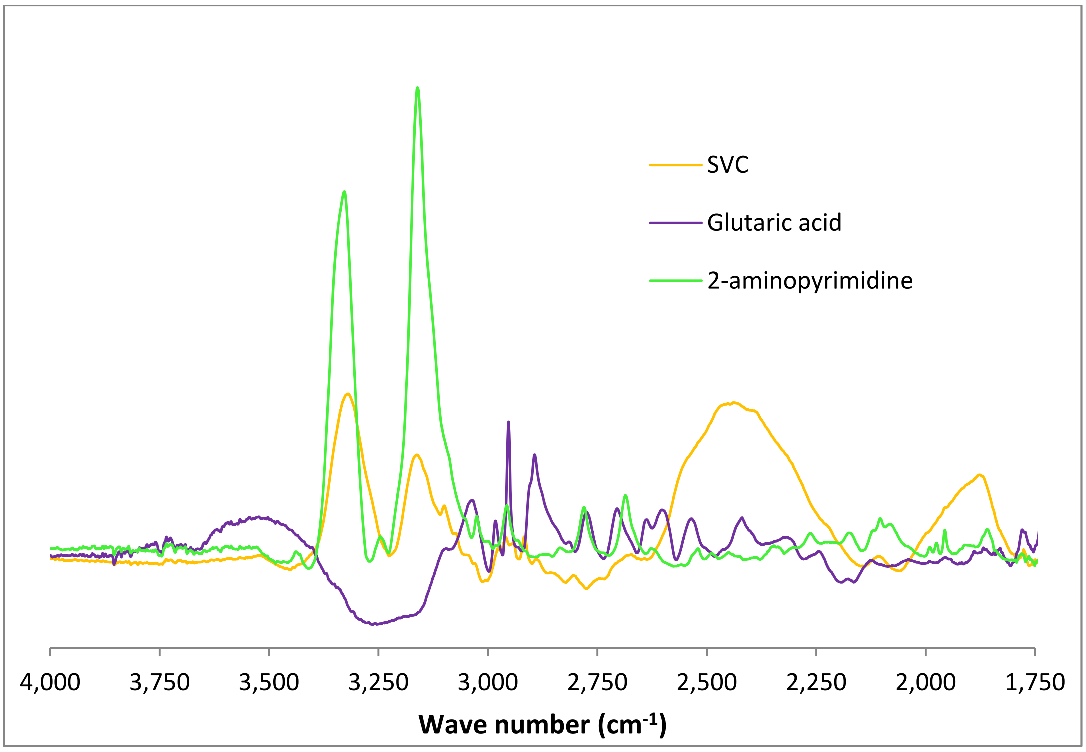

Fig. 6.61 FTIR comparison between 1750 cm^{-1} and 4000 cm^{-1} region for SVC sample.

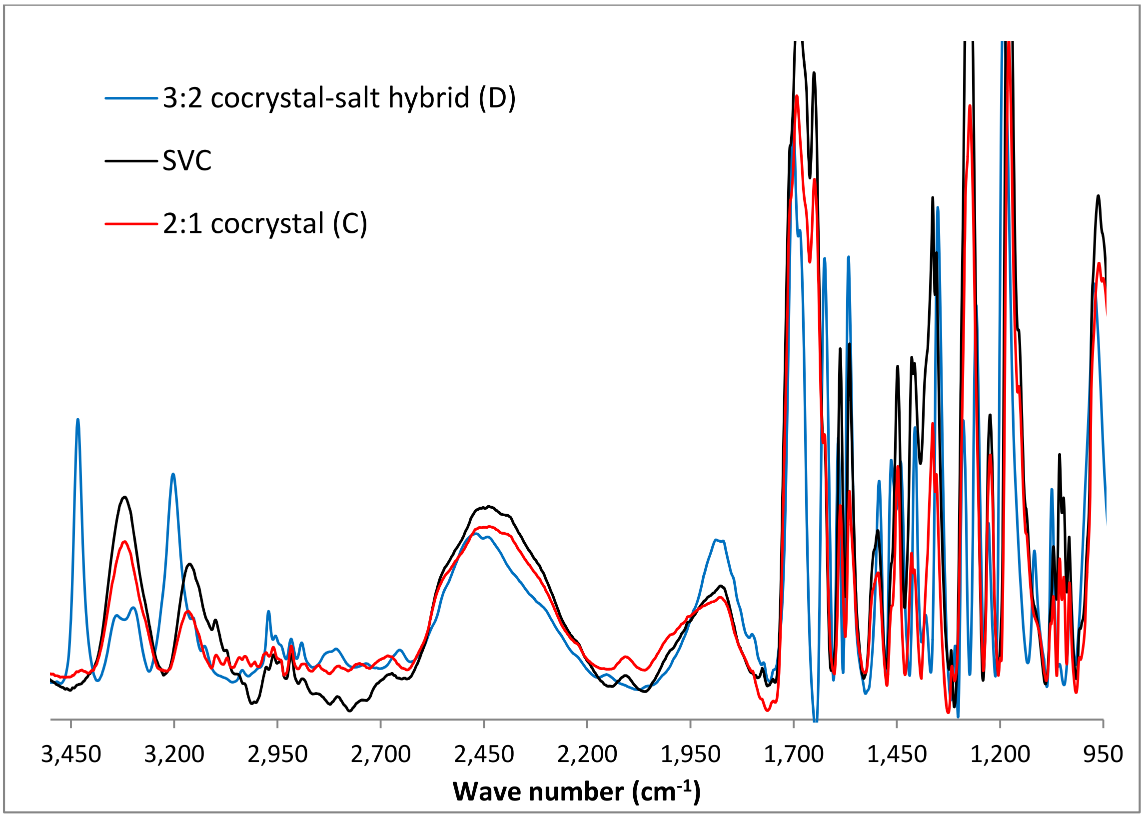

Fig. 6.62 FTIR spectrum of SVC sample, **C** and **D**. Showing that the FTIR spectrum of SVC sample is a better match with **C** than **D**.

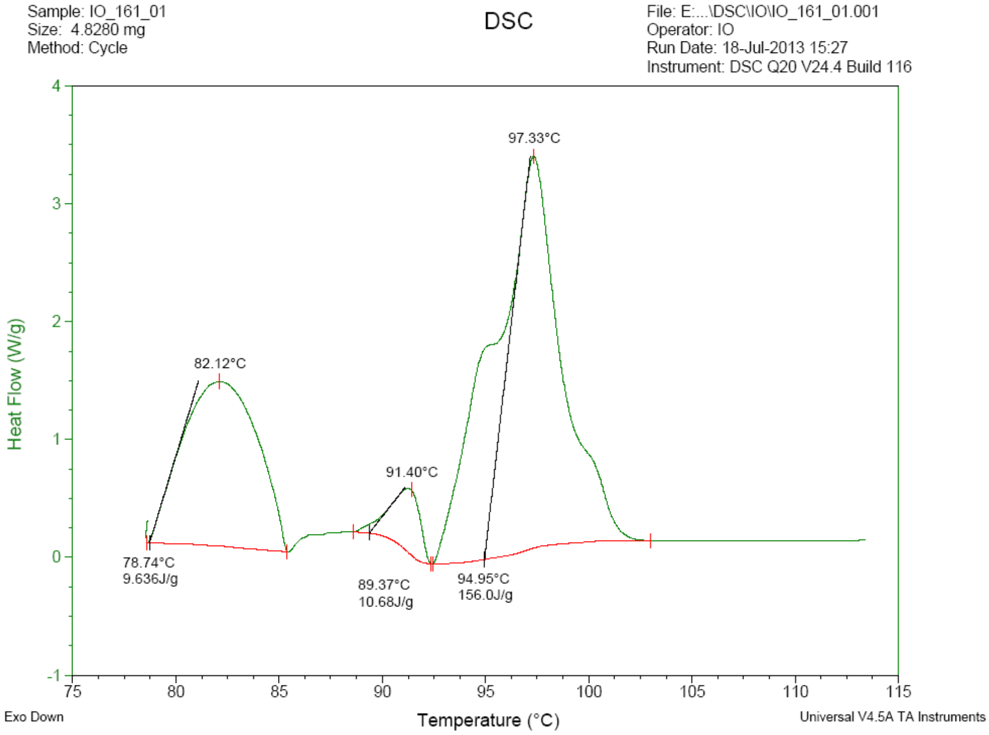

Fig. 6.63 DSC thermogram of the SVC sample. Showing three endothermic peaks.

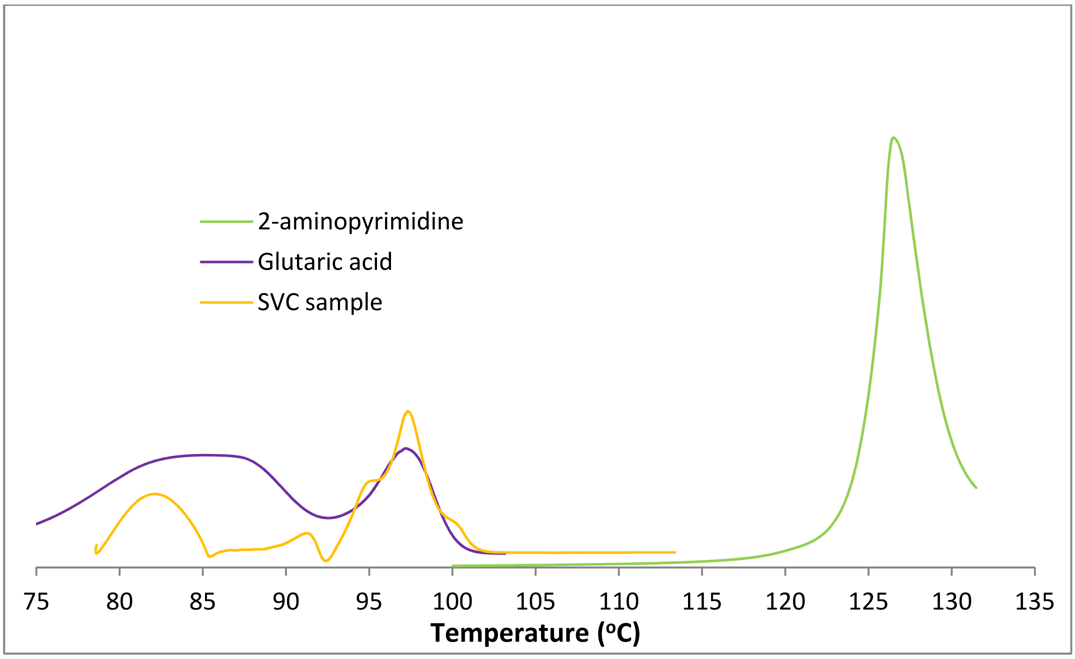

Fig. 6.64 A comparison of the DSC thermogram of the SVC sample and it's components.

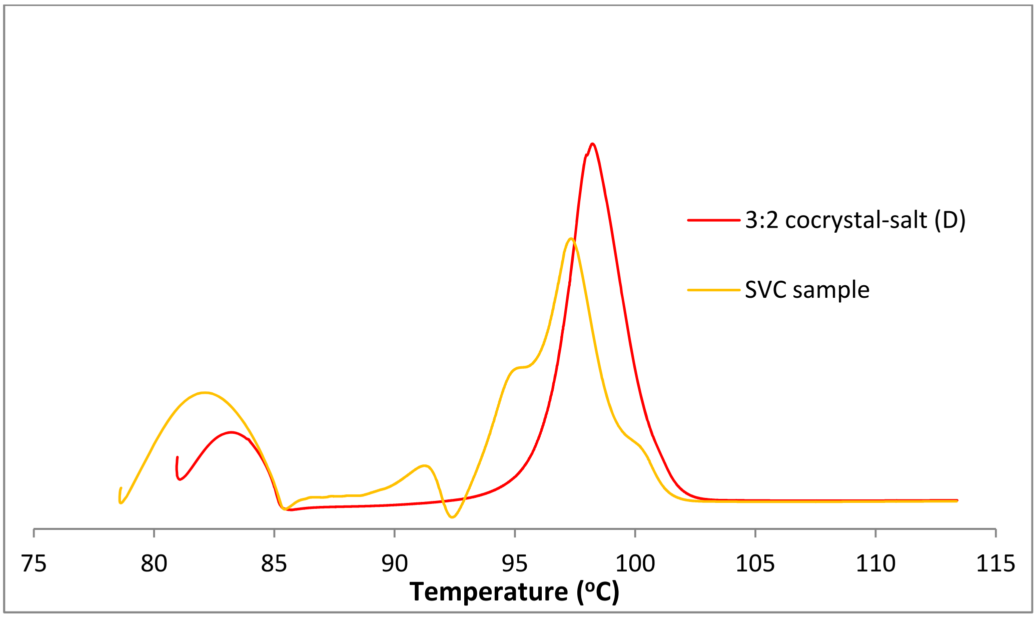

Fig. 6.65 Comparing **D** and SVC DSC thermogram.

6.9.2 STR slurry cocrystallisation in 100% chloroform

STR cocrystallisation of 2-aminopyrimidine-glutaric acid was carried out using 34.2 g of 100% chloroform, 0.01 mole of 2-aminopyrimidine and 0.01 mole of glutaric acid; the solid loading was 6.2%. After 60 minutes of mixing in a 250 ml flask, the slurry was filtered, dried a light yellow powder (Fig. 6.66) was isolated. The weight of solid recovered was 1.51g (66.52%).

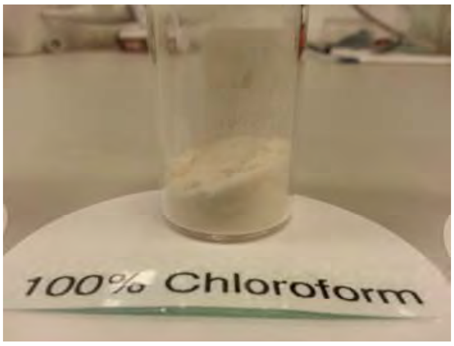

Fig. 6.66 Picture of light yellow powder from 100% chloroform.

The sample was analysed by PXRD. Overlaying the PXRD pattern with 2-aminopyrimidine and glutaric acid (Fig. 6.67), the intense diffraction peaks at 2θ = 11.61° and 32.93° in 2-aminopyrimidine; 31.53° and 32.11° in glutaric acid are absent in the cocrystal; the new peaks in the cocrystal are: 7.96°, 8.9° and 15.01°. The PXRD pattern of the 100% chloroform sample was compared with the four new 2-aminopyrimidine-glutaric acid cocrystals (Fig. 6.68).The peaks at 7.96° and 8.9° are similar to the peaks at 8.06° , 8.86° and 9.18° in **D**. However, the peaks at 13.78°, 15.08°, 22.63°, 23.9 and 27.3° in the 100% chloroform sample are absent in **D** (Fig. 6.68). These peaks are close to the peaks at 13.78°, 22.09°, 24.01° and 27.3° in glutaric acid and 15.7° peak in 2-aminopyrimidine (Fig. 6.67) suggesting glutaric acid and 2-aminopyrimidine were still present in the sample.

The sample was analysed by FTIR, overlaying the FTIR spectrum with that for 2-aminopyrimidine and glutaric acid (Fig. 6.69), the region between 1750 cm^{-1} and 4000 cm^{-1} (Fig. 6.70) shows two new broad peaks in the sample at 1900 cm^{-1} and 2350 cm^{-1} absent in glutaric acid and 2-aminopyrimidine. These peaks are characteristic of un-ionised O-H hydrogen bonding stretching of the carboxylic acid[7,17,18].

The DSC analysis of the 100% chloroform sample shows four transitions: three endothermic and one exothermic (Fig. 6.71). The first endotherm transition has an onset temperature of 40.4 °C, peak maximum of 46.3 °C and enthalpy of 27.44 J/g. This endothermic transition extends from 40 °C to 75 °C, which includes the boiling point of chloroform (61.2 °C) and could represent the desolvation of chloroform. The second transition is exothermic and has an onset temperature of 79.3 °C, peak maximum of 83.7 °C and enthalpy of 12.54 J/g, this is closely followed by an endothermic transition with an onset temperature of 86.1 °C, peak maximums of

87.1 ^{o}C and enthalpy of 8.46 J/g. The last exothermic transition has an onset temperature of 98.3 ^{o}C, a peak maximum of 100 ^{o}C and enthalpy of fusion = 122.8 J/g. The sequence of transitions follows this order: loss of chloroform, recrystallisation of crystal; followed by possibly a solid-solid transition or low level of an impurity (because of the low enthalpy of this transition of 8.4 J/g); and lastly another melt.

The onset temperature and peak maxima are different from those observed for 2-aminopyrimidine (122.4 ^{o}C and 126.5 ^{o}C) and glutaric acid (93.5 ^{o}C and 97.2 ^{o}C). Overlaying the thermograms (Fig. 6.72) shows the 100% chloroform sample has a slightly higher melting point than glutaric acid. The enthalpy of fusion in glutaric acid is 84.23 J/g that for the 100% chloroform sample is 122.8 J/g.

A comparison of the thermogram of **D** and the 100% chloroform sample was done (Fig.6.73) because of the similarity in their PXRD; the melt transition for **D** is slightly lower than that for the 100% chloroform sample. The enthalpy of fusion in the 100% chloroform sample (122.8 J/g) is different to that in **D** (151.8 J/g). The significant difference in enthalpies of fusion suggests both crystals are different.

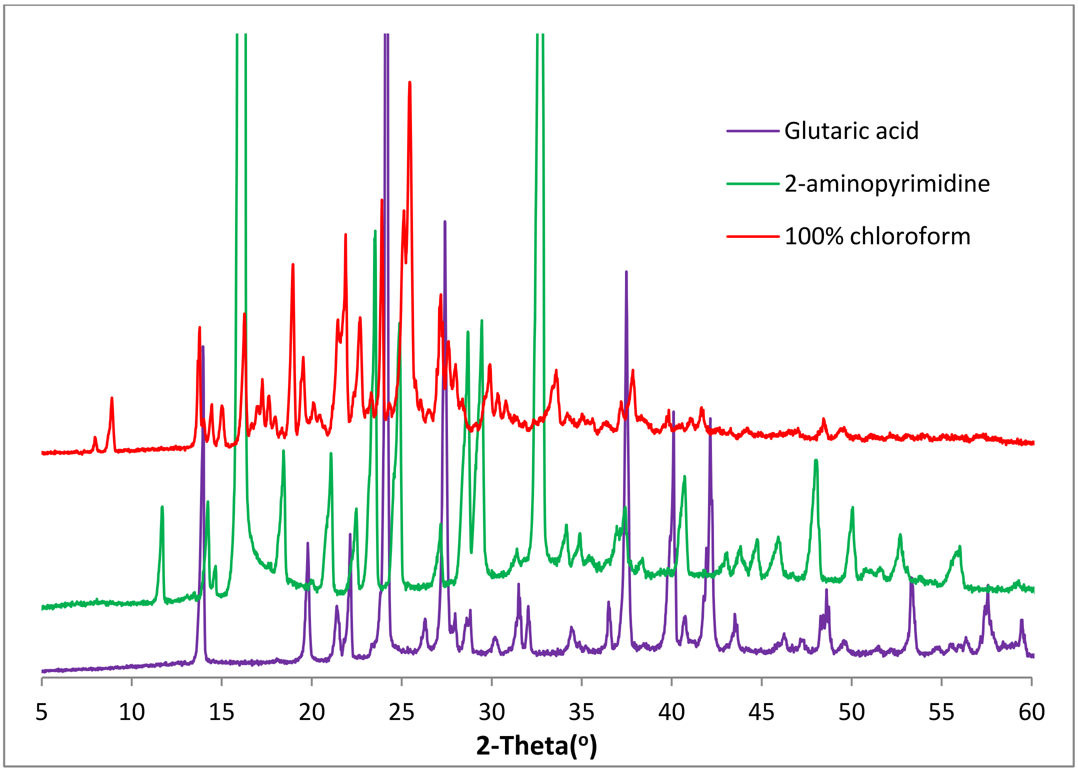

Fig. 6.67 Comparison of the PXRD of 2-aminopyrimidine-glutaric acid cocrystallisation in 100% chloroform with its components.

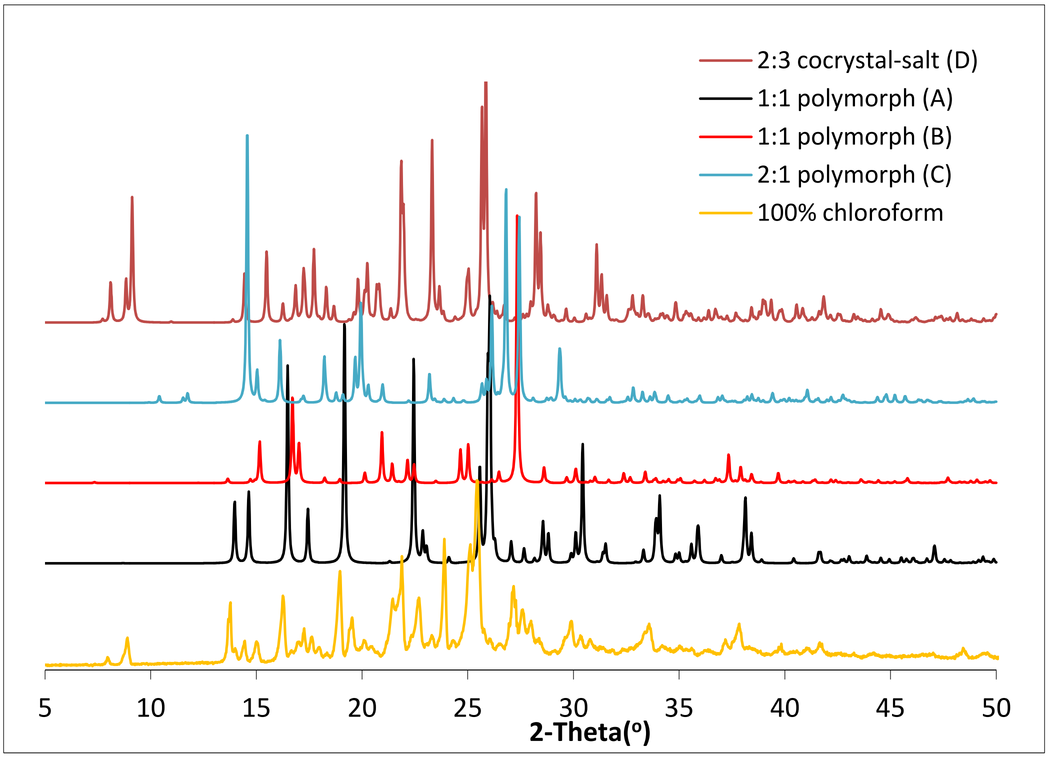

Fig. 6.68 PXRD for 2-aminopyrimidine-glutaric acid (100% chloroform) sample and simulated PXRD of 2-aminopyrimidine-glutaric acid cocrystals.

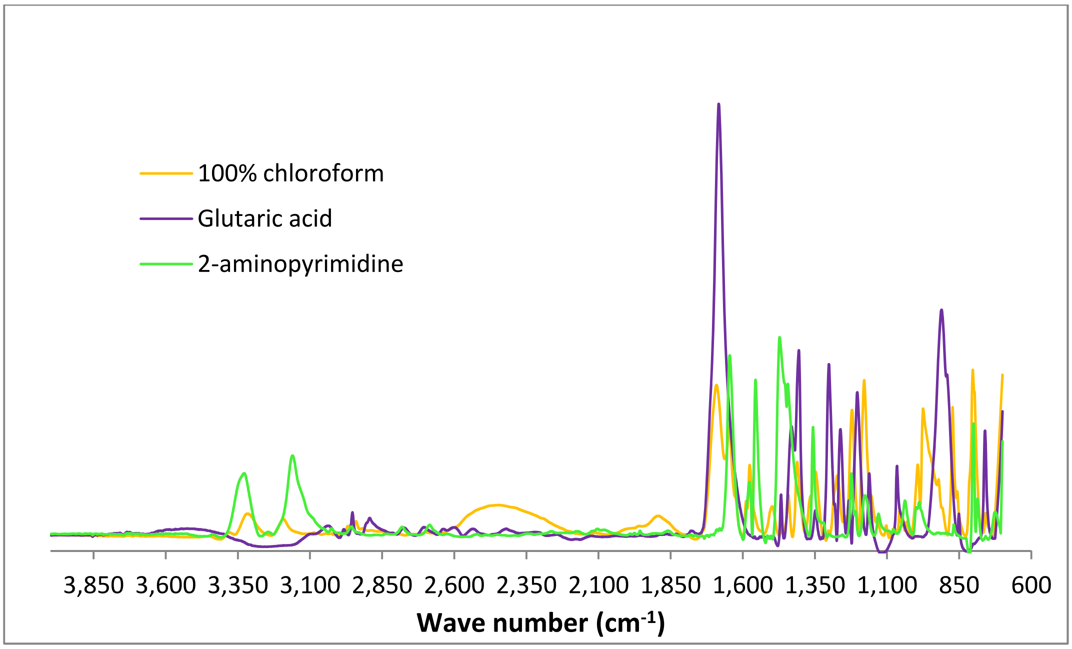

Fig. 6.69 FTIR spectrum of 2-aminopyrimidine-glutaric acid (100% chloroform) sample and components.

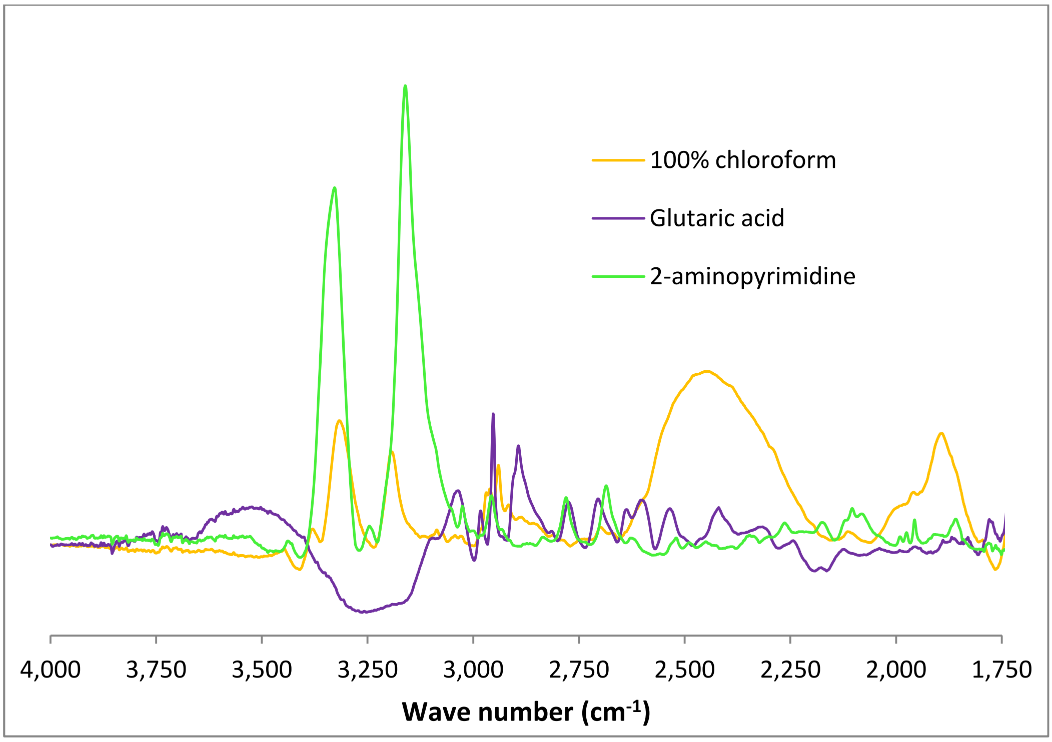

Fig. 6.70 FTIR comparison between 1750 cm^{-1} and 4000 cm^{-1} region for 2-aminopyrimidine-glutaric acid (100% chloroform) sample.

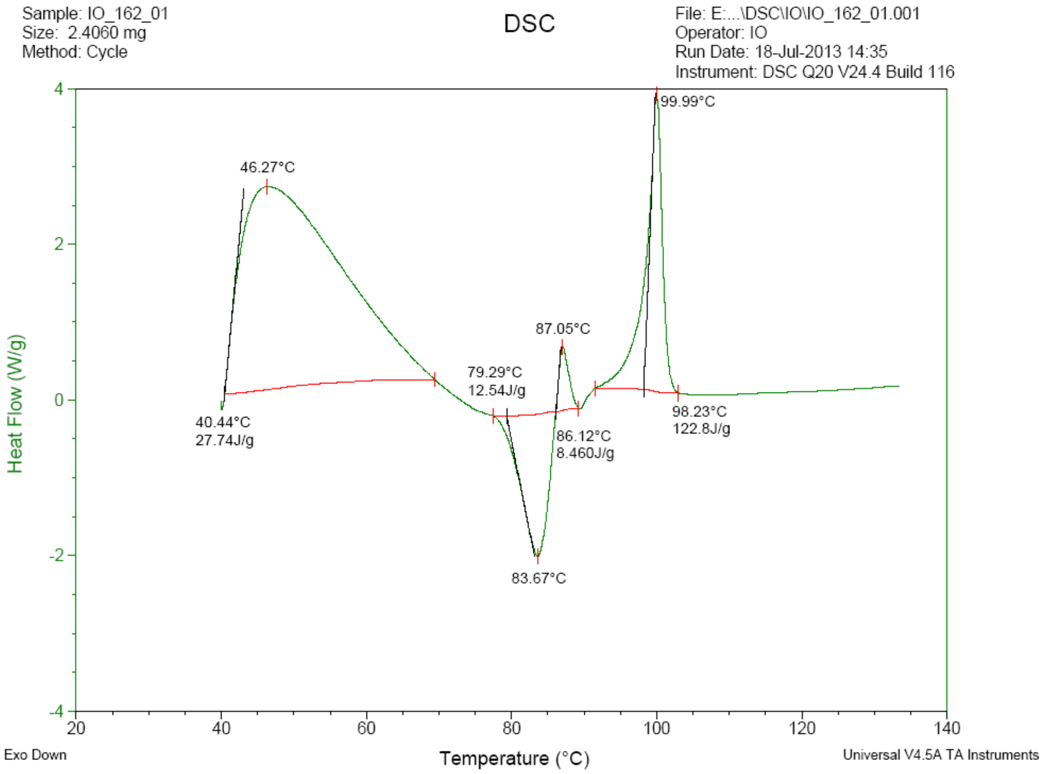

Fig. 6.71 DSC thermogram of the 2-aminopyrimidine-glutaric acid (100% chloroform) sample.

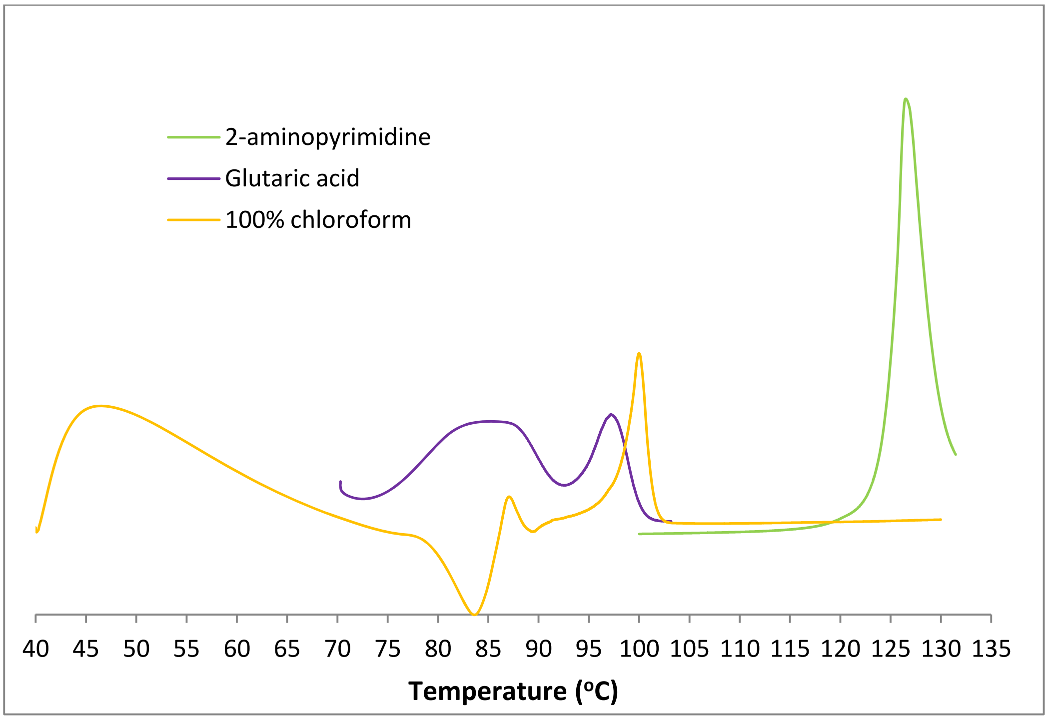

Fig.6.72 DSC thermogram of the 2-aminopyrimidine-glutaric acid (100% chloroform) sample and components.

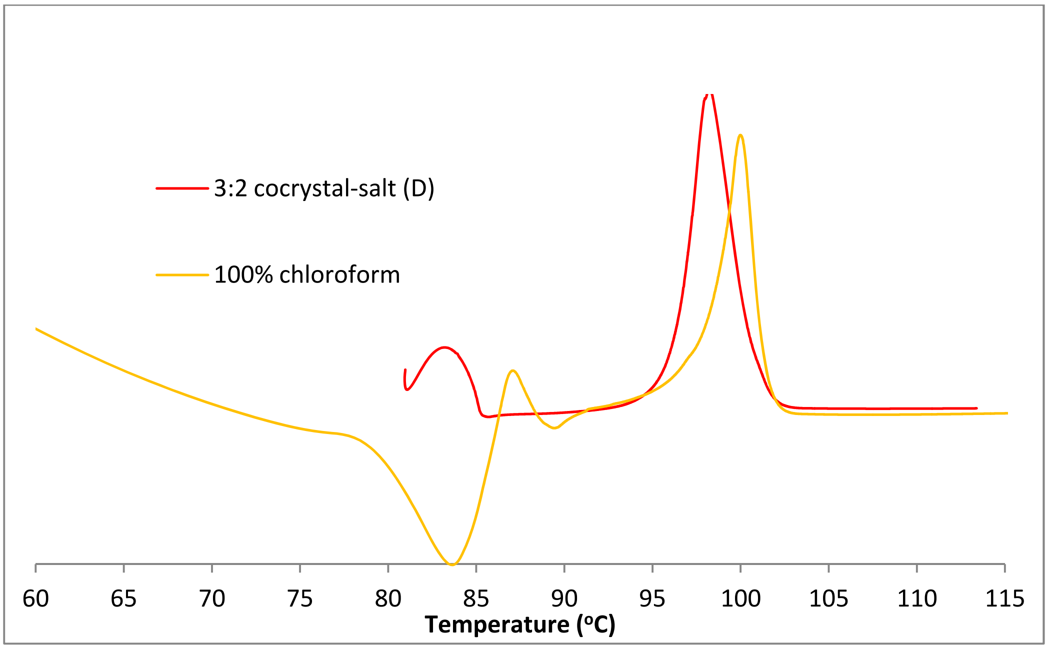

Fig. 6.73 Comparing **D** and 2-aminopyrimidine-glutaric acid (100% chloroform) sample DSC thermogram

6.9.3 STR slurry cocrystallisation with 100% methanol

STR cocrystallisation of 2-aminopyrimidine-glutaric acid was carried out using 17.1 g of 100% methanol, 0.02 moles of 2-aminopyrimidine and 0.02 moles of glutaric acid; the solid loading was 21%. The solid loading is higher than previous experiments because of the high solubility of 2-aminopyrimidine and glutaric acid in methanol.

After 60 minutes of mixing in a 250 ml flask, the slurry was filtered, dried and a yellow powder (Fig. 6.82) was isolated. The weight of solid recovered was 3.42 g (75.33%).

Fig. 6.74 Picture of yellow powder from 100% methanol.

The sample was analysed by PXRD. Overlaying the PXRD pattern with 2-aminopyrimidine and glutaric acid (Fig. 6.75), the intense diffraction peak at 2θ = 21.07°, 23.45°, 32.93° and 47.95° in 2-aminopyrimidine and 23.47° and 42.17° in glutaric acid are absent in the sample suggesting a cocrystal may have formed. The new peaks in the cocrystal are: 10.29°, 17.3°, 19.04° and 33.69°. The PXRD of the sample was compared with the four new 2-aminopyrimidine-glutaric acid cocrystals (Fig. 6.76). The 100% methanol sample does not have a diffraction peak below 10.29° so is different from the two previous slurry cocrystallisation samples. The new peaks at 10.29° and 19.04° matches the peaks at 10.42° and 19.1° in **C**, while the peaks at 17.3° and 33.69° matches the peaks at 17.44° and 34.08° in **A**.

The sample was analysed by FTIR. Overlaying the FTIR spectrum with the spectra for 2-aminopyrimidine and glutaric acid (Fig. 6.77), the region between 1750 cm^{-1} and 4000 cm^{-1} (Fig. 6.78) shows two new broad peaks in the sample at 1900 cm^{-1} and 2350 cm^{-1} absent in glutaric acid and 2-aminopyrimidine. These peaks are characteristic of un-ionised O-H hydrogen bonding stretching of the carboxylic acid[7,17,18].

The DSC analysis of the sample (Fig. 6.79) shows two endotherm peaks with onset temperatures of 80.4 °C and 94.5 °C; peak maxima of 83.6 °C and 97.1 °C; and enthalpies of 3.61 J/g and 164.8 J/g. When the thermogram is overlaid with that for 2-aminopyrimidine and glutaric acid (Fig. 6.80), the endothermic transitions in the 100% methanol sample overlaps significantly with that of glutaric acid. The enthalpy of fusion in glutaric acid is 84.23 J/g, whilst that for the 100% methanol sample is 164.8 J/g, which is twice that in glutaric acid, suggesting that the sample is different from glutaric acid. The first endotherm in the 100% methanol sample is much lesser than glutaric acid, and is likely to be a solid-solid transition.

Comparison of the PXRD shows similarity with that of **A** and **C**. Thermograms of **A**, **C** and the 100% methanol sample were compared (Fig.6.81); the melt transition for 100% methanol sample is slightly lower than that for **A** and **C**. The enthalpy of fusion in the 100% methanol sample (164.8 J/g) is slightly higher than that in **A** (159.4 J/g) and **C** (151.2 J/g).

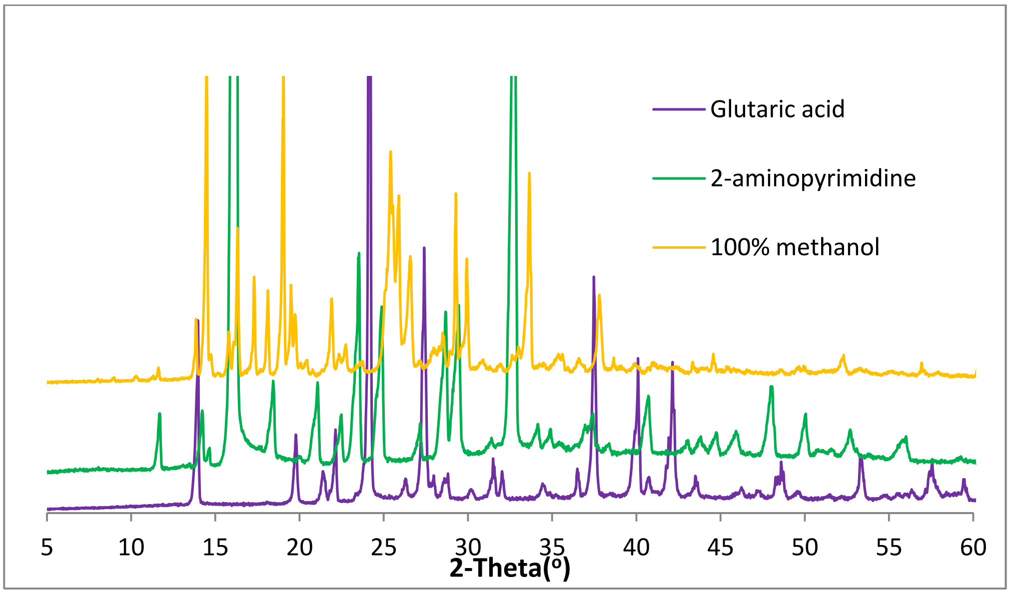

Fig. 6.75 A comparison of 2-aminopyrimidine –glutaric acid (100% methanol) cocrystallisation sample and components pattern.

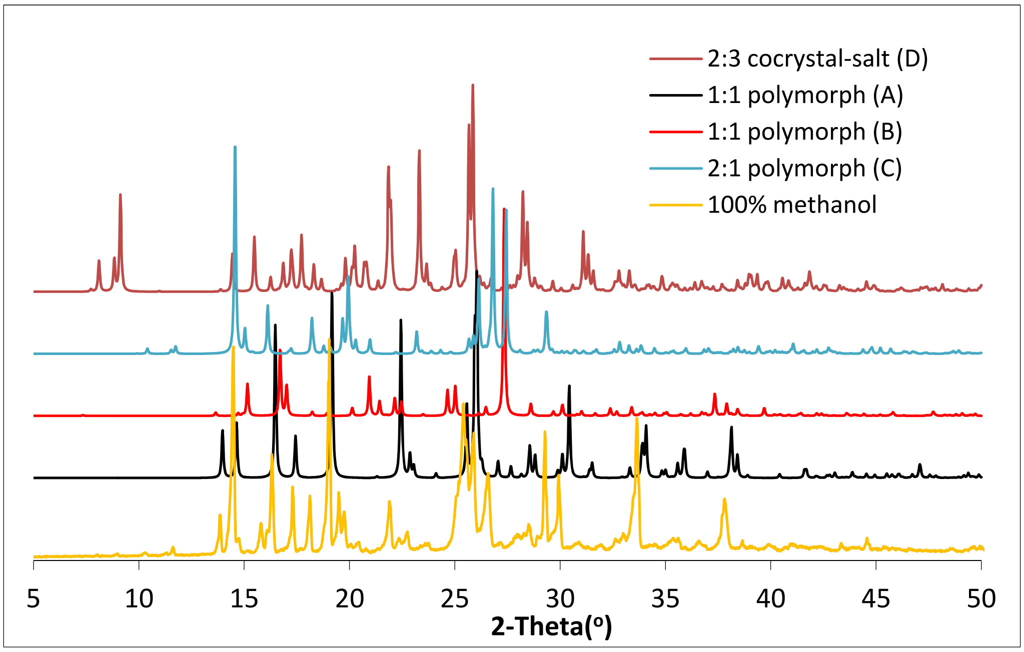

Fig. 6.76 PXRD for 2-aminopyrimidine –glutaric acid (100% methanol) sample and simulated PXRD of 2-aminopyrimidine-glutaric acid cocrystals.

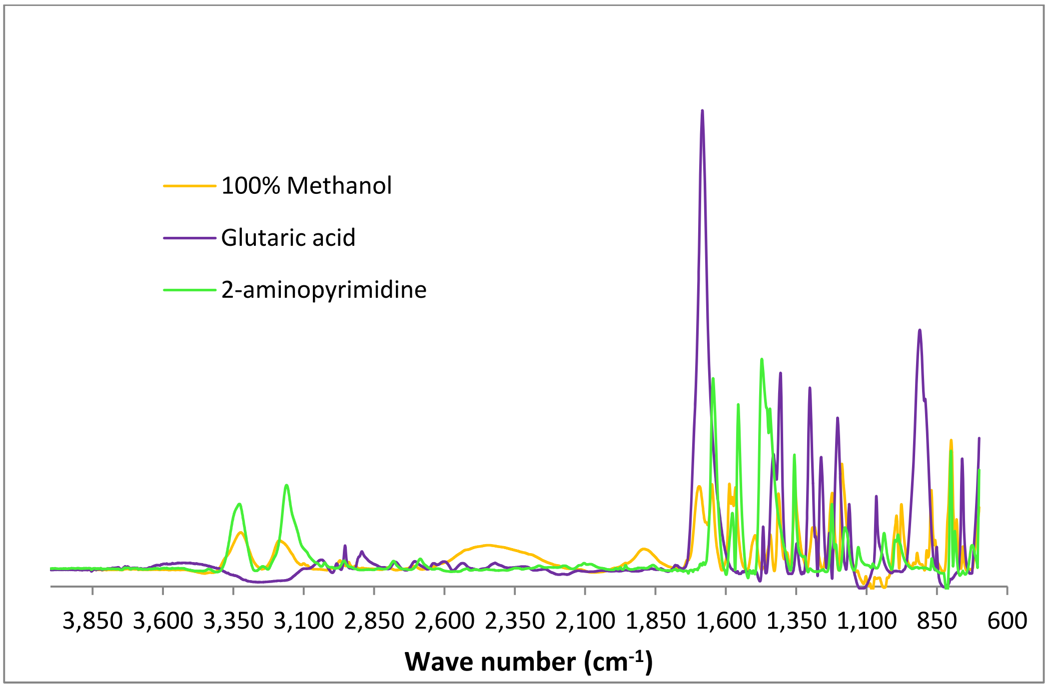

Fig. 6.77 Comparing FTIR spectrum of 2-aminopyrimidine –glutaric acid (100% methanol) sample and components.

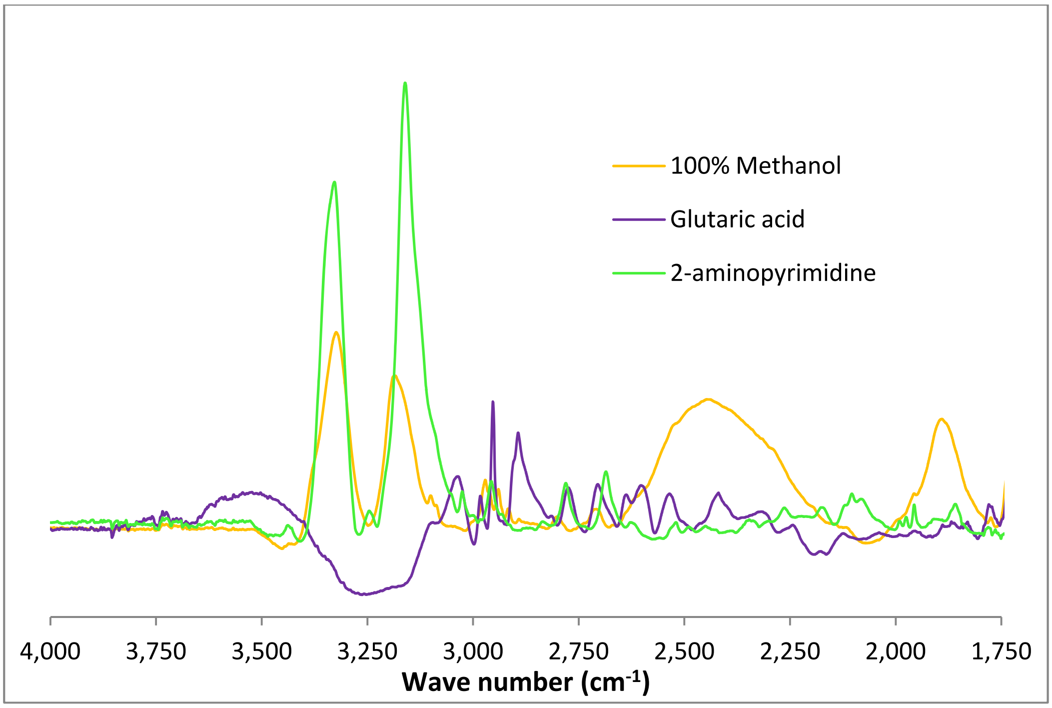

Fig.6.78 FTIR comparison between 1750 cm^{-1} and 4000 cm^{-1} region for 2-aminopyrimidine – glutaric acid (100% methanol) sample.

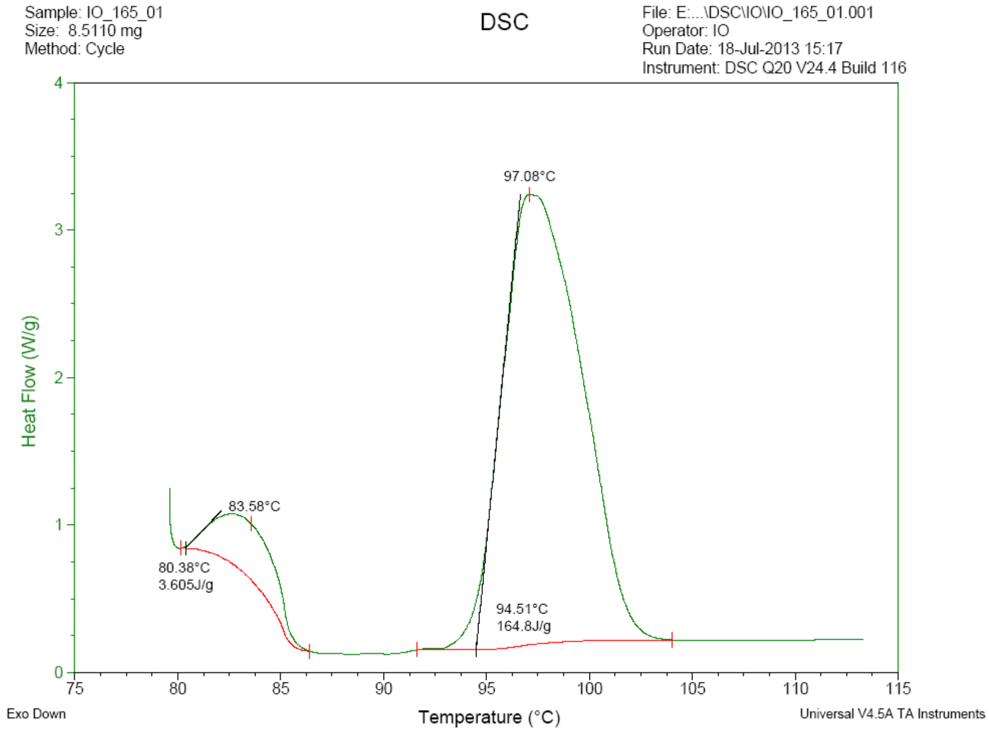

Fig. 6.79 DSC thermogram of the 2-aminopyrimidine –glutaric acid (100% methanol) sample.

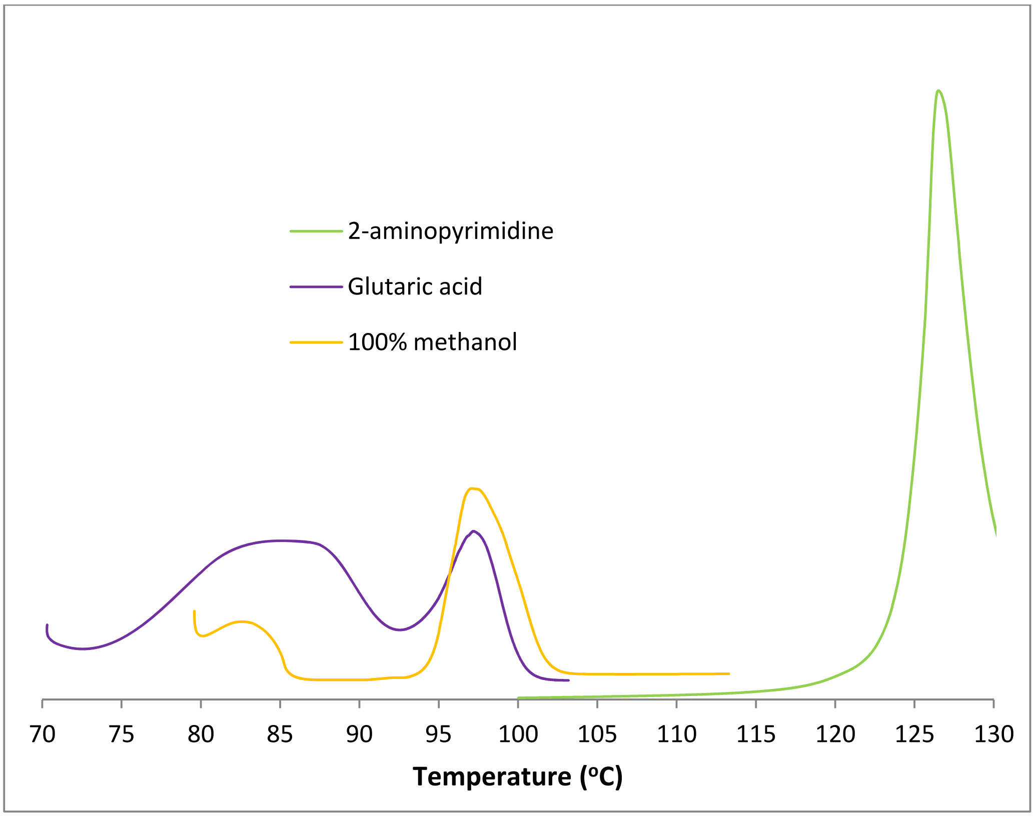

Fig. 6.80 DSC thermogram of the 2-aminopyrimidine –glutaric acid (100% methanol) sample and components.

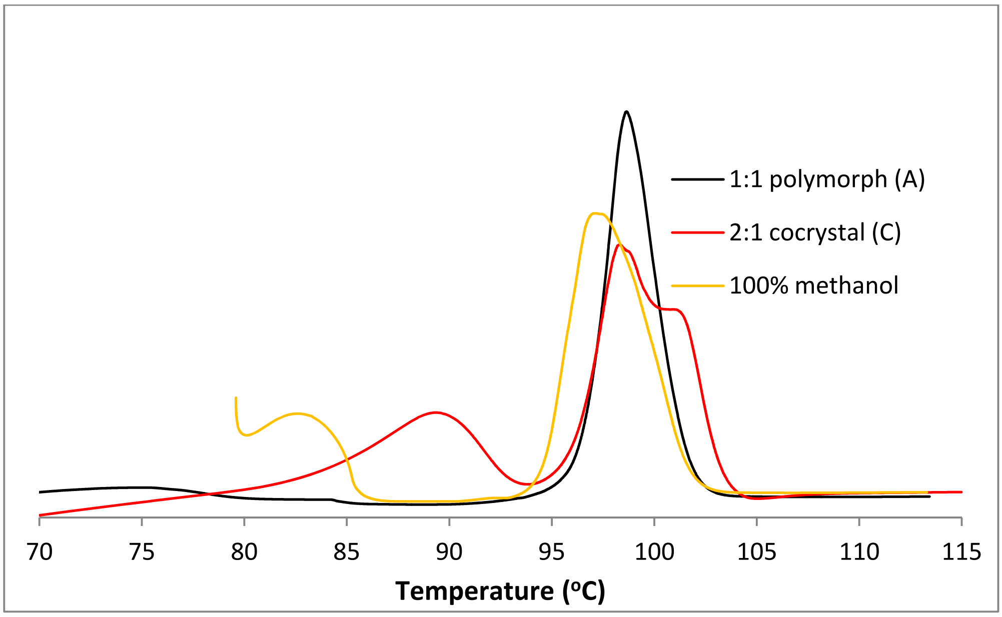

Fig. 6.81 Comparing **A**, **C** and 2-aminopyrimidine –glutaric acid (100% methanol) DSC thermogram.

6.9.4 100% acetonitrile slurry cocrystallisation.

STR cocrystallisation of 2-aminopyrimidine-glutaric acid was carried out using 17.05 g of 100% acetonitrile, 0.01 mole of 2-aminopyrimidine and 0.01 mole of glutaric acid; the solid loading was 11.8%. The higher loading used was due to the high solubility of glutaric acid and 2-aminopyrimidine in acetonitrile. After 60 minutes of mixing in a 250 ml flask, the slurry was filtered, dried and a light yellow powder (Fig. 6.82) was isolated. The weight of solid recovered was 1.74 g (76.65%).

Fig. 6.82 Picture of yellow powder from 100% acetonitrile.

The sample was analysed by PXRD. Overlaying the PXRD pattern with 2-aminopyrimidine and glutaric acid (Fig. 6.83), the intense diffraction peaks at 2θ = 11.61°, 23.45° and 29.02° in 2-aminopyrimidine are absent in the sample suggesting cocrystal formation; the new peaks in the cocrystal are: 8.12°, 9.06°, 14.00° and 15.58°. The PXRD pattern was compared with the four new 2-aminopyrimidine-glutaric acid cocrystals (Fig. 6.84).The new peaks at 8.12°and 9.06° in the 100%

acetonitrile sample matches the peaks at 8.06°, 8.86° and 9.18° in **D**. The new peaks at 14.00° and 15.58° match the peaks at 13.98° and 14.64° in **A** (1:1 2-aminopyrimidine-glutaric acid polymorph from acetonitrile).

The sample was analysed by FTIR, overlaying the FTIR spectrum with that for 2-aminopyrimidine and glutaric acid (Fig. 6.85), shows the region between 1750 cm^{-1} and 4000 cm^{-1} (Fig. 6.86) has a new broad peak at 1900 cm^{-1} absent in glutaric acid and 2-aminopyrimidine. This peak is characteristic of un-ionised O-H hydrogen bonding stretching of the carboxylic acid[7,17,18].

The DSC analysis (Fig. 6.87) shows three transitions: two endothermic and one exothermic. The first endotherm has an onset temperatures of 78.3 °C, peak maximums of 81.9 °C and transition enthalpy of 9.63 J/g. The exothermic transition has an onset temperature of 84.9 °C, peak maximum of 85.3 °C and enthalpy of 4.13 J/g. The last endotherm has an onset temperature of 96.3 °C, peak maximum of 97.7 °C and enthalpy of fusion = 171.0 J/g. The first broad endotherm peak (Fig. 6.87) overlaps with the boiling point for acetonitrile (82°C) and may be the vaporisation of acetonitrile from the sample. The next transition is an exothermic one and closely follows the first; this transition could be a recrystallisation event resulting from the desolvation of the crystals suggesting this is a solvate. Overlaying the thermogram with that for 2-aminopyrimidine and glutaric acid (Fig. 6.88), the sample has a slightly higher melting point than glutaric acid. The enthalpy of fusion in glutaric acid is 84.23 J/g, while for the 100% acetonitrile crystal sample it is 171.0 J/g , which is twice that in glutaric acid, confirming that the sample is not glutaric acid.

A comparison of the thermograms of **A, D** and the 100% acetonitrile crystal sample (Fig.6.89) was done because of their PXRD similarity. The melt transition for **A** and **D** are slightly higher than for the 100% acetonitrile sample. The enthalpy of fusion in the 100% acetonitrile sample (171.0 J/g) is significantly higher than in **A** (159.4 J/g) and **D** (163.7 J/g).

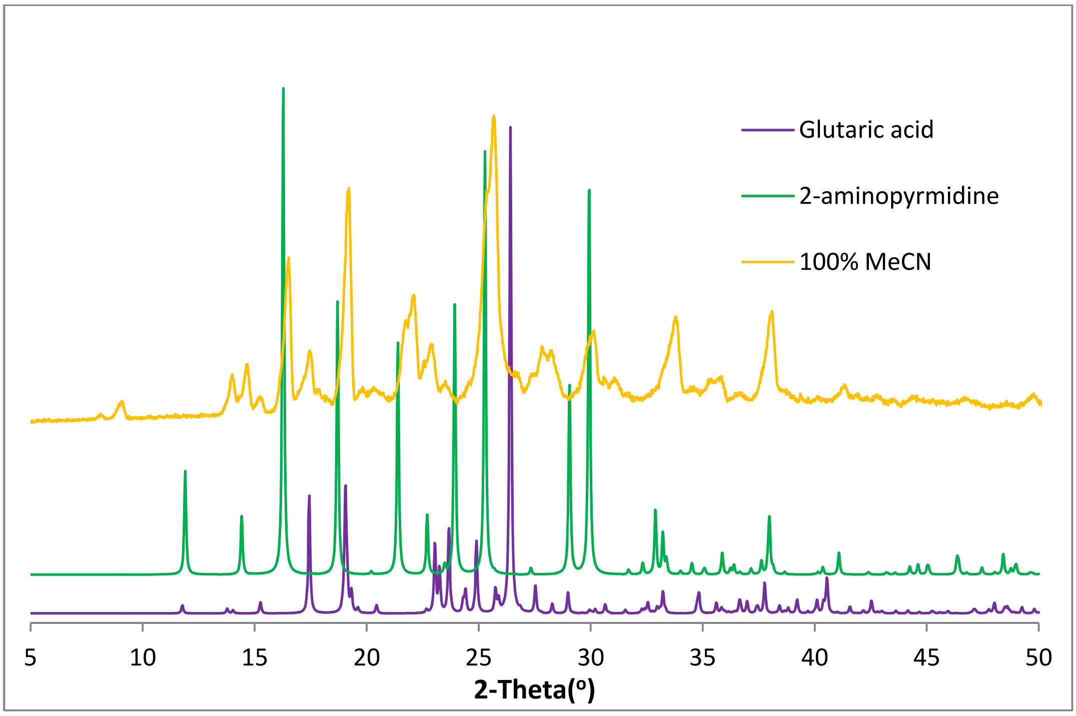

Fig. 6.83 2-aminopyrimidine-glutaric acid (100% acetonitrile) cocrystallisation with components.

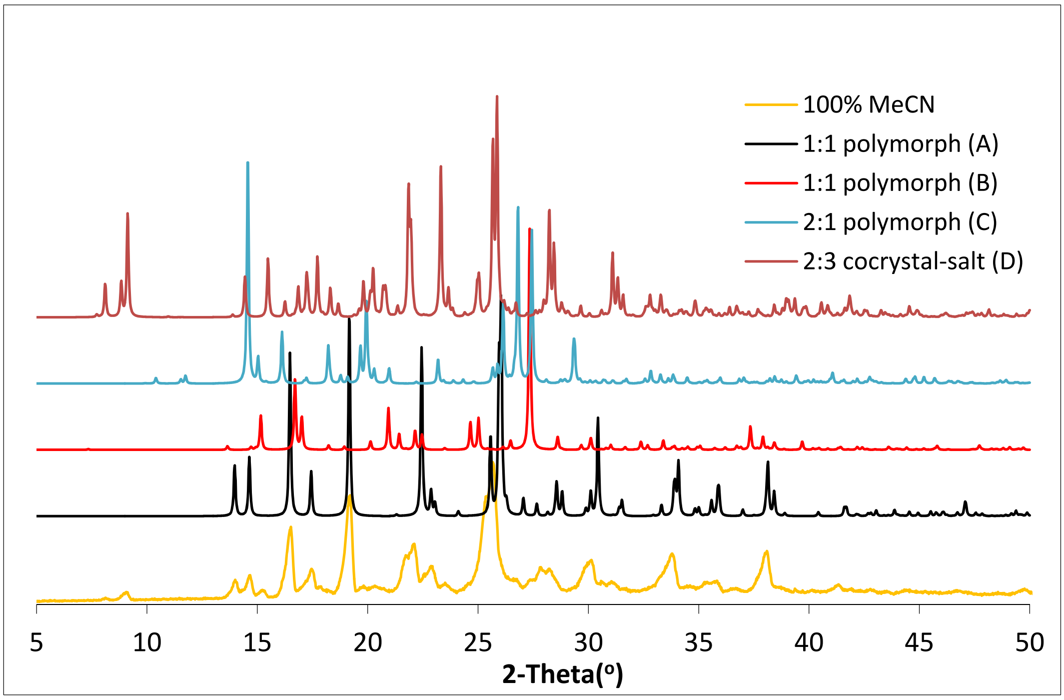

Fig. 6.84 PXRD for 2-aminopyrimidine-glutaric acid (100% acetonitrile) sample and simulated PXRD of 2-aminopyrimidine-glutaric acid cocrystals.

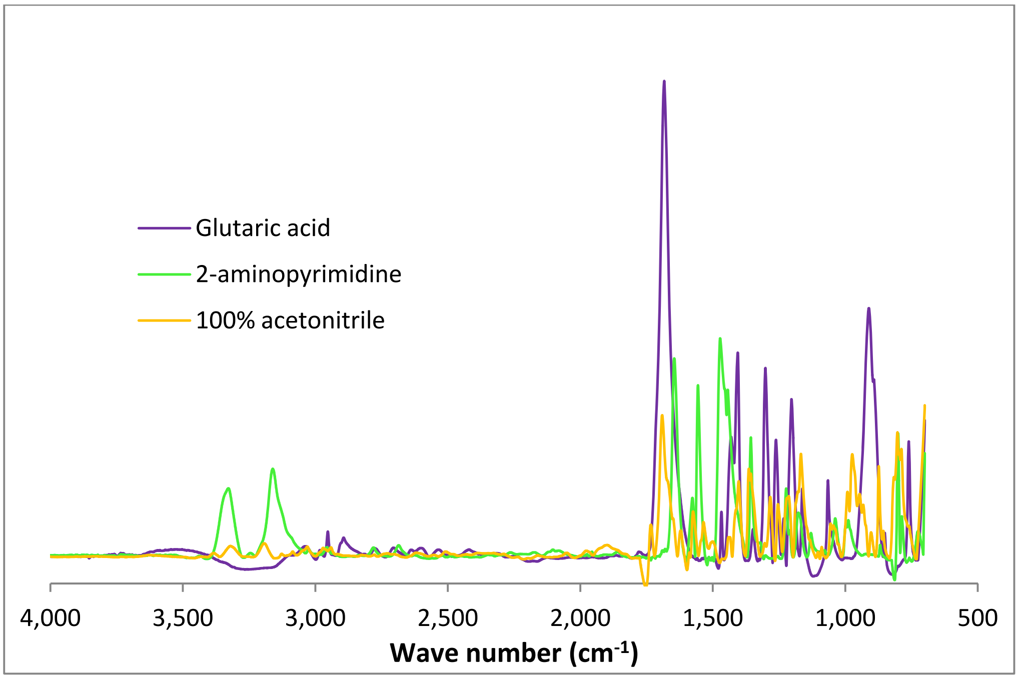

Fig. 6.85 Comparing FTIR spectrum of 2-aminopyrimidine-glutaric acid (100% acetonitrile) sample and components.

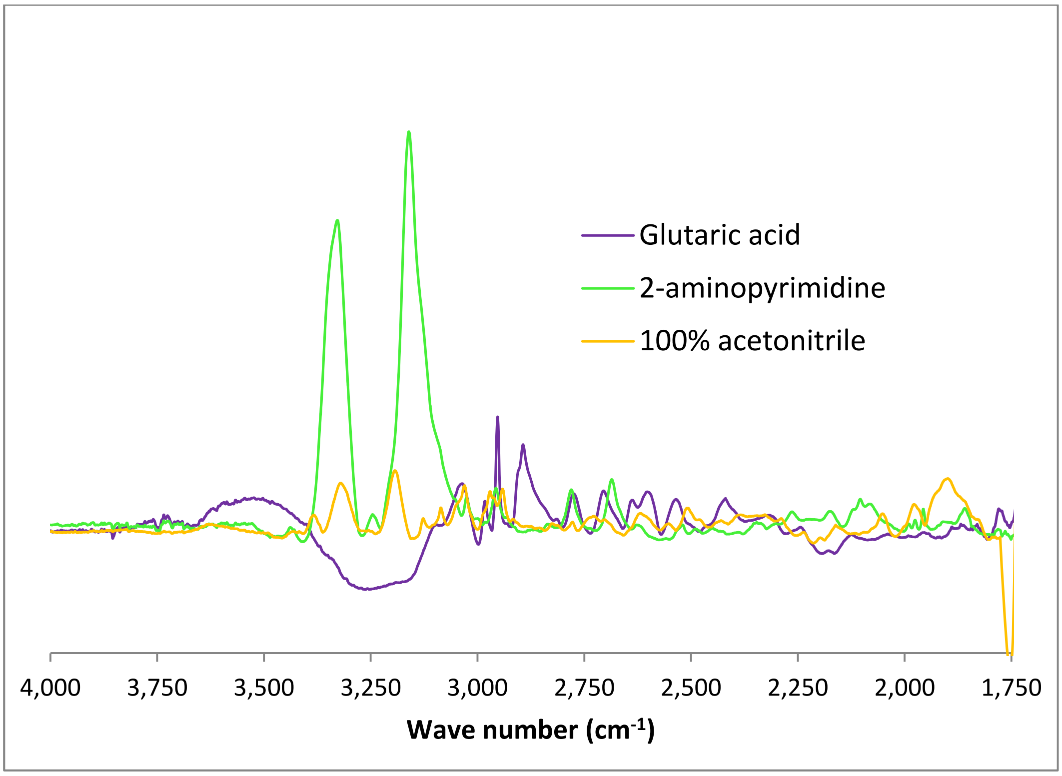

Fig. 6.86 FTIR comparison between 1750 cm^{-1} and 4000 cm^{-1} region for 2-aminopyrimidine-glutaric acid (100% acetonitrile) sample.

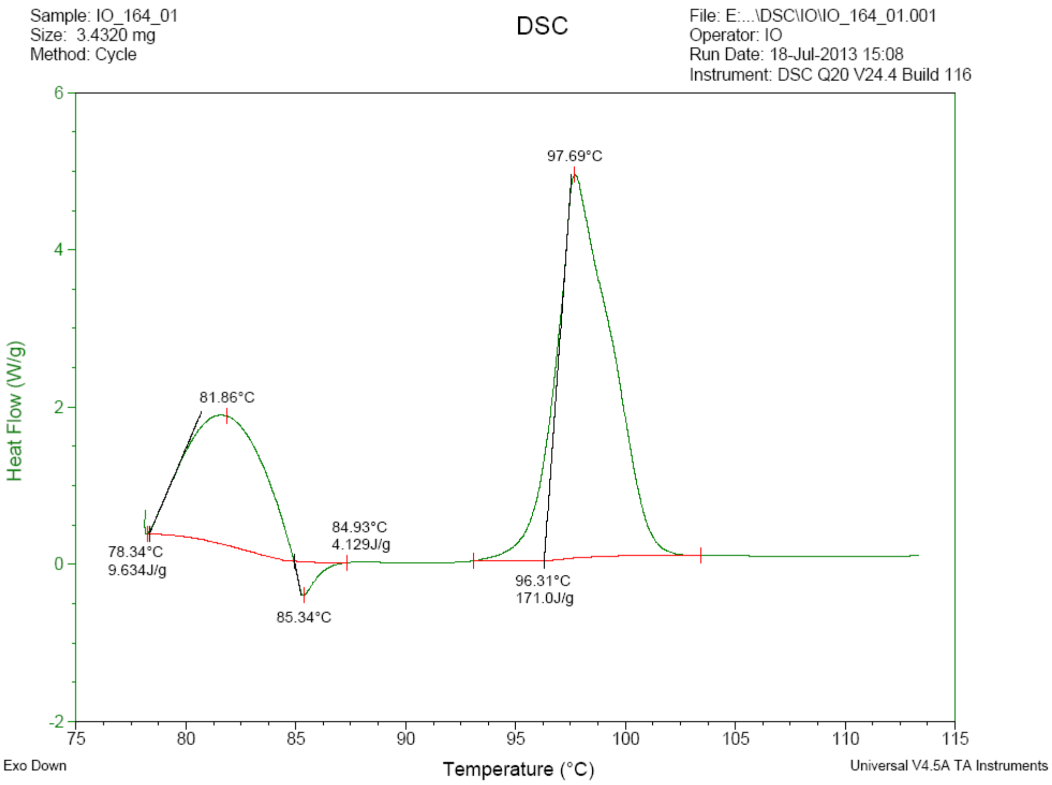

Fig. 6.87 DSC thermogram of the 2-aminopyrimidine-glutaric acid (100% acetonitrile) sample.

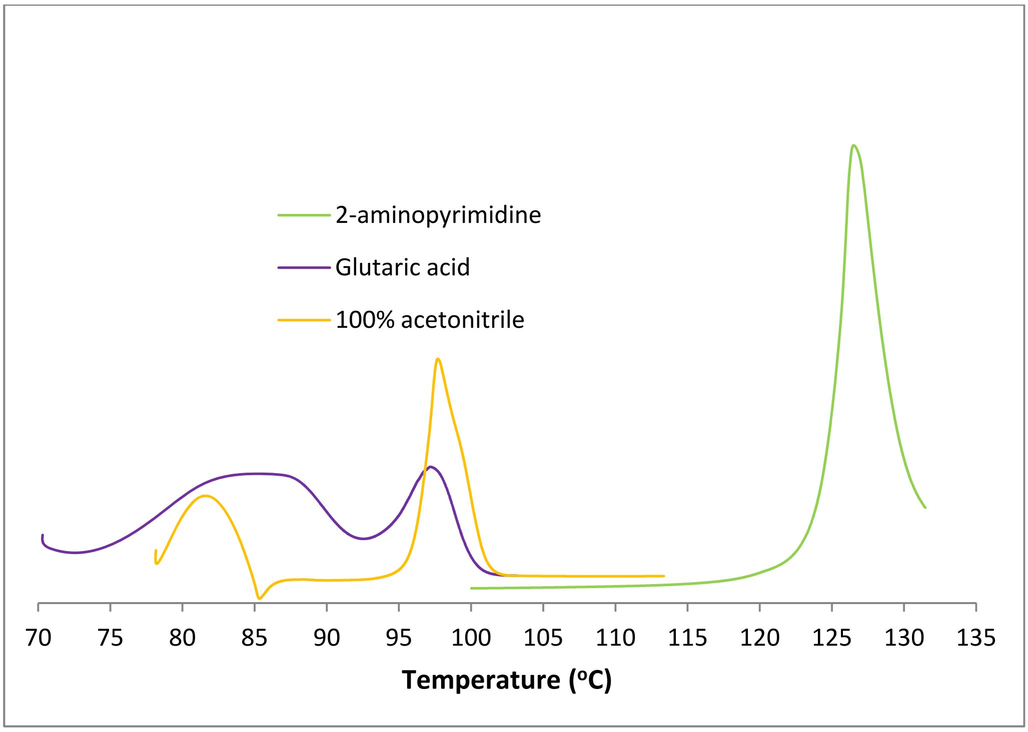

Fig. 6.88 DSC thermogram of the 2-aminopyrimidine-glutaric acid (100% acetonitrile) sample and components.

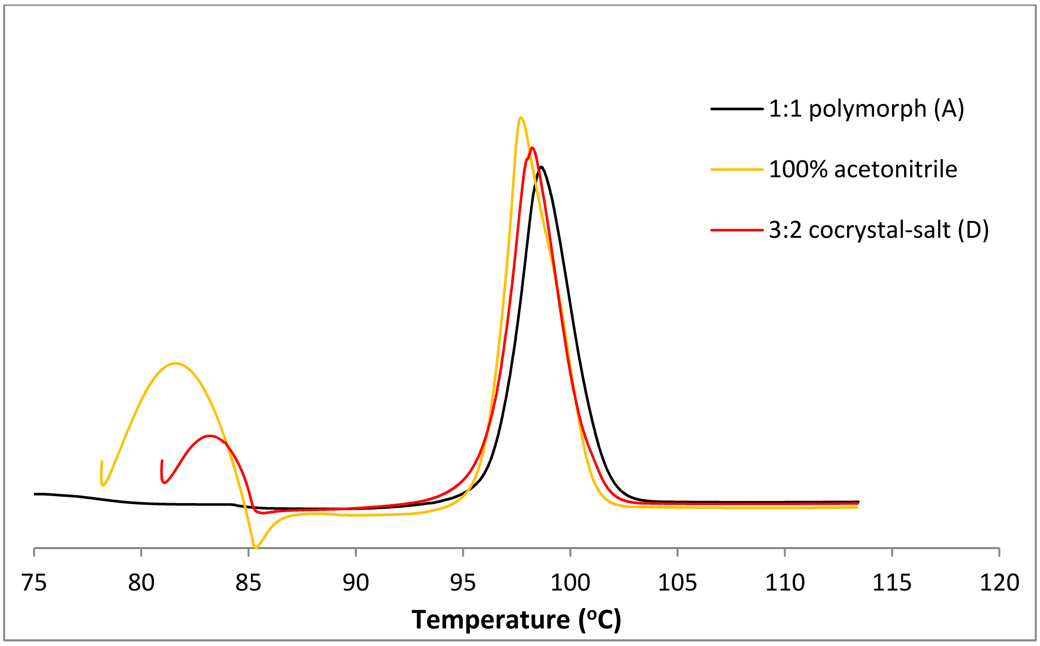

Fig. 6.89 Comparing **A, D** and 2-aminopyrimidine-glutaric acid (100% acetonitrile) sample DSC thermogram.

6.9.5 50:50 wt % of methanol and chloroform slurry cocrystallisation.

STR cocrystallisation of 2-aminopyrimidine-glutaric acid was carried out using 17 g of 50:50 *wt* % of methanol and chloroform, 0.02 mole of 2-aminopyrimidine and 0.02 mole of glutaric acid; the solid loading was 21%. The solid loading is higher than previous experiments because of the high solubility of 2-aminopyrimidine and glutaric acid in the methanol/chloroform mixture. After 60 minutes of mixing in a 250 ml flask, the slurry was filtered, dried and a yellow powder (Fig. 6.90) was isolated. The weight of solid recovered was only 1.22 g (26.9%).

Fig. 6.90 Picture of light yellow powder from methanol/chloroform.

The sample was analysed by PXRD. Overlaying the pattern with 2-aminopyrimidine and glutaric acid (Fig. 6.91), the intense diffraction peaks at 2θ = 11.61°, 23.45° and 29.02° in 2-aminopyrimidine, are absent in the sample; the new peaks in the cocrystal are: 8.12°, 9.06°, 14.00° and 15.58°. The PXRD pattern of the 50:50 wt % of methanol/chloroform sample was compared with the four new 2-aminopyrimidine-glutaric acid cocrystals (Fig. 6.92).The new peaks at 8.12°and 9.06° in the 50:50 wt% of methanol and chloroform sample matches the peaks at 8.06°, 8.86° and 9.18° in **D**. The new peak at 14.00° matches the peak at 13.98° in **A** (1:1 2-aminopyrimidine-glutaric acid polymorph from acetonitrile). The PXRD for the sample was overlaid with that from 100% acetonitrile and found to be a very good match (Fig. 6.93).

The sample was analysed by FTIR. Overlaying the FTIR spectrum with 2-aminopyrimidine and glutaric acid (Fig. 6.94) shows in the region between 1750 cm^{-1} and 4000 cm^{-1} (Fig. 6.95) that there are two new broad peaks in the sample at 1900 cm^{-1} and 2350 cm^{-1}, which are absent in glutaric acid and 2-aminopyrimidine. These peaks are characteristic of un-ionised O-H hydrogen bonding stretching of the carboxylic acid[7,17,18].

The DSC analysis (Fig. 6.96) shows three transitions: two endothermic peaks and one exothermic peak. The first endotherm has an onset temperature of 74.6 °C, peak maximum of 79.2 °C and transition enthalpy of 0.69 J/g. The exothermic transition has an onset temperature of 82.9 °C, peak maximum of 85.2 °C and enthalpy of 8.89 J/g. The last endotherm has an onset temperature of 96.6 °C, peak maximum of 98.4 °C and transition enthalpy of fusion = 171.7 J/g. The first broad endotherm peak is higher than the boiling points for methanol (64.7 °C) and chloroform (61.2 °C); but may still be due to the vaporisation of both solvent from the sample, which can occur at a higher temperature than their respective boiling points if these molecules are held firmly in the crystal lattice. The next transition is an exothermic one and closely follows the first; this transition could be a recrystallisation event as a result of the desolvation of the crystals.

Overlaying the thermogram with that for 2-aminopyrimidine and glutaric acid (Fig. 6.97), the sample has a slightly higher melting point than glutaric acid. The enthalpy of fusion in glutaric acid is 84.23 J/g, while for the 50:50 wt % of methanol/chloroform sample it is 171.7 J/g, which is twice that in glutaric acid, confirming that the sample is not glutaric acid.

Overlaying the thermogram with that for the sample obtained from 100% acetonitrile (Fig. 6.98), because of the matching PXRD; shows both are very similar, with enthalpies of 171.7 J/g and 171.0 J/g for 50:50 wt % of methanol/chloroform and 100% acetonitrile, respectively. This suggests both contain the same type of crystals.

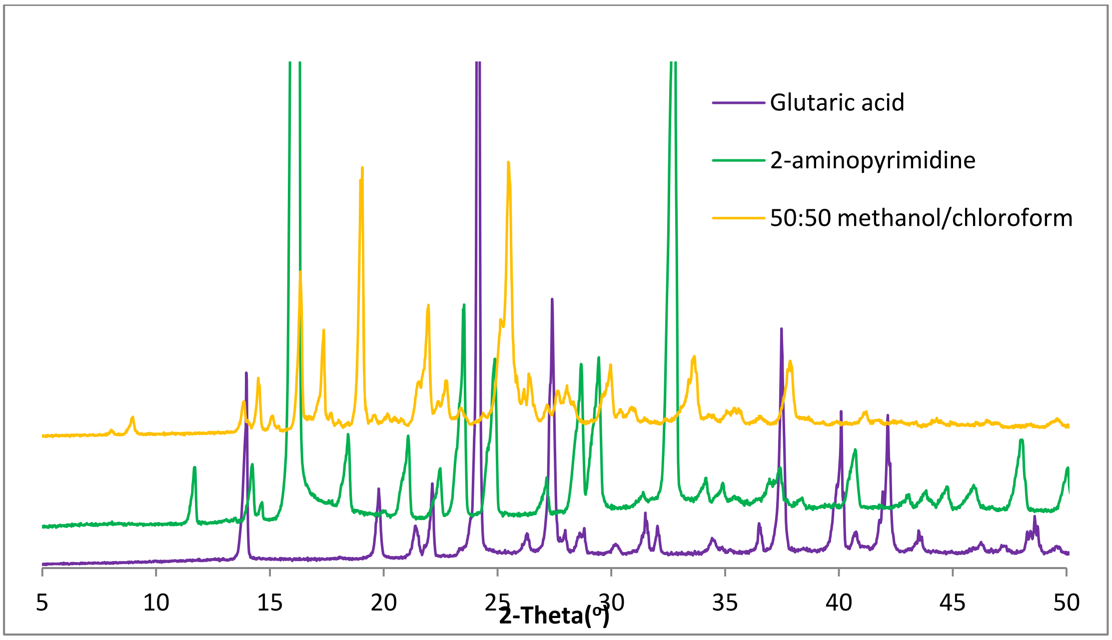

Fig. 6.91 Comparing PXRD for 2-aminopyrimidine-glutaric acid (methanol/chloroform) cocrystallisation sample with components.

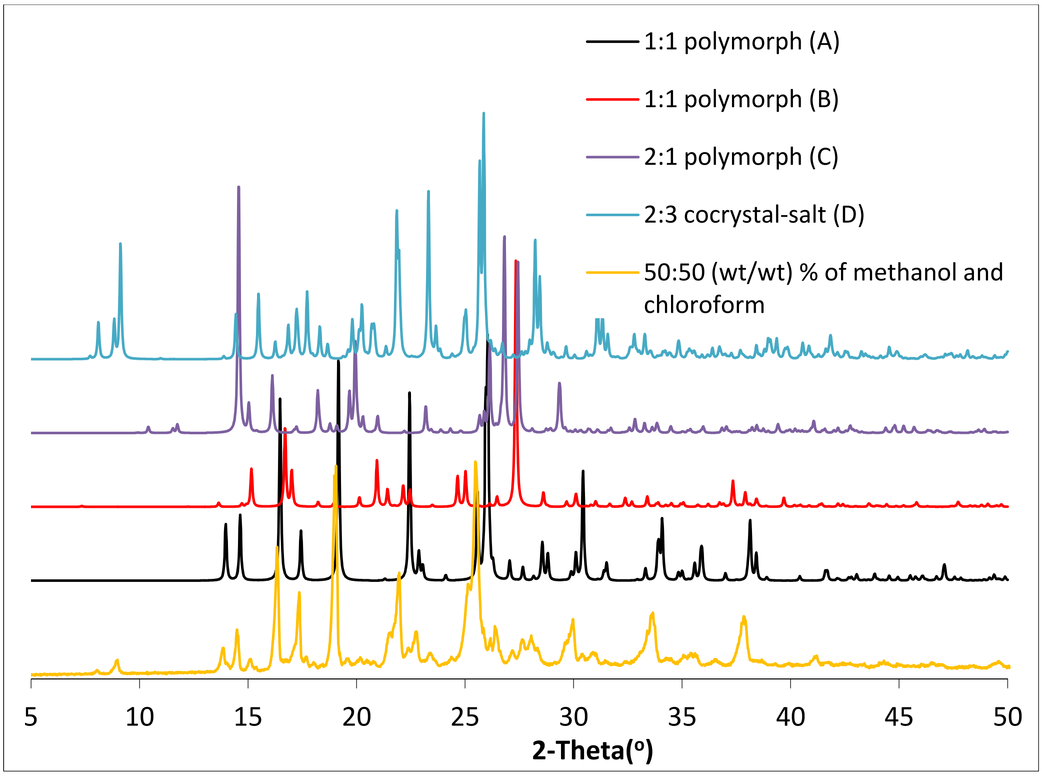

Fig. 6.92 Comparing PXRD for 2-aminopyrimidine-glutaric acid (methanol/chloroform) sample and simulated PXRD of 2-aminopyrimidine-glutaric acid cocrystals.

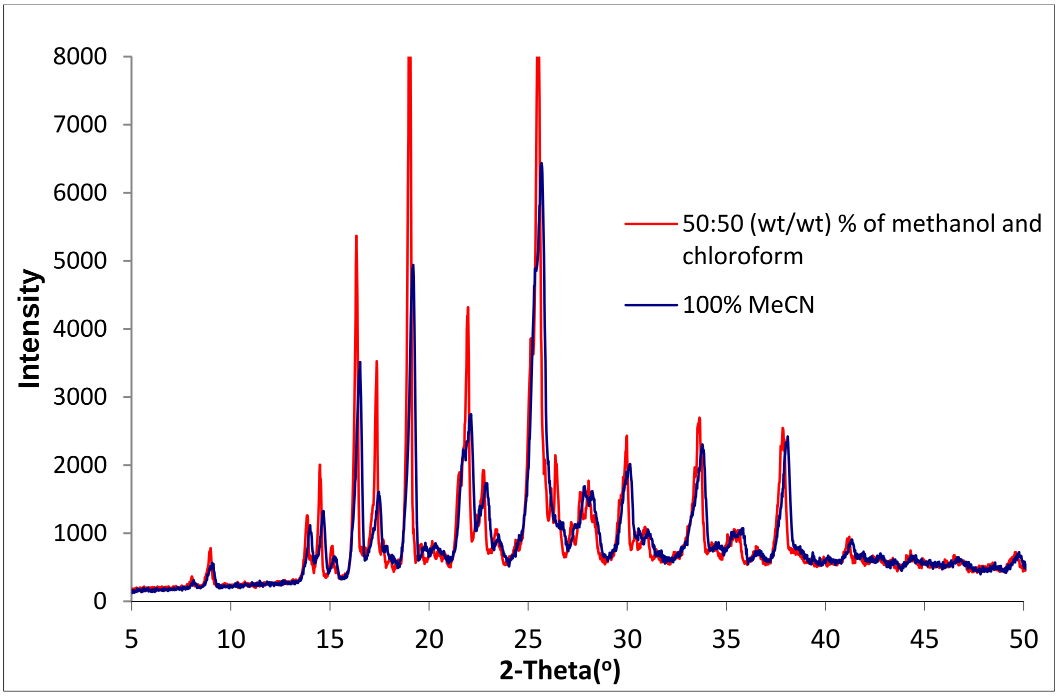

Fig. 6.93 Comparing PXRD of 2-aminopyrimidine-glutaric acid cocrystal PXRD samples from 50:50 methanol /chloroform and sample from 100% acetonitrile.

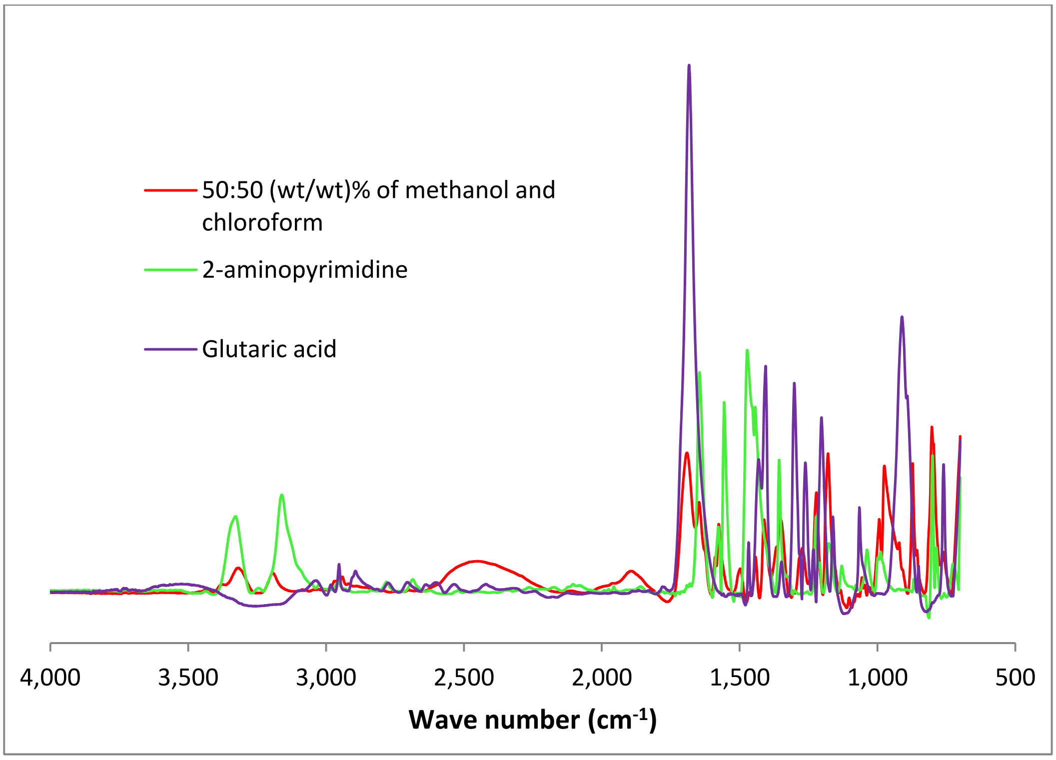

Fig. 6.94 A Comparison of FTIR spectrum of 2-aminopyrimidine-glutaric acid (methanol/chloroform) sample and it's components.

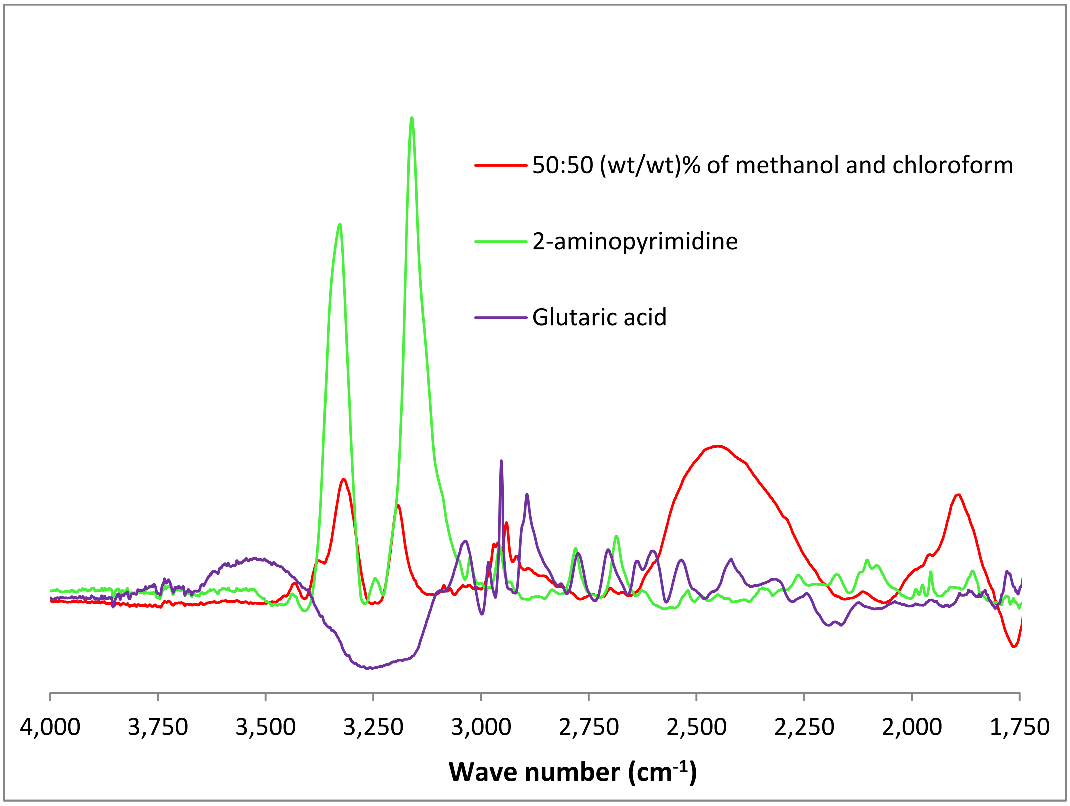

Fig. 6.95 FTIR comparison between 1750 cm^{-1} and 4000 cm^{-1} region for 2-aminopyrimidine-glutaric acid (methanol/chloroform) sample.

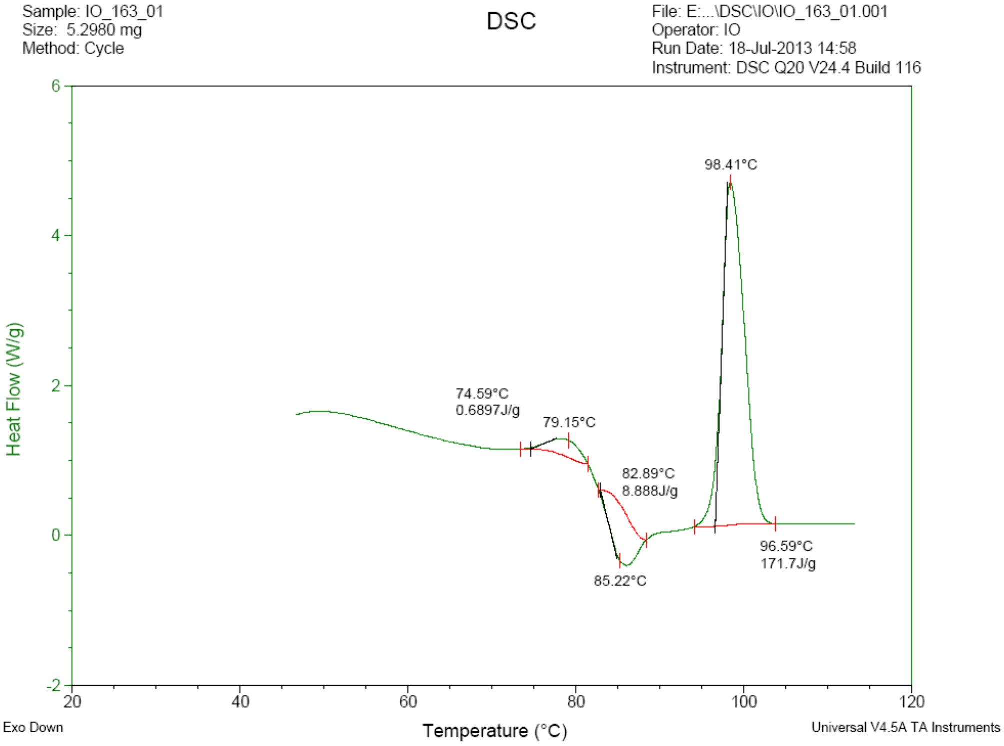

Fig. 6.96 DSC thermogram of the 2-aminopyrimidine-glutaric acid (methanol/chloroform) sample.

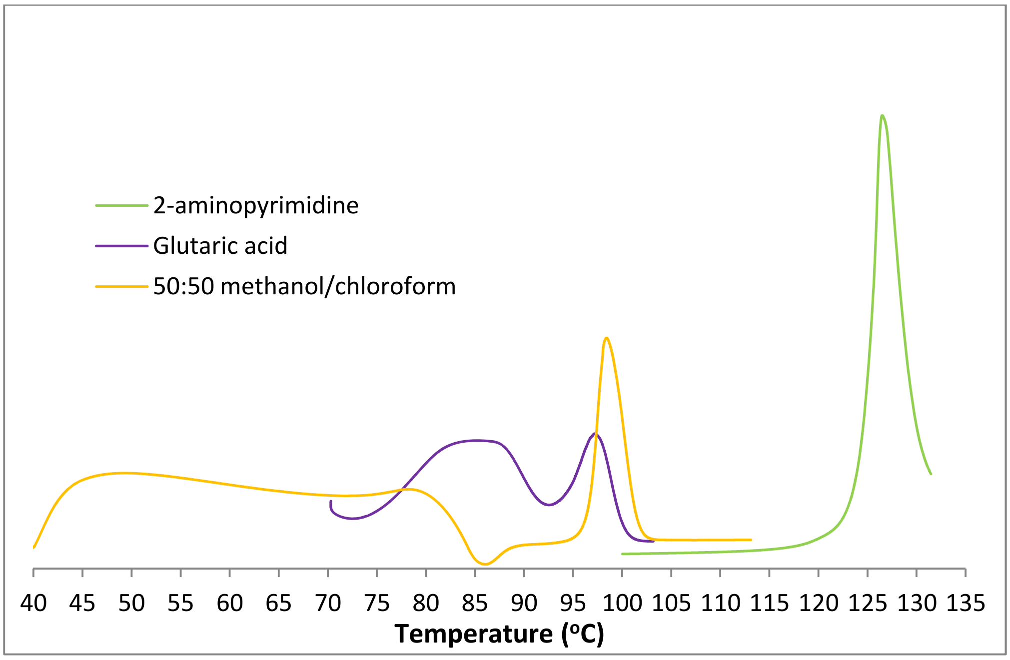

Fig. 6.97 DSC thermogram of the 2-aminopyrimidine-glutaric acid (methanol/chloroform) sample and components.

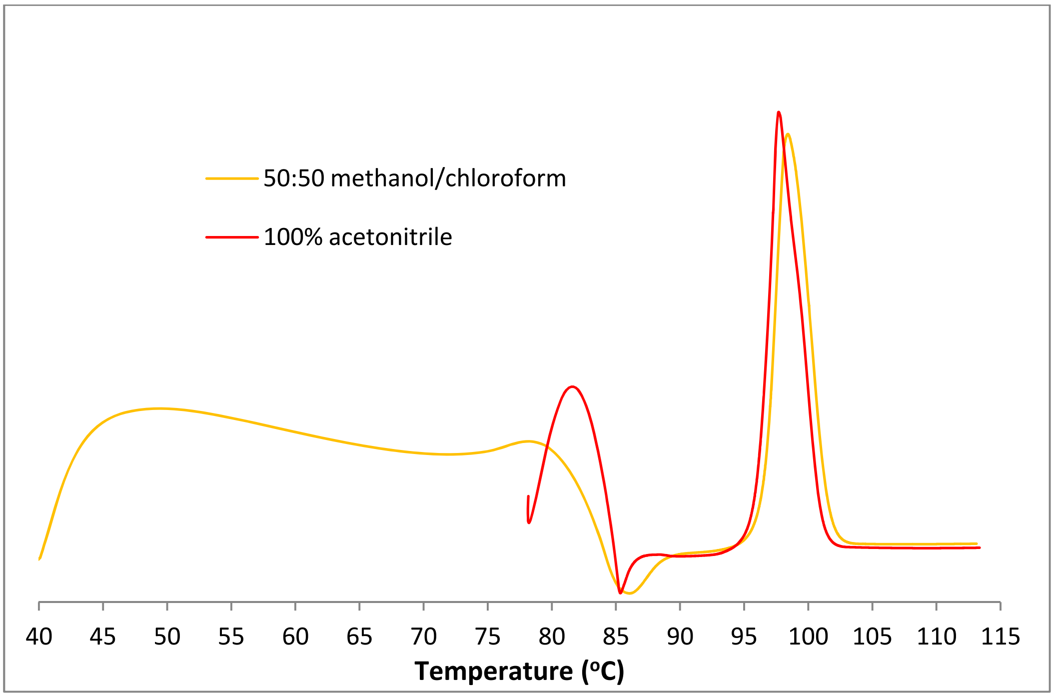

Fig. 6.98 Comparing 100% acetonitrile and 50:50 methanol /chloroform DSC thermogram.

6.10 Discussion on slurry cocrystallisation of 2-aminopyrimidine and glutaric acid.

The slurry cocrystallisation of 2-aminopyrimidine and glutaric gives a powder that is not suitable for single crystal x-ray analysis, so determination of the single crystal structures of the samples from the different experiments was not possible. The crystal structure could be solved in principle from a high enough resolution powder pattern but no one within my research group was able to this and there was not sufficient time to collaborate with other research groups.

A visual comparison of the PXRD from the 5 different slurry experiments (Fig. 6.99), shows that all the samples except 100% methanol have two early diffraction peaks below 10^o, these peaks are absent in 2-aminopyrimidine and glutaric acid. The PXRD for sample obtained from 100% acetonitrile and 50:50 methanol /chloroform are exact matches of one another (Fig. 6.93).

The FTIR spectra of the samples between 1750 cm^{-1} and 4000 cm^{-1} (Fig. 6.100), shows two new broad peaks with the exception of 100% acetonitrile sample, which has only one peak; these peaks are characteristic of un-ionised O-H stretching in hydrogen bonding acid functional group. It was not easy to observe distinguishing peaks in the FTIR finger print region for any of these samples.

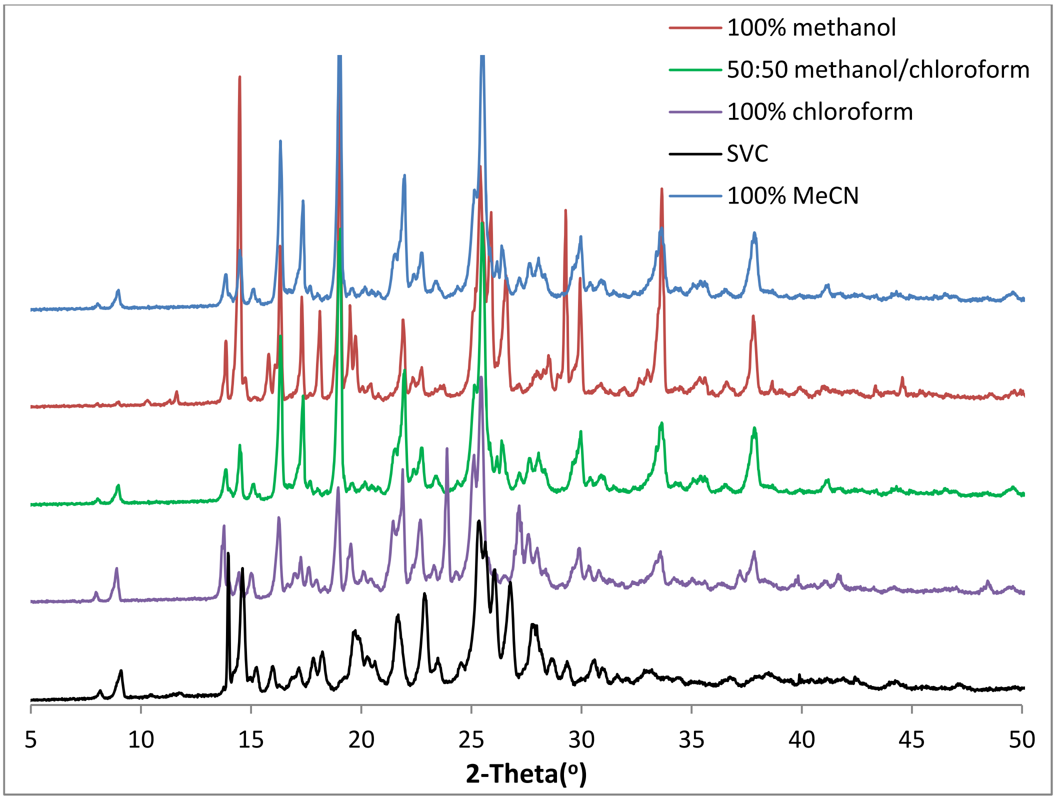

Fig. 6.99 Pxrd patterns for the 5 slurry cocrystallisation of glutaric acid and 2-aminopyrimidine.

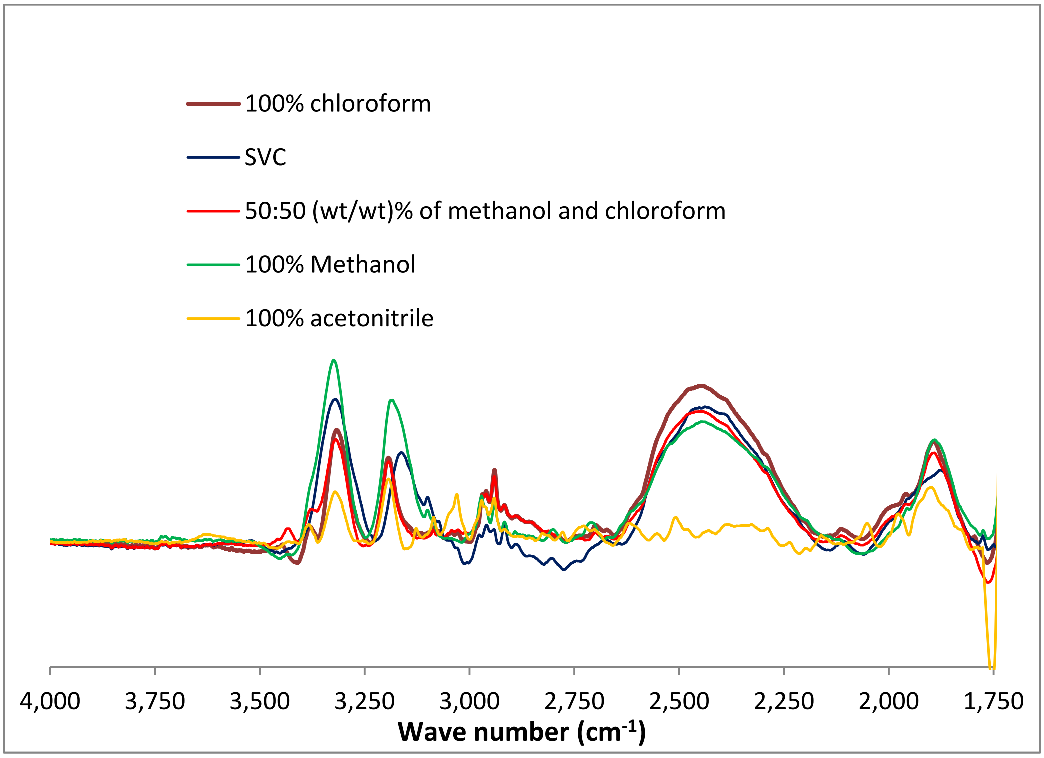

Fig. 6.100 FTIR comparison between 1750 cm^{-1} and 4000 cm^{-1} region.

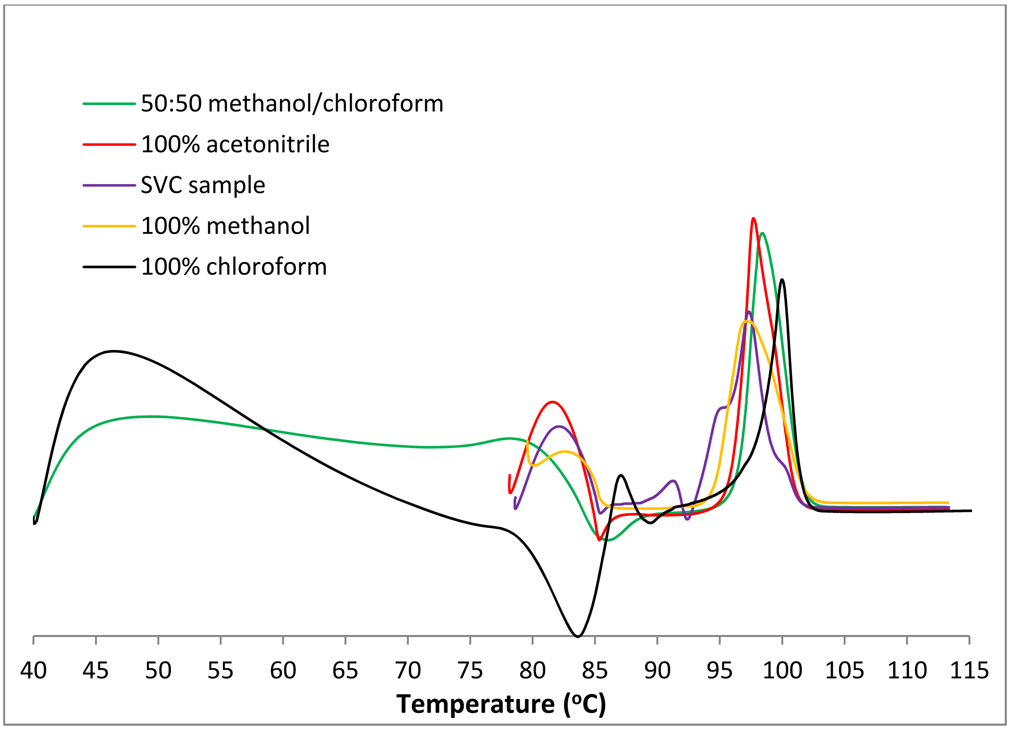

Fig. 6.101 DSC thermogram of 5 slurry cocrystallisation of 2-aminopyrimidine and glutaric acid.

The DSC thermograms show evidence of desolvation (Fig. 6.101). The thermogram for samples obtained from: 100% acetonitrile, 100% chloroform and 50:50 methanol /chloroform, show evidence of recrystallisation after desolvation, while that for 100% methanol and 2.2 *wt* % methanol in cyclohexane do not. The recrystallisation exotherm implies that the solvent being evaporated is incorporated into the crystal lattice of the molecule and after desolvation recrystallisation is necessary to give a stable anhydrous form. It means these samples are solvates and may be responsible for the difficulty in matching PXRD pattern with the four new cocrystals, which are all anhydrous. In the 100% methanol and 2.2 wt % methanol in cyclohexane samples, the absence of a recrystallisation event suggests that the solvent is not incorporated in the crystal lattice and may be trapped in crystal channels or wetting on the crystal surface.

A summary of the slurry cocrystallisation is presented in Table 6.2. The table shows that with a low loading and the highest solid recovery, the anti-solvent/solvent cocrystallisation approach gives the best condition for continuous cocrystallisation.

Though the aim of the investigation was for controlling polymorphism during cocrystallisation, the inability in determining the structure of the cocrystal formed in the experiments hindered this aim. Although similarity in PXRD patterns exists, making a definite conclusion based on the analytical data available would be over optimistic, and so the last column in Table 6.2 lists the likely solid product obtained, rather than stating this is the actual form crystallised.

Table 6.3 Summary of slurry cocrystallisation experiments.

Solvent	Reactor	Loading	Solid recovery	Likely solid
2.2 wt % methanol in cyclohexane	SVC	6.2%	85.02 %	C or D
100% chloroform	STR	6.2%	66.55%	D
100% methanol	STR	21%	75.33 %	A or C
100% acetonitrile	STR	11.8%	76.65 %	A or D
50:50 methanol/chloroform	STR	21%	26.9%	A or D

6.10.1 Particle size

A comparison of the particle size was done by viewing samples under the microscope. In the STR reactions, attrition by the stirrer on the crystal means that the particles sizes should be smaller than the corresponding SVC experiment, where attrition is more minimal.

The particle size for the 2.2 wt % methanol in cyclohexane in the SVC (Fig. 6.102) was the smallest, despite this reaction being conducted in the SVC and the others in STR. This shows that the anti-solvent/solvent cocrystallisation approach does give lower particle sizes compared to pure solvent systems. The particle sizes for the remaining experiments (Figs. 6.103 to 6.106) give substantially larger particle sizes even with attrition in the STR reactor. This suggests that the low solubility of the cocrystal components in the SVC leads to a relatively high nucleation to crystal growth rate compared to the STR system. This occurs perhaps because of the growth being diffusion limited, i.e. limited by the scarcity of crystallisable molecules in the surrounding solution arriving at the crystal surface, whereas the low solubility of the cocrystal still means that there is sufficient supersaturation for nucleation of the cocrystal to occur, or that nucleation can be initiated on a crystal of one (or both) of the cocrystal components, which lowers the nucleation barrier.

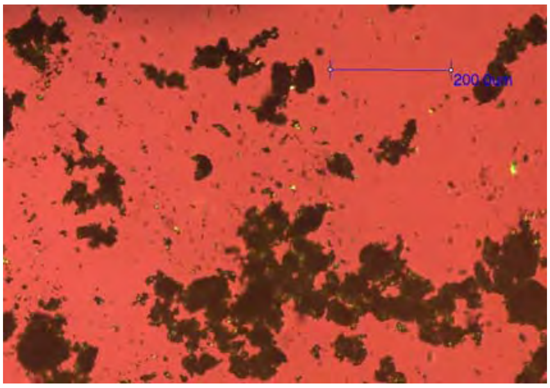

Fig. 6.102 Microscope view of PSD for 2.2 *wt* % methanol in cyclohexane in the SVC.

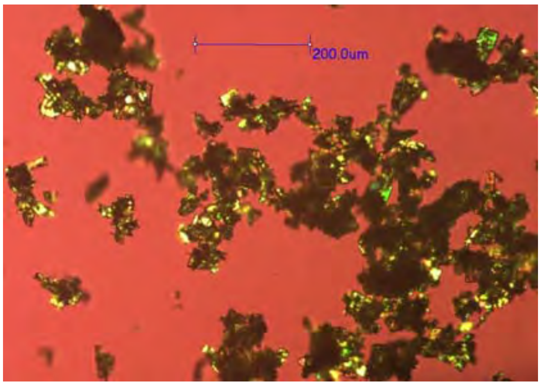

Fig. 6.103 Microscope view of PSD in 100% chloroform experiment.

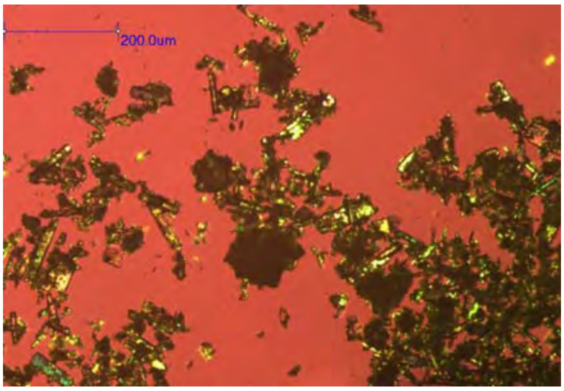

Fig. 6.104 Microscope view of PSD for 100% acetonitrile.

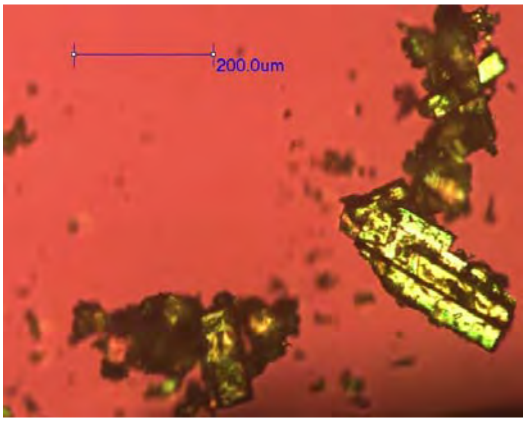

Fig. 6.105 Microscope view of PSD for 50:50 wt % of methanol and chloroform.

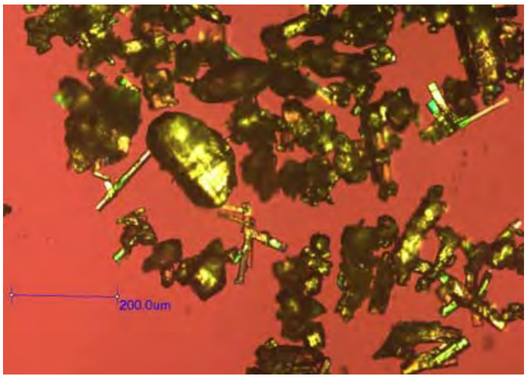

Fig. 6.106 Microscope view of PSD for 100% methanol.

6.11 Conclusion

The slurry cocrystallisation of 2-aminopyrimidine and glutaric acid was carried out in 5 different solvent systems and two different reactor (SVC and the STR); to investigate the influence of solvent in controlling cocrystal polymorphism. The solvents systems were: methanol, acetonitrile, chloroform, 50:50 wt % of methanol and chloroform mixture and 2.2 wt % methanol in cyclohexane.

The PXRD, FTIR and DSC analysis confirmed formation of new cocrystal phases in the experiments; the absence of suitable samples for single crystal x-ray diffraction analysis made it difficult to determine the actual crystal structure of the new phases, or if control of polymorphism was achieved. However, the PXRD for sample obtained from 100% acetonitrile and 50:50 methanol/chloroform matched one another and the DSC were similar, suggesting both contained the same phase, which could either be **A** or **D**. The most likely solid form crystallized from the other systems were as follows: 2.2 wt % methanol in cyclohexane could be either **C** or **D**, 100% chloroform could be **D** and 100% methanol could be either **A** or **C**.

The four new cocrystals of 2-aminopyrimidine-glutaric acid made via solution cocrystallisation from four different solvents. Two of them are monotropic conformational polymorphs of 1:1 2-aminopyrimidine glutaric acid (**A** and **B**). **A** and **B** were crystallised from acetonitrile and 50:50 wt % of methanol and chloroform mixture, respectively. The different orientation of the glutaric acid molecule is responsible for the polymorphism, with **B** being the most stable form at all temperatures. The four crystals all have different colours, linked to the orientation of the chromophore (2-aminopyrimidine) and the hydrogen bonding strength in the crystal structure, which can induce different dipole-dipole effect in the crystals.

Two multi-component crystals with different charges, one neutral cocrystal and the other a cocrystal-salt hybrid (**B** and **D**), were observed in solution cocrystallisation from 50:50 methanol/chloroform. This observation supports the existence of a salt-cocrystal continuum and that ΔpKa differences between the cocrystal components is not sufficient for determining if a salt or cocrystal is formed especially when ΔpKa lies between ≈0-3 where other factors can influence the outcome. **C**, solution crystallised from methanol, was found to be a 2:1 cocrystal.

A comparison of the slurry cocrystallisation experiments showed that cocrystallisation in the anti-solvent/solvent mixture with a low loading of 6.2% gave the best solid recovery of 85.02% and a smallest particle size by microscopy, which suggests slurry cocrystallisation using anti-solvent/solvent mixtures where the solvent is the minority phase, may be suitable for industrial cocrystallisation.

References

(1) *Pharmaceutical salts and co-crystals*; RSC Publishing: **2012**.

(2) Bauer, J.; Spanton, S.; Henry, R.; Quick, J.; Dziki, W.; Porter, W.; Morris, J. *Pharmaceutical Research* **2001**, *18*, 859.

(3) Davey, R. J.; Blagden, N.; Potts, G. D.; Docherty, R. *Journal of Americal Chemical Society* **1997**, *119*.

(4) Grunenberg, A.; Keil, B.; Henck, J. O. *International Journal of Pharmaceutics* **1995**, *118*, 11.

(5) Butterhof, C.; Barwinkel, K.; Senkerb, J.; Breu, J. *Crystengcomm* **2012**.

(6) Trask, A. V.; van de Streek, J.; Motherwell, W. D. S.; Jones, W. *Cryst. Growth Des.* **2005**, *5*, 2233.

(7) Etter, M. C.; Adsmond, D. A. *Journal of the Chemical Society Chemical Communications* **1990**, *8*, 589.

(8) Macrae, C. F.; Bruno, I. J.; Chisholm, J. A.; Edgington, P. R.; McCabe, P.; Pidcock, E.; Rodriguez-Monge, L.; Taylor, R.; van de Streek, J.; Wood, P. A. *J. Appl. Cryst.* **2008** *41*, 466.

(9) Medina, C.; Daurio, D.; Nagapudi, K.; Alvarez-nunez, F. *Journal of Pharmaceutical Sciences* **2010**, *99*, 1693.

(10) Shattock, T. R., University of South Florida, **2007**.

(11) Zhang, S., KTH Royal Institute of Technology, **2010**.

(12) Steed, W. J.; Atwood, J. L. *Supramolecular chemistry*; John Wiley&Sons, **2002**.

(13) Braga, D.; Grepioni, F.; Maini, L.; Sanctis, G.; Rubini, K.; Chierotti, M. R.; Gobetto, R. *Chemistry-A European Journal* **2003**, *9*, 5538.

(14) Haynes, A. D.; Jones, W.; Motherwell, W. D. S. *Crystengcomm* **2006**, *8*, 883.

(15) Aakeroy, C. B.; Fasulo, M. E.; Desper, J. *Molecular Pharmaceutics* **2007**, *4*, 317.

(16) Krygowski, T. M.; Szatyłowicz, H.; Zachara, J. E. *The Journal of Organic Chemistry* **2005**, *70*, 8859.

(17) Johnson, S. L.; Rumon, K. A. *Thc Journal of Physical Chemistry* **1965**, *69*, 74.

(18) Schultheiss, N.; Newman, A. *Cryst. Growth Des.* **2009**, *9*, 2950.

(19) Li, J.; Bourne, S. A.; Caira, M. R. *Chemical Communications* **2011**, *47*, 1530.

(20) Burger, A.; Ramberger, R. *Mikrochimica Acta II* **1979**, 259.

(21) Urakami, K.; Shono, Y.; Higahi, A.; Umemoto, K.; Godo, M. *Chemical and Pharmaceutical Bulletin* **2002**, *50*, 263.

(22) Hilfiker, R. *Polymorphism in the pharmaceutical industry*; WILEY-VCH, verlag GmbH: Federal Republic of Germany, **2006**.

(23) Trask, A. V.; Motherwell, W. D. S.; Jones, W. *Chemical Communications* **2004**, 890.

(24) Bernstein, J.; Hagler, A. T. *Journal of Americal Chemical Society* **1978**, *100*, 673.

(25) Thalladi, V. R.; Nusse, M.; Boese, R. *Journal of Americal Chemical Society* **2000**, *122*, 9227.

(26) Childs, S. L.; Stahly, G. P.; Park, A. *Molecular Pharmaceutics* **2007**, *4*, 323.

(27) Thakuriaa, R.; Deloria, A.; Jones, W.; Lipertb, M. P.; Roy, L.; Rodríguez-Hornedo, N. *International Journal of Pharmaceutics* **2013**.

(28) Almarsson, O.; Zaworotko, M. J. *Chemical Communications* **2004**, 1889.

(29) Aakeroy, C. B.; Desper, J.; Urbina, J. F. *Chemical Communications* **2005**, 2820.

(30) Bruno, I. J.; Cole, J. C.; Edgington, P. R.; Kessler, M.; Macrae, C. F.; McCabe, P.; Pearson, J.; Taylor, R. *Acta Cryst., B58* **2002**, 389.

(31) Nishijo, J.; Takenaka, F. *Yakugaku Zasshi* **1983**, *8*, 819.

(32) Zhao, W.; Pan, L.; Bian, W.; Wang, J. *ChemPhysChem* **2008**, *9*, 1593

(33) Figueras, J. *Journal of Americal Chemical Society* **1971**, *93*, 3255.

(34) Yadav, L. D. S. *Organic spectroscopy* Kluwer Academic Publishers, **2005**.

Chapter 7 Conclusion and future work

7.1 Conclusion

Interest in pharmaceutical cocrystals is driven by the low number of new drugs in the pipeline and by the fact that patents for drugs, worth about $145 billion of annual sales, will be expiring[1] between 2010-2014. Cocrystals open up the opportunity for new solid state forms for existing drug molecules and can be exploited to extend drug patent life and improve drug solid state form. One challenge to the development of cocrystal drug molecules is the dearth of robust processes for large scale manufacture of cocrystal molecules. This work is a feasibility investigation into large scale production of cocrystal.

A new pilot scale process for cocrystals and salts, using an anti-solvent/solvent mixture, was developed and used to cocrystallise five cocrystal systems, on a smaller scale in an SVC (Single Vertical Column) and STR (Stirred Tank Reactor), and on large scale in the PPU (Particle Processing Unit). This approach was also extended to an API salt. The solvent mixture typically consisted of > 97 % anti-solvent and < 3 % solvent. The approach did not require seeding, was quick and > 95 % cocrystal yield was achieved for the caffeine-oxalic acid cocrystal system. A patent has been filed for this process by CPI, the industrial partner on the project.

A quantitative analytical method using solid-state nuclear magnetic resonance (SSNMR), was developed for the model caffeine-oxalic acid cocrystal system in Chapter 3. Four analytical techniques: SSNMR, high pressure liquid chromatography (HPLC), differential scanning calorimetry (DSC) and powder x-ray diffraction were investigated. The analytical technique’s precision was assessed by comparing their coefficients of variance (CV) and SSNMR was selected because of its superior CV.

The SSNMR regression model for the caffeine-oxalic acid cocrystal system gave a good fit. The coefficient of determinant (R^2) and the correlation coefficient (r) for both caffeine and oxalic acid were above 90 %. The correlation coefficient (r) for oxalic acid (99.6 %) was higher than that for caffeine (96.6 %); this disparity was attributed to the need to resolve overlapping peaks in the caffeine regression model.

In Chapter 4, different caffeine-oxalic acid cocrystal yields were observed with different solvents. Using correlation analysis, it was shown that the hydrogen bonding Hansen solubility parameter (δ_H) and oxalic acid solubility in the solvent selected had the strongest correlation with caffeine-oxalic acid cocrystal yield. Yield was higher when a solvent with high δ_H and oxalic acid solubility was selected.

A new parameter for selecting solvents to use in cocrystallisation experiment was suggested. The model ($\frac{\mathrm{Ra}}{\mathrm{Oxalic\ acid}}$) incorporates both δ_H and coformer solubility. It also has a better correlation coefficient (94.2 %) than both δ_H (78 %) and coformer solubility (88 %).

In Chapter 4 and 6, it was shown that the anti-solvent/solvent approach gave smaller crystal particle sizes and higher solid recoveries compared to pure solvent slurry cocrystallisation in the SVC and STR for the cocrystallisation of caffeine-oxalic acid cocrystal and 2-aminopyrimidine-glutaric acid cocrystal systems. This was a result of the higher level of supersaturation achieved, which increases the rate of nucleation compared to crystal growth. The mixing of the anti-solvent and solvent prior to the introduction of API and conformer helps improve consistency in PSD. The anti-solvent/solvent cocrystallisation system also displayed a higher tolerance to solvent change compared with pure solvent. The particle size distribution observed with different anti-solvents showed a shift to higher particle sizes as the viscosity of the anti-solvent increased. This is due to the inverse relationship between the rate of nucleation ($\mathcal{J}$) and viscosity (η).

In Chapter 5, it was shown that the anti-solvent/solvent cocrystallisation method could be used successfully in the SVC and STR for 4 cocrystals and one salt system namely: caffeine-salicylic acid cocrystal, caffeine-oxalic acid cocrystal, carbamazepine-nicotinamide cocrystal, theophylline-salicylic acid cocrystal and 2-aminopyrimidine-salicylic acid salt. The PPU unit was also used to scale up the cocrystallisation of 3 cocrystal systems namely: caffeine-oxalic acid cocrystal, caffeine-salicylic acid cocrystal and theophylline-salicylic acid cocrystal. These systems include 1:1 and 2:1 stoichiometric cocrystal ratios and functional groups, highlighting the flexibility of the anti-solvent/solvent cocrystallisation method.

Similarly to Chapter 4, the anti-solvent/solvent cocrystallisation method was found to give higher cocrystal yields than when only using just anti-solvent, ruling out the possibility that a purely solid state cocrystallisation process occurs due to solid particles grinding together in the SVC. Instead, at least one of the coformer components must be in the solute state for the cocrystallisation to proceed at a reasonable rate.

Chapter 6 documented that four new cocrystals of 2-aminopyrimidine-glutaric acid were made via solution cocrystallisation from four different solvents. Two of them (**A** and **B**) are monotropic conformational polymorphs of 1:1 2-aminopyrimidine glutaric acid, with **B** being the more stable form at all temperatures. The four crystals have different colours; white, peach orange, rose and gold. The difference in crystal colour was explained using the hydrogen bonding strength in the crystal structure, which results in different dipole-dipole effects.

Two multi-component crystals, neutral cocrystal and a cocrystal-salt hybrid (**B** and **D**), were obtained from solution cocrystallisation in 50:50 methanol/chloroform. This supports the suggestion of the existence of a salt-cocrystal continuum between ΔpKa 0-3. In this region, the ratio of ionised and neutral species in solution is not sufficient for determining formation of salt or cocrystal, so other factors becomes relevant within this pKa region. The ΔpKa for glutaric acid and 2-aminopyrimidine is -0.46, this is close to the 0-3 region, using equation 1.21 from Chapter 1, the ratio of neutral to charged species was calculated to be 0.35:1, showing that similar quantities of both the charged and neutral species are present in solution and explains why two different multi-component crystals were observed from the same solvent system.

Slurry cocrystallisation of 2-aminopyrimidine and glutaric acid was carried out in 5 different solvent systems: methanol, acetonitrile, chloroform, 50:50 wt % of methanol and chloroform mixture and 2.2 *wt* % methanol in cyclohexane, to investigate polymorphic control in cocrystal synthesis. However, the absence of suitable samples for single crystal x-ray diffraction analysis made it difficult to determine the actual crystal structure of the new phases. A comparison of the slurry cocrystallisation experiments shows that cocrystallisation in the anti-solvent/solvent mixture with a low loading of 6.2% gives the highest solid recovery (85.02%) and the smallest crystal particle size.

The combined results of chapters 3 to 6 do suggest that the new scale-up process using an anti-solvent/solvent mixture with the anti-solvent forming the majority phase will be suitable for crystallising high yields of cocrystals with improved particle size distributions compared to crystallisation from pure solvent.

7.2 Future work

Polymorphic control in cocrystallisation is important, especially in the pharmaceutical industry where such details are required for drug registration. The work done in this investigation is not exhaustive, because of the inability to determine the crystal structure of the powder obtained from the slurry cocrystallisation in chapter 6. A study of the influence of solvents and anti-solvents, in controlling cocrystal polymorphism, needs investigating.

Ternary cocrystals are cocrystals with three different cocrystal components hydrogen bonded together. More of such systems are being reported in journal publications. It would be worthwhile exploring the application of the anti-solvent/solvent approach to ternary cocrystallisation.

Particle size distribution (PSD) is important in the pharmaceutical industry. This study shows the possibility of controlling PSD using anti-solvent viscosity. More work is required to further develop this concept into a veritable tool.

Bibliography

(1) Houlton, S., Chemistry world, **2013**; Vol. 10, p 33.

Appendix A

Table A.1 Standard PXRD TOPAS analysis

	Cocrystal	Caffeine	Oxalic acid
Standard 1	4.05%	47.72%	48.23%
Standard 2	49.26%	26.50%	24.24%
Standard 3	74.20%	12.44%	13.36%
Standard 4	93.70%	3.10%	3.20%

A.2 Topas refinement data

Standard 1		Refined 1	
Position	Area	Position	Area
7.973	0.806	8.039	0.005
11.741	2.156	11.805	0.072
12.551	1.5	12.52	0.049
14.728	1.601	14.737	0.06
15.485	2.147	15.552	0.083
16.179	0.98	16.335	0.028
18.588	2.412	18.665	0.247
22.097	1.514	22.25	0.107
22.543	1.934	22.655	0.191
26.172	3.275	26.127	0.655
27.288	3.56	27.291	0.742
29.053	11.534	29.002	3.858
39.384	4.333	39.43	2.787

Standard 2		Refined 2	
Position	Area	Position	Area
8.05	1.692	8.158	0.021
11.858	7.629	11.916`	0.326
12.608	5.149	12.66	0.227
15.01	1.098	15.001	0.071
16.292	1.978	16.06	0.063
16.719	2.185	16.615	0.153
17.826	2.556	17.885	0.121
18.735	2.126	18.813	0.195
22.368	12.016	22.525	1.149
22.368	12.016		
24.961	3.316	25.011	0.671
27.549	5.953	27.29	2.358
29.153	4.072	28.844	1.545

Standard 3		Refined 3	
Position	Area	Position	Area
8.033	2.667	7.996	0.033
11.732	6.321	11.804	0.265
12.397	6.425	12.498	0.283
14.96	0.931	14.797	0.041
16.332	3.607	16.203	0.28
18.0	2.506	17.352	0.035
18.352	3.483	18.346	0.282
22.118	5.596	22.452	0.994
24.685	3.761	24.715	0.791
26.92	5.761	26.946	1.422
27.431	6.373	27.576	1.178
28.755	4.469	28.709	1.313
32.273	4.423	32.319	0.941

Standard 4		Refined 4	
Position	Area	Position	Area
8.027	1.294	8.052	0.021
11.914	5.588	11.934	0.198
12.403	4.656	12.419	0.214
15.04	0.742	14.373	0.023
16.107	1.67	16.222	0.181
18.133	1.641	18.211	0.159
20.478	2.475	20.464	0.063
22.56	4.087	22.489	0.876
24.347	3.36	24.629	0.22
25.147	2.933	24.626	0.541
28.668	8.183	27.433	2.817

A.3 Correlation table peak area and cocrystal amount

For peak at 2θ≈8.0^{o}

	Cocrystal	Area
Area	0.777	1

For peak at 2θ≈16.11^{o}

	Cocrystal	Area
Area	0.78	1

Appendix B Crystallographic information file.

1:1 Polymorph A (12srv226)

Table 1 Crystal data and structure refinement for 12srv226	
Empirical formula	$C_4H_5N_3$ x $C_5H_8O_4$
Formula weight	227.22
Temperature/K	120
Crystal system	orthorhombic
Space group	Pbcm
a/Å	4.1667(4)
b/Å	12.6657(11)
c/Å	20.3238(18)
α/°	90.00
β/°	90.00
γ/°	90.00
Volume/Å^3	1072.57(17)
Z	4
ρ_{calc}mg/mm^3	1.407
m/mm^{-1}	0.112
F(000)	480.0
Crystal size/mm^3	0.44 × 0.36 × 0.14
2Θ range for data collection	4 to 59°
Index ranges	$-5 \le h \le 5$, $-17 \le k \le 17$, $-27 \le l \le 27$
Reflections collected	9365
Independent reflections	1525[R(int) = 0.0329]
Data/restraints/parameters	1525/0/105
Goodness-of-fit on F^2	1.061
Final R indexes [I>=2σ (I)]	$R_1 = 0.0540$, $wR_2 = 0.1364$
Final R indexes [all data]	$R_1 = 0.0665$, $wR_2 = 0.1490$
Largest diff. peak/hole / e Å^{-3}	0.38/-0.31

Table 2 Fractional Atomic Coordinates ($\times 10^4$) and Equivalent Isotropic Displacement Parameters ($Å^2\times 10^3$) for 12srv226. U_{eq} is defined as 1/3 of of the trace of the orthogonalised U_{IJ} tensor.

Atom	*x*	*y*	*z*	U(eq)
O1	812(3)	4550.3(8)	4238.7(5)	27.4(3)
O2	2865(3)	3070.0(9)	3812.0(5)	30.7(3)
N1	630(5)	3709.1(15)	2500	28.9(4)
N2	-2000(3)	5002(1)	3087.9(6)	23.6(3)
C1	-1154(5)	4585.7(16)	2500	22.8(4)
C2	-3857(4)	5863.9(11)	3079.1(7)	25.1(3)
C3	-4894(6)	6326.5(16)	2500	26.7(4)
C4	2530(3)	3673.1(11)	4270.3(7)	21.5(3)
C5	4034(4)	3515.6(11)	4938.7(7)	22.1(3)
C6	5961(5)	2500	5000	22.6(4)

Table 3 Anisotropic Displacement Parameters ($Å^2\times 10^3$) for 12srv226. The Anisotropic displacement factor exponent takes the form: $-2\pi^2[h^2a^{*2}U_{11}+...+2hka\times b\times U_{12}]$

Atom	U_{11}	U_{22}	U_{33}	U_{23}	U_{13}	U_{12}
O1	35.2(6)	24.1(5)	22.8(5)	-0.5(4)	-2.1(4)	8.0(4)
O2	43.6(7)	24.7(5)	23.8(6)	-2.2(4)	-1.2(5)	7.0(5)
N1	39.3(11)	26.2(9)	21.2(9)	0	0	8.4(8)
N2	26.7(6)	21.4(6)	22.6(6)	-0.4(4)	0.7(4)	-0.5(5)
C1	24.5(9)	20.9(9)	23.0(9)	0	0	-1.6(7)
C2	27.5(7)	21.9(7)	25.8(7)	-2.5(5)	1.5(5)	-0.6(6)
C3	28.6(10)	21.5(9)	30(1)	0	0	3.1(8)
C4	24.0(6)	18.3(6)	22.2(6)	2.1(5)	2.3(5)	-0.7(5)
C5	24.9(7)	18.5(6)	22.9(7)	-0.3(5)	0.0(5)	-0.7(5)
C6	22.3(9)	19.6(9)	26(1)	2.2(7)	0	0

Table 4 Bond Lengths for 12srv226.

Atom	Atom	Length/Å		Atom	Atom	Length/Å
O1	C4	1.3234(17)		C2	C3	1.3840(19)
O2	C4	1.2127(18)		C3	C2^1	1.3840(19)
N1	C1	1.336(3)		C4	C5	1.509(2)
N2	C1	1.3527(15)		C5	C6	1.5216(17)
N2	C2	1.3381(19)		C6	C5^2	1.5216(17)
C1	N2^1	1.3528(15)				

^{1}+X,+Y,1/2-Z; ^{2}+X,1/2-Y,1-Z

Table 5 Bond Angles for 12srv226.

Atom	Atom	Atom	Angle/˚		Atom	Atom	Atom	Angle/˚
C2	N2	C1	117.18(13)		O1	C4	C5	112.29(12)
N1	C1	N2	117.96(9)		O2	C4	O1	123.63(13)
N1	C1	N2^1	117.96(9)		O2	C4	C5	124.08(13)
N2	C1	N2^1	124.08(18)		C4	C5	C6	113.86(11)
N2	C2	C3	122.50(14)		C5	C6	C5^2	116.29(17)
C2^1	C3	C2	116.52(19)					

^{1}+X,+Y,1/2-Z; ^{2}+X,1/2-Y,1-Z

Table 6 Hydrogen Bonds for 12srv226.

D	H	A	d(D-H)/Å	d(H-A)/Å	d(D-A)/Å	D-H-A/°
N1	H1A	O2	0.86(2)	2.08(2)	2.9381(14)	173(2)
O1	H1	N2	0.91(3)	1.78(3)	2.6775(17)	170(2)

Table 7 Hydrogen Atom Coordinates (Å×10^4) and Isotropic Displacement Parameters (Å^2×10^3) for 12srv226.				
Atom	***x***	***y***	***z***	**U(eq)**
H1A	1320(60)	3467(18)	2868(11)	42(6)
H1	-120(70)	4621(19)	3836(12)	49(6)
H2	-4440(50)	6172(15)	3487(10)	27(5)
H3	-6200(70)	6920(20)	2500	34(7)
H5A	2320(40)	3555(14)	5261(9)	23(4)
H5B	5390(50)	4150(16)	5018(10)	35(5)
H6	7320(50)	2443(16)	4620(10)	30(5)

1:1 Polymorph B (13srv125)

Table 1 Crystal data and structure refinement for 13srv125	
Empirical formula	$C_4H_5N_3$ x $C_5H_8O_4$
Formula weight	227.22
Temperature/K	120
Crystal system	triclinic
Space group	P-1
a/Å	6.0184(4)
b/Å	7.4714(5)
c/Å	12.0911(7)
α/°	84.3710(10)
β/°	89.9060(10)
γ/°	76.094(2)
Volume/Å^3	525.07(6)
Z	2
ρ_{calc}mg/mm^3	1.437
m/mm^{-1}	0.114
F(000)	240.0
Crystal size/mm^3	0.56 × 0.3 × 0.24
2Θ range for data collection	3.38 to 58°
Index ranges	$-8 \le h \le 8$, $-10 \le k \le 10$, $-16 \le l \le 16$
Reflections collected	12033
Independent reflections	2794[R(int) = 0.0253]
Data/restraints/parameters	2794/0/197
Goodness-of-fit on F^2	1.035
Final R indexes [I>=2σ (I)]	$R_1 = 0.0416$, $wR_2 = 0.1140$
Final R indexes [all data]	$R_1 = 0.0510$, $wR_2 = 0.1258$
Largest diff. peak/hole / e Å^{-3}	0.35/-0.26

Table 2 Fractional Atomic Coordinates ($\times10^4$) and Equivalent Isotropic Displacement Parameters (Å$^2\times10^3$) for 13srv125. U_{eq} is defined as 1/3 of of the trace of the orthogonalised U_{IJ} tensor.

Atom	*x*	*y*	*z*	U(eq)
O1	4602.1(15)	3217.8(13)	6142.5(6)	30.9(2)
O2	6462.1(15)	1733.5(12)	4765.9(6)	31.2(2)
O3	1345.1(14)	2399.1(12)	1173.6(6)	27.9(2)
O4	-2146.8(15)	4291.1(12)	1127.7(7)	33.2(2)
C21	4752.0(19)	2673.3(15)	5126.9(8)	24.0(2)
C22	2489.8(18)	3396.5(16)	4508.9(8)	24.8(2)
C23	2443.4(18)	3002.9(15)	3303.5(8)	22.9(2)
C24	35.8(19)	3810.8(15)	2816.2(8)	23.1(2)
C25	-339.0(19)	3523.9(15)	1620.1(8)	23.9(2)
N1	6734.1(18)	3217.2(15)	9001.9(8)	31.9(2)
N2	10528.9(16)	1670.2(13)	9109.0(7)	24.2(2)
N3	8309.9(17)	1865.0(13)	7448.0(7)	24.8(2)
C1	8543.3(19)	2240.0(15)	8506.2(8)	23.2(2)
C2	12312(2)	661.8(17)	8622.0(9)	28.0(2)
C3	12216(2)	177.3(17)	7550.0(9)	29.2(2)
C4	10131(2)	842.7(16)	6994.5(9)	27.0(2)

Table 3 Anisotropic Displacement Parameters (Å$^2\times10^3$) for 13srv125. The Anisotropic displacement factor exponent takes the form: $-2\pi^2[h^2a^{*2}U_{11}+...+2hka\times b\times U_{12}]$

Atom	U_{11}	U_{22}	U_{33}	U_{23}	U_{13}	U_{12}
O1	32.2(4)	43.2(5)	15.1(4)	-9.6(3)	-5.2(3)	-2.1(4)
O2	29.4(4)	42.2(5)	19.7(4)	-9.4(3)	-3.4(3)	-1.7(3)
O3	27.6(4)	38.7(5)	16.3(4)	-8.2(3)	-4.3(3)	-3.8(3)
O4	34.9(5)	36.3(5)	23.1(4)	-8.7(3)	-12.4(3)	3.9(3)
C21	29.4(5)	29.6(5)	14.5(4)	-4.0(4)	-2.7(4)	-9.1(4)
C22	24.4(5)	34.9(6)	15.4(4)	-6.0(4)	-2.1(4)	-6.5(4)
C23	23.9(5)	30.5(5)	15.1(4)	-4.7(4)	-3.0(4)	-7.0(4)

C24	25.6(5)	27.4(5)	16.4(4)	-5.7(4)	-3.3(4)	-5.2(4)
C25	28.4(5)	25.9(5)	17.6(5)	-2.6(4)	-4.6(4)	-7.1(4)
N1	31.9(5)	39.1(6)	20.8(5)	-11.1(4)	-8.7(4)	2.7(4)
N2	27.3(5)	29.1(5)	17.0(4)	-4.1(3)	-4.2(3)	-7.4(4)
N3	34.0(5)	25.8(4)	15.0(4)	-3.1(3)	-5.5(3)	-7.6(4)
C1	30.3(5)	23.6(5)	16.1(4)	-2.6(3)	-5.0(4)	-7.1(4)
C2	26.5(5)	35.5(6)	23.3(5)	-5.6(4)	-2.6(4)	-9.0(4)
C3	29.9(6)	36.0(6)	23.2(5)	-8.2(4)	4.0(4)	-8.7(5)
C4	37.6(6)	28.7(5)	17.6(5)	-4.6(4)	-0.8(4)	-12.8(4)

Table 4 Bond Lengths for 13srv125.

Atom	Atom	Length/Å		Atom	Atom	Length/Å
O1	C21	1.3273(12)		N1	C1	1.3340(15)
O2	C21	1.2058(14)		N2	C1	1.3557(13)
O3	C25	1.3049(14)		N2	C2	1.3274(15)
O4	C25	1.2256(13)		N3	C1	1.3509(13)
C21	C22	1.5081(14)		N3	C4	1.3279(15)
C22	C23	1.5165(14)		C2	C3	1.3844(15)
C23	C24	1.5244(15)		C3	C4	1.3821(16)
C24	C25	1.5078(13)				

Table 5 Bond Angles for 13srv125.

Atom	Atom	Atom	Angle/˚		Atom	Atom	Atom	Angle/˚
O1	C21	C22	110.07(9)		C2	N2	C1	117.05(9)
O2	C21	O1	124.15(10)		C4	N3	C1	117.28(9)
O2	C21	C22	125.77(9)		N1	C1	N2	117.21(9)
C21	C22	C23	116.16(9)		N1	C1	N3	119.07(10)
C22	C23	C24	109.04(9)		N3	C1	N2	123.71(10)
C25	C24	C23	116.40(9)		N2	C2	C3	123.18(10)

O3	C25	C24	115.72(9)		C4	C3	C2	115.66(11)
O4	C25	O3	123.60(9)		N3	C4	C3	123.09(10)
O4	C25	C24	120.66(10)					

Table 6 Hydrogen Bonds for 13srv125.

D	H	A	d(D-H)/Å	d(H-A)/Å	d(D-A)/Å	D-H-A/°
O1	H1	N3	0.91(3)	1.76(3)	2.6659(12)	178(2)
O3	H3	N2[1]	0.92(2)	1.78(2)	2.6774(12)	166(2)
N1	H1A	O4[2]	0.872(19)	2.209(19)	2.9302(14)	139.8(16)
N1	H1B	O4[3]	0.860(19)	2.035(19)	2.8938(12)	176.0(16)

[1]-1+X,+Y,-1+Z; [2]-X,1-Y,1-Z; [3]1+X,+Y,1+Z

Table 7 Hydrogen Atom Coordinates (Å×10^4) and Isotropic Displacement Parameters ($Å^2$×10^3) for 13srv125.

Atom	*x*	*y*	*z*	U(eq)
H1	5870(40)	2730(30)	6584(19)	71(6)
H3	860(40)	2300(30)	469(19)	64(6)
H22A	1360(30)	2850(20)	4930(13)	34(4)
H22B	2010(30)	4740(20)	4558(13)	35(4)
H23A	3500(20)	3549(19)	2902(11)	23(3)
H23B	2860(20)	1700(20)	3265(11)	24(3)
H24A	-1050(20)	3244(19)	3239(12)	28(3)
H24B	-460(20)	5140(20)	2875(12)	26(3)
H1A	5470(30)	3760(20)	8634(15)	47(5)
H1B	7000(30)	3570(20)	9633(15)	41(4)
H2	13770(30)	240(20)	9054(14)	42(4)
H4	9990(30)	510(20)	6219(14)	39(4)
H3A	13470(30)	-560(20)	7205(14)	39(4)

2:1 Cocrystal C (12srv234)

Table 1 Crystal data and structure refinement for 12srv234	
Empirical formula	2 $C_4H_5N_3$ x $C_5H_8O_4$
Formula weight	322.33
Temperature/K	120
Crystal system	monoclinic
Space group	$P2_1/n$
a/Å	10.2625(4)
b/Å	15.0558(6)
c/Å	11.1755(4)
α/°	90.00
β/°	113.0320(10)
γ/°	90.00
Volume/Å^3	1589.08(11)
Z	4
ρ_{calc}mg/mm^3	1.347
m/mm^{-1}	0.103
F(000)	680.0
Crystal size/mm^3	0.34 × 0.32 × 0.15
2Θ range for data collection	4.58 to 59°
Index ranges	$-10 \le h \le 14$, $-20 \le k \le 20$, $-13 \le l \le 15$
Reflections collected	12296
Independent reflections	4412[R(int) = 0.0359]
Data/restraints/parameters	4412/0/280
Goodness-of-fit on F^2	0.990
Final R indexes [I>=2σ (I)]	R_1 = 0.0431, wR_2 = 0.1114
Final R indexes [all data]	R_1 = 0.0642, wR_2 = 0.1232
Largest diff. peak/hole / e Å^{-3}	0.31/-0.27

Table 2 Fractional Atomic Coordinates (×10^4) and Equivalent Isotropic Displacement Parameters (Å^2×10^3) for 12srv234. U$_{eq}$ is defined as 1/3 of of the trace of the orthogonalised U$_{IJ}$ tensor.

Atom	*x*	*y*	*z*	U(eq)
O1	6897.2(11)	6377.6(5)	10187.2(9)	32.1(2)
O2	6906.6(11)	4916.4(6)	10545.2(9)	34.6(2)
O3	3961.7(11)	3587.3(6)	4557.6(8)	33.4(2)
O4	4836.2(10)	2904.1(6)	6492.4(8)	31.7(2)
C31	6589.1(13)	5545.6(8)	9804.2(12)	26.4(3)
C32	5799.5(16)	5465.4(8)	8361.0(12)	29.1(3)
C33	5408.8(14)	4519.3(8)	7884.6(11)	25.2(3)
C34	4715.7(15)	4496.9(8)	6417.0(11)	25.8(3)
C35	4514.3(13)	3579.9(8)	5844.8(11)	24.8(3)
N1	8602.7(13)	5159.1(7)	3309.1(11)	29.3(3)
N2	8055.0(11)	6626.1(7)	2750.9(10)	27.9(2)
N3	9323.8(12)	6199.4(7)	4964.6(10)	28.9(2)
C1	8671.9(13)	6014.3(8)	3683.8(12)	25.3(3)
C2	8046.8(15)	7461.1(8)	3146.0(13)	31.1(3)
C3	8632.7(15)	7712.4(9)	4427.7(13)	31.7(3)
C4	9282.5(14)	7045.7(8)	5307.7(13)	30.7(3)
N21	4825.8(13)	1226.6(8)	5242.2(11)	35.1(3)
N22	3773.7(12)	2041.3(7)	3364.4(10)	29.6(2)
N23	4084.5(12)	468.3(7)	3297.8(11)	31.4(3)
C21	4220.8(14)	1244.0(8)	3950.5(12)	28.0(3)
C22	3179.6(15)	2049.3(9)	2069.6(13)	31.6(3)
C23	3008.7(15)	1290.4(9)	1331.3(14)	33.3(3)
C24	3480.9(14)	509.2(9)	2009.9(13)	32.6(3)

Table 3 Anisotropic Displacement Parameters ($Å^2\times10^3$) for 12srv234. The Anisotropic displacement factor exponent takes the form: $-2\pi^2[h^2a^{*2}U_{11}+...+2hka\times b\times U_{12}]$

Atom	U_{11}	U_{22}	U_{33}	U_{23}	U_{13}	U_{12}
O1	47.3(6)	20.4(4)	23.6(5)	-1.9(3)	8.4(4)	-2.1(4)
O2	49.7(6)	22.3(4)	25.0(5)	1.1(3)	7.2(4)	0.6(4)
O3	50.5(6)	23.7(5)	21.2(5)	-1.5(3)	8.7(4)	-2.3(4)
O4	46.4(6)	21.6(4)	25.8(5)	1.2(3)	12.5(4)	-1.6(4)
C31	31.7(7)	22.0(6)	25.7(6)	-1.7(4)	11.4(5)	0.2(5)
C32	42.0(8)	21.3(6)	22.7(6)	-0.7(4)	11.4(5)	0.2(5)
C33	33.1(7)	20.7(6)	21.9(6)	-0.3(4)	10.7(5)	-0.7(5)
C34	34.4(7)	21.0(6)	21.4(6)	-0.7(4)	10.3(5)	-0.6(5)
C35	28.8(7)	23.3(6)	22.7(6)	-1.2(4)	10.4(5)	-2.9(5)
N1	36.6(6)	22.7(5)	24.1(6)	-1.7(4)	7.1(5)	2.2(4)
N2	31.8(6)	22.4(5)	25.0(5)	-0.6(4)	6.4(4)	-1.3(4)
N3	34.6(6)	26.1(5)	23.9(5)	-1.7(4)	9.1(4)	0.9(4)
C1	25.8(6)	23.5(6)	25.7(6)	-0.9(4)	8.8(5)	-0.7(5)
C2	34.1(7)	22.7(6)	31.3(7)	0.2(5)	7.2(5)	-1.1(5)
C3	35.3(7)	23.3(6)	33.6(7)	-6.0(5)	10.3(5)	-2.2(5)
C4	33.9(7)	28.6(7)	27.3(7)	-5.6(5)	9.4(5)	-2.7(5)
N21	51.8(8)	22.3(6)	28.7(6)	-1.4(5)	13.1(5)	1.8(5)
N22	36.7(6)	22.4(5)	28.7(6)	-2.4(4)	11.6(4)	-3.0(4)
N23	36.0(6)	24.6(5)	34.0(6)	-4.8(4)	14.1(5)	0.5(4)
C21	29.7(7)	23.7(6)	31.8(7)	-2.4(5)	13.2(5)	-1.3(5)
C22	36.7(8)	26.1(6)	31.0(7)	-0.9(5)	12.3(5)	-3.6(5)
C23	36.7(8)	34.8(7)	27.8(7)	-4.5(5)	11.9(6)	-2.2(6)
C24	34.4(8)	29.5(7)	35.3(7)	-8.7(5)	15.3(6)	-1.9(5)

Table 4 Bond Lengths for 12srv234.

Atom	Atom	Length/Å		Atom	Atom	Length/Å
O1	C31	1.3215(14)		N3	C1	1.3508(16)
O2	C31	1.2157(14)		N3	C4	1.3361(16)
O3	C35	1.3239(14)		C2	C3	1.3721(18)
O4	C35	1.2170(14)		C3	C4	1.3806(18)
C31	C32	1.4999(17)		N21	C21	1.3299(17)
C32	C33	1.5187(17)		N22	C21	1.3584(16)
C33	C34	1.5113(16)		N22	C22	1.3324(17)
C34	C35	1.5013(16)		N23	C21	1.3548(15)
N1	C1	1.3472(15)		N23	C24	1.3271(17)
N2	C1	1.3490(16)		C22	C23	1.3799(18)
N2	C2	1.3336(16)		C23	C24	1.3804(19)

Table 5 Bond Angles for 12srv234.

Atom	Atom	Atom	Angle/˚		Atom	Atom	Atom	Angle/˚
O1	C31	C32	112.62(10)		N2	C1	N3	124.48(11)
O2	C31	O1	123.47(11)		N2	C2	C3	123.28(12)
O2	C31	C32	123.91(11)		C2	C3	C4	115.81(12)
C31	C32	C33	114.20(10)		N3	C4	C3	123.34(12)
C34	C33	C32	110.42(10)		C22	N22	C21	117.16(11)
C35	C34	C33	114.24(10)		C24	N23	C21	116.74(11)
O3	C35	C34	112.59(10)		N21	C21	N22	117.83(11)
O4	C35	O3	123.66(11)		N21	C21	N23	118.26(12)
O4	C35	C34	123.74(11)		N23	C21	N22	123.91(12)
C2	N2	C1	116.72(11)		N22	C22	C23	122.61(12)
C4	N3	C1	116.28(11)		C22	C23	C24	116.22(13)
N1	C1	N2	117.43(11)		N23	C24	C23	123.36(12)
N1	C1	N3	118.08(11)					

Table 6 Hydrogen Bonds for 12srv234.						
D	**H**	**A**	**d(D-H)/Å**	**d(H-A)/Å**	**d(D-A)/Å**	**D-H-A/°**
O1	H1	N2[1]	0.950(19)	1.719(19)	2.6639(13)	172.4(17)
O3	H3	N22	1.02(2)	1.64(2)	2.6518(13)	174.0(17)
N1	H1A	O2[2]	0.912(17)	2.031(17)	2.9149(15)	162.6(14)
N1	H1B	N3[3]	0.893(18)	2.149(18)	3.0367(16)	172.7(15)
N21	H21A	O4	0.915(18)	1.972(18)	2.8843(14)	175.1(15)
N21	H21B	N23[4]	0.948(18)	2.055(18)	2.9995(16)	174.6(14)

[1]+X,+Y,1+Z; [2]+X,+Y,-1+Z; [3]2-X,1-Y,1-Z; [4]1-X,-Y,1-Z

Table 7 Hydrogen Atom Coordinates (Å×10^4) and Isotropic Displacement Parameters (Å^2×10^3) for 12srv234.				
Atom	***x***	***y***	***z***	**U(eq)**
H1	7370(19)	6431(11)	11104(18)	54(5)
H3	3910(20)	2974(13)	4157(18)	73(6)
H32A	4931(17)	5837(11)	8104(15)	46(4)
H32B	6422(16)	5732(11)	7983(15)	43(4)
H33A	6298(15)	4162(10)	8216(13)	30(4)
H33B	4775(15)	4272(10)	8263(13)	31(4)
H34A	3760(16)	4792(10)	6086(14)	31(4)
H34B	5290(17)	4826(10)	6055(15)	38(4)
H1A	8247(17)	5046(10)	2438(17)	41(4)
H1B	9212(19)	4787(11)	3878(16)	46(5)
H2	7613(15)	7882(9)	2452(13)	29(4)
H3A	8596(16)	8299(11)	4692(14)	37(4)
H4	9753(16)	7183(10)	6248(15)	37(4)
H21A	4872(17)	1747(12)	5681(15)	48(5)
H21B	5110(17)	677(12)	5681(16)	46(4)
H22	2861(15)	2618(10)	1669(13)	30(4)
H23	2582(16)	1320(10)	399(16)	40(4)
H24	3369(15)	-50(10)	1539(14)	31(4)

2:3 Cocrystal-salt hybrid D (12srv225)

Table 1 Crystal data and structure refinement for 12srv225	
Empirical formula	$2[C_4H_6N_3]^+$ x $[C_5H_6O_4]^{2-}$ x $2[C_5H_8O_4]$
Formula weight	586.56
Temperature/K	120
Crystal system	triclinic
Space group	P-1
a/Å	5.4848(3)
b/Å	11.1944(5)
c/Å	22.9123(11)
α/°	91.7810(10)
β/°	92.3710(10)
γ/°	103.0110(10)
Volume/Å^3	1368.32(12)
Z	2
ρ_{calc}mg/mm^3	1.424
m/mm^{-1}	0.116
F(000)	620.0
Crystal size/mm^3	0.56 × 0.48 × 0.3
2Θ range for data collection	3.74 to 59°
Index ranges	$-7 \le h \le 7$, $-15 \le k \le 15$, $-31 \le l \le 31$
Reflections collected	15931
Independent reflections	7579[R(int) = 0.0192]
Data/restraints/parameters	7579/0/506
Goodness-of-fit on F^2	1.053
Final R indexes [I>=2σ (I)]	$R_1 = 0.0391$, $wR_2 = 0.1025$
Final R indexes [all data]	$R_1 = 0.0488$, $wR_2 = 0.1105$
Largest diff. peak/hole / e Å^{-3}	0.41/-0.22

Table 2 Fractional Atomic Coordinates (×10^4) and Equivalent Isotropic Displacement Parameters (Å^2×10^3) for 12srv225. U_{eq} is defined as 1/3 of of the trace of the orthogonalised U_{IJ} tensor.

Atom	*x*	*y*	*z*	U(eq)
N1	7416.4(19)	5011.5(9)	5584.5(4)	23.58(19)
N2	7525.1(19)	3566.1(10)	4849.5(4)	26.0(2)
N3	4107.9(18)	3315.0(9)	5467.4(4)	22.09(19)
C1	6367(2)	3965.2(10)	5303.4(5)	21.2(2)
C2	6365(2)	2524.8(12)	4572.1(5)	29.5(3)
C3	4055(2)	1810.4(12)	4723.1(6)	29.8(3)
C4	2966(2)	2250.0(11)	5183.8(5)	26.1(2)
N21	5181.9(19)	8737.1(9)	590.9(4)	22.89(19)
N22	1701.1(18)	7118.1(9)	509.2(4)	21.33(19)
N23	1967.5(18)	8833.4(8)	-80.9(4)	21.94(19)
C21	2961(2)	8232(1)	339.2(5)	19.7(2)
C22	-587(2)	6581.3(10)	268.4(5)	23.4(2)
C23	-1664(2)	7149.9(11)	-154.5(5)	24.4(2)
C24	-272(2)	8296.3(11)	-312.0(5)	23.3(2)
O31	2901.4(16)	-2872.5(7)	3371.6(4)	25.30(18)
O32	2853.4(16)	-1167.0(8)	3902.4(4)	29.88(19)
O33	13261.0(17)	2257.9(8)	3023.5(4)	31.2(2)
O34	10324.4(17)	2567.5(8)	3617.9(4)	33.3(2)
C31	3828(2)	-1717.3(10)	3549.4(5)	20.9(2)
C32	6234(2)	-1188.5(10)	3258.8(5)	23.0(2)
C33	7422(2)	135.1(10)	3438.6(5)	23.6(2)
C34	9763(2)	608.3(10)	3104.2(5)	22.8(2)
C35	11097(2)	1910.9(10)	3279.4(5)	21.2(2)
O41	5430.6(15)	4400.4(7)	3490.1(4)	25.15(17)
O42	8420.9(14)	6079.5(7)	3679.2(3)	22.03(16)
O43	6772.8(16)	7203.2(8)	1474.1(4)	30.2(2)
O44	3295.9(15)	5789.8(7)	1276.0(4)	24.90(17)

C41	7451.6(19)	5105.1(9)	3370.9(5)	18.4(2)
C42	8772(2)	4856.2(10)	2830.2(5)	20.0(2)
C43	8439.5(19)	5757.7(10)	2355.5(5)	19.3(2)
C44	5715(2)	5558.0(11)	2136.5(5)	22.9(2)
C45	5273(2)	6233.9(10)	1595.1(5)	20.6(2)
O51	1078.1(18)	-1586.9(8)	1914.7(4)	36.8(2)
O52	207.3(16)	-320.9(7)	1248.7(4)	27.48(18)
O53	10928.3(15)	3645.7(7)	1551.4(4)	25.12(18)
O54	7405.9(15)	3724.2(7)	1034.8(4)	26.63(18)
C51	1597(2)	-563.2(9)	1628.1(5)	19.9(2)
C52	4091(2)	242.5(10)	1825.4(5)	20.1(2)
C53	4849(2)	1396.0(9)	1481.4(5)	20.0(2)
C54	7494(2)	2056.7(10)	1679.4(5)	21.2(2)
C55	8541(2)	3227.3(9)	1380.4(5)	19.8(2)

Table 3 Anisotropic Displacement Parameters ($Å^2×10^3$) for 12srv225. The Anisotropic displacement factor exponent takes the form: $-2\pi^2[h^2a^{*2}U_{11}+...+2hka×b×U_{12}]$

Atom	U_{11}	U_{22}	U_{33}	U_{23}	U_{13}	U_{12}
N1	21.8(5)	25.3(5)	22.9(5)	1.6(4)	3.9(4)	3.1(4)
N2	24.8(5)	30.5(5)	23.0(5)	0.6(4)	4.1(4)	6.4(4)
N3	20.7(4)	24.5(4)	21.0(4)	3.7(4)	2.3(3)	4.3(4)
C1	20.0(5)	24.9(5)	19.5(5)	5.0(4)	0.7(4)	6.1(4)
C2	30.8(6)	32.2(6)	25.1(6)	-2.6(5)	4.1(5)	6.4(5)
C3	29.2(6)	30.0(6)	27.6(6)	-2.9(5)	-0.1(5)	1.7(5)
C4	23.6(5)	27.3(5)	25.8(5)	3.4(4)	0.0(4)	2.5(4)
N21	21.9(5)	21.3(4)	24.8(5)	3.4(4)	-1.4(4)	3.5(4)
N22	22.5(5)	20.0(4)	21.4(4)	3.7(3)	1.0(3)	4.4(4)
N23	22.9(5)	21.9(4)	21.2(4)	3.3(3)	1.2(3)	5.3(4)
C21	21.3(5)	18.8(5)	19.4(5)	0.2(4)	3.7(4)	5.1(4)
C22	22.2(5)	22.1(5)	25.1(5)	1.1(4)	3.3(4)	2.9(4)

C23	21.0(5)	25.7(5)	24.9(5)	-0.2(4)	0.9(4)	2.0(4)
C24	23.6(5)	25.4(5)	21.6(5)	3.8(4)	0.6(4)	6.5(4)
O31	19.5(4)	21.5(4)	31.2(4)	-0.3(3)	3.3(3)	-3.2(3)
O32	27.0(4)	26.2(4)	34.6(5)	-1.1(4)	6.6(4)	1.7(3)
O33	25.7(4)	22.6(4)	40.7(5)	-4.7(4)	13.5(4)	-5.1(3)
O34	28.5(5)	25.2(4)	42.7(5)	-5.6(4)	13.6(4)	-2.7(3)
C31	17.5(5)	19.6(5)	23.8(5)	5.1(4)	-1.7(4)	0.7(4)
C32	19.2(5)	18.8(5)	28.7(6)	3.4(4)	2.6(4)	-1.2(4)
C33	20.4(5)	19.1(5)	28.8(6)	1.6(4)	2.8(4)	-1.1(4)
C34	19.9(5)	17.6(5)	29.0(6)	2.1(4)	2.9(4)	0.1(4)
C35	18.1(5)	19.2(5)	24.5(5)	3.9(4)	0.9(4)	0.3(4)
O41	22.3(4)	21.6(4)	27.4(4)	-0.4(3)	7.0(3)	-4.5(3)
O42	19.1(4)	21.1(4)	22.7(4)	-1.1(3)	2.8(3)	-2.1(3)
O43	24.2(4)	25.7(4)	33.9(5)	12.7(3)	-6.7(3)	-8.7(3)
O44	20.4(4)	20.8(4)	29.5(4)	8.0(3)	-5.6(3)	-3.3(3)
C41	16.6(5)	17.9(4)	19.6(5)	4.3(4)	0.3(4)	1.7(4)
C42	19.2(5)	18.4(5)	21.7(5)	2.9(4)	3.5(4)	2.3(4)
C43	17.5(5)	20.1(5)	18.7(5)	3.2(4)	1.6(4)	0.1(4)
C44	18.9(5)	23.7(5)	23.0(5)	7.1(4)	-0.4(4)	-2.2(4)
C45	17.3(5)	18.6(5)	23.9(5)	3.4(4)	0.2(4)	-0.6(4)
O51	31.0(5)	27.4(4)	41.8(5)	18.1(4)	-14.6(4)	-13.9(4)
O52	22.0(4)	22.4(4)	35.2(5)	8.9(3)	-4.8(3)	-1.0(3)
O53	18.6(4)	18.5(4)	34.8(4)	6.6(3)	-3.2(3)	-3.0(3)
O54	21.7(4)	23.0(4)	33.9(4)	7.6(3)	-1.4(3)	2.1(3)
C51	19.2(5)	16.6(4)	21.9(5)	2.1(4)	2.3(4)	-0.6(4)
C52	18.8(5)	16.8(4)	21.7(5)	2.3(4)	0.4(4)	-2.3(4)
C53	16.9(5)	16.2(4)	25.1(5)	2.5(4)	0.6(4)	-0.5(4)
C54	19.1(5)	16.3(4)	26.0(5)	3.5(4)	-0.6(4)	-0.9(4)
C55	17.9(5)	15.5(4)	24.6(5)	-0.1(4)	1.9(4)	0.6(4)

Table 4 Bond Lengths for 12srv225.

Atom	Atom	Length/Å		Atom	Atom	Length/Å
N1	C1	1.3179(15)		C32	C33	1.5150(15)
N2	C1	1.3558(14)		C33	C34	1.5220(15)
N2	C2	1.3245(17)		C34	C35	1.5107(15)
N3	C1	1.3623(14)		O41	C41	1.2532(13)
N3	C4	1.3484(16)		O42	C41	1.2773(13)
C2	C3	1.4005(18)		O43	C45	1.2517(13)
C3	C4	1.3658(17)		O44	C45	1.2753(14)
N21	C21	1.3219(15)		C41	C42	1.5100(14)
N22	C21	1.3596(14)		C42	C43	1.5392(15)
N22	C22	1.3500(15)		C43	C44	1.5217(15)
N23	C21	1.3560(14)		C44	C45	1.5119(15)
N23	C24	1.3208(15)		O51	C51	1.3195(13)
C22	C23	1.3616(16)		O52	C51	1.2097(14)
C23	C24	1.4037(16)		O53	C55	1.3254(13)
O31	C31	1.3231(13)		O54	C55	1.2111(14)
O32	C31	1.2133(14)		C51	C52	1.5021(15)
O33	C35	1.3293(13)		C52	C53	1.5200(14)
O34	C35	1.2056(14)		C53	C54	1.5162(15)
C31	C32	1.5103(15)		C54	C55	1.5054(14)

Table 5 Bond Angles for 12srv225.

Atom	Atom	Atom	Angle/˚		Atom	Atom	Atom	Angle/˚
C2	N2	C1	117.28(10)		O33	C35	C34	112.42(10)
C4	N3	C1	120.79(10)		O34	C35	O33	123.14(10)
N1	C1	N2	119.60(10)		O34	C35	C34	124.44(10)
N1	C1	N3	119.27(10)		O41	C41	O42	122.31(10)
N2	C1	N3	121.12(11)		O41	C41	C42	120.32(10)
N2	C2	C3	124.25(11)		O42	C41	C42	117.30(9)
C4	C3	C2	116.26(12)		C41	C42	C43	110.42(8)
N3	C4	C3	120.29(11)		C44	C43	C42	111.55(8)
C22	N22	C21	121.03(10)		C45	C44	C43	115.21(9)
C24	N23	C21	117.21(9)		O43	C45	O44	121.71(10)
N21	C21	N22	119.32(10)		O43	C45	C44	120.91(10)
N21	C21	N23	119.66(10)		O44	C45	C44	117.37(9)
N23	C21	N22	121.02(10)		O51	C51	C52	112.22(9)
N22	C22	C23	120.12(10)		O52	C51	O51	123.03(10)
C22	C23	C24	116.21(11)		O52	C51	C52	124.75(9)
N23	C24	C23	124.39(11)		C51	C52	C53	114.20(9)
O31	C31	C32	111.24(9)		C54	C53	C52	108.98(9)
O32	C31	O31	123.73(10)		C55	C54	C53	115.86(9)
O32	C31	C32	125.03(10)		O53	C55	C54	109.69(9)
C31	C32	C33	114.65(10)		O54	C55	O53	124.34(10)
C32	C33	C34	111.02(10)		O54	C55	C54	125.97(10)
C35	C34	C33	113.74(10)					

Table 6 Hydrogen Bonds for 12srv225.

D	H	A	d(D-H)/Å	d(H-A)/Å	d(D-A)/Å	D-H-A/°
N1	H1A	O34[1]	0.900(16)	2.771(16)	3.1958(14)	110.2(12)
N1	H1A	O41[2]	0.900(16)	1.942(16)	2.8315(13)	169.4(15)
N3	H3	O42[2]	0.994(19)	1.618(19)	2.6022(12)	170.2(17)
N21	H21A	O43	0.873(17)	2.066(17)	2.9240(13)	167.4(15)
N21	H21B	N23[3]	0.917(19)	2.190(19)	3.1049(14)	174.9(16)
N22	H22	O44	0.933(19)	1.660(19)	2.5853(12)	170.7(17)
O31	H31	O42[4]	0.94(2)	1.68(2)	2.6094(11)	169.6(19)
O33	H33	O41[5]	0.93(2)	1.67(2)	2.6003(12)	173(2)
O51	H51	O43[4]	0.90(2)	1.69(2)	2.5899(12)	175(2)
O53	H53	O44[5]	0.91(2)	1.68(2)	2.5698(11)	169(2)

[1]2-X,1-Y,1-Z; [2]1-X,1-Y,1-Z; [3]1-X,2-Y,-Z; [4]-1+X,-1+Y,+Z; [5]1+X,+Y,+Z

Table 7 Hydrogen Atom Coordinates ($\text{Å}\times10^{4}$) and Isotropic Displacement Parameters ($\text{Å}^{2}\times10^{3}$) for 12srv225.

Atom	*x*	*y*	*z*	U(eq)
H1A	6670(30)	5281(14)	5889(7)	33(4)
H1B	8960(30)	5412(16)	5491(7)	39(4)
H3	3270(30)	3632(17)	5796(8)	47(5)
H2	7200(30)	2254(14)	4249(7)	31(4)
H3A	3240(30)	1027(15)	4517(7)	31(4)
H4	1370(30)	1865(14)	5329(7)	28(4)
H21A	5880(30)	8363(15)	858(7)	31(4)
H21B	6070(30)	9470(17)	463(8)	47(5)
H22	2430(30)	6699(16)	788(8)	45(5)
H22A	-1360(30)	5779(14)	423(7)	27(4)
H23	-3290(30)	6789(14)	-341(7)	28(4)
H24	-920(30)	8750(13)	-608(6)	26(4)
H31	1320(40)	-3180(18)	3518(9)	58(6)

H33	14000(40)	3050(20)	3164(9)	61(6)
H32A	7390(30)	-1737(15)	3332(7)	37(4)
H32B	5830(30)	-1301(14)	2823(7)	31(4)
H33A	6170(30)	641(14)	3361(7)	31(4)
H33B	7910(30)	211(15)	3874(7)	38(4)
H34A	11000(30)	120(14)	3155(7)	28(4)
H34B	9350(30)	581(15)	2674(8)	39(4)
H42A	8040(30)	4006(13)	2680(6)	23(3)
H42B	10560(30)	4955(14)	2930(7)	30(4)
H43A	9090(30)	6618(13)	2518(6)	25(3)
H43B	9490(30)	5657(13)	2019(7)	28(4)
H44A	4980(30)	4672(16)	2050(7)	40(4)
H44B	4620(30)	5834(15)	2420(7)	39(4)
H51	-420(40)	-2042(19)	1775(9)	60(6)
H53	11610(40)	4396(19)	1419(9)	58(6)
H52A	5370(30)	-277(14)	1782(7)	29(4)
H52B	4030(30)	443(14)	2238(7)	28(4)
H53A	3680(30)	1932(14)	1547(7)	31(4)
H53B	4810(30)	1175(14)	1061(7)	28(4)
H54A	8660(30)	1519(14)	1616(7)	30(4)
H54B	7550(30)	2283(14)	2105(7)	33(4)

Appendix C Enthalpies of transition.

C.1 2-Aminopyrimidine.

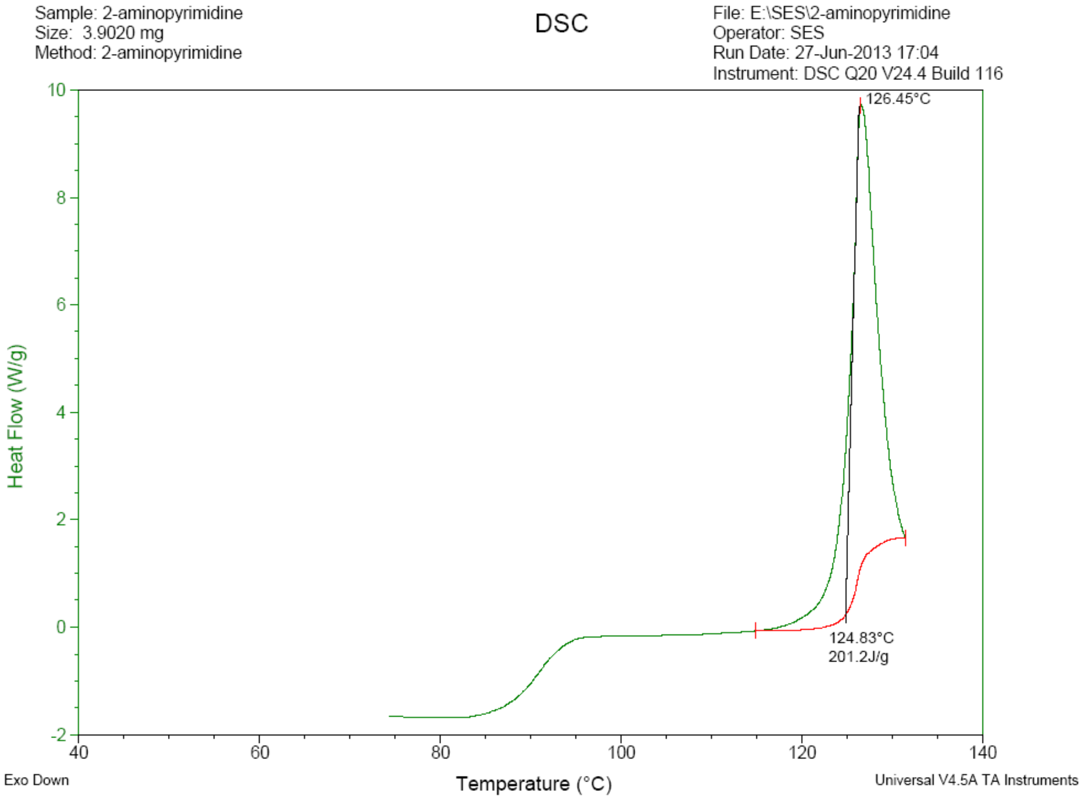

C.2 Glutaric acid